Optomechanical transducer based on a single quantum dot

Nitika Vaish

Communauté
UNIVERSITÉ Grenoble Alpes

THÈSE

Pour obtenir le grade de

DOCTEUR DE LA COMMUNAUTE UNIVERSITE GRENOBLE ALPES

Spécialité : **NANOPHYSIQUE**

Arrêté ministériel : 25 mai 2016

Présentée par

NITIKA VAISH

Thèse dirigée par **Jean-Philippe POIZAT,**
Communauté Université, Grenoble Alpes

préparée au sein du **Institut Néel – CNRS Grenoble**
dans **l'École Doctorale de Physique de Grenoble**

Optomechanical transducer based on a single quantum dot

Thèse soutenue publiquement le **17 décembre 2019**,
devant le jury composé de :

Monsieur Pierre-François COHADON
Maître de Conférences, Laboratoire Kastler Brossel, ENS, Paris,
Rapporteur
Monsieur Stéphane BERCIAUD
Professeur, Institut de Physique et Chimie des Matériaux de Strasbourg,
Rapporteur
Madame Anaïs DRÉAU
Chargée de Recherche, Laboratoire Charles Coulomb, Montpellier,
Examinateur
Monsieur Maxime RICHARD
Directeur de Recherche, Institut Néel, Grenoble, Président

Dedicated to my beloved parents,
and to my late grandmother

Acknowledgements

Firstly, I would like to express my sincere gratitude to the members of jury Dr. Pierre-François Cohadon, Prof. Stéphane Berciaud, Dr. Anaïs Dréau and Dr. Maxime Richard for taking the time and effort to evaluate this work.

This work would not have been possible without the contributions of many colleagues in Institut Néel and CEA Grenoble. I would like to thank each one of you who helped me to gain perspectives by imparting knowledge both scientifically and otherwise and thereby impacted my individual development as a scientific researcher.

First of all I would like to acknowledge my supervisor Dr. Jean-Philippe Poizat for giving me such a great opportunity. We have started working together five years back when I was an intern and a fresher in research. His wisdom, enthusiasm and support over the last few years had really helped me to understand and focus on the project and leading it to a successful end. Without his critical comments and productive suggestions this would have been a very difficult task. He was always there to guide me through any obstacle and those daily discussions had made the work much more easier and played a major role in the successful completion of a very difficult and complex project. I also appreciate him for helping me in settling down in Grenoble at the beginning of my PhD. I wish you all the very best for future research projects and hope to see you back sometime.

I would like to acknowledge the support and contribution of Dr. Jan Kettler, who was the Post doctorate in our small team, during the major part of my PhD. He had made this complex experiment simpler both scientifically and technically. His knowledge and experience helped me to understand the challenges in a better way and guided me towards the efficient solution. In addition to this, he developed Pyhton programs which played a major role in performing complicated and long measurements easily and effectively. I really enjoyed working with him and wish him good luck for his future endeavours.

I would like to thank Dr. Julien Claudon, Dr. Jean-Michel Gérard and their team,firstly, for fabricating the samples investigated during this PhD and secondly, for their fruitful insights during the discussions and meetings we have had.

I would also like to thank Dr. Maxime Richard, Dr. Alexia Auffèves and their team for the theoretical support. They guided us through this sophisticated experiment and helped us to verify the observed results with the theory.

Expertise of Dr. Olivier Arcizet and Dr. Benjamin Pigeau on the optomechanics

subject have indeed helped me during the course of this work. I would like to acknowledge their productive suggestions whenever we hit an obstacle in the experiment which allowed us to continue our quest towards the goal of this work.

I would like to express my gratitude towards Dr. Pierre Verlot. His knowledge and expertise on the subject of opto-mechanics gave us new insights to the experiment and his calculations helped us in improving the experiment. Besides, I would also like to thank Dr. Olivier Bourgeois for the fruitful calculations on understanding the photothermal effect.

I would like to appreciate Dr. Pierre-Louis de Assis for his constant help from Brazil together with few months we spent together in the lab chasing the quantum hammer signal. He provided us with Comsol simulations for different situations we faced during this work. His knowledge and enthusiasm have inspired me to improve myself.

I would like to thank former PhD students Dr. Dmitrii Tumanov and Dr. Hoai Anh Nguyen who have helped me in settling down in the lab during the internship period and made me comfortable with the experiment. Besides, I would also like to appreciate the time invested by Dr. Laure Mercier de Lépinay and Dr. Benjamin Besga during the beginning of my PhD to assist me with the experiments.

I would like to extend my gratitude towards my fellow colleagues who have been there for all the scientific and non-scientific exchanges we have had during the lunch and coffee breaks when needed the most to vent out the stress. I would also like to appreciate the administrative and technical support from the institut which have been a huge help.

This PhD work would not have been possible without the financial support. I would like to thank ANR for funding the project QDOT and Foundation Nanosciences for funding my PhD scholarship. I would also like to acknowledge Dr. Alain Fontaine for all the fruitful exchanges both scientific and otherwise.

Last but not the least I would like to thank my family and friends for always being there and supporting me no matter what. A special thanks to my parents Rajeev Kumar Vaish and Neetu Vaish for the unconditional love and support not only during this PhD but all my life. Whatever I could achieve today is only because of you. I love you both. I would like to thank my sister, brother and cousins for always motivating me and make me feel part of all the missed events over the video calls.

Next I want to thank my small family here in Grenoble, my very close friends: Monika Tripathi and Akanksha Kapoor. They have been a constant support for the last three years both mentally and emotionally. Our dinner times together were one of the moments I used to look forward in a day to discuss anything or everything. Thank you so much guys. Thank you Kritika Narang for being there throughout and especially for flying down form Sweden and support me on one of the important day of my life. The delicious Tiramisu was perfect to mark the completion of this journey. I would also like to thank my other Indian friends (list is long) who have been there in all good and bad times. Thank you for the wonderful memories which I will cherish for the rest of my life.

Abstract

In the context of nanomechanics, quantum hybrid systems are mechanical oscillators coupled to a single individual quantum system. These systems offer radically new possibilities for the fabrication of extremely sensitive and ultra-compact optomechanical transducers, which can serve as position sensors or nano engines.

The hybrid system investigated in this work consists of a single semiconducting quantum dot (QD) embedded in a vibrating photonic wire. It has been shown in the team, a few years ago, that the transition energy of the QD depends on the strain generated by the wire oscillations.

In this thesis, we demonstrate the reverse effect, where each photon emitted by the QD comes along with a strain induced force which drives the oscillations of the photonic wire. This realizes a nano engine run by a single laser driven quantum object. The effect has been coined "Quantum Hammer effect". This result opens the possibility for the future realization of a quantum state of motion via the transfer of the "quantumness" of a two-level system towards the motion of a macroscopic mechanical oscillator.

Résumé

Dans le contexte de la nanomécanique, les systèmes hybrides quantiques sont des oscillateurs mécaniques couplés à un seul objet quantique individuel. Ces systèmes offrent des possibilités radicalement nouvelles pour la fabrication de transducteurs optomécaniques extrêmement sensibles et ultra-compacts, qui peuvent servir de capteurs de position ou de nano-moteurs.

L'objet étudié dans ce travail est un système hybride constitué d'une boite quantique semi-conducteur unique couplée aux vibrations d'un fil photonique. Il a été démontré dans l'équipe, il y a quelques années, que l'énergie de transition de la boite quantique dépend de la contrainte générée par les oscillations du fil.

Dans cette thèse, nous démontrons l'effet inverse, où chaque photon émis par la boite quantique s'accompagne d'une force qui entraîne l'oscillations du fil photonique. Ceci permet de réaliser un nano moteur fonctionnant grâce à la contrainte générée par une seule boite quantique pilotée par laser. L'effet est appelé "effet marteau quantique". Ce résultat ouvre la possibilité de la réalisation future d'un état quantique du mouvement par le transfert de la « quanticité » d'un système à deux niveaux vers le mouvement d'un oscillateur mécanique macroscopique.

Contents

Chapter 1

Introduction

1.1 Context

With the advances in nanofabrication, it is now possible to develop micro and nano-mechanical devices. It has enabled the realization of ultra-small mechanical oscillators that are used in ultra-sensitive position, force, or mass measurement devices leading to the development of micro-electromechanical systems (MEMS). To enhance the sensitivity, it is necessary to further scale down the size leading to the development of nano-electromechanical systems (NEMS). In this work, we will present a hybrid optomechanical system [1] consisting of a quantum dot (QD) embedded in a mechanical oscillator. In this system, the position of the mechanical oscillator is coupled to the energy of the QD. This appears as an influence of mechanical motion on the optical properties of quantum dots (QDs) and conversely as driving of the mechanical oscillator by modulating the QD population. This reverse effect allows us to develop a nano engine [2, 3] based on a single quantum dot, and its experimental realization is the main goal of this thesis. This hybrid system opens the perspective to develop and optimize a quantum-limited integrated sensor that will overcome the limitations of the proposed nano-electromechanical [4, 5], nano-optomechanical [6, 7] systems.

1.2 Mechanical oscillator as transducers

A mechanical oscillator has the ability to respond to a physical stimulus (such as electric, magnetic, or optical forces) with a deformation that can be easily detected by an optical or electrical mean. It, therefore, acts as a transducer leading to a broad range of phenomena accessible for detection. Several readout protocols can be used to probe external fields such as measurements of resonance frequency shifts, changes of mechanical damping rates, or modification of the driven oscillating amplitude when the oscillator enters into interaction with the force under investigation.

The advances in fabrication technology allow the realization of micromechanical oscillator, which leads to a major milestone in the application of mechanical oscillators with

the invention of atomic force microscopy (AFM) [8] in 1986. This method revolutionized surface science by allowing to image surfaces with a resolution in the sub-nanometre range by scanning them with a sharp tip attached to a resonating cantilever. Following the invention of AFM, mechanical oscillators have constituted a key component in a wide variety of sensing experiments. The outstanding success of such systems is related to their reduced mass, which leads to very low power consumption and increased sensitivity. Therefore, they have attracted the attention of physicists and are used in ultra-sensitive position [9, 10], force [7, 11], mass [12], charge [13] or single spin [14] detection. This has led to the development of microelectromechanical systems (MEMS) that are now omnipresent in our daily life in the form of gyroscopes or loudspeakers in smartphones, accelerometers in vehicles or gas sensing devices in medical applications

In the strive for even higher sensitivities and faster operation, the miniaturization of the mechanical oscillators have become important, leading to the development of nanoelectromechanical systems (NEMS) [15], in the late 1990's. The reduced masses of such devices results in higher force sensitivities and resonance frequencies (scales inversely with size). However, this extreme down-sizing has its own challenges. Firstly, because of the extremely reduced dimensions, these systems are extremely difficult to detect as the diffraction of light limits the current optical detection scheme. Thus, optical detection of the motion of structures whose size is less than 100 nm is difficult and requires the development of new detection techniques. One such method is the detection using an electron beam [16]. Secondly, their ultra-low mass makes them extremely sensitive to the backaction noise. Backaction noise describes the perturbations of the mechanical system arising from the measurement process itself. According to the quantum mechanical principle, an increasingly precise measurement of the position of the oscillator is accompanied by a significant force acting back on the oscillator, setting a lower limit for quantifying the noise of a measurement. This limit is known as the standard quantum limit (SQL) [17]. Within the two decades of NEMS, researchers have successfully observed the motion of sub-wavelength nanomechanical systems with quantum-limited imperfection [6, 18]. Moreover, quantum backaction noise [19], and quantum ground state of motion [4, 5, 20] using a piezoelectric resonator, a superconducting resonator, and an optomechanical crystal was also observed.

The majority of these outstanding demonstrations have been achieved with devices that were designed explicitly for enhanced backaction effects [5, 19], with the nanomechanical resonator being generally embedded into a complex geometry. Therefore, such systems are not adapted to sensing applications. This project proposes to tackle these technological challenges and to develop an optomechanical transducer based on a single quantum dot embedded within a photonic wire.

1.3 Hybrid nanomechanical systems

Advances in nanofabrication allows the coupling of a mechanical oscillator with a large variety of other quantum systems such as atoms and ions, electronic spins, etc leading to the development of so called hybrid systems [1]. Figure 1.1 shows the principle of one such hybrid system where a quantum two-level system is coupled to a nanomechanical oscillator.

Figure 1.1: Quantum hybrid system: Coupling of a mechanical oscillator to a controllable quantum system.

The benefits of such hybrid systems are quite diverse. On one hand, the motion of the mechanical oscillator can be used as a sensitive probe and readout device for static and dynamic properties of the quantum system. On the other hand, coupling the oscillator to a coherent and fully controllable two-level system provides a way to prepare and detect the states of mechanical motion. However, from a practical point of view, the realization of a hybrid system by combining a mechanical oscillator with quantum systems faces substantial challenges. For the observation of truly quantum effects, both the oscillator and the quantum system must be exceptionally well isolated from the environment to avoid de-coherence. Various hybrid systems have been proposed and some of them have already been implemented in experiments. This includes coupling a mechanical oscillator with solid-state single spin [14, 21–28], a superconducting qubits [4, 29, 30], or a quantum dot (QD) [31–35].

The hybrid system investigated in this study consists of a semiconductor InAs QDs embedded in a GaAs photonic wire [35, 36]. Figure 1.2 shows the scanning electron microscope image of the photonic wire containing InAs QDs. This trumpet waveguide system was developed in order to have efficient photon extraction emitted by the coupled QDs. Extraction efficiencies up to 75 % have been obtained [36] therefore allowing the realization of efficient single-photon sources [37, 38]. The choice of the "trumpet-like" design of the photonic wire is to have efficient extraction which will be described in detail in Chapter 2.

There are several important advantages of this approach over previous nano optomechanical systems: Firstly, the system combines ultra-high optical coupling to the QD [36], ultra-high strain coupling rate [35, 39]. Secondly, this large strain coupling features an embedded motion read-out capability by having their position coupled to the energy of a QD [35, 39]. Conversely, with the reverse effect studied in this work, it is possible to monitor the QD state via nanomechanical motion detection.

1.3.1 Strain-mediated optomechancial coupling

The two components of the hybrid system investigated in this study i.e. the QD and the photonic wire, are coupled through strain. This section will give a brief description of this strain mediated optomechanical coupling. The detailed description of the coupling is presented in the last part of Chapter 2.

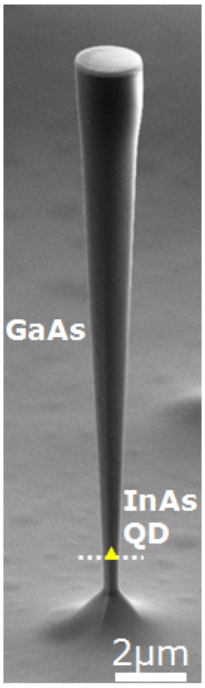

Figure 1.2: Scanning electron microscope (SEM) image of the hybrid system, investigated in this work, consisting of InAs QD embedded within a GaAs photonic wire. Image taken by J. Claudon.

1.3.1.1 Dynamic and static modulation of QD transition energy

As shown in figure 1.2, the QDs are located near the base of the photonic wire, where the strain field is most significant for the two flexural modes of the wire. When vibrating along one of the flexural mode, the photonic wire experiences deformations yielding to strain changes at the QD location. These strain changes result in frequency shifts of the excitonic resonance [34,35], whose detection can, therefore, be used for probing the nanomechanical motion in an extremely sensitive manner [40]. This aspect of the optomechanical coupling has been demonstrated successfully in the team recently, both via dynamic [35,41] and static modulation [39,42].

The strain experienced by the QD will depend on its position from the wire axis, being maximum for the QD at edge and zero for the dot at center. This opens the possibility to map the QD position based on the coupling. Thus, it offers a non-destructive way to determine the QD position within the photonic wire with an uncertainty of $\pm$ 1 nm, for dots close to the axis of the wire, and of at most $\pm$ 35 nm, for dots close to the edges [43]. Moreover, with the static tuning of QD energy, it is possible to have relative strain-tuning of several QDs embedded in the same wire [39]. It opens up the possibility of realization of collective effects based on these structures, in which several (at least 2) QDs have to be brought in resonance.

1.3.1.2 Quantum Hammer effect

In the reverse effect of this strain coupling, the photonic wire will experience frequency shifts and damping or amplification depending on the state of the two-level system. In other words, each photon emitted by the QD comes along with a force that may drive the nanomechanical motion. Therefore, this effect is coined as the Quantum Hammer effect, as each photon gives a kick to the photonic wire and therefore acts like a hammer. Detecting the nanomechanical motion can, therefore, be utilized for monitoring the QD state in a non-demolition way. Theoretical approaches have been developed to predict and control the effect of this backaction effect [44]. It scales as the ratio of hybrid coupling rate g_m to mechanical resonance frequency Ω_m i.e., g_m/Ω_m. With the system parameters that we already have from [35], the effect is predicted to bring the photonic wire to an energy hundred times above the Brownian motion at a temperature T = 5 K.

1.4 Motivation for this thesis

The quantum hammer effect, as presented in the previous section, is unexplored so far, and therefore its realization is the primary goal of this thesis. This will realize a nano engine run by a single driven quantum object, on the one hand, and allows non-optical detection of QD resonance on the other hand. In this work, the QD is driven by a laser modulated at the mechanical frequency, and the effect of the strain-induced "hammer force" is observed on the optically detected motion of the photonic wire. We have proven that using a single quantum object we can induce motion in a photonic wire. This result opens the possibility for the future realization of a quantum state of motion via the transfer of the "quantumness" of a two-level system towards the motion of a macroscopic oscillator.

1.5 Thesis Outline

This thesis is organized in 4 upcoming chapters:

Chapter 2 describes in detail the hybrid system investigated in this study, which consists of InAs QDs embedded in a GaAs trumpet-like photonic wire. The chapter begins with the general description of the fabrication, structure, and properties of self-assembled InAs QDs. Following is the description of the design of the photonic wire (trumpet-like), which is the result of enhancing the extraction efficiency. The fabrication of the final hybrid structure will be presented. The chapter will conclude with a detailed presentation of reciprocal strain mediated optomechanical coupling in detail. Theoretical aspects of the quantum hammer effect will be presented in detail.

Chapter 3 gives the details on the basic optical characterization of self-assembled InAs QD. The experimental setup is presented for photoluminescence (PL) and resonant excitation (RE) spectroscopy. The characterization of different emission lines on the basis of non-resonant laser power dependence and polarization dependence is then demonstrated.

The chapter then focuses on the resonant excitation of the QD. An experimental procedure to detect the emitted signal via phonon side band is presented. Effect of the probe laser (laser used for optical detection of the motion of photonic wire top facet) on the PL and RE signal is then presented. Other experimental challenges faced in the realization of RE spectroscopy and hence quantum hammer effect, are then presented together with the measures taken to overcome them. Finally, the resonant characterization of the QD line mainly studied in this work is presented.

Chapter 4 focuses on the optical detection of photonic wire's motion. Principle of the optical motion detection technique is presented first. Following is the description of the detection sensitivity β, an important parameter in the motion detection process. Dependence of β values on different experimental parameters is presented and compared with the simulation results. The experimental setup for optical detection is then presented together with the description of different experimental components. This technique allows us to measure the Brownian motion of the photonic wire at 5 K, which is on the order of few pm. The last section of this chapter presents the possibility of optical actuation of photonic wire motion.

Chapter 5 presents the experimental realization of the quantum hammer effect. It presents the main results and challenges (and measures taken to overcome them) faced during the realization of this experiment. The chapter starts with the description of the experimental setup used for the quantum hammer experiment. The experimental protocol is presented, and a detailed description of the data analysis is given. Finally, the experimental results are presented, proving the successful realization of the quantum hammer effect.

Chapter 6 summarizes the thesis and gives the basis for future investigations.

Chapter 2

Introduction to Quantum Hammer effect

This chapter will give a detailed presentation of the sample studied in this thesis. Section 2.1 gives an overview, fabrication and properties of semiconductor quantum dots (QDs). Section 2.2 presents the hybrid system obtained by coupling the QD inside a photonic nanostructure followed by the details on the fabrication process and summary of the final sample investigated in section 2.3. The final section 2.4 will present the Quantum Hammer effect which is the result of the inverse strain mediated optomechanical coupling between the QDs and the photonic wire. The coupling from the photonic wire point of view has been studied in the group before, both statically [35] and dynamically [39]. The goal of this thesis is to study the reverse effect.

Contents

2.1 Self assembled quantum dots

2.1.1 Overview

Quantum dots (QDs), are the semiconductor nanostructures generally formed of II-VI or III-V semiconductors. QDs were first discovered in 1980 by Alexei Ekimov in a glass matrix and in 1982 by Louis E. Brus in colloidal solution [45]. Since then they have been studied and are the core of nanotechnology. QD is a droplet of one semiconductor material surrounded by other semiconductor material of larger band gap. The typical size of the structure is in the range 1 to 100 nm. Inside such a QD, both the charge carriers, electrons and holes are confined in all three dimensions. Due to quantum confinement effects, energy spectrum of charge carrier is completely quantized or discrete. Therefore, semiconductor QDs possess optical properties similar to the one of atoms and are thus referred to as "artificial atoms".

QDs have unique size dependent optical and electronic properties. QDs have attracted considerable interest in the research field and have led to wide range of high-performance new applications, especially in fields of biology (imaging, drug delivery, and diagnosis) [46], optoelectronics such as lasers, photodetectors, photovoltaics, light emitting diodes [47–50], quantum communications [36, 51–53], and other multimodal applications [54].

2.1.2 Self-assembled InAs QDs

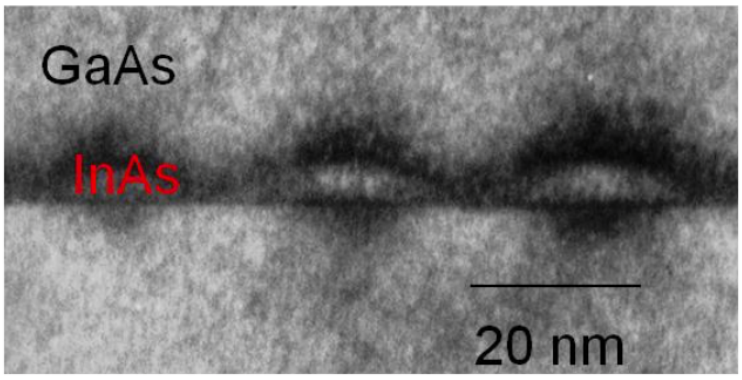

Figure 2.1: Transmission electron microscopy (TEM) image of the cross section of a self-assembled InAs quantum dot embedded in a GaAs matrix. [55].

The QDs used in this study are self-assembled InAs QDs embedded in GaAs matrix. They are grown by molecular beam epitaxy (MBE), using the layer-by-layer growth method ("Stranski-Krastanov" growth mode). This method uses the relief of elastic energy between

two materials with a large lattice mismatch to form an epitaxial structure. The lattice parameter of InAs is 7% larger than the one of GaAs. Initially, deposition of one material on the substrate of the other material lead to formation of strained layer which is referred to as 'wetting layer'. During the growth process when layer thickness reaches above critical value (which depends on strain and the chemical potential of the deposited film), the strain accumulated in the InAs layer is elastically relaxed through the generation of three-dimensional InAs islands, which are the QDs. The QDs are then capped with a GaAs layer in order to protect it from oxidation and to prevent interactions with surface states. Resulting QDs have dimensions of about 20-30 nm in diameter and 2-3 nm in height. Figure 2.1, shows the transmission electron microscopy (TEM) image of the InAs QDs capped by GaAs. The average size, shape and surface density of the dots can be controlled to some extent by the growth parameters (temperature, deposition rate, etc..).

2.1.3 Electronic states in single quantum dots

To determine the structure of the energy levels of an electron in a crystal, we solve the time independent Schrödinger equation:

$$\mathtt{H}\Psi(\overrightarrow{\mathtt{r}}) = \mathtt{E}\Psi(\overrightarrow{\mathtt{r}}) \tag{2.1}$$

where Ψ is the wave function of the electron in the crystal and H is the Hamiltonian:

$$\mathtt{H} = \frac{\overrightarrow{\mathtt{p}}^2}{2\mathtt{m}} + \mathtt{V}(\overrightarrow{\mathtt{r}}) \tag{2.2}$$

with V $(\overrightarrow{\mathtt{r}})$, the interaction potential between the electron and the crystal. Because of the periodic structure of the crystal, Bloch's theorem states that wave functions can be put in the form:

$$\Psi_{\mathtt{n},\overrightarrow{\mathtt{k}}}(\overrightarrow{\mathtt{r}}) = \mathtt{u}_{\mathtt{n},\overrightarrow{\mathtt{k}}}(\overrightarrow{\mathtt{r}})e^{\mathtt{i}.\overrightarrow{\mathtt{k}}.\overrightarrow{\mathtt{r}}} \tag{2.3}$$

where $\overrightarrow{\mathtt{k}}$ is a wave vector and n is the band index. The eigen values $\mathtt{E}_{\mathtt{n},\overrightarrow{\mathtt{k}}}$ associated with the vectors $\Psi_{\mathtt{n},\overrightarrow{\mathtt{k}}}$ are called crystal energy bands, which can usually be approached with a parabolic law for a wave vector in the vicinity of $\overrightarrow{\mathtt{k}} = 0$:

$$\mathtt{E}_{\mathtt{n},\overrightarrow{\mathtt{k}}} = \mathtt{E}_{\mathtt{n},0} + \frac{\hbar^2\overrightarrow{\mathtt{k}}^2}{2\mathtt{m}^*} \tag{2.4}$$

where m* is the effective mass of the electron in band n.

In case of semiconductor QDs, the confinement potential energy along the growth direction results in a series of quantized energy levels. The confinement potential of a QD can be described simply by a square-well potential as shown in figure 2.2(a). In general, the quantized energy spectrum of a QD can be found by solving the Schrödinger equation [56].

In order to give the complete description of the electronic states in InAs QDs surrounded by GaAs, we have to consider the entire system. The carriers can not only populate the confined electronic states of the InAs QDs but also the electronic states of the GaAs barrier and the InAs wetting layer, characterized by three different types of confinement. The corresponding energy levels of the entire system is illustrated in figure 2.2(b). A QD can sustain trapped states for both the carriers, i.e. electrons in the conduction band and holes in the valence band at cryogenic temperature. An exciton is formed by an electron and hole pair due to the attractive Coulomb force which can be spatially localized inside the QD during its lifetime (in order of ns). These excitons can recombine either radiatively or non-radiatively.

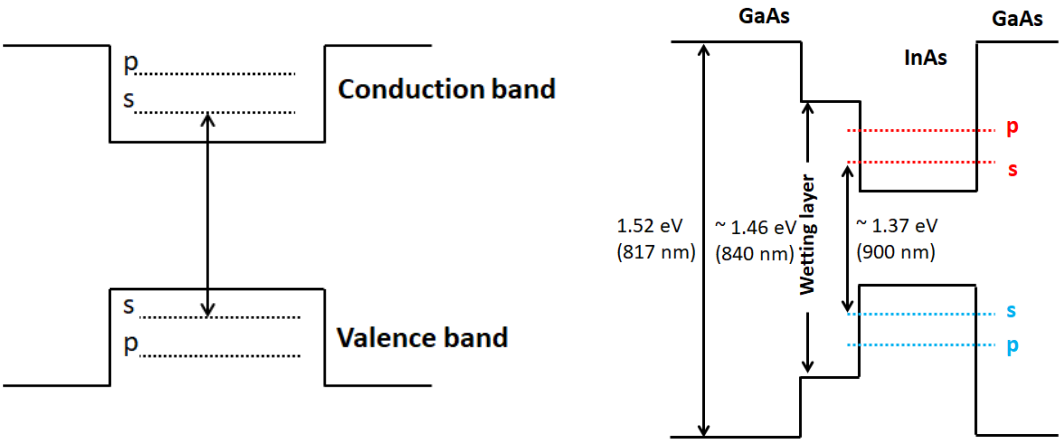

(a) (b)

Figure 2.2: (a) **Conduction band and Valence band energies in a QD:** The confinement potential energy in the growth direction results in a series of quantized levels. (b) **Sketch demonstrating of energy levels for a InAs/GaAs QD:** Band-gap of wetting layer has a value in between the value for GaAs and InAs. Dashed red and blue lines are the discrete energy levels of electrons in conduction band and holes in valence band respectively.

2.1.4 Optical excitation methods

The energy levels of conduction band and valence bands in a InAs QDs surrounded by GaAs are shown in figure 2.3. There are three possible mechanisms for exciting the carriers in the QD.

The first way is the "above band excitation". In this case, as shown in figure 2.3(a), the excitation energy is above the band gap of GaAs (surrounding material of the QD). The band gap of GaAs at cryogenic temperature is 1.52 eV (corresponding to a wavelength of 817 nm). This excitation scheme generates charge carriers in GaAs and only a fraction of these charge carriers can be captured by the wetting layer. These carriers then relax into the QD excited state via emission of phonons. When an electron reaches its ground state within the conduction band, the only remaining decay path is the inter-band transition to the valence band. This transition is radiative with a lifetime on the order of 1 ns [57]. This process is called "photoluminescence (PL)" of the QD and is a standard tool to study optical emission properties of a single QD. Photoluminescence spectroscopy performed in this work is presented in detail in Chapter 3.

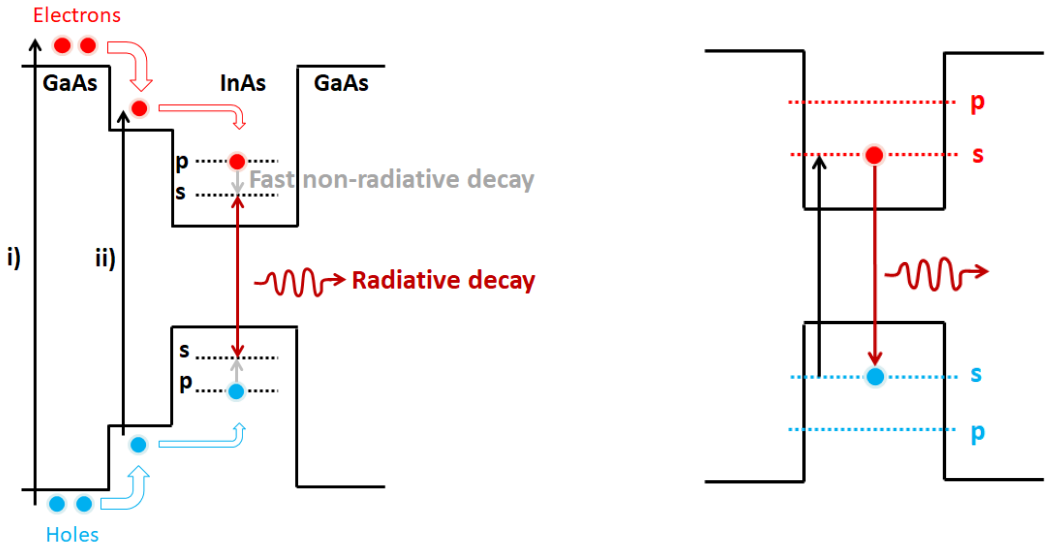

Figure 2.3: (a) **Schematic of non-resonant excitation methods:** i) Above band excitation. and ii) Wetting layer excitation. The generated carriers are trapped by the QD potential well. Once inside the QD, these carriers then relax quickly to the QD ground states via non-radiative decay process. The carriers at the ground state then recombine via inter-band transition from conduction band to valence band and emit a photon after a characteristic lifetime of about 1 ns. (b) **Schematic of resonant excitation method:** The ground state of the QD is directly probed.

The second method is the "wetting layer excitation". The excitation energy is chosen

slightly below the GaAs band gap, within the wetting layer continuum as shown in figure 2.3(a). In this excitation scheme, the carriers are generated directly in the wetting layer and relaxes to the QD states, to be finally decayed radiatively. The advantages of this scheme over the above band excitation scheme are a) it helps decreasing the time required for particles to relax within the conduction and valence band (on the order of 10 ps) and b) it prevents unwanted heating of GaAs and allow the exciting light to propagate within the photonic wire without being absorbed. In this work, we used this approach when performing non-resonant excitation experiments. These two excitation schemes are non-resonant and do not depend highly on the particular wavelength used.

In addition to these non-resonant excitation methods, InAs QDs can also be excited by the resonant excitation method, in which the excitonic ground states are directly probed as shown in figure 2.3(b). It can be performed by tuning the laser on resonance with the ground states of the QD i.e. by creating the electron and hole in the s-shell (or creating a "s-shell exciton). Since, the carriers are generated directly within the s-shell of QD, no additional relaxation process is needed before the radiative recombination process. In this method, the excitation laser frequency has to be exactly the same as the emission frequency. Thus, the scattered light from the laser is a serious problem for the detection of QD emission in this method. In our study, to overcome this problem, we will perform the resonant excitation spectroscopy using the cross-polarization technique to suppress the back-scattered light, already adapted by A. H. Nguyen in his work [38]. This technique is discussed in chapter 3. In case of the resonant excitation of higher energy states of the QD i.e. "p-shell" excitation, charge carriers quickly (in order of ps) decay to the corresponding ground states.

2.1.5 Multi-excitonic states

So far it has been stated that only a single electron-hole pair i.e. a single exciton state is created within the QD. However, QDs can contain multiple electron and/or holes, which leads to additional transitions besides the single neutral excitons. In general, the occupation of QD shells follows the Pauli's exclusion principle which states that the ground state of the QD can be occupied by only two electrons or two holes of opposite spins. This creates four types of excitonic quasi-particles as shown in figure 2.4.

In the first case (see figure 2.4(a)), one single exciton (X) occupies the QD and its recombination generates a photon at energy $\hbar\omega_{\mathrm{X}}$. This emission energy depends on the discrete energy levels of the ground state of conduction and valence band. In the second case (see figure 2.4(b)), two pairs of electron-hole occupy the QD. Therefore, it is called biexciton (XX). Its emission frequency ω_{XX} corresponds to the transition from XX to X. When a carrier is captured inside a neutral dot, the Coulomb interactions plays a crucial role. When more than one electron-hole pair are created in the dot, net exchange interactions has to be considered in addition to the Coulomb interactions between the two excitons.

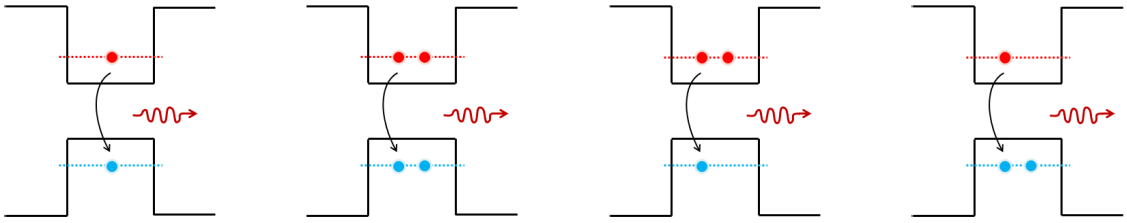

(a) exciton **(b)** biexciton **(c)** negative trion **(d)** positive trion

Figure 2.4: Schematic of multi-particle states of a single quantum dot: Four types of excitonic quasi-particles exist due to Pauli exclusion principle.

The energy difference between the exciton and biexciton transitions is called the binding energy. This binding energy changes from dot to dot depending on the degree of carrier confinement. The binding energy can vary form a few meV to a few tens of meV.

In case of a charged dot (see figure 2.4(c) and 2.4(d)), the dot consist of one exciton plus an additional charge, electron or hole to form either negative trion (X^-) or positive trion (X^+) respectively. The presence of the additional charge makes the emission energies of the charged excitons different from the neutral exciton (X). Therefore, it is possible to observe spectrally a PL spectrum which corresponds to the recombination of a charged exciton [58].

2.2 Quantum dots embedded in photonic wires

QDs embedded in a bulk semiconductor material emit light in all directions. Moreover, the QD is surrounded by a high refractive index material, which causes internal reflections at the semiconductor-air interface. As a result, only a few percent of light can be finally extracted. To improve the photon collection efficiency, one can couple the quantum emitter to a well defined mode of an optical field. One such approach is to couple the QDs with the photonic wires [37,59,60]. The 'trumpet like' or 'inverted cone' geometry of the photonic wire is adapted for efficient collection of light. Unlike resonant structures [61–66], this structure does not feature cavity and relies on a geometrical screening of radiation modes to ensure large coupling between the QD and the guided mode [60]. In practice, this geometry was reported to have a broadband and efficient spontaneous emission (SE) control [59] with extraction efficiency upto 0.75 [36].

Let us first consider an infinite cylindrical photonic wire with diameter d as shown in figure 2.5. These structures provides a confinement of the optical field inside the photonic wire in the two lateral dimensions (x and y) and the mode propagates freely in the z direction. Depending on the diameter of the photonic wire, the emitter is coupled to

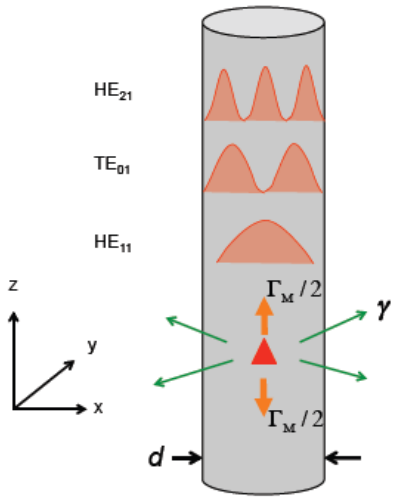

Figure 2.5: Schematic of different guided modes for an emitter embedded within a cylindrical photonic wire. Figure taken from [55]

one or several guided modes that are supported by the structures (HE_{mn}, EH_{mn}, TE_{mn}, TM_{mn}) and to a continuum of free-space modes. The relevant figure of merit of the one-dimensional photonic waveguide is the b_o factor describing the spontaneous emission rate into the desired mode Γ_M over the total emission rate Γ_{tot},

$$b_o = \frac{\Gamma_M}{\Gamma_{tot}} \tag{2.5}$$

2.2.1 Effect of photonic wire diameter and QD position on b_o

If γ is the rate of decay in all other modes. Then, $\Gamma_{tot} = \Gamma_M + \gamma$. Here, Γ_M is considered as the decay rate into the fundamental guided mode HE_{11}. Therefore, in order to have high b_o, γ has to be minimized. Figure 2.6 [59] shows the evolution of spontaneous emission as a function of the photonic wire diameter, for a QD located at the center of the wire. It has been noted that the value of b_o exceeds 90% when the photonic wire diameter is in the range 0.2λ - 0.29λ, with a maximum value of 95% at 0.24λ (λ is the wavelength of the emitter).

In addition to the photonic wire diameter, influence of the QD position on b_o is also considered. If the QD is off-axis as shown in figure 2.7, where the QD is located at the position ρ from the central axis of the photonic wire. A self-assembled QD features optical dipole components perpendicular to the growth axis [67], that coincides with the

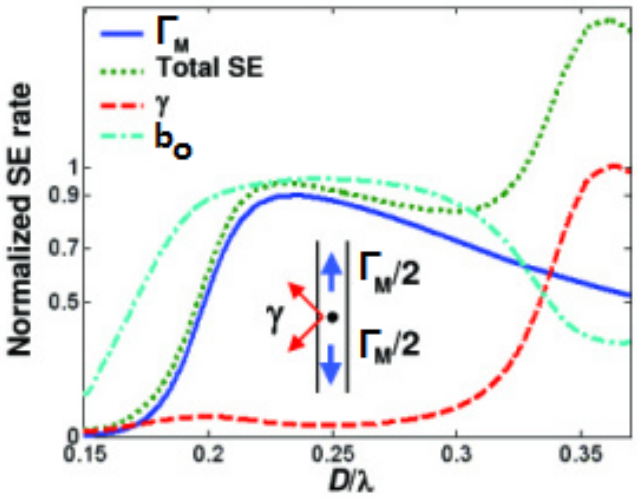

Figure 2.6: Dependence of spontaneous emission rate on the diameter of the photonic wire: Blue solid curve shows the emission Γ_M into the fundamental mode HE_{11}. Red dashed curve shows the emission in leaky modes. QD is located at the center of the photonic wire. Figure taken from [59].

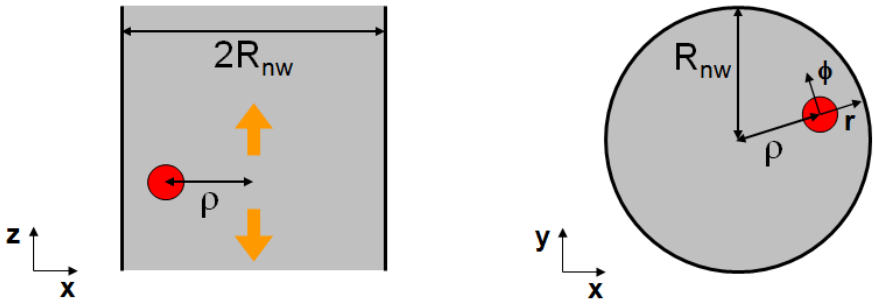

Figure 2.7: Sketch demonstrating the case for a QD at a random position inside the photonic wire: considering a QD located at a position ρ away from the center axis of the photonic wire. The calculation of spontaneous emission coupling rate b_o as a function of ρ is carried out for two orthogonal directions ϕ and r. Figure provided by N. Gregersen.

axis of the photonic wire. In the following calculations, the QD is, therefore, modelled as two orthogonal, linear optical dipoles oriented along the radial (r) and the azimuthal (ϕ) directions. The results of b_o for three different photonic wire diameters are presented in figure 2.8, where b_o is plotted as a function of the ratio between the distance of the QD from the axis and the wire radius. $\rho/r = 0$ corresponds to the dot located at the center of the photonic wire. The calculation was done by Niels Gregersen (DTU Fotonik,

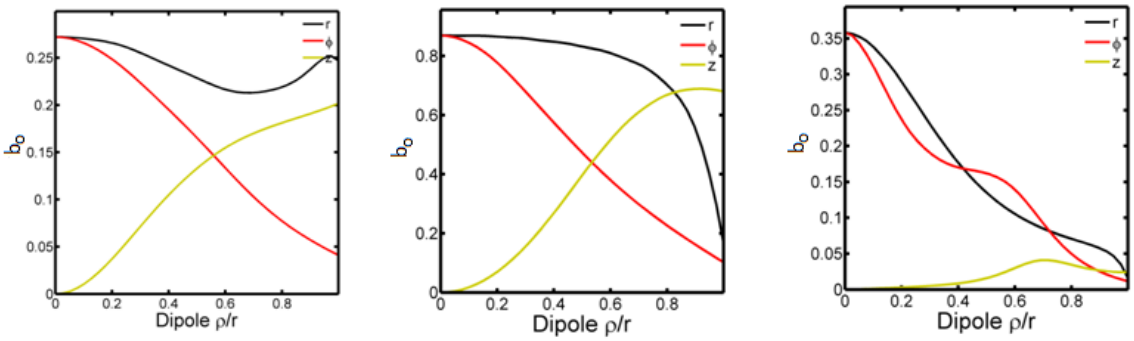

(a) d = 160 nm **(b)** d = 260 nm **(c)** d = 480 nm

Figure 2.8: Calculated results for the spontaneous emission rate into HE_{11} guided mode for three different diameters of a cylindrical photonic wire: (a) d = 160 nm, the wire diameter is too small to obtain a good b_o even for an on-axis QD. For the off-axis QD, different behaviours of b_o are observed for two orthogonal directions ϕ and r; (b) d = 260 nm, $b_o > 0.9$ is predicted for QDs located at the center of the photonic wire; (c) d = 480 nm, increasing the diameter of the photonic wire results in the appearance of other guided modes, thus decreasing b_o value into mode HE_{11}. These calculations have been done by N. Gregersen.

Denmark). In figure 2.8(a) for a wire with diameter d = 160 nm, it is visible that even for an on-axis QD, b_o is small. Moreover, it is evident that b_o changes drastically when a QD is located off-axis and the behaviour is different for the two orthogonal-oriented dipoles ϕ and r. When the diameter of the photonic wire is around 480 nm, there are other guided modes, resulting in the decrease in b_o value in to the mode HE_{11}.

2.2.2 Enhancing extraction efficiency

So far we have considered an infinite wire but in reality, we have to consider a finite photonic wire as shown in figure 2.9. The photons emitted by the QD are collected at the top facet of the photonic wire. For efficient system, all the photons from the QD must be collected. There are two main factors that could affect the global extraction efficiency. First, since the photons are guided equally into upward and downward directions, the collection efficiency will be reduced by a factor of 2. This issue can be addressed easily by placing a mirror at the bottom of the photonic wire and obtain the interference between the field reflected from the mirror placed at bottom and the field emitted upward [55]. As a result of this interference between the two fields, the spontaneous emission rate into HE_{11} is multiplied by a factor of $[1 + |r| \cos(\phi + \phi_b)]$. To take advantage of this interference effect, the position of the emitter is set on one of the maximum of the standing wave pattern existing between the

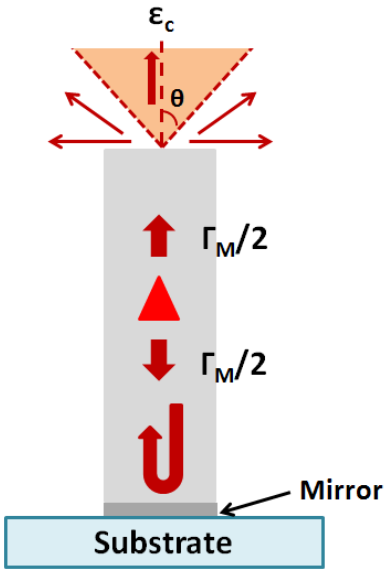

Figure 2.9: Sketch of the photon collection from quantum dot embedded inside a finite photonic wire: A mirror is integrated at the bottom to reflect upward the emission going towards the bottom of the wire. The light exiting the top of the wire will be collected by an optical lens.

bottom mirror and the emitter. The total spontaneous emission rate then given by

$$\Gamma_{tot} = \Gamma_M(1 + |r|) + \gamma \tag{2.6}$$

It has been shown that by putting a planar gold-silica mirror at the bottom of the photonic wire, the modal reflectivity can be reached more than 95% [36]. However, it is important to note that for the sample investigated in this thesis does not have mirror at the bottom of the photonic wire.

Second, is the extraction efficiency ϵ of the finite length wire. ϵ is defined as the fraction of light exiting the wire that is collected above the top facet in a cone. ϵ_c is the transmission into a cone when the top facet is illuminated by the upward-propagating HE_{11} mode. According to Fabry-Perot (FP) model, the number of photons collected into this cone is equal to $\epsilon_c\ |A^+|^2$, where $A^+ = (\frac{\Gamma_m}{2})^{1/2}\,[1 + |r|]$ is the amplitude of HE_{11} mode propagating in the upward direction. Thus, ϵ is given by [36, 55],

$$\epsilon = \epsilon_c \frac{|A^+|^2}{\Gamma_{tot}}$$
$$\epsilon = \frac{b_o(1+|r|)^2}{2(1+b_o|r|)}\epsilon_c \tag{2.7}$$

The parameter ϵ is the figure of merit for the global efficiency of the one-dimensional system. To have a large ϵ, high ϵ_c is required, which means that a low divergence of the output beam is necessary. For the photonic wires with small diameter, the fundamental mode waist is narrow. Therefore, the confined HE_{11} photons are diffracted with a high angle into free space leading to wide far-field radiation pattern. Thus, it prevents an efficient collection of light with standard optics. In order to increase the collection rate, one has to reduce the output beam divergence by expanding the mode waist as discussed in the following section.

2.2.3 Tapering the photonic wire top facet

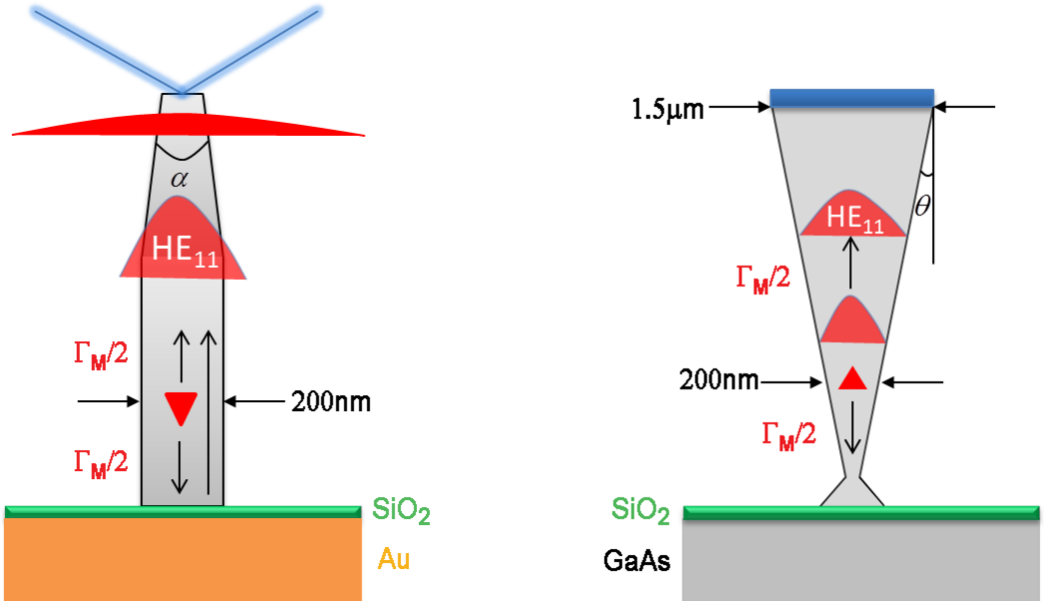

(a) d = 160 nm **(b)** d = 260 nm

Figure 2.10: Schematics of two approaches for the top facet of the photonic nanowire: (a) Sketch of a needle-like GaAs photonic wire and (b) Sketch of a trumpet-like GaAs photonic wire. InAs QD embedded within the wire is shown with a red triangle. Figure taken from [41].

There are two possibilities to achieve the mode expansion, by either decreasing or increasing the top diameter of the photonic wire as shown in figure 2.10. The first approach

is to decrease the diameter of the top facet, thus featuring a conical taper of opening angle α [37,59,60,68], as shown in figure 2.10(a). It has been reported in [36] that $T_{HE_{11}}$ depends drastically on the angle α for such needle type taper ($T_{HE_{11}} \approx 60\%$ for $\alpha = 5°$ and $\approx 50\%$ for $\alpha = 7.5°$). Such device features a measured efficiency of 0.72 combined with a very clean single photon emission with $g^{(2)}$ ($\tau = 0$) of 0.008 [37]. However, this design encounters several drawbacks. Firstly, the fabrication of the regular conical tapering with an opening angle $\alpha \leq 5°$ is quite challenging using the top down approach [37] . Secondly, the emission is poorly matched to a Gaussian free-space beam [36].

To overcome the drawbacks of photonic wires with needle taper, new inverted cone or trumpet-like taper of opening angle α are designed as shown in figure 2.10(b). This geometry ensures a nearly perfect adiabatic expansion of HE_{11} for $\alpha < 5°$, leading to $T_{HE_{11}} > 0.994$. For α upto 15°, the modal transmission is maintained above 0.95. Since the far-field emission is essentially governed by the diffraction of HE_{11} when it reaches the top facet, thus the high value of $T_{HE_{11}}$ is a critical. The figures of merit of the efficiency of the taper design are the total transmission ϵ_c in to the collection lens and the transmission T_g into a Gaussian beam. For a photonic wire with a fixed height, it has been calculated that for the trumpet design photonic wires, ϵ_c and T_g increase with the angle α and reach the optimal value $T_g = 0.97$ for $\alpha = 11.5°$, which corresponds to the top diameter of about 2.6 µm. On the other hand, for needle-like photonic wires, ϵ_c and T_g decrease drastically with α and the maximum value for T_g is just 0.43. This implies that the trumpet design of the photonic wire is much more favourable for light propagating in the mode HE_{11} to be collected when escaping from the top facet of the photonic wire. The photonic wires studied in this thesis are such trumpet design wires as presented in the following section.

2.3 Photonic trumpets

2.3.1 Fabrication of photonic trumpets

The trumpet photonic wires studied in this thesis were developed and grown in the group of J.Claudon and J-M Gérard, from the joint Nanophysics and Semiconductors (NPSC) team between CEA/INAC and Institut Néel. The main fabrication steps are demonstrated in figure 2.11. The device is made out of a planar structure grown by molecular beam epitaxy on a GaAs (100) wafer, in which a single layer of InAs self-assembled QDs is located in a GaAs matrix. To make sure all the incoming light could enter the structure with highest efficiency, a layer of anti-reflection coating made of 115 nm thick Si_3N_4 is deposited on the top facet using plasma enhanced chemical vapor deposition. The inverted trumpet-shape is then obtained through a top-down approach. Using electron-beam lithography, a Nickel hard mask is defined and consists in arrays of circular disks with diameter ranging from 1 µm to 4 µm with 10 nm steps. The following step is the reactive ion etching (RIE) process to transfer the pattern of the mask into the GaAs wafer. By a careful control of the etching

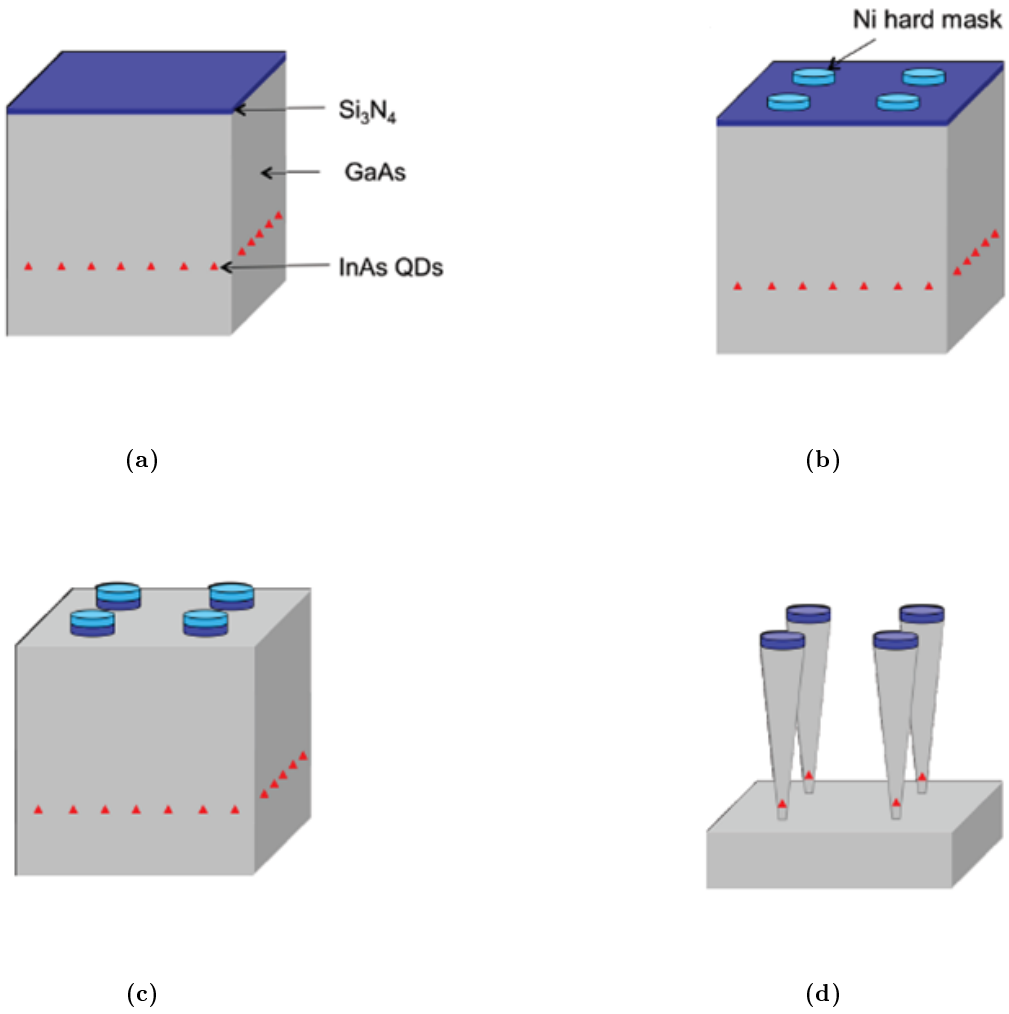

Figure 2.11: Schematic illustration of 'trumpet-like' photonic wire fabrication steps: (a) Deposition of anti reflection coating layer Si_3N_4 on top of a planar GaAs wafer, (b) Ni deposition, which defines the top shape of the trumpet, (c) Reactive ion etching (RIE) with Si_3N_4 layer and (d) RIE to form the inverted trumpet shape. Figure taken from [38].

parameters, the conical shape with high aspect ratio and smooth sidewalls is formed.

Finally, the remaining Ni mask is removed in a diluted nitric acid solution. To suppress spurious surface effects, the wire sidewalls were passivated and covered with a 20 nm thick Si_3N_4 layer [35, 69]. This fabrication process is applied for a non-mirror sample. For samples with integrated metallic mirror at the bottom, a more sophisticated fabrication is required to deposit the mirror into the structure [36, 55].

These photonic wires were reported to feature large b_o value exceeding 90% over a broad wavelength range of 70 nm (centred at λ = 950 nm) [37]. Self assembled QDs are located close to the bottom of the photonic wire, where the dynamical strain is larger for the first flexural mode of the wire. Thus, making it favourable for strain tuning of QDs [35,39,41,42].

2.3.2 Sample design

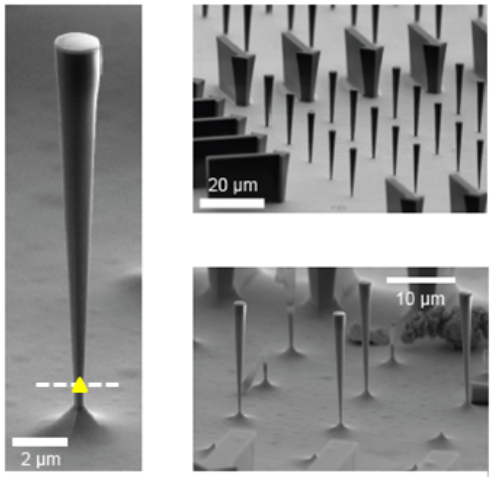

Figure 2.12: Scanning electron microscope (SEM) images of the trumpets: The sample contains several arrays of trumpets with top facet diameter ranging from 1 µm to 4 µm with a step of 10 nm. The opening angle is fixed at 5°. SEM images taken by J. Claudon.

Figure 2.12 shows the SEM images of the photonic trumpets. A series of trumpets is obtained with top diameters varying by a 10 nm step from 1 µm to 4 µm. The height of the trumpets is about 17.2 µm, the QD layer is located 0.8 µm above the waist. Each trumpet is estimated to contain approximately 100 QDs. These photonic trumpets have been investigated in the team before [35,38,41]. However, the anti reflection coating on the top facet of the photonic wire was removed in the beginning of this work. This step has been taken in order to get more reflected light from the top facet. It will be shown in chapter 4, that signal to noise ratio increases with the laser power falling on the photodiode. Thus, removal of the anti reflection coating increases the amount of reflected light and helps in optimizing the motion detection. In the rest of the thesis these trumpets like photonic wire will be referred to as photonic wires.

In order to identify the photonic wire, there are numbers (not visible in the figure) and arrows (shown in figure 2.12) on the sample. The sample has numerous matrix labelled as A1, A2,....C3,C4,...D3, D4.. and so on. We investigated only a part of the whole sample

which has only four matrices namely, C3, C4, D3 and D4. Each matrix has 7 rows and 5 columns. One such matrix is shown in figure 2.13. All columns are identical and consists of photonic wires ranging from 4 µm to 1 µm such that each cell of the matrix has 50 photonic wires with a difference of 0.5 µm in the top diameter of the first and last wire. The number on the left of each row represents the top diameter of the corner most wire surrounded by two arrows. The photonic wire investigated mainly in this work is in C3 matrix second column with top diameter 1.86 µm. Therefore, it is called "C3_2_1.86" and is marked on the figure below.

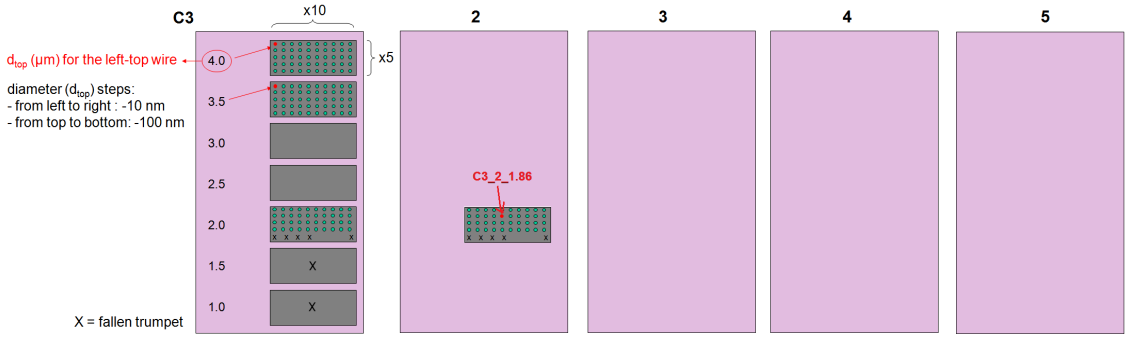

Figure 2.13: Sketch demonstrating the arrangement and identification of photonic wires on the sample.

2.4 Optomechanical coupling

As mentioned in chapter 1, that the hybrid system investigated in this work exhibit a strain mediated optomechanical coupling between the QD and the photonic wire. The hybrid system under investigation is well described by the independent spin-boson Hamiltonian [1]:

$$H = \frac{\hbar\omega_o}{2}(\hat{\sigma}_z + 1) + \frac{\hbar g_m}{2}(\hat{\sigma}_z + 1)(b + b^\dagger) + \hbar\Omega_m(b^\dagger b + \frac{1}{2}), \tag{2.8}$$

where $\omega_o/2\pi$ is the QD transition frequency, $\hat{\sigma}_z = |e\rangle\langle e| - |g\rangle\langle g|$ is the Pauli operator of the QD population, b is the phonon annihilation operator, $\Omega_m/2\pi$ is the mechanical resonance frequency, and g_m is the hybrid coupling strength between the QD and the photonic wire given by

$$g_m = \frac{\partial\omega}{\partial x}\delta x_{ZPF} \tag{2.9}$$

where x represents the photonic wire position, $\hbar\omega$ is the x-dependent QD transition energy, and δx_{ZPF} is the zero point fluctuations given by

$$\delta x_{ZPF} = \sqrt{\frac{\hbar}{2m_{eff}\Omega_m}} \tag{2.10}$$

where m_{eff} is the effective mass of the photonic wire.

This strain mediated coupling is the result of the interactions between the excitonic transition and the lattice uniaxial deformation which can be traced back to the following effects [35, 70–72]:

- Hydrostatic component of the strain tensor is responsible for the change in QD band gap, i.e. shift of the conduction band and the valence band depending on the strain direction,
- Biaxial component of the strain tensor influences the valence band energy levels,
- Increase in external tensile uni-axial stress decreases the QD height, which tends to increase the confinement energy (the energy difference between the discrete energy levels).

The following sections will present both the aspects of this strain coupling, which appear as the influence of the mechanical motion on the optical properties of QDs and conversely as driving of the mechanical motion by modulating the QD population.

2.4.1 QD response to mechanical strain

Since the QDs are located near the base of the photonic wire as shown in figure 2.14(a), the strain field is largest at this location for the flexural modes of the wire. Thus, when the photonic wire is set into vibrations along one of the flexural mode, it experience deformations yielding to strain changes at the QD location. In response to the wire bending to one side, QDs located on its side are under compression while those on the other side are dilated. This is depicted in figure 2.14. The strain field is plotted in blue to red color scale. There is a strain gradient, which increases linearly, from the central neutral axis to the edge of the wire. As a result, each dot will experience different strain depending on its position within the wire. If the dot is at the center of the photonic wire, there will be no effect on the transition energy of the dot. Farther the dot is located from this axis, larger will be the effect. In other words, dots close to the edge of the wire will experience larger shifts and thus shows larger coupling.

In the case depicted in figure 2.14(a), the QD will experience a compressive strain that shifts its transition energy from $\hbar\omega_o$ to $\hbar\omega_o + \hbar\delta\omega$ i.e. there is an increase in the transition

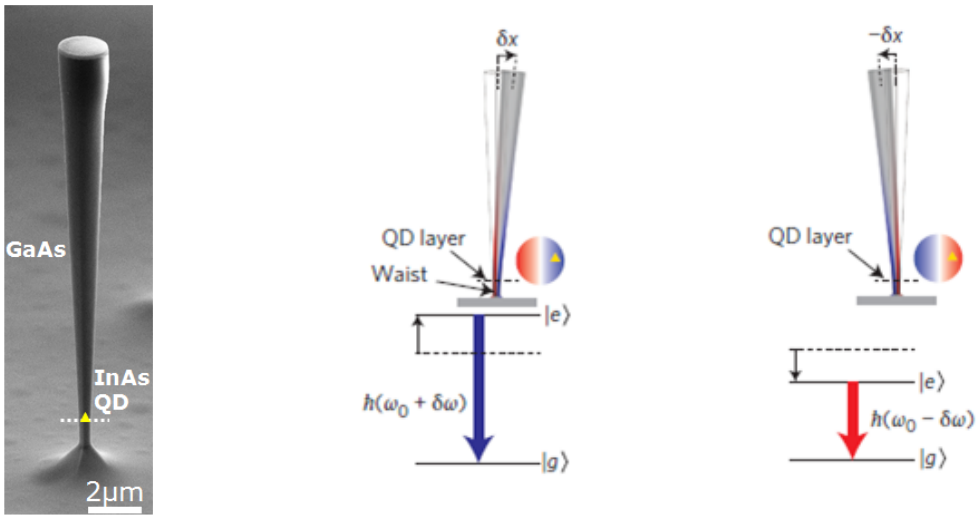

(a) (b) (c)

Figure 2.14: Optomechanical coupling in a hybrid system: (a) Scanning electron microscope (SEM) image of GaAs photonic wire consisting of InAs QDs. (b) and (c) Stress field is plotted in blue to red color scale: the QD (yellow triangle) experiences a compressive strain that increases the transition energy by $+\hbar\delta\omega$ in (b) and a tensile strain that decreases the transition energy by $-\hbar\delta\omega$ in (c) due to its excentric position in plane of the photonic wire. [35]

energy. On the other hand, in the case depicted in figure 2.14(b), the dot will experience a tensile strain, resulting in decrease in the transition energy from $\hbar\omega_o$ to $\hbar\omega_o$ - $\hbar\delta\omega$.

The dynamic [35,41] and static [39,42] tuning of InAs QDs embedded in GaAs photonic wires has been realized experimentally in the team, using the trumpet-like structures. The reported strain induced energy shift for these structures is about 30 μeV per 1 nm of structure's displacement. This position dependent strain induced shift of the QD transition energy allows to bring two or more QDs in resonance. This opens the possibility of studying collective light emission effects such as superradiance [73]. Moreover, it allows a non destructive method to determine the position of the QDs within the photonic wire. It has been reported that the position of the QDs inside the photonic wire can be determined easily with an uncertainty of ± 1 nm, for dots close to the axis of the wire, and of at most ± 35 nm, for dots close to the edges [43].

2.4.2 Inverse coupling: Quantum Hammer effect

On one hand nanomechanical strain could be used to control QDs, conversely, QDs could be used to probe and control nanomechanical systems. This inverse optomechanical coupling

can be viewed from the photonic wire point of view. The theoretical approach has been developed by A. Auffèves and M. Richard [44], to predict and control the consequences of reverse coupling. Their approach is based on the assumption that the quantum dot physical size changes when the dot hosts an exciton and as a result exerts a force on the photonic wire. If the optical drive of the quantum dot is modulated at the mechanical resonance frequency, each absorption-emission cycle will exert the force always in the same direction, resulting in the net force which sets the wire in motion.

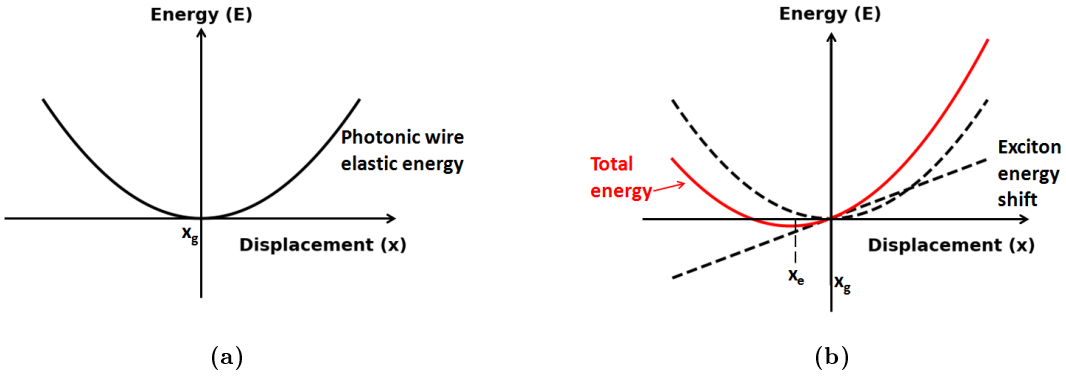

(a) (b)

Figure 2.15: Sketch describing the quantum hammer effect via the energy of the hybrid system. (a) Elastic energy of the photonic wire when the QD is in ground state, (b) Total energy of the system when the QD hosts an electron-hole pair. The total energy is the result of the elastic energy of the photonic wire and the exciton energy.

The other way to understand this would be in terms of the energy of the system. Initially, when the QD is in ground state (i.e. no electron-hole pairs), the total energy of the hybrid system will be equal to the elastic energy (sum of kinetic and potential energy) of a harmonic oscillator given by

$$E_{elastic} = \frac{m_{eff}\Omega_m^2(x - x_g)^2}{2} \tag{2.11}$$

where m_{eff} is the effective mass, Ω_m is the mechanical resonance frequency and x_g is the rest position of the photonic wire corresponding to the ground state of the QD. The energy is plotted in figure 2.15(a).

Now, when the QD is excited i.e. it hosts an exciton (an electron-hole pair), the total energy of the system will be given by the red curve in figure 2.15(b). This results from the addition of the elastic energy of the photonic wire and the QD energy. It has been verified [35,39] that when wire vibrates, the strain field at QD location modulates the QD transition energy. The amount and direction of shift will depend on the QD position with respect to the photonic wire axis. This energy shift is proportional to the position x of the top facet of the photonic wire and given by (from eq. 2.9)

$$E_{exciton} = \frac{\hbar g_m x}{x_{ZPF}} \tag{2.12}$$

Therefore, the total energy of the system will be the sum of the parabola and the line, resulting in a shifted parabola (as shown by the red trace in figure 2.15(b)) and is given by

$$\begin{aligned} E' &= E_{elastic} + E_{exciton} \\ &= \frac{m_{eff}\Omega_m^2(x - x_g)^2}{2} + \frac{\hbar g_m x}{x_{ZPF}} \end{aligned} \tag{2.13}$$

The new rest position of the photonic wire, say x_e corresponding to the excited state of the QD, can be estimated by taking the derivative of the total energy E' with respect to x and setting it to zero. Therefore,

$$\begin{aligned} \frac{\delta E'}{\delta x}|_{x=x_e} &= 0 \\ m_{eff}\Omega_m^2(x_e - x_g) + \frac{\hbar g_m}{x_{ZPF}} &= 0 \end{aligned} \tag{2.14}$$

Thus, the effect of the excited dot will be such that the rest position of the photonic wire will be shifted to say, x_e given by

$$\begin{aligned} \Delta x &= x_e - x_g \\ &= -\frac{\hbar g_m}{m_{eff} x_{ZPF} \Omega_m^2} \\ &= -2\frac{g_m}{\Omega_m} x_{ZPF} \end{aligned} \tag{2.15}$$

When the QD is excited, the photonic wire will try to go towards this new rest position and thus experience a force, F$\propto$ (x_e - x_g). However, it is important to note, that the relaxation time of QD τ ($\approx$ 1.4 ns for neutral exciton [38]) is much faster than the mechanical time period of the photonic wire (few micro seconds). Therefore, this force will be momentary and as soon as the QD will return to ground state, the rest position of the photonic wire will be again x_g. If the dot is excited again at this instant, the wire will be pushed again in the same direction and will try to reach towards x_e. This is achieved by exciting the QD by a resonant laser, modulated at the mechanical resonance frequency, such that it is "ON" for half a mechanical period and "OFF" for the other half. Each QD absorption-emission cycle is like a "quantum hammer" (QH) kick on the photonic wire, the accumulation of which sets the wire in motion. In the rest of the thesis we will refer to

this effect as "quantum hammer effect" and its experimental realization is the main goal of this thesis.

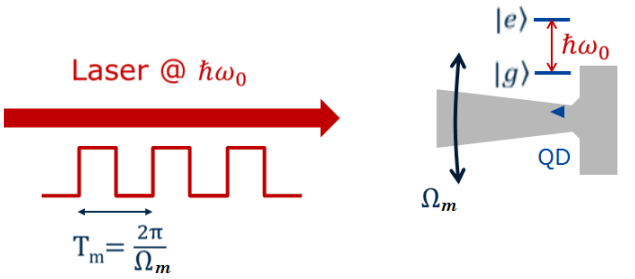

(a)

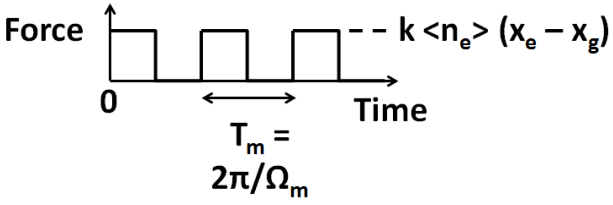

(b)

Figure 2.16: Sketch demonstrating (a) the excitation scheme used for the experimental realization of the quantum hammer effect, and (b) Resulting quantum hammer induced force acting on the photonic wire.

In the excitation scheme used in our setup, we have a continuous wave laser which is resonant with the $|g\rangle$ - $|e\rangle$ transition and is modulated at the mechanical resonance frequency Ω_m with a 50% duty cycle as shown in figure 2.16(a). As a result, the force acting on the photonic wire due to the quantum hammer effect will also be modulated as shown in figure 2.16(b). For half of the mechanical period, the resulting force will be zero whereas for the other half it will be proportional to ($k\ \langle n_e \rangle\ (x_e - x_g)$), where k is the spring constant which is related to the mechanical resonance frequency via $\Omega_m = \sqrt{\frac{k}{m_{eff}}}$, $\langle n_e \rangle$ is the average population of the QD. Using the Fourier series expansion of the square periodic function (see Appendix A for details) the resulting hammer induced force can be written as,

$$F_{QH}(t) = k(x_e - x_g)\langle n_e \rangle \left[\frac{1}{2} + \frac{2}{\pi}\sin(\Omega_m t) + ...\right] \tag{2.16}$$

If the excitation laser power is such that the two-level system (i.e. the QD) is in saturation, which is the case in our experiment, it contains a fixed average population of one half i.e. $\langle n_e \rangle = \frac{1}{2}$. Using eq. 2.15 and 2.16, the force experienced by the photonic wire when the dot is excited is given by,

$$F_{QH}(t) = -kx_{ZPF}\frac{g_m}{\Omega_m}\left[\frac{1}{2} + \frac{2}{\pi}\sin(\Omega_m t) + ...\right] \tag{2.17}$$

The equation of motion of a harmonic oscillator is given by:

$$m_{eff}\frac{d^2x(t)}{dt^2} + m_{eff}\Gamma_m\frac{dx(t)}{dt} + kx(t) = F_{ex}(t) \tag{2.18}$$

where Γ_m is intrinsic damping rate and $F_{ex}(t)$ denotes the sum of all forces that are acting on the mechanical oscillator. In our case, let us assume for the moment that $F_{ex}(t) = F_{QH}(t)$ i.e. force due to the quantum hammer effect is the only force acting on the photonic wire. Therefore, eq. 2.18 becomes

$$m_{eff}\frac{d^2x(t)}{dt^2} + m_{eff}\Gamma_m\frac{dx(t)}{dt} + kx(t) = F_{QH}(t) \tag{2.19}$$

Let us assume solution to the eq. 2.19 of the form

$$x(t) = Ae^{-i\Omega t} \tag{2.20}$$

where A is the motion amplitude. Substituting 2.20 in 2.19:

$$\begin{aligned}(-m_{eff}\Omega^2 - im_{eff}\Omega\Gamma_m + k)x(t) &= F_{QH}(t)\\ (\Omega_m^2 - \Omega^2 - i\Omega\Gamma_m)x(t) &= \frac{F_{QH}(t)}{m_{eff}}\end{aligned} \tag{2.21}$$

At mechanical resonance i.e. at $\Omega = \Omega_m$, we have,

$$x(t) = Ae^{-i\Omega t} = \left[\frac{F_{QH}(t)}{im_{eff}\Omega_m\Gamma_m}\right] \tag{2.22}$$

The amplitude of quantum hammer induced motion is,

$$x_{QH} = \left|Ae^{-i\Omega t}\right| = \left|\frac{F_{QH}(t)}{im_{eff}\Omega_m\Gamma_m}\right| \tag{2.23}$$

From eq. 2.17 and 2.23, we have

$$\begin{aligned} x_{QH} &= \frac{2.k.x_{ZPF}.g_m}{\pi\Omega_m}\left[\frac{1}{(m_{eff}\Omega_m\Gamma_m)}\right] \\ x_{QH} &= \frac{2}{\pi}Q.x_{ZPF}\frac{g_m}{\Omega_m} \end{aligned} \tag{2.24}$$

Therefore, the amplitude of displacement due to the quantum hammer force will be proportional to the Quality factor ($Q = \frac{\Omega_m}{\Gamma_m}$) and the ratio $\frac{g_m}{\Omega_m}$.

In order to estimate the possibilities of this effect with state of the art parameters , we calculated the displacement induced due to the quantum hammer effect for the photonic wires studied in this work. One of these photonic wire was optically characterized and presented in [35]. The mechanical resonance frequency was found to be $\Omega_m/2\pi = 530$ kHz, for the horizontally polarized mode with a quality factor Q = 3000 at T = 5K. x_{ZPF} was reported around 1.1 $\times 10^{-14}$ m. The coupling strength for one of the dot studied was found to be $g_m/2\pi = 450$ kHz, which is nearly as large as the mechanical resonance frequency. Putting all these parameters in eq. 2.24 we get the expected amplitude x_{QH}, due to the quantum hammer effect around 1.78 $\times 10^{-11}$ m, giving the root mean value $x_{QH_{rms}} = 1.26 \times 10^{-11}$ m. The variance of the Brownian motion amplitude $x_{th_{rms}}$ for this wire was found to be about 2.3 $\times 10^{-12}$ m, giving:

$$\frac{x_{QH_{rms}}}{x_{th_{rms}}} \approx 5.5 \tag{2.25}$$

Thus, the expected displacement due to the quantum hammer effect is approximately five times the Brownian motion amplitude. Since, the optical detection technique employed in our setup for motion detection is sensitive enough for the Brownian motion detection (on the order of few pm range). Therefore, the detection of the quantum hammer effect induce motion should not be a problem.

In order to realize this effect experimentally, we used two techniques simultaneously. One, to excite the QD (with good coupling g_m) resonantly, by a laser resonant with the QD energy and modulated at the mechanical resonance frequency Ω_m, we performed the resonant excitation spectroscopy (presented in chapter 3. Second, the induced motion is detected by the optical detection technique (presented in chapter 4). Both the techniques have been realized independently before in the team. Goal of this work is to combine them together for simultaneous measurements of the resonant excitation and motion detection.

In addition to building the combined setup, another important thing is to find the better coupled QDs to perform the measurements. However, it is clear from the experiments done

earlier in the group [35, 39] that g_m is higher for the dots which are close to the side of the photonic wire. In other words, in order to have strong mechanical coupling it is better to work with QDs that are away from the axis of the wire. However, optical coupling will reduce for such dots and it will not be possible to excite such dot resonantly (see section 2.2.1). Therefore, in order to have successful realization of the hammer effect, we will have to settle down for QDs with moderate coupling such that their resonant excitation is possible. We have characterized different QDs in different photonic wires to find the best candidate for the experiment. This is discussed in detail in chapter 5.

2.5 Conclusion

This chapter focused on the hybrid system investigated in this work and the strain coupling between the system components. Chapter begins with the description of general properties of the semiconductor QDs and their energy levels. The "trumpet-like" design of the photonic wires, which was the result of enhancing the extraction efficiency was also presented. Followed by the details on the fabrication process and the final sample investigated. Last part of this chapter focused on the strain mediated optomechanical coupling. The influence of this strain coupling on the QD optical properties were evidenced both via dynamic and static modulation in our group over the last few years. The quantum hammer effect, which is the result of the inverse effect of strain coupling and is mainly studied in this work, is presented in detail while focusing mainly on the theoretical aspects.

Chapter 3

Photoluminescence spectroscopy and resonance excitation of quantum dots

Photoluminescence (PL) spectroscopy is a fundamental study when investigating semiconductor QDs. This chapter will present PL spectroscopy, together with one of the two techniques necessary to realize the quantum hammer effect experimentally, namely, resonant excitation spectroscopy. Section 3.1, presents the experimental setup, where we could perform both micro-PL measurement and resonant excitation of a single QD. A detailed description of different components of the experimental setup is made. The full characterization of the PL spectra will be then presented and discussed in section 3.2. Section 3.3 is dedicated to the resonant excitation technique. The effect of the high power probe laser (laser used for optical detection of the induced motion of the photonic wire, presented in Chapter 4) on the PL spectra and resonant emission (RE) signal will then be presented. Section 3.4 talks about other experimental challenges faced in the realization of resonant excitation and hence quantum hammer experiment. Finally the RE spectra for the QD studied mainly in this project is presented in section 3.5.

Contents

3.1 Experimental setup

Resonant excitation, as explained in the previous chapter, is one of the different methods to excite carriers in the QD. In this method, the excitation laser wavelength is tuned on resonance with the fundamental transition of the QD. Resonance excitation spectra has been observed firstly for an atom [74], then with dye molecules [75], superconducting macroscopic two-level system [76]. During the last ten years, resonant excitation of a single semiconductor QD has been studied intensively [53, 77–84]. Since, the excitation laser wavelength is same as that of the excitonic (X) transition, the back-reflected signal of the excitation laser imposes some restrictions on the efficient detection of the QD emission. The back-reflected light from the laser comes mostly from the back-reflection on top facet of the photonic wire. With the anti reflection coating removed (see section 2.3.2 for details), we have even more reflection from the top facet of the wire then what is reported in [38,84]. In addition to this, internal reflections inside the optical elements (such as waveplate, objective, beam splitters and so on) will also add to this parasitic signal. This unwanted laser background may cover up the resonant signal emitted by the QD. Therefore, it is highly important to suppress this back-reflected laser background as much as possible. This is achieved by using the cross-polarized detection scheme [75], together with a spatial filter (by using a pinhole) to select only the light emitted from the QD to reach the spectrometer. This scheme has already been realized in the team before [38].

The experimental setup is shown in the figure 3.1. The lasers are directed towards the top of the photonic wire (green arrow) and the light emitted by the quantum dot (red arrow) is collected in the opposite direction. The sample is placed on a cold finger in vacuum inside a Helium-flow cryostat. On its way to the sample, each laser passes through a beam spatial filtering system (not shown in the figure), which is a combination of two lenses with a pinhole in between. The pinhole helps to spatially filter the elliptical shape of the laser beam which is then collimated by the second lens. The size of the beam on top of the photonic wire is also controlled by this lens and the microscopic objective. The two beams shown in figure 3.1 are combined using a 50/50 beam splitter (BS). Next both the lasers are directed towards the polarizing beam splitter (PBS). The purpose of using a PBS instead of a normal BS is to establish the cross-polarized detection scheme, which will be demonstrated in section 3.1.1.4. Finally, the lasers are focused by the microscopic objective (see section 4.3.1.2 for more detail on objectives) on top of the photonic wire. Part of the light emitted by the QD travel towards the top facet of the photonic wire and together with the back-reflected light is collected back by the same objective. The cross-polarized setup allows the QD emission to pass through the PBS to the detection system and suppress the back-reflected laser. To spatially select only the light going out of the trumpet, the top facet of the trumpet is imaged on the pinhole placed in the detection path. The output of this pinhole is then directed to the 1.5m focal length spectrometer. At the output of the spectrometer, the light is either detected by a charged coupled device (CCD) camera or an avalanche photodiode (APD). The following section presents the role of different important components of the experimental setup.

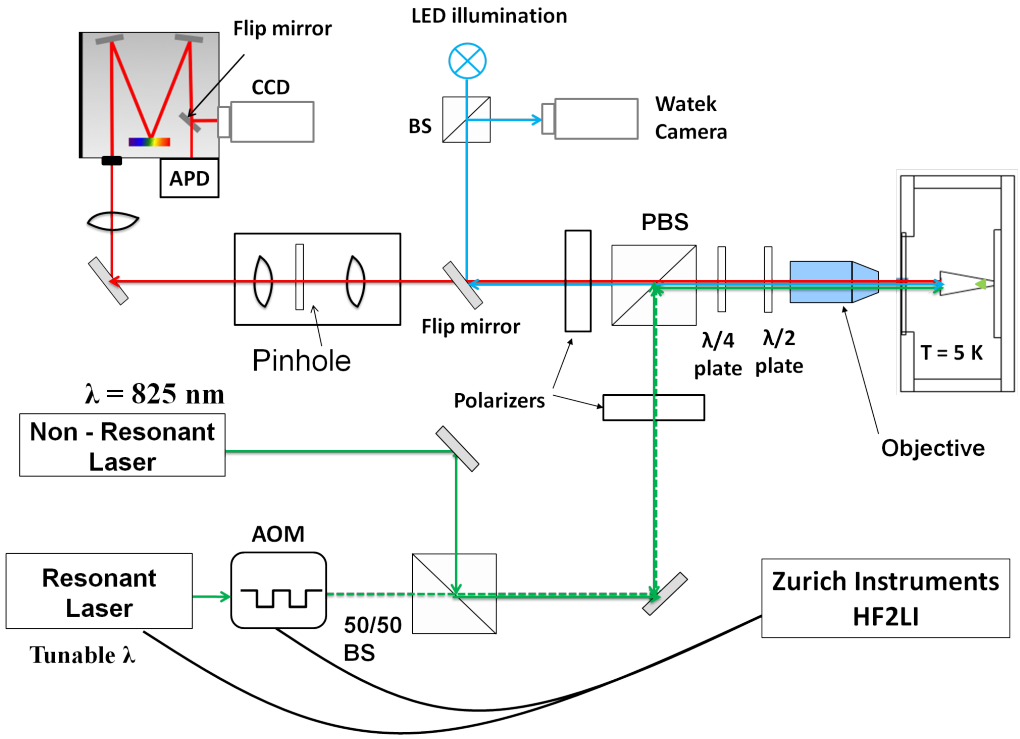

Figure 3.1: Experimental setup for resonant excitation and non-resonant micro-photoluminescence of QDs. See text for details on the elements.

3.1.1 Experimental components

3.1.1.1 Optical source

To perform resonant excitation, a Toptica DL 100 diode laser is used. It is continuous-wave (CW) with tunable wavelength in the range 900 - 960 nm. Coarse wavelength tuning can be done with a micrometer screw on the grating. Fine tuning can be achieved with a piezo actuator controlled by Toptica DC 110 controller. The piezo actuator voltage can be scanned either internally or externally with the help of either a HF2LI box (presented in Chapter 4, section 4.3.1.6) or python based user interface developed to control the experiment. The mode-hop free tuning range of this laser is up to 24 GHz (100 μeV). This laser will be referred as resonant laser (RL)

In order to tune the resonant laser wavelength to the QD ground state transition, one has to know the wavelength of this excitonic transition. To find this, we will use the second non-resonant excitation method (presented in the previous chapter, section 2.1.4), namely the wetting layer excitation. To perform this, another CW diode laser is used with wavelength around 825 nm.

3.1.1.2 Optical isolator

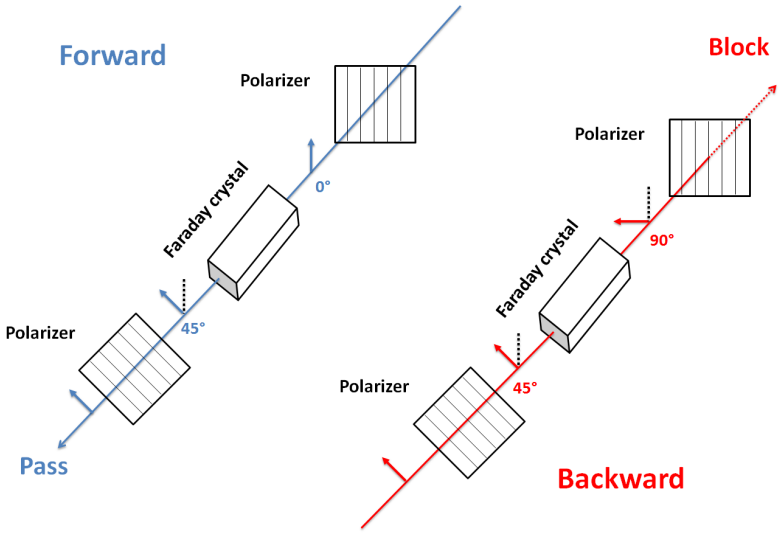

Figure 3.2: Working principle of optical isolator.

To prevent the unwanted back reflection, which may cause a number of instabilities to the excitation beam such as intensity noise, mode hopping or even damage to the source, an optical isolator is placed just after the laser source (not shown in the figure). An optical isolator is a magneto-optic device which allows the transmission of light in only one direction. It works on the Faraday effect. As shown in figure 3.2, it consists of two polarizers with angle of 45 degree between their axes and a Faraday rotator in between, which rotates the polarization of incoming beam by 45 degree. Therefore, the incoming beam (forward mode) enter into the input polarizer and become linearly polarized. On passing through the Faraday rotator, it will be rotated by 45 degree and will finally leave the output polarizer. However, the back reflected beam (backward mode), enters the output poalrizer with 45 degree polarization. As it passes through the Faraday rotator, it will be further rotated by 45 degree. Therefore the beam will be perpendicular to the input polarizer and will be blocked.

3.1.1.3 Cryogenics

Optical properties of QDs are studied at cryogenic temperature. Therefore, the sample is kept inside a continuous flow helium flow cryostat (by Oxford Instruments). Liquid helium storage tank connects with a cryostat via a transfer tube, which allows to collect liquid helium and send the gas back to the recovery system. The cryostat is placed on a 2-axis translation stage (not shown in the experimental setup in figure 3.1), with the precision of 10 µm. The stage helps to perform the initial adjustments of the sample position. Circular entrance window of the cryostat has a diameter of 10 mm and thickness of 0.5 mm. The

temperature inside the cryostat is controlled by the temperature controller ITC 601, which can tune the temperature from 3.5 K up to room temperature with accuracy of 0.1 K.

3.1.1.4 Cross-polarized detection

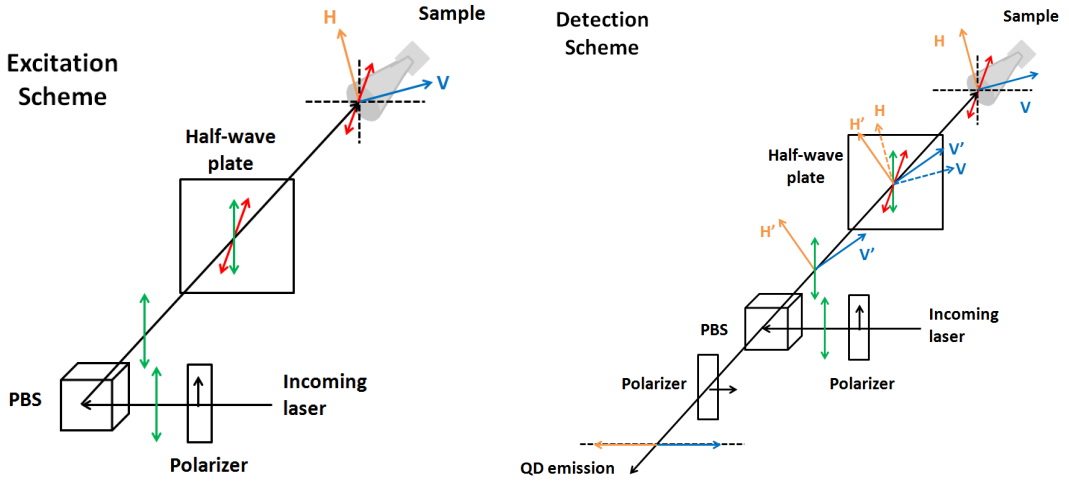

Figure 3.3: Schematic illustration of cross-polarized excitation/detection scheme for the case of a neutral exciton containing linearly polarized orthogonal dipoles: (a) Excitation path: An incoming beam passes through the polarizer with vertical polarization and reflected by the polarizing beam splitter (PBS). On passing through a half-wave plate ($\lambda/2$), the polarization of the beam is rotated by an angle θ, if the angle between the laser polarization and the plate axis is $\theta/2$. The laser then excites the two orthogonally polarized excitonic dipoles H and V. (b) Detection path: The polarizations of light emitted by the QD (the dipoles H and V) and the back-reflected laser are rotated by an angle θ on passing through a half-wave plate to H', V' and vertical polarized (green arrow) respectively. The PBS reflects the vertical component (laser back-reflection) and passes the horizontal components (QD emission) to the spectrometer.

The method used for the rejection of laser back-reflection in the detection path is based on an orthogonal excitation/collection polarization. A polarizing beam splitter (PBS) is used for this purpose. PBS splits the incident light into two beams of orthogonal linear polarization. It reflects the s-polarized or vertically polarized light (light polarized perpendicular to the plane of reflection) and transmits the p-polarized or horizontally polarized (light polarized parallel to the plane of reflection). Thus, the polarization of the excitation light is set to be s-polarized such that the incoming beam is reflected towards the sample and also the back-reflected signal on top facet of the photonic wire is perpendicularly reflected by the PBS. Therefore, back-reflected beam is filtered out from the path to the spectrometer. To optimize the rejection rate, two linear film polarizers are placed at the input and output of the PBS as shown in figure 3.3. The two polarizers are mounted on a high-precision rotation mounts PRM1/M from Thorlabs. This rotation mount is func-

tioned with a locking screw, which engages micrometer for fine adjustment. When locked, the micrometer provides $\pm 7°$ of rotation at the accuracy approximately 2.4 arcmin (0.04°) per micrometer division.

A) Excitation and detection of linearly polarized dipoles:

The first polarizer placed before the input of the PBS optimizes a vertical polarization of the laser before reaching the PBS. After being reflected by the PBS, the vertically-polarized laser passes through a half-wave plate, where its polarization is rotated by an amount θ (if the incident beam angle with the half-wave plate axis is $\theta/2$). Thus, by rotating the $\lambda/2$ plate, we can control the polarization of the excitation laser. This will help in optimizing the excitation of linearly polarized orthogonal dipoles as in the case of a neutral exciton. Figure 3.3(a) describes the input configuration for one such dot which has two linearly polarized orthogonal dipoles X_x and X_y, denoted as H and V, respectively.

For the detection of emitted light, as described in Figure 3.3(b), the back-reflected laser signal and the light emitted by the QD hit the half-wave plate, where their polarizations are rotated by the same amount θ. The back-reflected laser signal is now polarized vertically again, while H and V are rotated to new positions H' and V'. The light then passes through the PBS where horizontal polarized components is transmitted. The laser background, which is vertically polarized, is reflected and hence isolated from the detection channel. Afterwards, a second linear polarizer is placed with a chosen horizontal polarization direction, to ensure the suppression of the remaining laser background and transmission of p-polarized components of the QD emission.

The laser suppression efficiency can be evaluated by the extinction ratio. Extinction ratio is defined as the ratio of the maximum and minimum transmissions of the laser back-reflection, when its polarization is horizontal and vertical respectively. The best extinction ratio achieved in the setup is about 5×10^2. The value is lower than the one reported in [38] by a factor of 20. This is mainly because of the removal of anti-reflection coating from the top facet of the wire. The reflection coefficient now is about 30% (10 times more than with the anti-reflection coating [38]). Also, with the anti-reflection coating removed, comparatively higher laser power is required to excite the dot. Nevertheless, with precise alignment it is still possible to obtain the resonant emission spectra from the sample. It will be shown in the following section. However, there is another approach to obtain RE spectra without worrying much about the laser background. This will be presented in section 3.4.2.

Figure 3.4, describes three simple cross-polarized excitation-detection schemes that could possibly happen when rotating the half-wave plate. Two worst cases are when the laser polarization coincides with the polarization of one of the dipoles (Figure 3.4(a) and 3.4(b)). In this case, one dipole is fully excited but not at all detected whereas the other dipole is not at all excited. Therefore, the preferred scheme is the situation corresponding

to Figure 3.4(c), where the laser polarization is at a position in between the two dipoles.

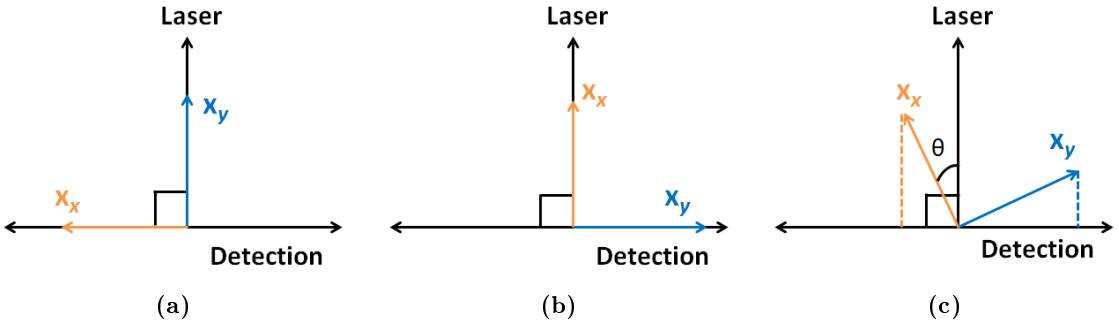

Figure 3.4: Sketch demonstrating different excitation and detection schemes: (a) and (b) Laser polarization coincident with one of the dipoles, (c) The laser polarization is set to an angle θ between the two dipoles.

To understand how the configuration in figure 3.4(c) affects the detection of QD emission, let us assume that the two excitonic dipoles have equal strengths. The laser with a power P_{in} is on resonance with X_x dipole. The laser polarization is at an angle θ with respect to X_x, as described in figure 3.5(a). In this case, the actual power applying on X_x is $P_{in_x} = P_{in}\cos^2(\theta)$. Under the excitation power P_{in_x}, the dipole emits an amount I_x. The projection of I_x on the horizontal detection channel is $I_{x\text{-}H} = I_x \sin^2(\theta)$. Overall, in the weak-excitation of the laser, assume I_0 is what the two level system emitted when $\theta = 0$ with the same power P_{in}, we then have,

$$\begin{aligned} I_{x-H} &= \left[\cos^2(\theta)\sin^2(\theta)\right] I_0 \\ &= \left[\sin^2(2\theta))\right] \frac{I_0}{4} \end{aligned} \tag{3.1}$$

Similarly, for the X_y dipole with the same laser power P_{in} in a weak-excitation regime, we have,

$$\begin{aligned} I_{y-H} &= \left[\sin^2(\theta)\cos^2(\theta)\right] I_0 \\ &= \left[\sin^2(2\theta))\right] \frac{I_0}{4} \end{aligned} \tag{3.2}$$

This indicates that at P_{in} well below saturation power, a spectrometer detects the same amount of photons for both FSS dipoles regardless of the angle θ. When increasing the laser power, the dipoles will be saturated. Figure 3.5(b) illustrates this situation. Since two dipoles are identical, at saturation, they emit the same amount $I_{sat\text{-}x} = I_{sat\text{-}y}$. Therefore, the amount of photons emitted by the dipoles at saturation that are detected in the horizontal and vertical channel scales as

$$\frac{I_{sat-x-H}}{I_{sat-y-H}} = \frac{\sin^2(\theta)}{\cos^2(\theta)} = \tan^2(\theta) \tag{3.3}$$

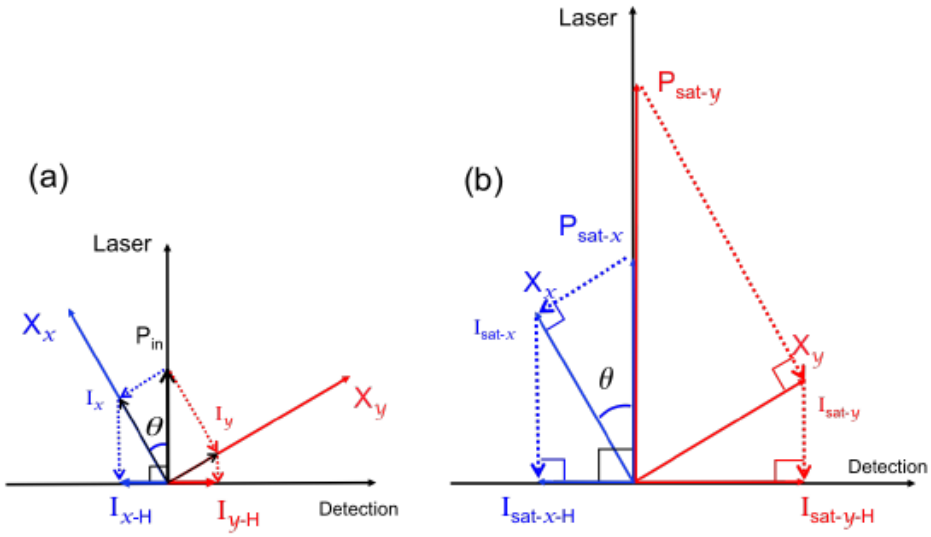

Figure 3.5: Configuration of the resonant excitation in cross-polarization scheme: (a) Weak excitation regime in which P_{in} is well below saturation power P_{sat}. The amount of photons detected in horizontal channel is equal for two dipoles. (b) Strong excitation regime in which P_{in} is at the saturation level. In this situation, the saturation powers and the amount of photons detected from two dipoles both depend on the angle θ. Figure taken from [38]

B) Excitation and detection of Circularly polarized light:

There are few QDs which features circular polarizations. For example, in case of a negatively (or positively) charged trion X^- (or X^+), the two s-electrons (or holes) must have opposite spins due to the Pauli exclusion principle, whereas both spin orientations are allowed for the hole (or electron). As a consequence, there is no fine structure splitting (FSS). The transient matrix elements for the decay of a trion to a single electron or hole are circularly polarized with the helicity (or handedness) depending on the spin of the additional carrier. It will be shown later that the QD used to perform the quantum hammer experiment is found out to be a charged exciton. Therefore, it is important to know how this cross-polarized setup will effect the excitation and detection of circular polarized states.

Each state of polarization can be split into two linearly polarized orthogonal components, in which one is oriented along the x direction and other in the y direction. If both components have equal magnitudes and the phase shift of the y component relative to the x component is + $\pi/2$ or - $\pi/2$, the light is circularly polarized. The sign of the phase

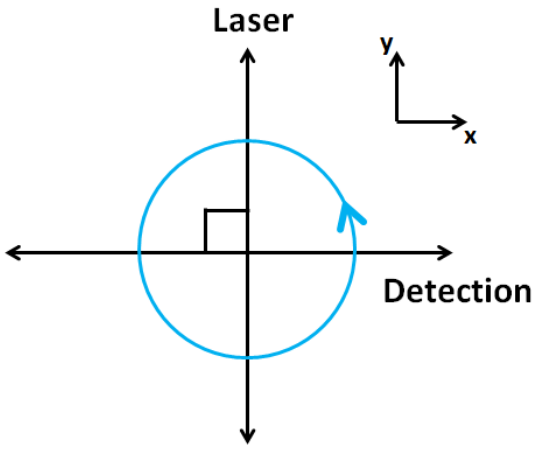

Figure 3.6: Sketch demonstrating the excitation and detection scheme for a circularly polarized light. For a circularly polarized light, the components along the two orthogonal axis X and Y will always have equal magnitudes. Therefore, irrespective of the polarization axis of the excitation and detection, the strength of both excitation and detection will always be same, giving uniform intensity in the detection path independent of the $\lambda/2$ plate angle.

difference determines the handedness of the rotation. It is, therefore, represented as a circle with an arrow showing the handedness as presented in figure 3.6. Because of the equal components along the x and y direction i.e. along the excitation (laser) and detection axis, both the excitation and detection of a circularly polarized light is independent of the angle of the half-wave plate. Considering the transmission though the experimental setup as shown in figure 3.3(b). The emitted circularly polarized light when collected by the objective will undergo a change in its handedness on passing through the half-wave plate. PBS will pass the horizontally polarized component of the QD emission, which will be same for all the angles of half-wave plate. Therefore, this cross-polarized setup should not affect the excitation and detection of the circularly polarized light and one should expect to record the same intensity for all the angles of half-wave plate, unlike the case of linearly polarized light.

3.1.1.5 Visualization system

To be able to observe the experimental sample and the relative laser spot position on its top facet, in the real time, we used a visualization system consisting of an infrared (IR) LED with wavelength at peak emission of 935 nm and a Watek WAT-920N camera (sketch of the Figure 3.1), whose chip is sensitive to near infra-red light. The LED emits a quickly diverging light beam, which is delivered to the sample through 2 lens system (one mounted after the LED and second is the objective). The LED is mounted not in focus of the first lens so that it is unfocused at the focal plane of the objective, where the sample is

located. This is done in order to illuminate the sample uniformly. The reflected light from the sample is imaged on the camera's chip using again a two lens system (one of which is the objective and the other mounted before the camera). The image from the camera is displayed either on a TV screen or on the computer using the software "WinTv". One such image of the sample with a laser beam focused on the substrate in between the photonic wires is shown in the figure 3.7.

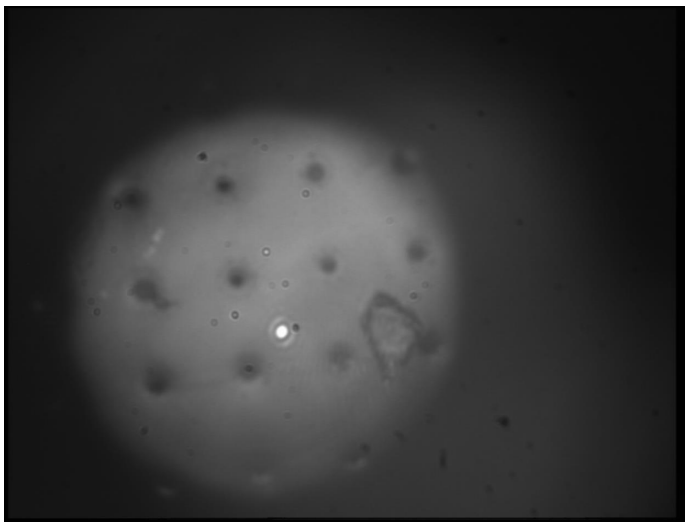

Figure 3.7: LED illuminated image, captured on the Watek camera, of the sample together with a laser beam focused on the substrate. Small black circles represents photonic wires and a big piece towards the right is used as an identification of the cell where the photonic wire C3_2_1.86 is.

3.1.1.6 Quarter wave plate

The purpose of using a quarter-wave plate $(\lambda)/4$ is to optimize the laser rejection. It has been reported in [85] that a quarter-wave plate helps to compensate any distortion of the beam, thus it could help enhancing the back-reflected laser rejection rate. In addition, the quarter-wave plate behaves as a half-wave plate for the reflected laser light since the laser beam passes it twice. Thus, by rotating the $(\lambda)/4$ wave plate, it is possible to visualize the laser beam on the screen which is necessary at some alignment stages. Because with a cross polarization scheme, the laser is also isolated from the Watek camera used for imaging the sample.

The quarter-wave plate using in this setup is Thorlabs AQWP05M-980, which is optimized for the near-infrared region. The wave plate is mounted on a motorized precision rotation mount Thorlabs PRM1/MZ8. The rotation of the mount is driven via a DC servo motor that provides 1 arcsecond of resolution (2.8×10^{-3} degree). The motion of the motor can also be controlled by a software interface.

3.1.1.7 QD emission detection: Spectrometer

The spectrometer we use is a Jobin-Yvon THR1500, with a focal length of 1.5 m. It has a grating with 1200 grooves/nm, blazed at 750 nm, which offers a spectral resolution of about 0.0088 nm at 930 nm ($\approx$ 12.3 μeV). The movement of the grating can be rotated by a motor controlled by computer. The light filtered by the spectrometer is then detected either by the charged coupled device (CCD) camera or an avalanche photodiode (APD).

The CCD camera is the PIXIS: 100 B from Princeton Instruments. It is a fully integrated, low noise camera with a 1340 $\times$ 100 pixels format. The working temperature of the camera is -70°C. This camera offers very low electronics noise and a very high quantum efficiency in the near-infrared region, up to more than 80% at 900 nm.

The photodiode used is a Silicon APD from excelitas integrated with a single photon counting module SPCM-AQR14. This APD has an active area diameter of 180 μm. The dark count rate of this module is 100 Hz. We used APD to perform RE detection measurement. This allows synchronized measurement of QD resonance and photonic wire motion, basic requirement of realizing the quantum hammer experiment (details in Chapter 5).

Details on the detection using CCD and APD is given in section 3.3.3.

3.2 Photoluminescence (PL) spectroscopy

3.2.1 PL measurement

To perform resonant excitation, it is necessary to know the exact wavelength of excitonic transition. This can be determined by performing the non-resonant excitation or wetting layer excitation using the 825 nm laser. PL measurements are done at 5 K, the temperature is maintained by adjusting the amount of He flowing through the cryostat by a needle integrated in the He transfer tube. PL spectrum is taken by a home-made python program (developed by Jan Kettler), which has integrated all the necessary functions from Winspec (an integrated spectroscopy package for cameras and spectrographs, by Princeton Instruments). To select the preferred wavelength range, the grating inside the spectrometer is rotated by a Labview program.

Figure 3.8 shows a typical PL spectra of self-assembled InAs QDs embedded in the photonic wire. The QD emits photons in the near-infrared region (900-930 nm). The different emission lines can be attributed to one of the many QDs embedded in the photonic wire. As discussed in Chapter 2, factor $b_\circ$, the coupling efficiency between the QDs and the guided mode of the photonic wire, depends strongly on the QD position with respect

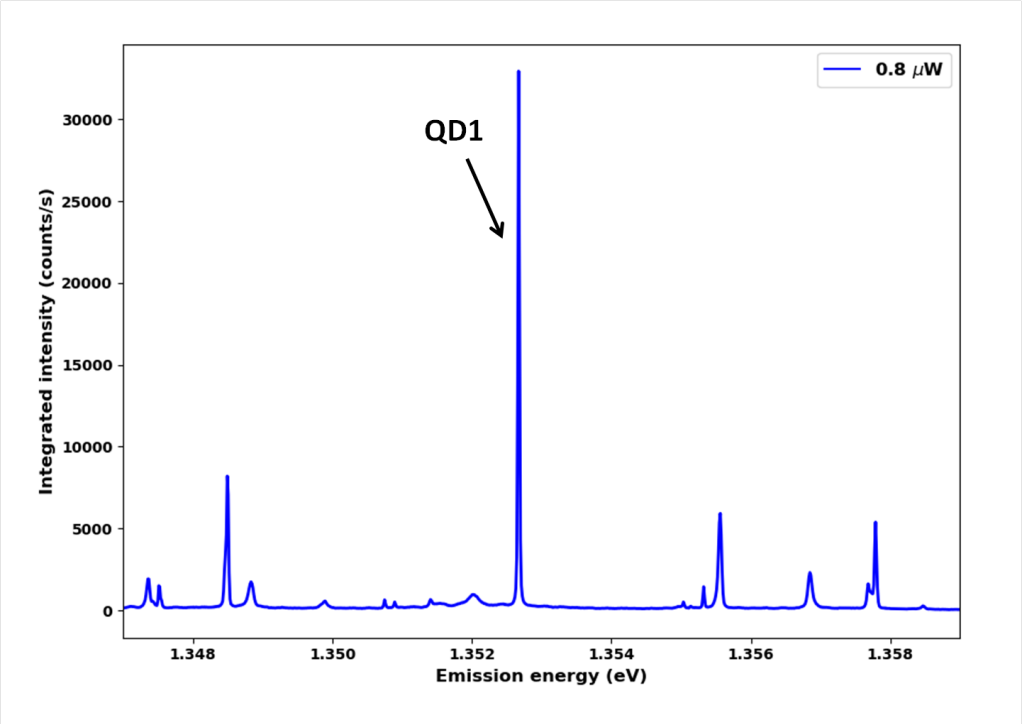

Figure 3.8: PL spectrum of self assembled InAs QDs embedded in the GaAs photonic wire. The spectrum is recorded at T = 5 K. Non-resonant lase power measured before the objective is 800 nW and the integration time is 1 sec. The grating is centred at 916.6 nm.

to the central axis of the photonic wire. Owing to larger b_o, the QDs closer to the central axis of the wire exhibit stronger PL than QDs located further away. In addition, if a QD is located close to the center, it will be coupled better to the excitation beam, as the laser beam is also guided to propagate along the central optical axis of the photonic wire. As a result, QD that is closer to the center of the wire will require less power to saturate. The power required to saturate different QDs in this wetting layer PL excitation is about a few hundreds nW to few μW. Although the non-resonant laser has the wavelength of 825 nm, which is not guided by the mode with the highest efficiency, but the level of excitation power is still significantly smaller than that in QDs in bulk GaAs. For QDs in bulk GaAs, the required power has been reported to be in a range from 1 mW to a few mW [86]. The following section will discuss about the power dependence of PL in detail.

3.2.2 Power dependence

The PL emitted by a QD can be described by a simple model considering a two-level system consisting of a ground state and an excited state. Following the Pauli's exclusion

principle, each state can be occupied by only two electrons or two holes of opposite spin. As a result, the QD in excited state can have up to two excitons. Therefore, as already mentioned in Chapter 2, section 2.1.5, there are multiple possibilities: an empty dot, a neutral dot with either one exciton (X) or with two excitations (XX), and a charged dot with one exciton and an additional charge to form either negative trion (X^-) or positive trion (X^-). Sęk et al. [87], have described a model for the neutral exciton and the biexciton power dependencies using rate equations:

$$\frac{dn_{XX}}{dt} = gn_X - \frac{n_{XX}}{\tau_{XX}} \tag{3.4}$$

$$\frac{dn_X}{dt} = gn_o - \frac{n_X}{\tau_X} + \frac{n_{XX}}{\tau_{XX}} - gn_X \tag{3.5}$$

$$\frac{dn_o}{dt} = -gn_o + \frac{n_X}{\tau_X} \tag{3.6}$$

where n_o, n_X, n_{XX} are respectively the probabilities that the QD is in ground, X and XX states. The times τ_X and τ_{XX} are respectively the radiative lifetimes of X and XX. g is the pumping rate (proportional to the excitation power). Neglecting the occupation probability of higher levels, gives $n_o + n_X + n_{XX} = 1$. Hence Eq. 3.5 becomes

$$\frac{dn_X}{dt} = -\frac{n_X}{\tau_X} + \frac{n_{XX}}{\tau_{XX}} + g(1 - 2n_X - n_{XX}) \tag{3.7}$$

In steady state regime, $\frac{dn_X}{dt} = 0$ and $\frac{dn_{XX}}{dt} = 0$. Therefore,

$$n_X = \frac{g}{\frac{1}{\tau_x} + g + g^2\tau_{XX}} \tag{3.8}$$

$$n_{XX} = \frac{g^2\tau_{XX}}{\frac{1}{\tau_x} + g + g^2\tau_{XX}} \tag{3.9}$$

The emission intensities of the exciton (I_X) and the biexciton (I_{XX}) are proportional to the occupation rates, given by

$$I_X \propto \frac{n_X}{\tau_X} = \frac{g}{1 + g\tau_X + g^2\tau_X\tau_{XX}} \tag{3.10}$$

$$I_{XX} \propto \frac{n_{XX}}{\tau_{XX}} = \frac{g^2 \tau_X}{1 + g\tau_X + g^2 \tau_X \tau_{XX}} \tag{3.11}$$

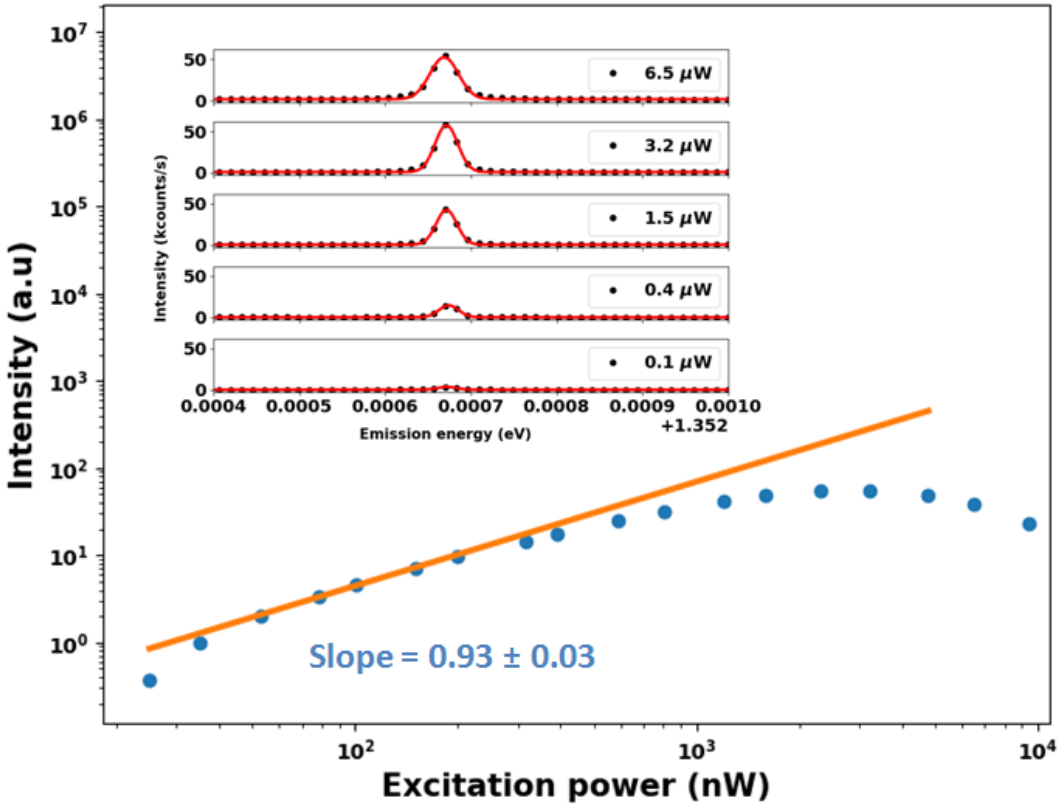

Figure 3.9: Integrated intensity of QD1 as a function of non-resonant laser power: Circular blue points is the measured intensity and solid orange line shows the fitting. At low excitation powers, emission intensity follows linear dependence on the power. The saturation power for this line is around 4 μW. The inset shows the PL spectra at different excitation powers. Resonant laser and probe laser (used for motion detection in Chapter 4) were blocked during this measurement, whereas locking laser (used for position locking, see Chapter 5 for details) is at 100 μW. Camera settings were: High Gain, Low noise and exposure time = 0.5 s.

Thus, at low excitation power i.e. for low pumping rate limit, intensity for X and XX transition varies linearly and quadratically with the pumping rate.

In case of a charged dot, all excitonic transitions with one or more additional charge carrier exhibit the same slopes as their neutral counterparts with the same number of electron-hole pairs. This is because of the absence of any escape channel for a single charge carrier. Thus, below saturation, the occupation probability of the empty dot, as

well as that of a QD with only charge carriers of the same type, is almost independent of the excitation rate, leading to dynamics governed by the probability to capture an electron - hole pair [88].

Figure 3.9 shows the power dependence of the QD studied in this work (QD1 in figure 3.8). This QD line is embedded in the photonic wire with top diameter 1.86 μm. Reason for studying this dot for Quantum Hammer experiment is because it exhibits both good hybrid coupling g_m and optical coupling b_o. Figure shows the integrated PL intensity as a function of the excitation laser (non-resonant laser) power. The dependence is plotted in log-log scale. A fit of the power function, $I \propto P^k$ yields $k = 0.93 \pm 0.03$. Thus, Intensity goes linearly with the excitation power and line could either be a neutral exciton or a charged exciton. The exact nature of the line can be determined from the polarization-sensitive measurement as presented in the following section.

The saturation power for this particular line is around 4 μW. It should be noted that at very low power (below 50 nW) the measured intensity deviates slightly from the fitted line. This is because at such low powers, because of the charge fluctuations around the QD, excitation is not efficient. Once the QD is stabilized,the intensity goes linearly with the power up to few hundreds of μW and eventually saturates. This is why an ultra-weak non-resonant laser is also used in resonant excitation spectroscopy to optimize the resonant emission (RE) signal as shown in section 3.3.4.1.

3.2.3 Polarization dependence

In order to identify the nature of QD1 line, whether it is a neutral or charged exciton, one way is to rely on the fine structure splitting (FSS) of the exciton (X). For a neutral exciton, the energy state of a QD is twofold degenerate, since there are two possible spin configurations for the electrons and holes. However, the electron-hole exchange interaction leads to a small energy splitting of the degenerate levels, referred as FSS. Figure 3.10(a) shows the radiative cascade for neutral biexciton-exciton decay. The exchange interaction splits the excitonic state into two orthogonally polarized levels (say X_x and X_y). As a result, biexciton (XX) level has two possible recombination channels either through X_x or X_y. Therefore, the PL spectra is composed of two doublets (one for exciton and other for biexciton) with the two components linearly polarized along perpendicular directions. Thus, on rotating the polarization of the emission by rotating the half-wave plate, if the line exhibits these doublets, then it is identified to be either exciton or biexciton, which can be further distinguished using the power dependence as explained in the previous section. Moreover, an exciton and biexciton will show the same amount of fine structure splitting and show mirror symmetry in the polarization sequence, if they belong to the same dot.

The case of a charged XX-X radiative cascade is more complex, since the decay of the charged biexciton includes additional decay channels related to the excess p-shell carrier.

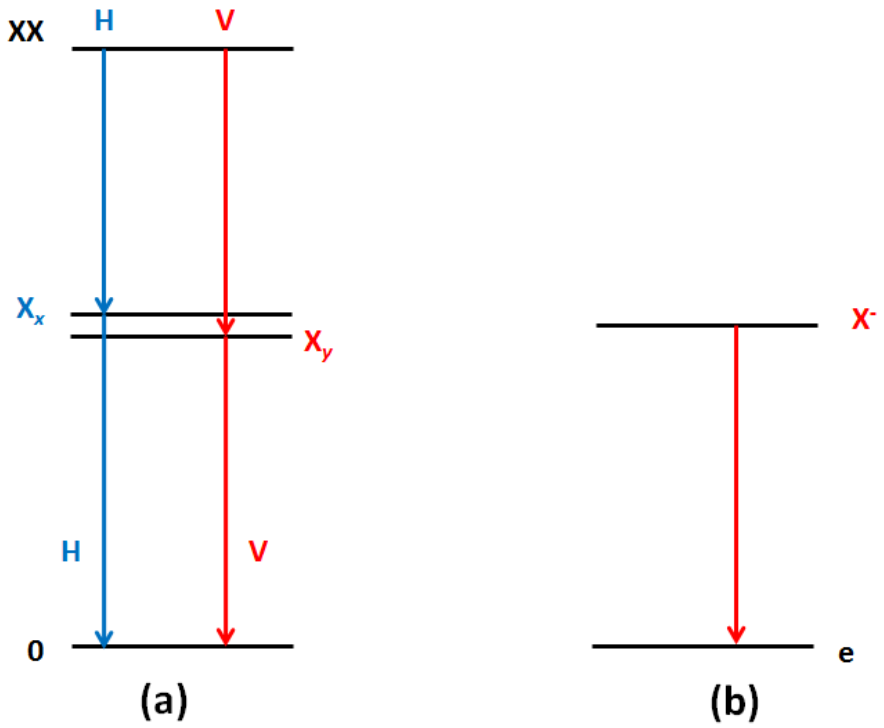

Figure 3.10: Radiative neutral and negatively charged biexciton-exciton decay cascade: (a) Neutral XX-X cascade involving a fine structure splitting exciton state, resulting from anisotropy in electron-hole pair exchange interaction. (b) Radiative cascades in negatively charged QD.

However, from the power dependence measurement presented in previous section, it is clear that QD1 is either a exciton or a charged exciton. Thus, without going into details about the charged biexciton decay path, lets consider the one for a charged exciton.

The radiative cascade for a negatively charged exciton is shown in figure 3.10(b). The transition from negatively charged exciton to a single electron ($X^- \rightarrow e$) will exhibit circular polarization and appears as unsplit transition. This is because, the two like charges occupies the s shell with anti-parallel spins and hence the exchange interaction energies are quenched. For the emission spectrum, not only the initial state but also the final state after recombination of an electron-hole pair are important. This final state is given by a single electron. Consequently no exchange energy splitting is observed in the emission of X^-. Thus, charged excitons do not exhibit FSS [89–91]. Therefore, charged exciton can be assigned to the emission line with no FSS and neutral exciton to the one with FSS. Thus, the polarization-sensitive measurements would help to finally identify the line.

The result of the polarization-sensitive measurement at different angles θ (by rotating the half-wave plate by $\theta/2$) is shown in figure 3.11 for QD1. Figure shows the variation of

the QD emission intensity as a function of the angle of polarization. The change in intensity indicates the linear polarization; however, there is no clear indication of a doublet in the PL spectra. We do measure a small energy shift of the PL line of 4 μeV between the polarizations corresponding to maximum and minimum PL. The linewidth measured with this non-resonant excitation is about 30 μeV, therefore the 4 μeV shift is not significant enough to indicate a FSS from a neutral exciton. Moreover, this shift could have resulted from the jittering of the QD line (see section 3.3.2). To confirm the presence of FSS, we repeated the same measurement by recording the RE spectra at each point. The results are presented in section 3.5.3. However, no asymmetry in the resonant emission spectra of this line was observed, further confirming the absence of FSS. Therefore, this line is identified as charged exciton.

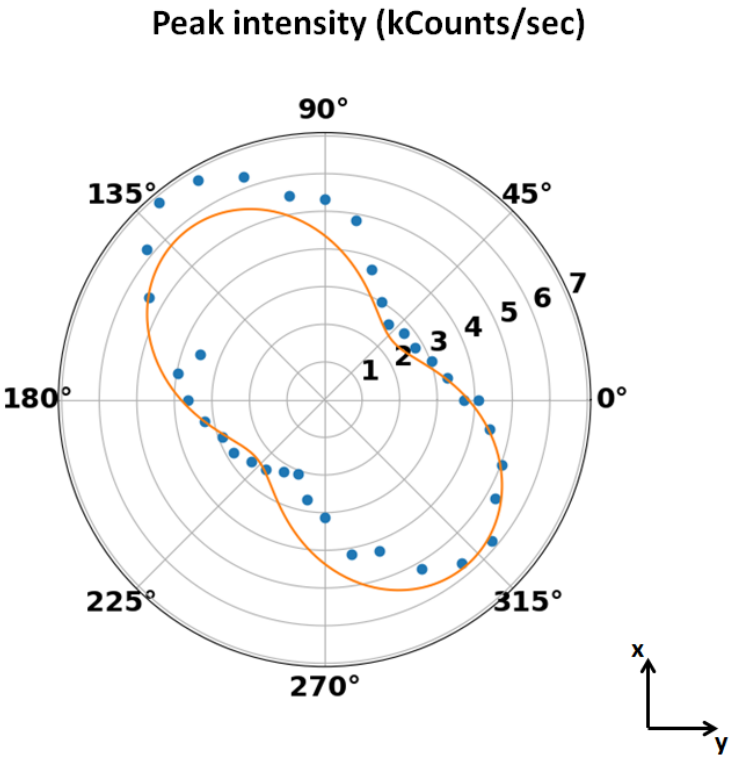

Figure 3.11: The evolution of QD emission intensity at different angles of rotation. The intensity for each position of the half-wave plate is taken from the Gaussian fit of the PL spectra. The polarization axis is 45° with respect to the horizontal (or x) axis (0° corresponds to the y direction). Resonant laser power = 50 nW, non-resonant laser power = 150 mW, probe laser power (used for motion detection in Chapter 4) = 100 μW, and locking laser power (used for position locking, see Chapter 5 for details) = 100 μW. Camera settings were: Medium Gain, Low noise and exposure time = 1.0 s.

However, the question is: If it is a charged exciton, why do we see intensity change? This observed change in intensity could be explained by the fact that the photonic wires studied in this work features a moderately anisotropic cross section. It has been shown

experimentally [92,93] that such a dielectric photonic wire with an elliptical cross section defines an electromagnetic environment dominated by a single guided mode with a linear polarization. The polarization of the QD emission is defined by the polarization of the guided optical mode which transmits this emitted light towards the top facet of the trumpet. Thus, the fact that the QD is not centred within the wire can lead to polarization anisotropy as it will experience different coupling with different radiation modes. Linear polarizations with degree of polarization $> 90\%$ have been achieved with such elliptical wires [92,93]. However, the degree of linear polarization, $P = \frac{I_{max} - I_{min}}{I_{max} + I_{min}}$, for QD1 is only about 60%, implying that the photonic wire in our sample is less elliptical. Thus, QD1 can be attributed as a charged exciton with elliptical polarization, with the main polarization axis along 45° with respect to the x axis.

3.3 Resonant excitation spectroscopy

3.3.1 The two level system under resonant excitation

The excitation laser, which excites the excitonic transition between the ground state $|g\rangle$ and the excited state $|e\rangle$ has to be resonant with the QD transition: $E_L = \hbar\omega_L = \hbar\omega_o = E_X$. This interaction is described by optical Bloch equations [94].

$$\begin{aligned} \frac{d\langle S_\pm\rangle}{dt} &= \mp i\delta_L\langle S_\pm\rangle - \frac{\gamma}{2}\langle S_\pm\rangle \mp \frac{i\nu}{2}\langle S_z\rangle \\ \frac{d\langle S_z\rangle}{dt} &= -\gamma\left(\langle S_z\rangle + 1\right) + i\nu\left[\langle S_-\rangle - \langle S_+\rangle\right] \end{aligned} \tag{3.12}$$

where $\langle S_\pm\rangle$ and $\langle S_z\rangle$ are expectation values of atomic operators $S_\pm = e^{\mp i\omega_L t}|g\rangle\langle e|$ and $S_z = \frac{1}{2}(|e\rangle\langle e| - |g\rangle\langle g|)$, respectively, δ_L is the detuning between the QD resonance and the laser field ($\delta_L = \omega_L$ - $\omega_o \ll \omega_o$), ν is the Rabi frequency of the excitation field, characterizing the strength of the light-matter coupling (ν^2 is proportional to the excitation power P or the average phonon number $\langle n\rangle$). In steady-state regime, where $\frac{d\langle S_\pm\rangle}{dt} = \frac{d\langle S_z\rangle}{dt} = 0$, we obtain a steady state solution for the population of the two-level system,

$$\begin{aligned} \langle S_-\rangle &= \left(\frac{2\nu}{\gamma - 2i\delta_L}\right)\left(\frac{1}{1+s}\right) \\ \langle S_z\rangle + 1 &= \frac{1}{2}\left(\frac{s}{1+s}\right) \end{aligned} \tag{3.13}$$

where s is the saturation parameter defined as

$$s = \left(\frac{2\nu^2}{\gamma^2 + 4\delta_L^2} \right) \tag{3.14}$$

The detected intensity will be given by

$$\langle I \rangle \propto \langle S_-(t) S_+(t) \rangle \tag{3.15}$$

This intensity corresponds to the integrated intensity over the whole emission spectral range. The expression in equation 3.15 can be written as

$$\begin{aligned} \langle I \rangle &\propto \frac{\nu^2}{\gamma^2 + 2\nu^2 + 4\delta_L^2} \\ \langle I \rangle &\propto \frac{1}{2} \left(\frac{s}{1+s} \right) \end{aligned} \tag{3.16}$$

The saturation parameter is directly related to $\frac{P}{P_o}$, where P is the excitation power and P_o is the two level system saturation power. For the realization of Quantum hammer experiment, the basic requirement is to have the QD excited. From equation 3.16, it is clear that the resonant emission (RE) intensity increase linearly at low excitation laser power and saturates at higher excitation power. This is because at high excitation powers, the ground and excited states of the system tend to be equally populated with a constant population of 1/2. Therefore, for the realization of quantum hammer effect the QD is excited resonantly close to the saturation power. The power dependence of RE intensity is presented in section 3.5.2.

3.3.2 Effect of spectral diffusion

The resonant emission lineshape is characterized by a Lorentzian profile (see equation 3.16). When the spontaneous emission is the only relaxation process which limits the coherence of the two level system (TLS), the decoherence time is given by $T_2 = 2T_1$, where T1 is the QD population lifetime. However, in semiconductor QDs there are structural defects that play a role in the QD relaxation. Therefore, the coherence of this artificial atom is not only limited by the spontaneous emission processes but also by the coupling with the phonons in the solid matrix and the charges that are trapped in surrounding defects. This leads to an additional decoherence processes arising from fast fluctuations of the medium

that cause rapid vibrations of energy levels in a time scale faster than the recombination time of the emitter. This is defined as pure dephasing time as it affects only the phase of the excited state not the population. In conclusion, the decoherence time of the QD in the TLS picture is given by the more general relation:

$$\frac{1}{T_2} = \frac{1}{2T_1} + \frac{1}{T_2^*} \tag{3.17}$$

These two contributions results in the homogeneous broadening of the QD.

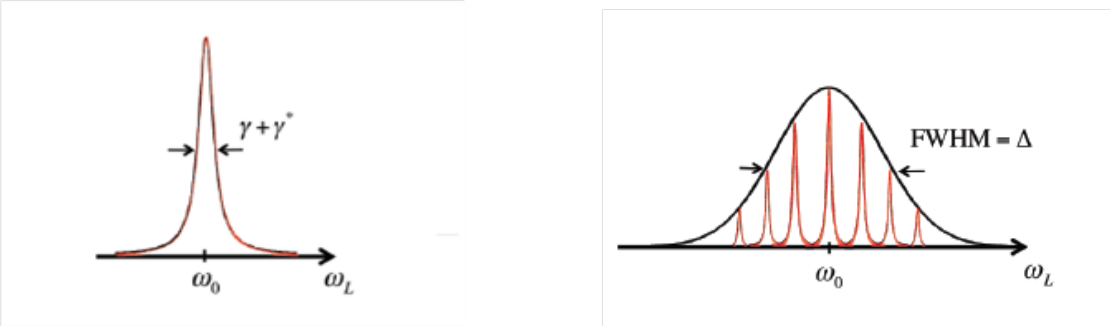

(a) (b)

Figure 3.12: Illustration of the emission linewidth of a quantum emitter in the presence of spectral diffusion: (a) Without spectral diffusion, the spectrum is characterized by a Lorentzian lineshape with homogeneous broadening due to radiative lifetime and pure dephasing. (b) With spectral diffusion, due to fluctuation of the environment surrounding the emitter, the frequency of the emitter varies at the time scale of 10 ns, which is higher than the radiative lifetime but much shorter than the response time of CCD devices, resulting in the inhomogeneous broadening of the spectra with a Gaussian lineshape.

However, in practice, the resonance frequency of the QD also suffers from fluctuations of the surrounding environment, which causes static random jumps and fluctuations of the resonant frequency. Such phenomenon is called spectral wandering or spectral diffusion [95–97]. These fluctuations occur at the nanosecond time scale (normally more than 10 ns), which is higher than the radiative lifetime of the QDs ($\approx$ 1.4 ns), and much shorter than the response time of the usual CCD devices (which normally have the time resolution in the range of more than few milliseconds). Thus, spectral diffusion results in an inhomogeneous broadening of the resonant excitation spectra. Figure 3.12 illustrates the situation in the presence of spectral diffusion. It has been shown that this inhomogeneous broadening features a Gaussian shape [97,98]. Figure 3.12(a) shows a Lorentzian lineshape, which is dynamically broadened by radiative lifetime γ and pure dephasing γ^*. When there are fluctuations in the transition frequency ω_o on a time scale larger than the lifetime, the line features a Gaussian broadening as shown in figure 3.12(b).

Spectral diffusion is an important issue in spectroscopy as it prevents an access to the intrinsic line properties. In resonant excitation spectroscopy, reducing the environment fluctuation effect is an important condition to be able to obtain a narrow lineshape. This issue will be discussed in section 3.3.4.1.

3.3.3 Experimental procedure

The basic requirement to perform the resonant excitation spectroscopy is to tune the laser energy exactly in resonance with the emission energy of the QD transition. Experimentally, we use resonant laser (RL) (with tunable wavelength) to perform resonant excitation. The resonant laser energy is scanned with very small steps over the QD transition to ensure obtaining the resonance during the scan. The resonant laser is a external cavity laser diode whose wavelength can be finely tuned via piezo mount supporting the external grating. The laser is scanned with the help of this piezo actuator which is controlled by the python program where we can set the range, the step size and the integration time of a scan. The experiment procedure contains several steps. First, the QD transition energy can be determined using the non-resonant PL spectroscopy presented in the previous section. Then the resonant laser wavelength is approximately set around this energy (using the grating) to perform the scan.

3.3.3.1 Measurement using CCD

Figure 3.13(a) shows a CCD spectrum when the laser wavelength is off-resonant. The scanning range is marked in the graph (dashed red lines). Each point corresponds to one pixel of the CCD. It is evident from the graph that even when the laser is off-resonant, there is a fraction of back-reflected laser signal that has not been rejected by the cross-polarized system and is therefore detected by the CCD. The linewidth of the laser spectrum is limited by the spectrometer resolution (1 pixel $\approx$ 12.3 μeV). In addition to the laser back-reflection, the CCD camera always possesses a background, which is an accumulation of the CCD electronic noise. This CCD background has a constant value for each pixel of the CCD ($\approx$ 700 counts) as shown in the graph.

To produce resonance emission (RE) spectra, at each step of the scan, an integrated value of the pixels within the defined integration range is recorded. The integration range is selected to make sure that it contains the whole laser scan process and the QD emission line. The integration time for each such scan is taken from 0.1 s to 1 s. The integrated value is the sum of the background and the resonant emission from the QD,

$$I_{\text{integrated}} = I_{\text{CCD}} + I_{\text{laser}} + I_{\text{QD}} \tag{3.18}$$

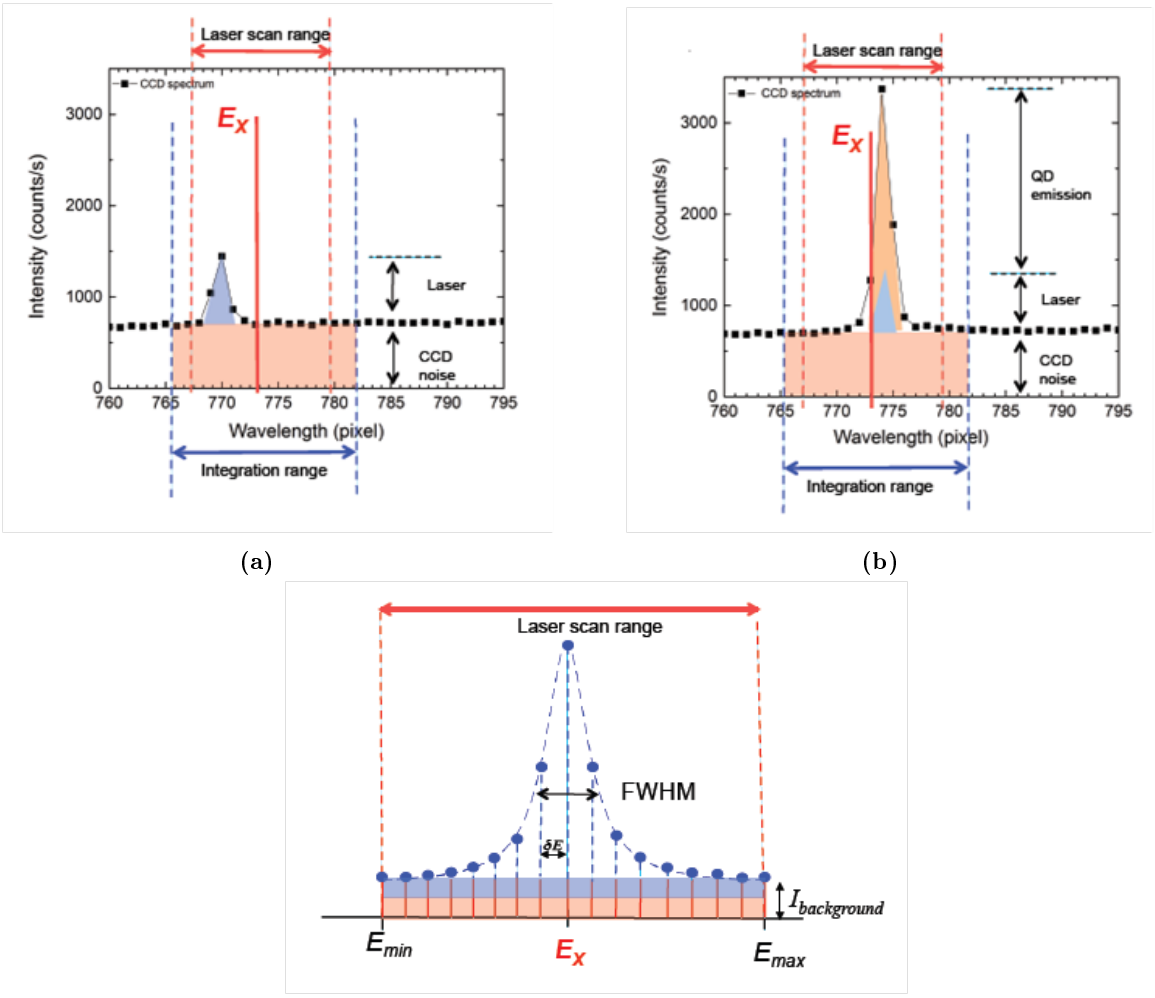

Figure 3.13: Illustration of the data collection procedure in resonant excitation spectroscopy: The vertical straight line E_X corresponds to the wavelength of the QD transition (a) CCD spectrum when the laser is off-resonant with the QD levels, only the back-reflected laser background and the CCD background are detected. (b) CCD photoluminescence spectrum when the laser is very close to resonance, the X emission on top of the laser background is obtained. The spectra is integrated over the range marked by pink dashed lines. (c) Integrated values at each laser detuning are taken and then plotted to form a resonant emission spectra. Figures taken from [38]

For each step of the excitation laser, we obtain one integration value. Finally, the resonant spectrum can be created as described in figure 3.13(c). Each step corresponds to a circle. When the resonant laser is off-resonant, $I_{QD} = 0$. As the laser approaches the QD transition wavelength (or energy) as shown in figure 3.13(b), the integration value starts to grow because of resonant emission of the QD (i.e. $I_{QD} \neq 0$). Eventually, the final spectrum can be obtained by subtracting the flat background intensity. In practice, during

one scan, the laser intensity changes from start to end point. This change varies from day to day depending on the wavelength (or energy) range and laser alignment through the cross-polarized setup but on an average we have about 30 ± 10% intensity change per sweep. In order to remove this change in laser intensity during the sweep over QD resonance, a feedback loop is designed to maintain the resonant laser power constant over the sweep range. However, even with the feedback loop we still see 1-5% change in the laser power over one sweep which is not so critical for the measurement of QD emission but will impact the amplitude of optically induced motion (see chapter 4) and hence the quantum hammer measurements. Chapter 5 presents the detailed analysis procedure followed to take into account this power change and other drifts during the experiment. This method to acquire the RE spectra via CCD was used in the early stages of the experiment, but has been replaced by the APD method as explained in the next section.

3.3.3.2 Measurement using APD

As shown in figure 3.1 there is a flip mirror at the end of the spectrometer which allows us to send light either to CCD or through the exit slit towards APD. In the quantum hammer experiment, APD is preferred over CCD to detect the resonant emission of the QD, as it allows synchronized measurements of the QD emission and mechanical motion. This is important because the quantum hammer effect is coherent with the optical resonance. Therefore, we expect to see change in the amplitude of the wire motion when the dot is excited. To realize this effect experimentally, we used the HF2LI box from Zürich Instruments (see Chapter 4 and 5 for detail), to be able to have synchronized QD emission and motion detection measurements (explained in Chapter 5).

In order to read the signal from the APD, we need to first bring the detection pixel on the center of the exit slit which is around 830 pixels. But due to the flip mirror (used to switch between CCD and APD), this number is not exact and needs some precise calibration from time to time. Once, you have the signal on APD we can connect it to either the computer to use the python based user interface or the Zürich box to perform the resonant scans.

3.3.4 Resonant emission of QD1

This section will present the resonant emission spectra from the QD studied mainly in the course of this work. The effect of the ultra-weak non-resonant laser on the RE signal will also be demonstrated. Finally, the influence of the probe laser on the RE signal is described. Probe laser is the laser used for optical motion detection presented in next chapter.

3.3.4.1 Effect of ultra-weak non-resonant laser

Following the procedure explained in the previous section, a RE signal of a QD can be obtained by sweeping the resonant laser over the QD emission. This has been realized successfully in the team by A.H Nguyen [38]. He obtained the resonant emission spectra for some of the QDs from the same sample studied in this work. Lifetime measurement of an excitonic line of a QD on this sample gave a value of $\tau = 1.4$ ns, which corresponds to the homogeneous radiative-decay linewidth of $\gamma = 1/\tau = 0.5$ $upp\mu$eV. We assume that the charged exciton studied in this work has a similar lifetime, which is generally the case. The linewidth of the measured RE spectrum by scanning the resonant laser over the QD resonance was found to be about 15 times larger than the expected homogeneous linewidth (see figure 3.14 blue trace). As discussed in the previous sections, this broadening may arise from pure dephasing [77] and/or spectral diffusion [77, 99, 100]. Spectral diffusion could originate from interplay of carriers in the dots with loosely trapped charges around the QDs [100]. The presence of this random charge trapping and untrapping of charges leads to spectral diffusion of the transition energy and as a result, broad and weak optical emission lines are obtained.

It was proposed to use an ultra-weak non-resonant laser to overcome the influence of spectral diffusion. The non-resonant laser controls the QD ground state, neutralizes the QD surroundings and therefore contributes to the narrowing of the optical transition of the QD. This technique has been used efficiently in several groups to optimize RE signal [101, 102] and to minimize the environment fluctuations to reduce the QD linewidth [99, 103]. This is achieved by using the non-resonant laser (at wavelength of 830 nm) used for PL characterization.

Figure 3.14 shows a typical resonant excitation spectra for the QD studied in [38] in the photonic wire "C3_2_1.88 of the same sample (it will be referred to as 'Champion line' from now on) for both without (blue) and with (red) the presence of an ultra-weak NRL. It is an exciton with FSS of about 25 μeV. Figure shows the RE signal for only one of the dipole. It is evident that by shining an ultra-weak power of about 1 nW (10^{-3} of the saturation power) of this laser, narrower linewidth (almost by a factor of 2, from 8 μeV (blue trace) to 4.5 μeV (red trace)) and higher RE intensity (also by a factor of 1.5) can be obtained. Thus, a weak NRL is always present while performing the RE measurements.

3.3.4.2 Effect of probe laser

As mentioned at the end of Chapter 2, successful realization of resonant excitation spectroscopy contributes to only half a step towards the quantum hammer experiment. The other half involves the optical motion detection. Details on this technique will be given in next Chapter. However, it is important to note that since it is optical detection, there

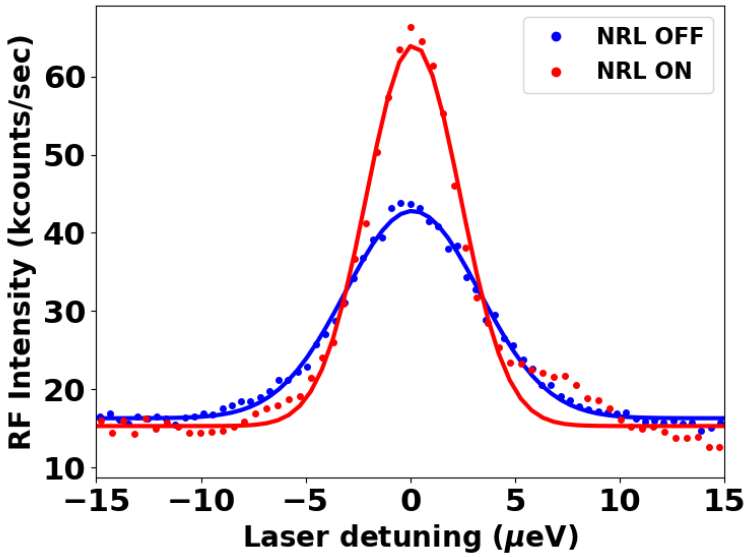

Figure 3.14: Typical resonant emission spectra of a champion line: The power of resonant laser = 1 nW (about 3×10^{-1} of the saturation power) and non-resonant laser = 1 nW (about 10^{-3} of the saturation power).

will be another laser, referred to as probe laser, shining on top of the photonic wire together with the RL and NRL at the time of quantum hammer experiment. Therefore, it is important to understand the influence of this probe laser, if any, on the RE signal.

The probe laser used for optical motion detection is a Toptica DL Pro, CW laser with wavelength chosen at 950 nm. Although at this wavelength, the energy of the laser is below the band gap of QDs (emits in the range 900 nm - 930 nm), yet we do see some influence on shining probe laser even at few hundreds of μW. At higher powers (few mW) the PL spectrum (not shown) is dominated by the back-reflected probe laser reaching the spectrometer CCD. This is mainly because, even though the laser peak is set at 950 nm, it indeed has a tail extending towards the QD emission energies, thereby affecting the PL spectrum both in the excitation (pumping the states at high powers) and detection (back-reflected light which is not fully suppressed by the cross-polarized setup). To suppress this back-reflected probe laser light, we placed a short pass wavelength filter FES950 in the spectrometer path, which is optimized to minimize the back-reflected probe laser. To reduce the pumping of carriers, we need to suppress the probe laser power around QD energies (900 nm - 930 nm) before it reaches the sample. For this purpose we placed two long pass filters FEL950 (one after the other) in the probe laser path (incoming path to the sample) such that it only allows the wavelength component $>$ 950 nm to pass. These filters are slightly rotated to tune the cut-on wavelength. Figure 3.15 compares the PL spectrum at different probe laser powers after placing one and two filters. It is evident that the PL intensity increases with the probe laser power but by placing the two filters the effect has been reduced as expected. Moreover, the lines are red-drifting (i.e. towards

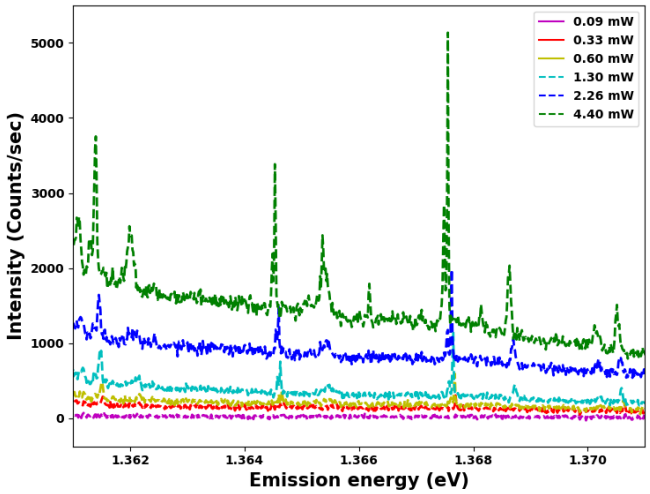

(a) With one FEL950 filter

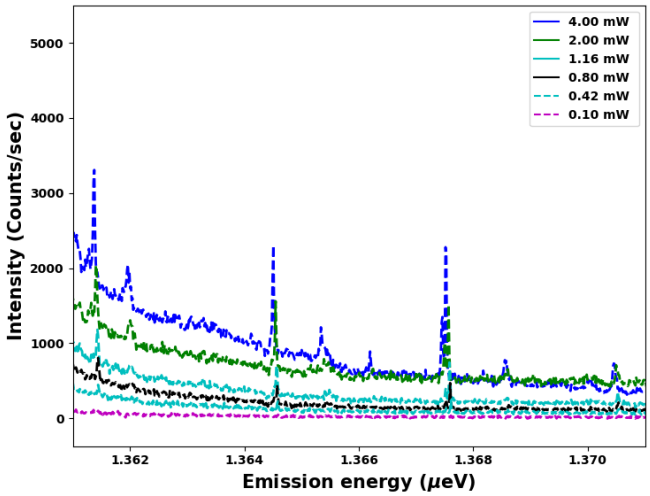

(b) With two FEL950 filters

Figure 3.15: Influence of probe laser on the non-resonant PL intensity: PL spectra obtained as a function of probe laser power, in the absence of non-resonant laser, for the case (a) With one long pass wavelength filter FEL950, placed in the laser path to the sample to reduce the influence of probe laser at QD energies, and (b) With two long pass wavelength filter FEL950. It is evident that with two filters overall impact is reduced.

higher wavelength and lower energy) with increasing laser power. This red drift is related to the fact that as the power shining on the photonic wire increases there will be more heating, leading to increase in temperature and as a result QD energy shows red-drift [104].

The important thing is to obtain resonant emission spectra in the presence of probe laser

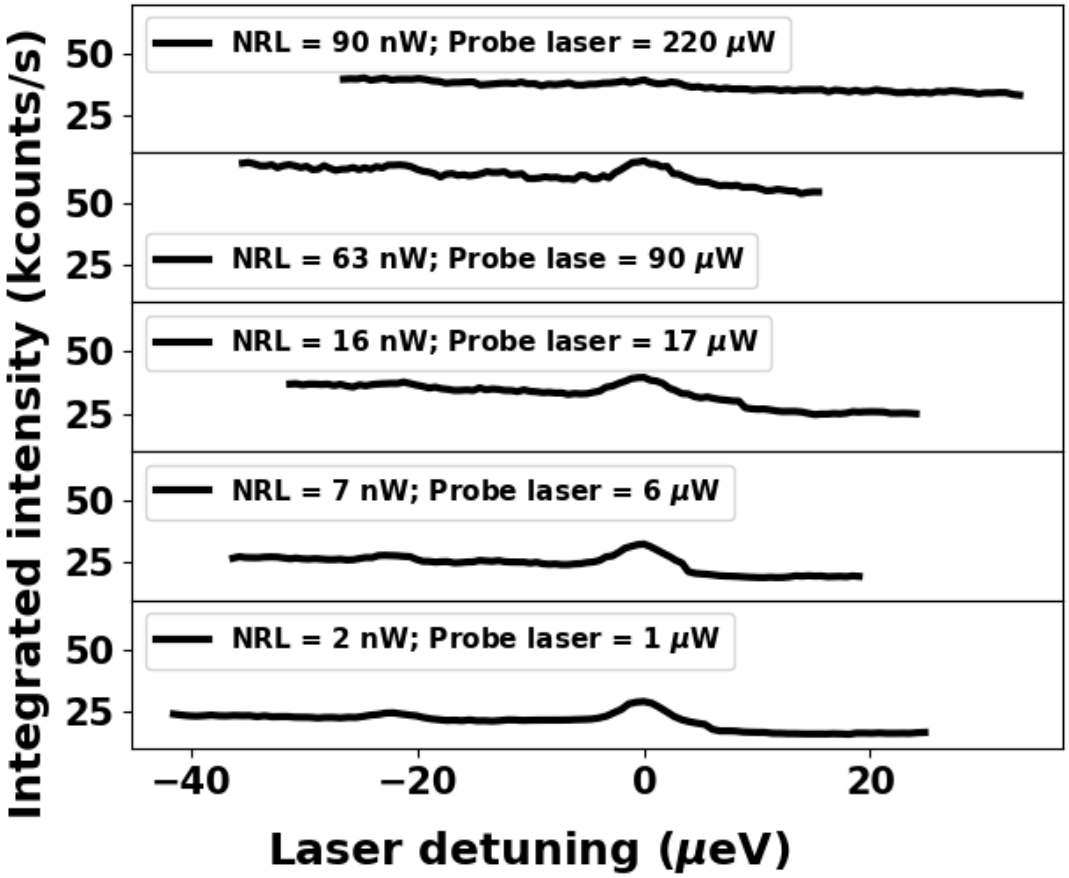

Figure 3.16: Resonant emission spectra for one of the dipoles of the champion line at different probe laser powers. Resonant laser power is 1 nW for all spectra's. Required NRL power is increasing with the increasing probe laser power.

to be able to realize the quantum hammer experiment. A careful series of RE spectrum's at different probe laser power is made for the champion line. The scan range is set to cover one of the two dipoles. There is a gap of few minutes between each plot, as every time the probe laser power is increased, QD line starts red-drifting (towards higher wavelength) and needs some time to become stable. The result is plotted in figure 3.16. Each spectrum is shifted horizontally and optical background (change in RL power when sweeping over the resonance) has been subtracted. There are few important points to notice. First, as the probe laser power increases, the required NRL power to stabilize the dot also increases. As a result, the total background (CCD noise + laser back-reflection + non-resonantly pumped signal) also increases. Second and most important, the RE signal is decreasing as probe laser power increases. Therefore, to obtain RE spectra in the presence of probe laser, it is better to work with lower probe laser powers (< 100 μW). However, this is a problem for optical motion detection as at low powers we are less sensitive to the motion amplitude

and moreover limited by the electronic noise of the detector (split photodiode SPD). Thus, it is important to find the suitable power of probe laser at which both resonant excitation and motion detection techniques can be performed simultaneously. The solution we have chosen is to use rather low probe laser power and to detect it using avalanche photodiodes (APD) for motion detection. With higher sensitivity and lower electronic noise it allows us to detect photonic wire motion at lower probe laser power. This issue will be addressed in detail in next chapter.

3.4 Other experimental challenges

In addition to the presence of probe laser, there are some other challenges that have to be taken into account for the realization of quantum hammer experiment. The following section will address them in detail.

3.4.1 Spectral drift

The emission energies of the QD states tend to drift with time. These drifts were attributed to the sticking of oxygen molecules onto the wire, which modified the surface charge and hence the electric field seen by the QD [69]. Since the resonant excitation spectroscopy requires the scanning of RL over the QD resonance and total scan range is about 100 μeV, it is therefore important to know the drift speed and to develop ways to reduce these drifts. Monitoring the evolution of the PL spectra over one cool down cycle (i.e. over one week, with cool down on Monday), we observed red-drift (i.e. towards higher wavelength) with all QDs. Th drift speed decreases slowly with time, being maximum in the first few hours of cool down. However, the pattern is not always the same. Most of the times, QDs keeps drifting but at slower rates and thus requires realignment of the sweep range every 2 hours on an average. Usually, after one or two days at low temperature, QDs become stable enough to stay in the scanning range for few hours. Sometimes, we have also observed change in the drift direction (from red drifting to blue drifting), mostly on the third day after cool down. However, we found no definite pattern to predict the behaviour of drift and it varies from one week to other.

In order to minimize the drifts various methods have been proposed. One such strategy, as mentioned in [69], is by passivating the sidewall of the photonic wire with a 20 nm thick Si_3N_4 layer. But unfortunately, it could not entirely suppress the drift and the emission lines still shift during the measurement. Other strategy is to use the temperature effect on the QD emission energy. It was investigated in [41] for InAs QD embedded in GaAs photonic wire. As the temperature of the system increases, it could cause surface effects on the wire environment surrounding the QDs. This leads to the red-shift the emission lines. Based on this temperature effect, the idea is to shine the extra intense laser beam,

to heat up the photonic wire and red shift the emission lines. This strategy is proposed in [38] to stabilize the natural temporal blue-drift of the QDs by inducing red-drift at the same speed.

However, in our case QDs are already red-drifting. But as mentioned before, the drift speed decreases with time. One way to understand this would be that the QD is drifting towards some stable value and with time as it reaches close to this value drift speed decreases. Therefore, we used the third strategy mentioned above to shine an extra intense laser and assist the QD to reach its stable energy faster. The laser used for this flashing purpose is a Thorlabs laser diode BL976-PAG500. This laser has maximum power up to 600 mW and a wavelength of 975 nm (1.27 eV) which is much higher than the emission wavelength of InAs QDs (900 nm - 930 nm). Moreover, this intense laser flashing could also help to bring the blue-drifting QD back in the scanning range on third and fourth day of the experiment. Nevertheless, keeping spectral diffusion in mind, the best time to perform quantum hammer experiment (requires multiple sweeps over the QD resonance, see Chapter 5 for details) is at least after 24 hours after the cool down, with real time monitoring of the QD line.

3.4.2 Suppression of resonant laser back-reflection

As mentioned earlier, the suppression of the resonant laser back-refection is very critical for obtaining the resonant emission spectra. This is because the resonant laser wavelength is exactly the same as the QD emission and could mask the QD emission in case of bad suppression. The suppression efficiency depends on the alignment through the cross-polarized setup and on the position of the resonant laser on top of the photonic wire. Even small misalignment of the resonant laser with respect to the position of optimum suppression on top of the photonic wire could result in a completely unacceptable suppression situation. Therefore, to obtain a resonant emission spectra, in addition to have the stable QD emission line, it is necessary to have stable setup in order to have low back-reflected parasitic signal from the laser. However, there is a way to avoid this critical alignment issue.

The emission spectrum can be decomposed into a central so-called zero-phonon line (ZPL) and the phonon side band (PSB). ZPL is related to the radiative recombination, without any net energy exchange with the phonons reservoir, i.e. when no phonon is absorbed or emitted. The side bands of the ZPL come from the emission of photons at lower or higher energy. The spectral extent of the side bands is mainly given by the mean energy of the acoustic phonons involved in the process. The wavelength of these phonons is of the order of the lateral size of the QD, thus giving a mean energy in meV range. At low temperature (kT $\ll$ meV), the probability of absorbing phonons is negligible and only the emission processes take place, i.e. the lateral side bands are thus asymmetric with only the low energy component as shown in figure 3.17. At high temperature (kT $\gg$ meV), absorption and emission get the same efficiency and the side bands become symmetric.

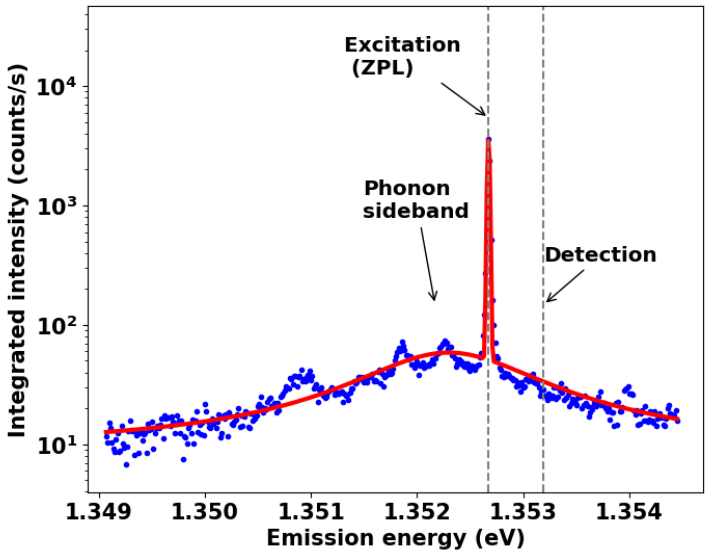

Figure 3.17: Illustration of the detection on the phonon side band (PSB): Non-resonantly excited PL spectrum of QD1 in semilog scale showing the phonon side band on the lower energy side.

The strategy to avoid the precise alignment and suppression control is to detect the QD emission on PSB. The idea is to sweep the resonant laser over the ZPL and collect photons from the PSB [105]. Thus we can separate the laser background from the RE signal. The detection is done on the high frequency side in spite of the fact that phonon side band is better on the lower energy side. This is because resonant laser has larger spread on lower energy side which would again impact the signal contrast and make it alignment sensitive. The RE spectra obtained at ZPL and PSB (on the higher energy side) is shown in figure 3.18. Since, PSB is less intense as compared to ZPL, therefore, we will have less RE counts but signal to noise ratio is much better. Moreover, during the quantum hammer experiment, we do not care much about the number of photons detected as long as we know we are exciting the dot close to saturation. We need to obtain a clean RE spectra to know when the dot is excited and whether or not we see the effect on the photonic wire at that instant.

3.5 Resonant emission (RE) spectra of QD1

This section will characterize the QD line studied mainly in this work for realizing the quantum hammer experiment. As mentioned in section 3.2.3, this line is identified to be a charged exciton and the saturation power on NRL is about 4 μW (section 3.2.2). Probe

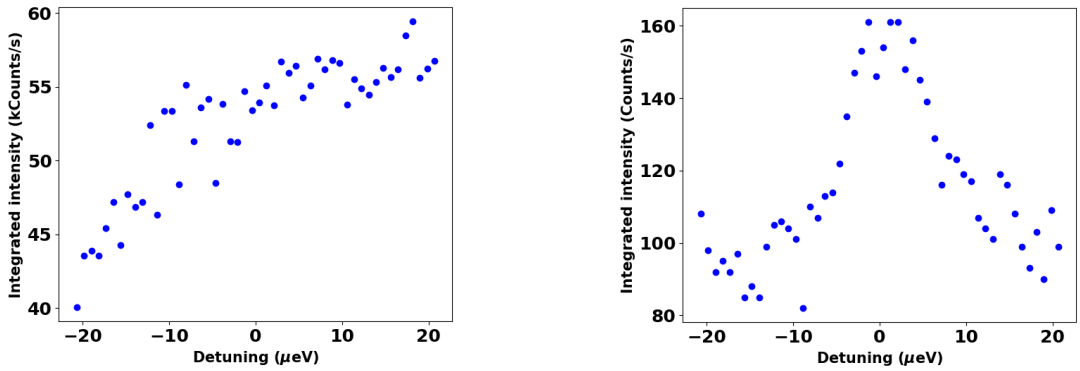

(a) at ZPL **(b)** at PSB

Figure 3.18: RE spectra for QD1 obtained at (a) ZPL and (b) PSB. At ZPL laser bakground is dominating the RE signal whereas at PSB we obtain a clear RE spectra, although with less counts. The integration time for both the spectra is 1 sec. Probe laser power = 100 μW, NRL power = 100 nW, and RL power = 100 nW and locking laser (used for position locking, see Chapter 5 for details) = 100 μW.

laser influence was observed for this line and RE spectra series was made similar to the one shown in figure 3.16 for champion line. The optimum power for probe laser was found to be 100 μW. At this power, it is possible to obtain RE spectra and to detect the motion of the photonic wire. The RE spectra obtained in the presence of 100 μW probe laser, 100 nW NRL and 100 nW RL, is shown in figure 3.19. The measured inhomogeneous linewidth is about 28 μeV. This measurement is done by the strategy explained in section 3.4.2 i.e. exciting the ZPL and detecting at PSB. The spectra shown in the figure is the average of about 300 such spectra's where each spectra is obtained by making a 21 points sweep over the QD resonance (each sweep takes approximately 1 min). It is important to note that before taking the average of 300 spectra's, drifts in the QD line are corrected by shifting the spectra horizontally (details in Chapter 5).

3.5.1 Non-resonant laser power dependence

As mentioned in section 3.3.4.1, an ultra-weak non-resonant laser is necessary to optimize the RE signal. This section will present how does the RE signal intensity depends on the NRL power. It has been observed in [38,83] that on increasing the NRL power, RE intensity increases and reaches maximum at a power about three to four decades lower than the power required to saturate the dot. On further increasing the NRL power, RE intensity decreases as the non-resonant PL contribution starts to be significant. Therefore, it is important to know the required NRL power for maximum RE intensity. This dependence for QD1 is shown in figure 3.20. Resonant spectra was recorded at different non-resonant laser powers in the presence of probe laser of 100 μW to take into account the contribution

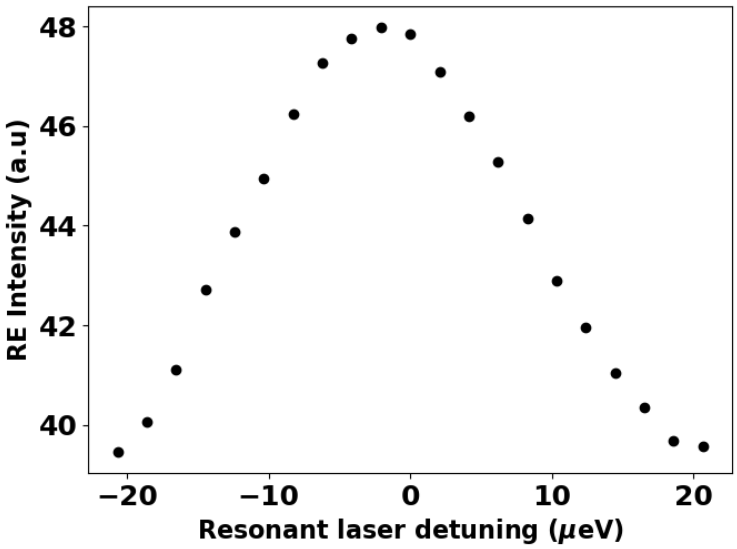

Figure 3.19: RE spectra of QD1 in the presence of probe laser of 100 μW, NRL of 100 nW and RL of 100 nW. Resulting spectra is the average of about 300, 1 min sweeps, over the QD resonance. The detection is done at PSB using APD. The linewidth is about 28 μeV.

of probe laser as well. The peak value of the scan is plotted as a function of non-resonant laser power. It is evident from the plot that the required NRL power is around 100 nW, which is roughly 2.5×10^{-2} times the saturation power (≈ 4 μW). Therefore, all the RE measurements were performed in the presence of 100 nW NRL. The required NRL power is comparatively higher than the reported values [38,83] because of the presence of probe laser.

3.5.2 Resonant laser power dependence

It has been shown in section 3.3.1 that the RE intensity increases linearly at low excitation powers and saturates at higher excitation powers. For the quantum hammer experiment, the measurements are done closer to the saturation power so that the effect is maximum. Therefore, one important step before realizing the quantum hammer experiment is to perform a RE power dependence measurement. RE measurement is done at different resonant laser powers in the presence of 100 μW probe laser and 150 nW of non-resonant laser. The peak value of each scan measured at the phonon side band is plotted as a function of resonant laser power as shown in figure 3.21 for QD1. The saturation power is around 100 nW. Therefore, quantum hammer measurements are done at 150 nW of resonant laser power and 150 nW of non-resonant laser power.

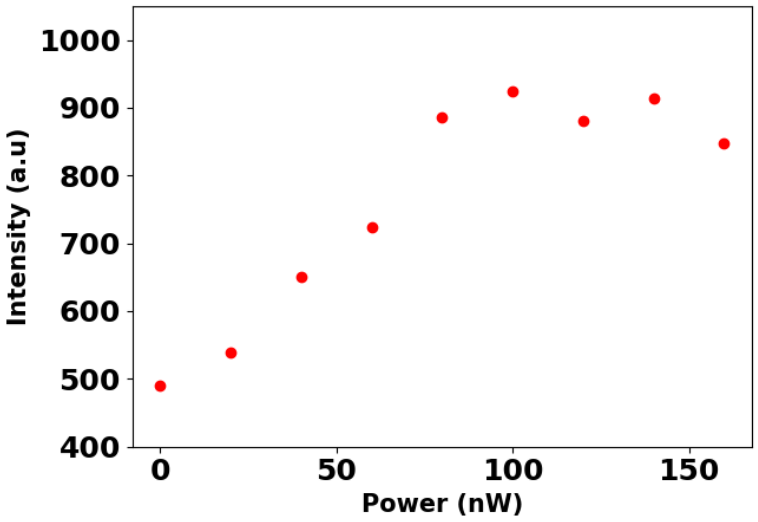

Figure 3.20: Dependence of RE intensity on the non-resonant laser power: RE spectra for QD1 are obtained at phonon side band using CCD. The peak value of each scan is plotted as a function of non-resonant laser powers. The measurements are done in the presence of 100 μW of probe laser, 100 μW of locking laser (used for position locking, see Chapter 5 for details) and 150 nW of resonant laser at different non-resonant laser powers. Camera settings: Low gain and High capacity with an exposure time = 1.0 s.

3.5.3 Polarization-sensitive resonant excitation intensity

From the non-resonant PL sensitive measurement presented in section 3.2.3, we concluded that there is no FSS in the spectra, omitting the possibility of a neutral exciton. However, we do observed change in the intensity with degree of linear polarization about 50%, which was explained on the basis of the coupling of the emitted light with one of the polarized mode of the photonic wire. In addition to the PL spectra at different half-wave plate angle, we also recorded the RE spectra. The RE intensity (height of the peak from the Gaussian fit of each spectra acquired on phonon side band) is plotted as a function of the angle of polarization. We observe the change in the RE intensity with the same period as in the case of PL measurements. This implies that RE does not depend on the polarization of the excitation light (as explained in section 3.1.1.4), thereby confirming the circular polarization of QD1. Thus, we can conclude QD1 is a charged exciton. However, there is a shift of 60° - 45° = 25°, in the polarization axis between the two plots shown in figure 3.22 and 3.11 respectively. The reason of this shift is not understood so far and needs further investigation.

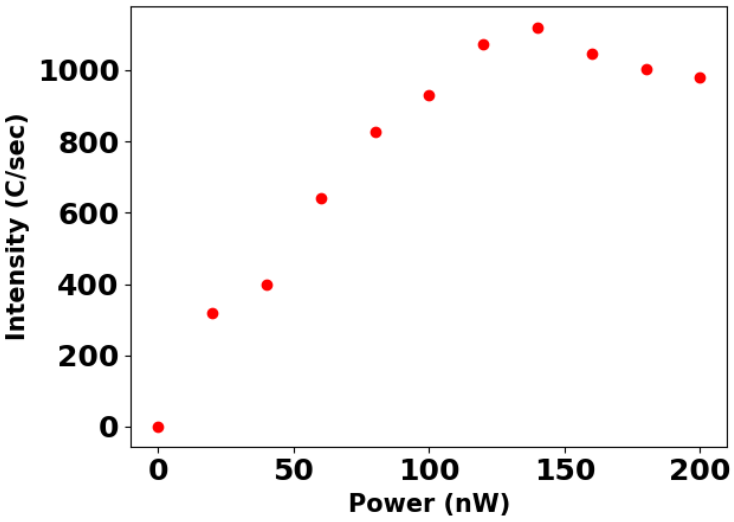

Figure 3.21: Dependence of RE intensity on the resonant laser power: RE spectra for QD1 are obtained at phonon side band using CCD. The peak value of each scan is plotted as a function of resonant laser power. The measurements are done in the presence of 100 μW of probe laser, 100 μW of locking laser (used for position locking, see Chapter 5 for details) and 150 nW of non-resonant laser at different resonant laser powers. Camera settings: Low gain and High capacity with an exposure time = 1.0 s.

3.6 Conclusion

This chapter presented the photoluminescence spectroscopy and resonant excitation spectroscopy used to characterize the QDs investigated during the course of this work. Resonant excitation spectroscopy was performed in the cross-polarized setup to suppress the back-reflected laser from the emission detection. To improve the RE signal to noise ratio, the QD light was detected on the phonon side band (PSB). One of the main QD which is used in the quantum hammer experiment is characterized using the non-resonant and resonant power and polarization measurements. Following the results from power and polarization-sensitive measurements, the line is identified as charged exciton. However, the change in intensity of the resonant emission spectra with the angle of polarization is not completely understood. This chapter also presented the power series of the resonant emission (RE) signal of QD1 (used for the quantum hammer measurement) with both the non- resonant laser and resonant laser to find the optimum powers for the quantum hammer experiment.

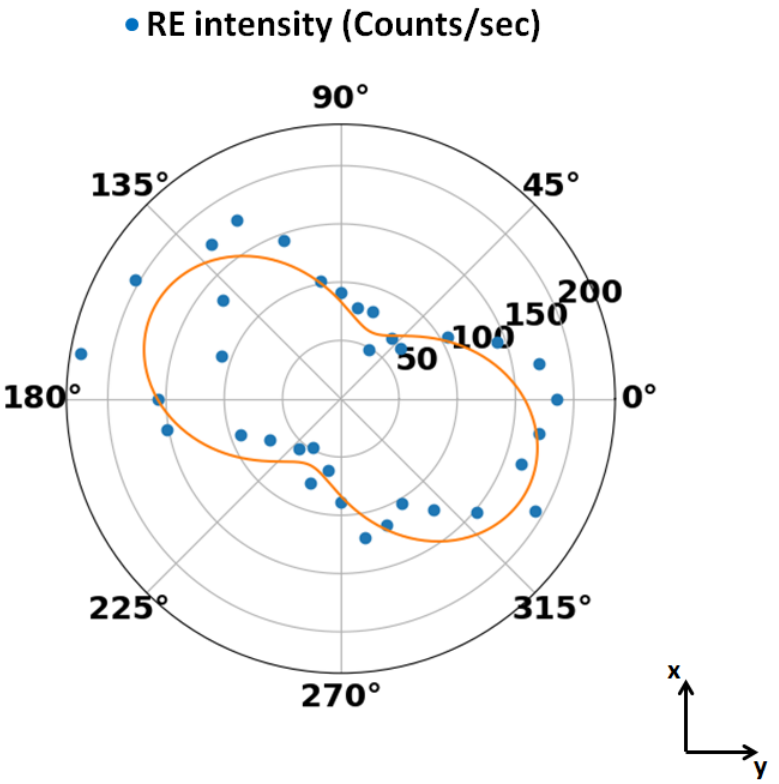

Figure 3.22: The evolution of resonant emission intensity at different angles of rotation: The intensity for each angle of the half-wave plate is taken from the Gaussian fit of the RE spectra measured at phonon side band. The polarization axis is 60° with respect to the horizontal (or x) axis (0° corresponds to the y direction). Resonant laser power = 50 nW, non-resonant laser power = 150 mW, probe laser power = 100 μW, and locking laser power (used for position locking, see Chapter 5 for details) = 100 μW. Camera settings were: Medium Gain, Low noise and exposure time = 1.0 s.

Chapter 4

Optical detection of photonic wire motion

As mentioned earlier the second technique required to implement the Quantum Hammer effect experimentally is the optical detection of the motion induced in the photonic wire. This chapter will firstly present the detection principle, which is based on the optical detection technique, followed by the discussion on the important parameter, detection sensitivity. Both simulations and experimental data are presented for understanding the influence of various factors on detection sensitivity value. Experimental setup is then presented together with the main components. The second part of this chapter is based on the optical actuation of photonic wires. This technique has been studied earlier in the team and is presented in the work [42].

Contents

4.1 Optical detection

It has been observed [35, 39, 41, 42] that trumpet photonic wires exhibit interesting mechanical properties. The optical readout of the displacement of such an oscillator is based on the detection of the deviation of laser beam reflected from the oscillator's surface using photodiode as a detector. The approach is similar to a position-sensitive photodiode (PSPD) used in standard atomic force microscopy (AFM) [8] to detect the motion of the cantilever as shown in figure 4.1. A laser beam reflected off the cantilever is used to monitor deflection in the cantilever as it interacts with the sample surface. Any deflection in the cantilever will cause slight changes in the direction of the reflected beam which can be detected by the photodiode.

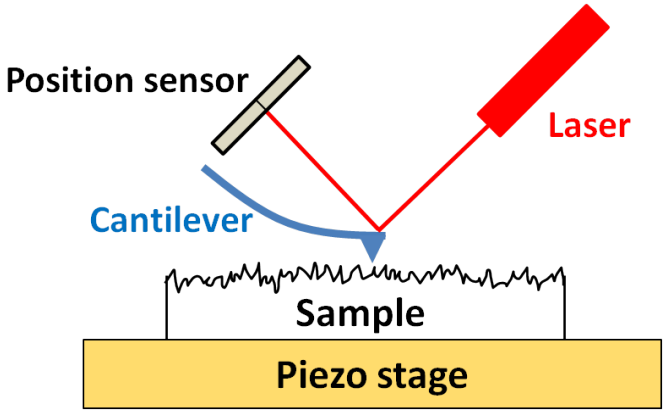

Figure 4.1: Demonstrating an operating principle of atomic force microscopy using laser beam reflection.

Figure 4.2: (a) Split photodiode (SPD) and Quadrant photodiode (QPD) as detectors. (b) Working principle and equation for SPD.

One can use either a split photodiode (SPD) or a quadrant photodiode (QPD) as detector. As shown in Fig 4.2(a) SPD and QPD are photo detectors with two and four identical photodiodes located very close to each other respectively. The interesting feature of SPD (or QPD) is a possibility to measure the difference between signals of these photodiodes.

They are discussed in detail in section 4.3.1.5. Figure 4.2(b) demonstrates the detection using SPD as detector. In this case, the measured signal V_d, is the difference between the signal of photodiodes A and B i.e. $V_d = V_A - V_B$. Initially, the laser spot is placed in the center of SPD (red spot in the figure 4.2(b)) which implies that both parts A and B have equal laser intensity resulting in the zero difference signal. Now, when the structure shifts along any one axis (lets say X), it changes the distribution of reflected light intensities on the parts of SPD leading to non-zero difference signal which is proportional to the displacement amplitude. It will be shown later in this chapter that one can also use a simple detector with only single photodiode (PD) for motion detection. The choice of the photodiode will depend on the required sensitivity of the experiment and the laser power. It will be discussed in detail in section 4.4.5.

This method of motion detection is very sensitive and allows us to detect even Brownian motion of the photonic wire, whose amplitude at T = 5 K is about few tens of picometers. The detection sensitivity, named $\overrightarrow{\beta}$ (V/m) of these detectors is a measure of how many nanometers of motion correspond to a unit of voltage measured on the detector. It is discussed in detail in the following section.

4.2 Detection sensitivity

In order to understand what is the detection sensitivity, let us consider SPD as detector. As already mentioned, the output voltage signal from SPD, V_d is proportional to the difference between the voltage signal generated on the two photodiodes A and B. The signal generated on a photodiode is proportional to the photocurrent produced as a result of exposure to the incident light. Therefore, the signal generated on both photodiode A and B of SPD is proportional to the intensity of reflected light from the top facet of the photonic wire. Initially, when the photonic wire is at rest (i.e. there are no oscillations) and the laser is focused somewhere on the top facet of the photonic wire (for simplicity of understanding, let us assume it to be at center). The reflected light is imaged on the center of the SPD as shown in figure 4.3(a) such that both A and B have equal laser intensity resulting in the generation of same amount of signal on photodiode A and B leading to $V_d = V_A - V_B = 0$. Now, if the photonic wire is shifted along X direction of SPD as shown in figure 4.3(b), the distribution of the reflected laser intensity changes on the two parts of the SPD, with less intensity on diode A as compared to that of diode B, resulting in a non-zero V_d. This is because when the wire moves out of the beam focused on its top facet, that part of the beam is not reflected and therefore changes the distribution of reflected intensity on SPD. On the other hand, if the photonic wire shifts along Y direction of SPD as shown in figure 4.3(c), the change in the reflected laser intensity will still be symmetrically distributed between diode A and B, resulting in $V_d = 0$.

The ability to detect the displacement of the photonic wire is defined by the possibility

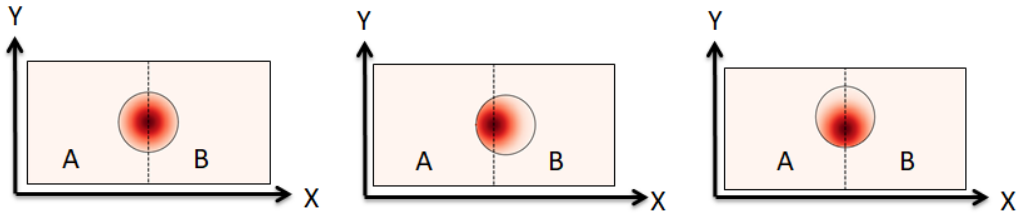

(a) (b) (c)

Figure 4.3: Laser intensity distribution on split photodiodes (SPD's) surface (a) Laser and photonic wire at the center of the SPD such that $V_d = 0$. (b) Photonic wire is shifted horizontally, resulting in non-zero difference signal ($V_d \neq 0$). (c) Photonic wire is shifted vertically, and V_d remains zero. Black circle shows the position of photonic wire and red spot shows the distribution of laser intensity on SPD. Assumption: reflection from the substrate is zero and gap between the two diodes A and B is not taken into account.

to distinguish between values of V_d signal at two positions of wire. Thus, detection sensitivity β is the derivative of V_d signal with respect to the coordinate. The difference signal V_d is a two-dimensional function and therefore detection sensitivity can be represented as a vector, $\overrightarrow{\beta}$

$$\overrightarrow{\beta} \equiv \begin{pmatrix} \beta_x \\ \beta_y \end{pmatrix} = \begin{pmatrix} \frac{dV_d}{dx} \\ \frac{dV_d}{dy} \end{pmatrix}$$

Therefore, how sensitive are we to detect the photonic wire's displacement depends on the angle between $\overrightarrow{\beta}$ and direction of the wire displacement. More precisely, it is the projection of $\overrightarrow{\beta}$ on the direction of motion. For example in the case described above i.e. when the reflected laser from the top of the wire is focused on the center of the SPD, the detection sensitivity vector is coincident with X direction of the SPD (as $\beta_y = 0$), which means that we can detect the photonic wire oscillations which are along X direction with maximum sensitivity and can not detect any oscillations in Y direction. However, it will be shown later in section 4.3.1.4, we can change the orientation of the wire oscillations with respect to SPD axis using the Dove prism.

4.2.1 Optimizing detection sensitivity

Detection sensitivity is an important quantity which defines how sensitive are we to detect the photonic wire oscillations. Therefore, it is important to optimize it by keeping in mind all the parameters that could influence its magnitude and direction. It depends on

various parameters such as laser intensity, laser position and size with respect to the top of the photonic wire, position on the photodiode and also on the direction of photonic wire's oscillation as seen in previous section. Since, detection sensitivity is the derivative, with respect to the wire position, of the measured photodiode voltage signal which is proportional to the intensity of light falling on the photodiode. Thus, increasing the laser power will directly increase the sensitivity of the measurement.

This section is devoted to understand how detection sensitivity vector changes its magnitude depending on laser parameters such as laser position and size with respect to the top facet of the photonic wire. Here, I presented the numerical simulation where the goal is to calculate the detection sensitivity vector for 2D grid (defined by the photodiode area) of all possible positions of laser with respect to the photonic wire (position dependence) and also for different size ratios between laser beam diameter and the top diameter of photonic wire (size dependence). These simulations are carried out in python, inspired by the one presented in the work of D. Tumanov's thesis [42]. In practice, the laser is positioned at the center of the top facet of the wire and as the wire oscillates the amount of reflected light changes. For this simulation, the laser is fixed at the center of the 2D grid whereas the photonic wire position is changed. For each position of the photonic wire (defined by the center of the photonic wire), I calculated the amount of light reflected to the photodiode. To avoid the distortion at the edge of the photodiode, the photonic wire position is limited to the range spaced away from the border by the wire radius. For example, if we have the photodiode of dimensions 100 a.u along the horizontal axis and the radius of photonic wire is 30 a.u, then good results are in the range (30,70) instead of the full range (0,100).

Laser Intensity Profile: Since there is a spatial filter mounted in the beam path (section 4.3), laser profile is expected to be centrally symmetric with $\sigma_X \equiv \sigma_Y \equiv \sigma$, where σ_X and σ_Y are the spreads of the Gaussian spot along the axes. Therefore, in these simulations laser profile is approximated as centrally symmetric 2D Gaussian which can be defined as:

$$G(x, y) = A.e^{-[(x-x_o)^2+(y-y_o)^2]/[2\sigma^2]} \tag{4.1}$$

Photonic wire top facet profile: Profile of the top facet of the photonic wire is expected to be circular in shape as it is defined by the mask used during the growth. However, for some real structures top facet is slightly elliptical. In these simulations, I assumed a circular profile for photonic wire's top facet that can be defined as:

$$\frac{(x - x_o)^2 + (y - y_o)^2}{R^2} = 1 \tag{4.2}$$

where R is the radius of the top facet of the wire. Let's define the ratio between the

laser diameter and the photonic wire top facet diameter as r = $(4\sigma)/(2R)$.

For one fixed ratio r, we calculate the light reflected from the wire for each relative position of wire with respect to the laser (fixed at the center of the photodiode). When the wire is completely outside the laser beam, the reflected light to the photodiode will be zero. This is because the Rayleigh length (distance over which the beam radius spreads by a factor of $\sqrt{2}$ times more than it is at the focus and the wavefront curvature is maximum) is equal to 1.5 µm and the height of the photonic wire is about 18 µm. Therefore, the light rays reflected from the substrate will be highly diverging and can not be collected back by the microscopic objective. Now, when the wire enters the laser beam, only the part of the laser beam will be reflected back to the photodiode that shines the top facet of the photonic wire. Figure 4.4 demonstrates both the top view image of the photonic wire and the photodiode (SPD taken as an example) with laser beam on top. Therefore, we can define a function of photonic wire's top profile as

$$T(x,y) = \begin{cases} 1 & \text{if } x^2 + y^2 \leqslant 1, \\ 0 & \text{otherwise} \end{cases} \tag{4.3}$$

and therefore the intensity profile on photodiode will be the product of G(x,y).T(x,y).

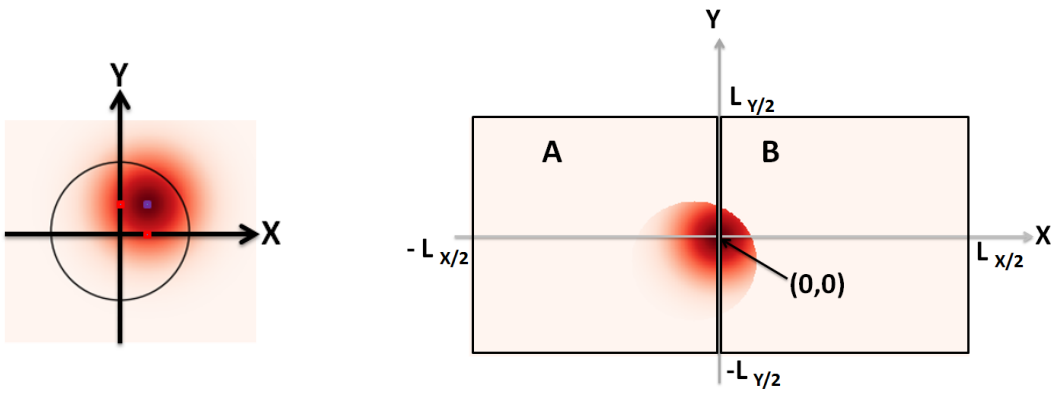

(a) (b)

Figure 4.4: (a) Sketch demonstrating a top view image of the photonic wire. Black circle shows the edge of photonic wire's top facet. 2D Gaussian laser beam on top of the wire is shown by red color. Colour brightness is proportional to the intensity of the laser. Violet dot demonstrates central position of beam. Red dots on the axes shows the relative displacement x and y of the laser with respect to the center of photonic wire. (b) Sketch demonstrating a top view image of SPD. Two parts of SPD are marked A and B. Laser is initially aligned with the center of SPD, but only a part of the laser light reflects to SPD from the photonic wire. This amount depends on the relative displacement of the laser with respect to the center of photonic wire.

A) **For the case of split photodiode (SPD):**

In case of SPD, we have two photodiodes close to each other and initially the beam is placed at the center of these photodiodes as shown in figure 4.4(b). The integrated intensities are therefore given by the following expressions:

$$\begin{cases} I_A(x,y) & = \int_{-L_{Y/2}}^{L_{Y/2}} \int_{-L_{X/2}}^{0} G(x',y').T(x'-x,y'-y)dx'dy' \\ I_B(x,y) & = \int_{-L_{Y/2}}^{L_{Y/2}} \int_{0}^{L_{X/2}} G(x',y').T(x'-x,y'-y)dx'dy' \\ I_{tot}(x,y) & = I_A(x,y) + I_B(x,y) = \int_{-L_{Y/2}}^{L_{Y/2}} \int_{-L_{X/2}}^{L_{X/2}} G(x',y').T(x'-x,y'-y)dx'dy' \\ I_d(x,y) & = I_A(x,y) - I_B(x,y) \end{cases} \tag{4.4}$$

where

- I_A (or I_B) = integrated intensity on the part A (or B) of SPD;
- I_{tot} = integrated intensity on SPD (total intensity);
- I_d = difference in integrated intensity between photodiodes A and B of SPD;
- x,y = coordinates of the relative position of centres of the laser beam and photonic wire's top facet;
- r = ratio between laser diameter and top diameter of the photonic wire;
- L_X, L_Y = size of SPD along X and Y.

The detection sensitivity components along direction X(Y) is then calculated as the derivative of intensity difference using the expression:

$$\beta_{x[y]}(x,y) = \frac{dI_d(x,y)}{dx[y]} \tag{4.5}$$

One more thing to mention is that in these simulations the gap between the two parts of the SPD is taken as zero. Nevertheless, it should not affect a lot on the quality of the result, because the gap is only about 20 μm size, whereas the laser beam size on SPD is about 500 μm.

B) **For the case of a single photodiode (PD):**

In case of a single photodiode there will be no difference signal and we can only calculate the total intensity on the photodiode by integrating over the photodiode size which is given by

$$I_{tot}(x,y) = \int_{-L_{Y/2}}^{L_{Y/2}} \int_{-L_{X/2}}^{L_{X/2}} G(x',y').T(x'-x,y'-y)dx'dy' \tag{4.6}$$

where L_X and L_Y are the lengths of the PD along X and Y. The detection sensitivity components will then be calculated from the derivative of total intensity signal using the expression:

$$\beta_{x[y]}(x, y) = \frac{dI_{tot}(x, y)}{dx[y]} \tag{4.7}$$

Since the measured signal in this case is the total intensity signal unlike the difference signal in case of SPD. Therefore, the strategy in this case will be to position the laser close to the edge of the photonic wire so that small displacement of photonic wire will change the reflected light intensity on photodiode resulting in larger detection sensitivity values as compared to when laser is placed at the center of wire. This is discussed in detail in the following section together with the simulation results for both SPD and PD as detector.

4.2.1.1 Dependence on the size and position of laser beam with respect to the photonic wire

A) Split photodiode (SPD)

Result of the simulations, for the case, when the ratio between the laser beam diameter and photonic wire top facet diameter is equal to one, i.e. r = 1, with SPD as detector are shown in figure 4.5. The plots in figs. 4.5(a) to 4.5(d) represents the image of the position of photonic wire on SPD. The size of SPD along X and Y axis is chosen to be equal to 200 a.u each (from -100 to 100 a.u) with origin at center of SPD as shown in the figure 4.4(b) and the radius of photonic wire is taken as 30 a.u. Therefore, the plotted results are in the range -70 to 70 a.u on both axis. The Gaussian beam is fixed at the center of SPD i.e. at (0,0). For each position we calculate the integrated laser intensity I_{tot} (x,y) (plotted in figure 4.5(a)) and difference in intensity I_d (x,y) between the two parts of SPD (plotted in figure 4.5(b)) using formulas from eq. 4.4, where x and y are the relative distance between the center of photonic wire and center of Gaussian beam. Figure 4.5(c) and 4.5(d) shows the detection sensitivity components β_x and β_y respectively, calculated using eq. 4.5.

It is clear from the figures that along the central horizontal cross-section i.e. along the the axis marked by horizontal dashed line in figure 4.5(d), the y component of detection sensitivity (β_y) is equal to zero, therefore for this axis, the magnitude of detection sensitivity is equal to absolute value of the sensitivity along X axis of detector i.e. $|\overrightarrow{\beta}(x, 0)| = |\beta_x(x, 0)|$. Therefore, the value of β_x along the central horizontal cross-section gives us the estimation of detection sensitivity vector for this axis.

Figure 4.5(e) shows the plot of β_x values along the central horizontal cross-section of

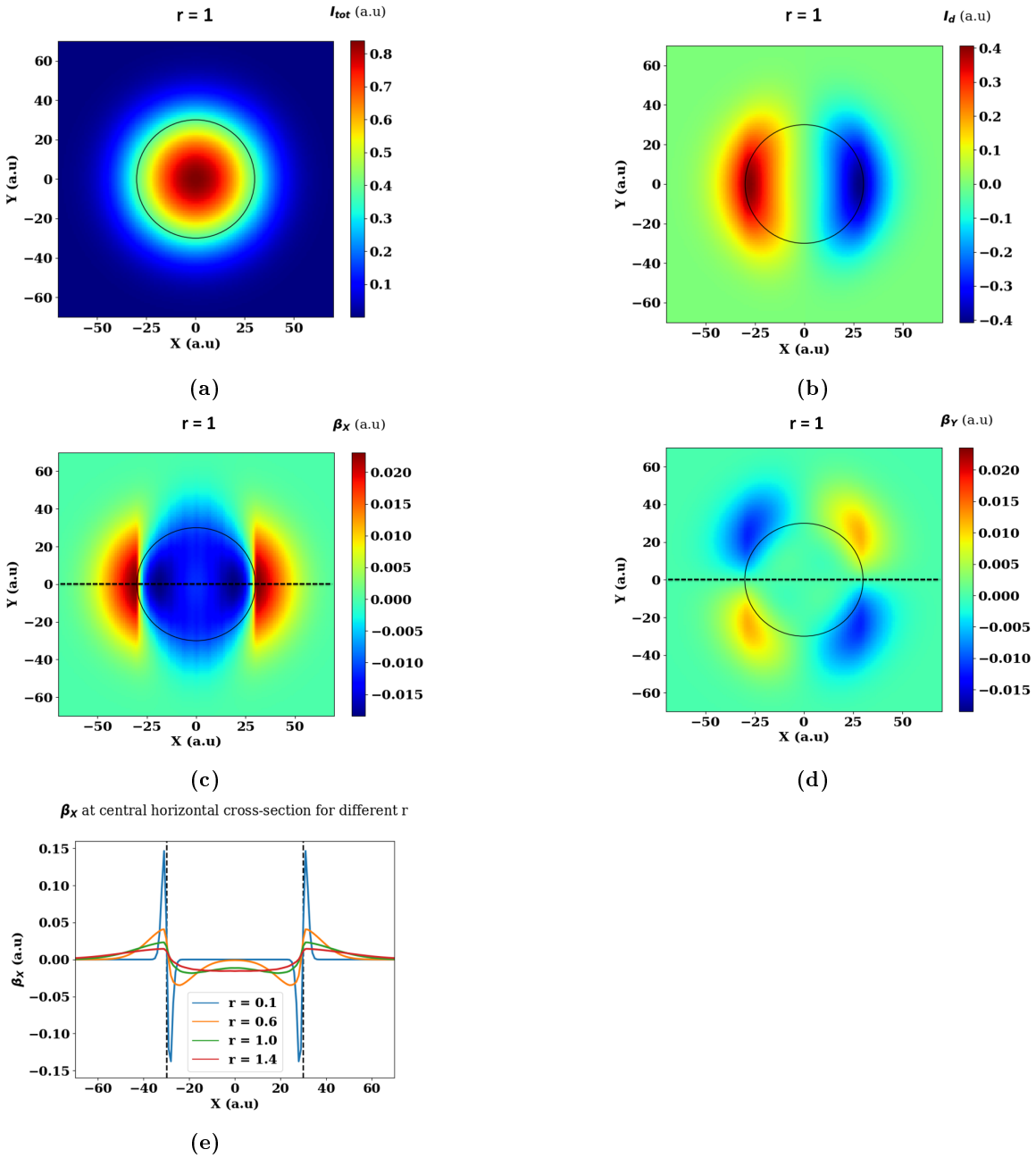

Figure 4.5: Simulation of integrated laser intensity for SPD as detector for the case when the laser beam diameter is equal to the top diameter of the photonic wire i.e. r = 1: (a) total laser intensity on SPD (b) difference in intensity between photodiodes A and B of SPD. **Detection sensitivity:** (c) X component: β_x (d) Y component: β_y; calculated from the results of simulation. Black circle on each plot demonstrates the edge of the photonic wire's top facet. (e) Detection sensitivity β_x magnitude along central horizontal cross-section, when ratio between laser beam diameter and photonic wire top facet diameter is r = 0.2 (blue), r = 0.6 (orange), r = 1 (green) and r = 1.4 (red). Dashed vertical line shows the edges of the photonic wire.

the 2D plot of β_x shown in figure 4.5(c) for different ratios (r) between laser beam diameter and photonic wire's top facet diameter. When the laser beam size is small compared to the photonic wire's top diameter (i.e. r = 0.2), sensitivity is large only when the laser is placed close to the edge of the wire. This is because at such points, when wire oscillates, it goes in or out of the laser beam spot and therefore changes the reflected intensity distribution on SPD; whereas if laser is placed at the center of the photonic wire, the change in the reflected intensity will be very little as the wire oscillates. However, it is not practically possible to have such small beam. The diffraction limited focused laser beam diameter on top of the photonic wire can vary from 2 to 1 µm depending on the microscopic objective (see section 4.3.1.2) used and the photonic wire top diameter in consideration ranges between 1.7 to 1.9 µm. Therefore, minimum possible value of r will be around 0.5. However, for r around 0.5 (orange trace in figure 4.5(e)), the detection sensitivity is still zero when the beam is at center of wire and maximum close to the edge. Therefore, for r around 0.5, the best way is to position the laser beam close to the edge of the photonic wire and on one of the photodiode of SPD.

On the other hand, when laser diameter is comparable to the photonic wire's top diameter (i.e. r = 1), detection sensitivity when the laser is placed at the center of the wire is more or less equal to when it is placed close to the edge (green trace in figure 4.5(e)). This is understandable as when the beam size is comparable to the diameter of the photonic wire, there will be more or less similar change in the reflected intensity distribution between A and B photodiodes of SPD as the wire oscillates, when the beam is placed at the center or at the edge of the photonic wire. The maximum sensitivity at central point can be obtained when laser beam is about 1.4 times the wire's top diameter. Further increase of the beam size decreases the sensitivity, because it decreases the difference in reflected intensity between the two parts of SPD.

Therefore to conclude, in case of SPD, best position of laser with respect to the wire and the corresponding position on SPD depends on the ratio r. When $r < 1$, beta value is larger but is limited to very small range of operation and decreases drastically for even small positional drifts. On the other hand, for $r \geq 1$, even though the beta value is comparatively small but the operation range is rather broad so that beta is not too sensitive to position drifts. Therefore, in case of SPD, we chose the diameter of the beam ($1/e^2$ diameter) equal to 1.4 µm, which is comparable to the top diameter of the photonic wires in consideration (around 1.5 - 2 µm). Hence, it would be best to put the laser at the center of the wire and the reflected light to the center of SPD.

B) Photodiode (PD)

Figure 4.6 shows the result of the simulations with PD as a detector, for the case, when

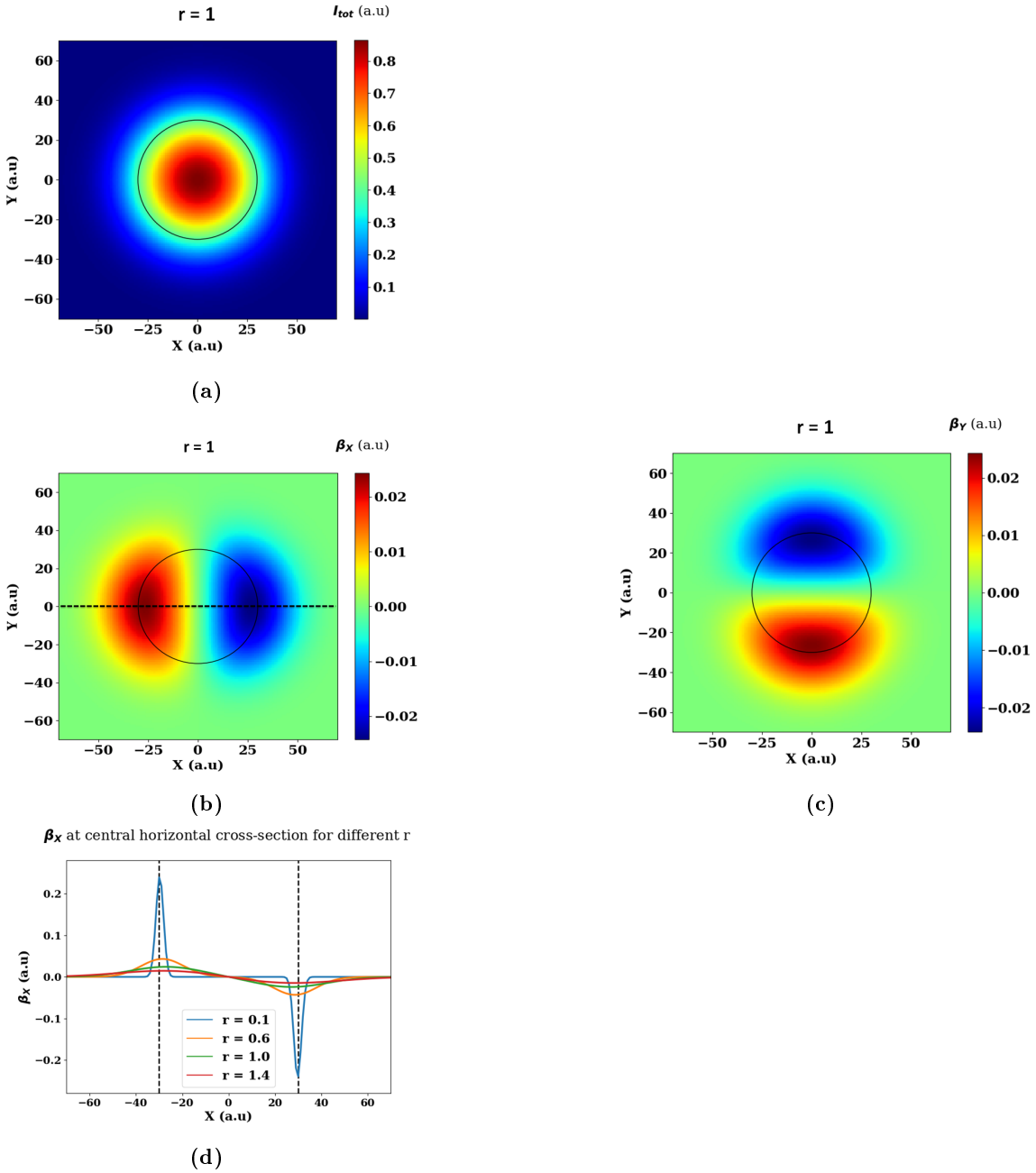

Figure 4.6: Simulation of integrated laser intensity for the case when the probe laser beam diameter is equal to the top diameter of the photonic wire i.e. r = 1: (a) total intensity on PD. **Detection sensitivity:** (b) X component: β_x (c) Y component: β_y . Black circle on each plot demonstrates the edge of the photonic wire's top facet. (d) Detection sensitivity $mathrm\beta_x$ magnitude along central horizontal cross-section, when ratio between laser beam diameter and photonic wire top facet diameter is r = 0.2 (blue), r = 0.6 (orange), r = 1 (green), and r = 1.4 (red). Dashed vertical line shows the edges of the photonic wire.

the ratio between the laser diameter and photonic wire top facet diameter is r = 1. The plots shown in figs. 4.6(a) to 4.6(c) represents the image of the position of photonic wire on PD. The size of PD along X and Y axis is chosen to be equal to 200 a.u each (from -100 to 100 a.u) with origin at center of PD like in the case of SPD and the radius of photonic wire is taken as 30 a.u. Therefore, the plotted results are in the range -70 to 70 a.u on both axis. The laser in this case is also fixed at the center of PD i.e. at (0,0). Since, there is no difference signal in case of a single photodiode therefore, for each position of the photonic wire on PD we calculate the integrated total intensity I_{tot} (x,y) (plotted in figure 4.6(a)) using eq. 4.6. Figure 4.6(b) and 4.6(c) shows the detection sensitivity components β_x and β_y respectively which is calculated using eq. 4.7.

Similar to SPD, the y component of detection sensitivity (β_y) is equal to zero for the central horizontal cross-section i.e. for this axis $|\overrightarrow{\beta}(x,0)| = |\beta_x(x,0)|$. Therefore, the value of β_x along the central horizontal cross-section gives us the estimation of detection sensitivity vector along this axis.

Figure 4.6(d) shows the plot of β_x values along the central horizontal cross-section of the 2D plot of β_x shown in figure 4.6(b) for different ratios r between laser beam diameter and photonic wire's top diameter. It is clear that, for any r, detection sensitivity is always maximum when the laser is placed closer to the edge of the wire and is always zero when the laser is placed at the center of wire. This is because when the laser is at center, there will be no change in the reflected intensity as the wire oscillates, as we are measuring the total intensity unlike intensity difference in case of SPD. Therefore, in case of PD, best position is closer to the edge of the wire. It is also clear from the figure 4.6(c) that β_y is also maximum when the laser is close to the edge of the wire (along the central vertical axis). Therefore, we can place the beam along the edge (circumference) of the photonic wire, coincident with the direction of oscillation, in order to obtain maximum possible detection sensitivity for its detection.

Although, the detection sensitivity value is higher for smaller r i.e. for smaller beam size, but as already mentioned it is not practically possible to have such a small beam. Moreover, if the beam is slightly drifted from this position the sensitivity decreases significantly; whereas when the beam size is comparable to the wire diameter, the absolute value is less but even if we move slightly to left and right, sensitivity will not change much. Since the Nanomax stage which holds the microscopic objective has an open loop piezo actuators, there are slow drifts in the sample position resulting in small changes in the laser position with respect to the wire. However, this has been taken into account with the position stabilization technique discussed in chapter 5. Therefore to conclude, in case of PD, detection sensitivity will be best when the probe laser is placed closer to the edge of the photonic wire and at the center of PD irrespective of the ratio r. However, the value of detection sensitivity decreases with increasing r. So, the best case would be to have r as small as possible. The microscopic objective (Olympus LCPLan) with NA = 0.65 (see section 4.3.1.2) used in the setup, the ratio $r \approxeq 0.7$ can be obtained.

4.2.2 Detection limit

Detection of structure's motion is limited by the noises in the system. First comes the noise floor of the measuring device which is either spectrum analyzer (SA), vector network analyzer (VNA) or Zürich instruments lock-in amplifier. All these devices are discussed in detail in section 4.3.1.6. The noise floor of a device determines the lowest possible signal level that can be measured by it. It is measured when there is no external signal connected to the device.

Second are the noises associated with the detector used which in our case is an amplified photodiode either SPD, QPD or an avalanche photodiode (APD) (see section 4.3.1.5). Sensitivity of a detector is limited by the unavoidable noises present in any electronic device. It consists of (a) thermal noise (Johnson-Nyquist noise) generated by the random thermal motion of charge carriers. Thermal noise is approximately white, meaning that its power spectral density is nearly equal throughout the frequency spectrum. (b) shot noise generated by the discreteness of carriers of electric charge. Shot noise is also white and is proportional to the square root of number of carriers. (c) Flicker (1/f) noise with a frequency spectrum that falls off steadily into the higher frequencies. It occurs in almost all electronic devices. These all noises together are termed as electronic noise and can be measured by connecting the signal from the detector to the measuring device in the absence of any laser light on detector.

Third is when the laser is shone on the detector, it creates charge carriers proportionally to the laser's intensity. But laser's intensity fluctuates in time, known as laser intensity noise (optical noise). Intensity noise of a laser results partly from optical shot noise due to discreteness of photons and partly from technical noise sources such as noise of the pump source, vibrations of resonant mirrors, thermal fluctuations in gain medium etc. The fluctuations due to shot noise scales as the square root of the average power whereas the technical noise scales linearly with average power on detector. We can reduce the technical part of intensity noise by using a feedback system which will be discussed in detail in chapter 5. Therefore, the optical noise in the laser is shot noise limited. Figure 4.7 shows the three types of noises discussed above for SPD (figure 4.7(a)) and APD (figure 4.7(b)) as detector. The electronic noise level for APD is about 30 dB lower than that of SPD thereby increases the detection range and allows us to work with lower optical power levels.

4.3 Experimental setup for optical motion detection

As explained in section 4.1, the basic principle of the detection scheme is to reflect the laser beam from the structure and detect the beam deviation on the photodiode as the structure oscillates. Figure 4.8 shows the experimental setup for optical motion detection with SPD

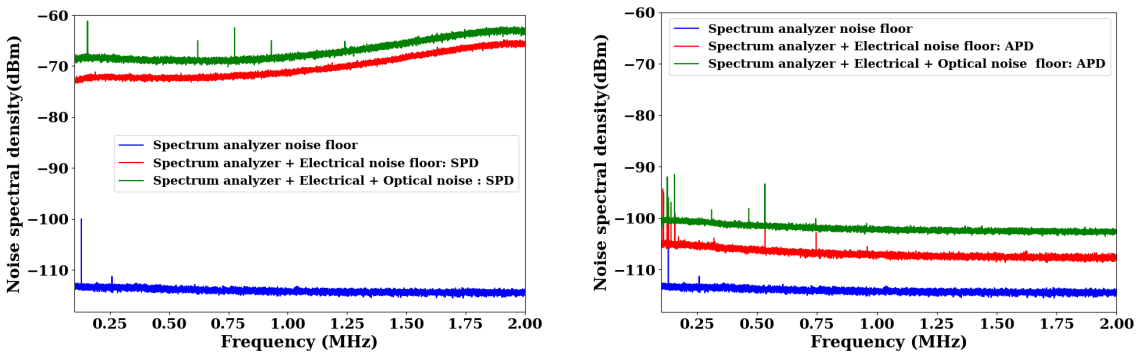

Figure 4.7: Different noise floors limiting the detection. Blue is the noise floor of the spectrum analyzer used in measurements (a) For SPD as detector : red is the electronic noise and green is the optical noise when the probe laser of 150 µW (measured before SPD) is shone. (b) For APD as detector : red is the electronic noise and green is the optical noise when the probe laser of 600 nW (measured before APD) is shone.

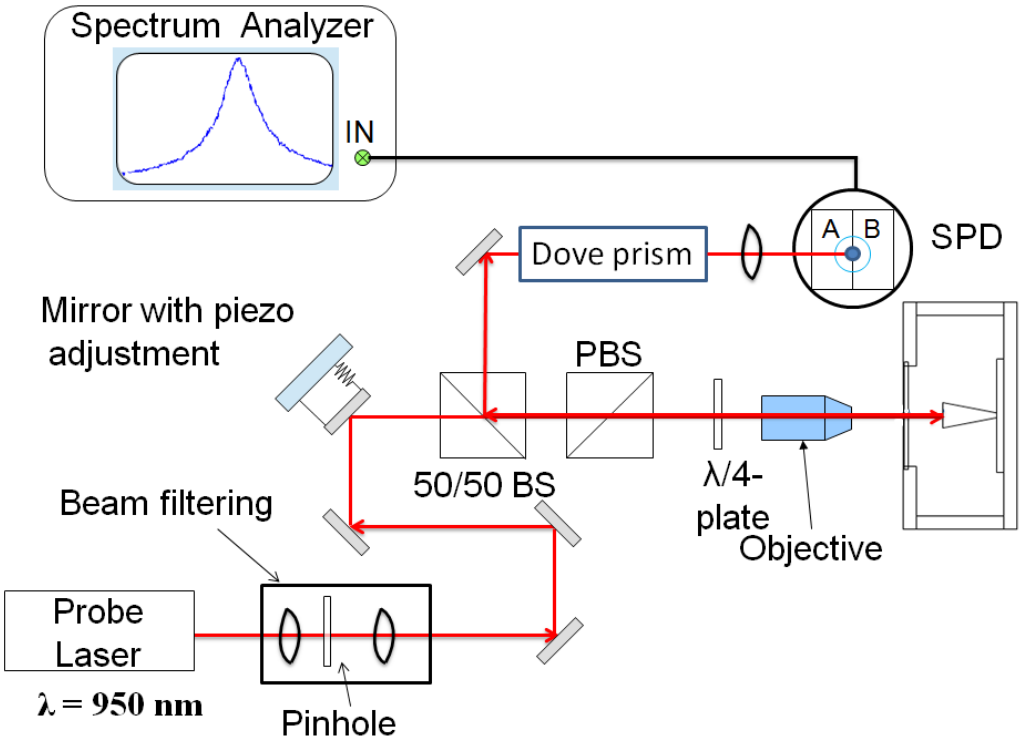

Figure 4.8: Experimental setup for motion detection of photonic wires. See text for details on the elements.

as the detector. The laser used for motion detection (referred to as probe laser) is directed towards the photonic wire placed in a cryostat, while passing through an optical isolator

(not shown in the figure 4.8), and a beam filtering system, consisting a combination of two lenses and a pinhole in between, to adjust its shape and size. Next, the beam is passed through mirrors and beam splitters and finally focused on top facet of the wire using a microscopic objective. The reflected light is again collected by the objective and directed towards the detector (SPD in this case). The voltage signal from the photodiode is then fed into the measurement device (spectrum analyzer) which gives the frequency dependent power spectral density (PSD) of its input voltage. The measurement using different devices is discussed in detail in section 4.3.1.6. In the following section, I presented the role of different important components of the experimental setup.

4.3.1 Experimental components

4.3.1.1 Optical source

The laser used for the motion detection (probe laser) is a diode laser with an external cavity (Topica DL Pro). It is a continuous-wave (CW) laser with tunable wavelength from 910 to 985 nm. In our case, the wavelength of 950 nm (corresponding to 1.3 eV) was chosen, firstly, so that the energy of the laser is below the band gap of GaAs (1.52 eV at 5 K), secondly, to reject the QD excitation laser (which is around 920 nm and modulated at mechanical resonance frequency as explained in Chapter 3) from reaching the photodiode by using a long pass wavelength filter (FEL950), and lastly, when we will combine the setup for the resonant excitation and motion detection together (discussed in detail in chapter 5), then this allows us to suppress the probe laser from reaching the spectrometer using the short pass wavelength filter (FES950). These wavelength filters allows the transmission of light with wavelength below (short pass filter) or above (long pass filter) the cut-off/cut-on value. For example, a short pass wavelength filter (FES950) with a cut-off at 950 nm, will transmits light with wavelength $\leq$ 950 nm and blocks the light above 950 nm.

4.3.1.2 Objective

As discussed in section 4.2, the size of the probe beam is one of the important factor which has to be taken into account while optimizing detection sensitivity. To change the laser beam size we can choose either an objective with numerical aperture (NA) = 0.4 (Olympus LMPLN) or NA = 0.65 (Olympus LCPLan) or NA = 0.75 (ZEISS LD Plan_NEOFLUAR). The working distance of 0.4, 0.65 and 0.75 objectives are respectively 8.1 mm, 4.5 mm and 2.2 mm.

To precisely control the focus and the position of the optical beam on the photonic wire, the microscopic objective is mounted on a 3-dimensional translation stage (Nanomax-312D/M). This stage offers the positioning in three directions, including coarse adjustment

of 4 mm with 10 µm precision, plus 300 µm manual adjustment with 1 µm precision. In addition to this manual tuning, there is also the possibility to control the stage by piezoelectric actuators (open loop), with approximately 20 µm of fine travel at a resolution of 20 nm.

4.3.1.3 Mirror mounted on a piezo-actuated mount

To adjust the position of probe laser on top of the photonic wire we use a mirror mounted on a piezo-actuated mount. This mirror works on the principle of piezoelectric effect i.e. there is a deflection along the two angular directions as the voltage is applied to them. It has two closed loop piezo-elements allowing to tilt the mirror from 0 to 2 mrad vertically and horizontally on applying external voltage from 0 to 10 V via a piezo-controller. Tilting the mirror by some angle tilts the laser by twice this angle and will move the laser on the sample.

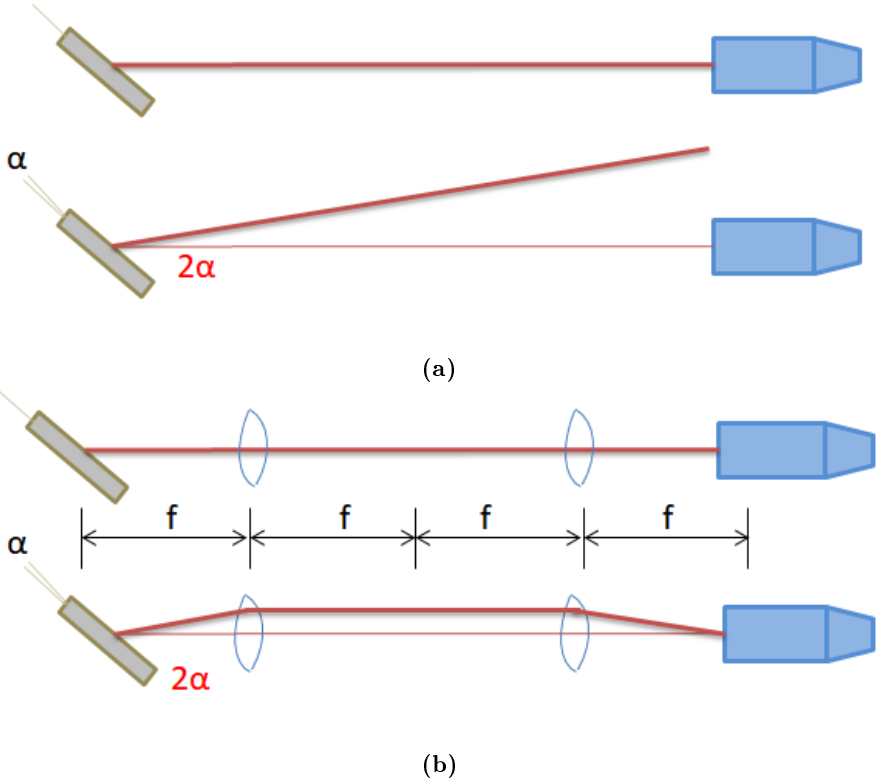

Figure 4.9: Demonstration of probe laser manipulation by (a) piezo mirror alone and (b) together with a telescopic system.

However, this method requires to be complemented by a telescopic system as shown in figure 4.9 to change the angle of incoming laser at the entrance of the objective without changing its position. This opens the possibility to have large tilt angle without hitting

the side of the objective or even go completely out of the objective as shown in figure 4.9(a). In our case, we used symmetric telescopic system (known as 4f system), i.e. the focal distances of both the lenses are equal with f = 400 mm.

4.3.1.4 Dove prism

Owing to the slight asymmetry, the photonic wire has two linear orthogonal mechanical eigenmodes. In case of SPD as detector, the detection of these modes depends on their orientation with respect to the SPD axis. If the mode is along the X axis of the SPD, it will be detected with maximum sensitivity whereas if it is along the Y axis then it will not be detected at all (discussed in detail in section 4.2). To manipulate the orientation of the photonic wire's oscillations with respect to the axis of the SPD, we used Dove prism in our setup.

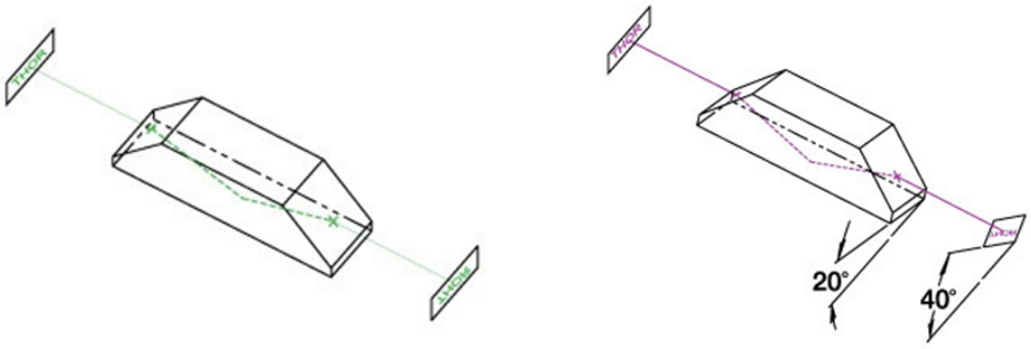

(a) **(b)**

Figure 4.10: Demonstration of operating principle of Dove prism (a) non-rotated Dove prism: light propagated along the longitudinal axis is inverted by 180°. (b) rotated Dove prism: rotation of prism by some angle results in a rotation of the image by twice that angle. Figure source: Thorlabs website.

Dove prism is a truncated right angled prism. The beam of light entering one of the slopped faces of the prism undergoes total internal reflection from the bottom face before emerging out from the opposite slopped face. Therefore, image passing through the prism goes out inverted as shown in figure 4.10(a). They have an interesting property that rotating it along its longitudinal axis by some angle will rotate the image by twice this angle as shown in figure 4.10(b). Thus, in our case we use it to rotate the image of the photonic wire on the SPD in order to obtain desirable orientation of the mode to be detected. We can use it to obtain one of the following configurations:

1. **Detection of one mode:** Rotate the Dove prism such that the mode we want to detect should be coincident with the direction of detection sensitivity vector.

Figure 4.11(a) shows the point by point 2D scan of difference signal from SPD, recorded when laser is moved over the photonic wire with the help of mirror with piezo adjustments presented above in section 4.3.1.3, controlled by the python program developed in [106] by Laure Mercier de Lepinay from the team of O.Arcizet and has been adapted according to our experiment. The 2D map is consistent with the results of the simulation presented in section 4.2. Therefore, the detection sensitivity vector will be along the X axis of SPD and we are only sensitive to detect the wire oscillations in this direction (horizontal mode) and not the one in vertical direction.

2. **Detection of both modes:** Rotate the Dove prism such that the direction of detection sensitivity vector is placed in between the two orthogonal modes. Therefore, starting from above case we should rotate the Dove prism by 22.5 degrees to have both the modes at 45 degrees with respect to the detection sensitivity vector as shown in figure 4.11(b). In this situation we can detect both the modes with same sensitivity.

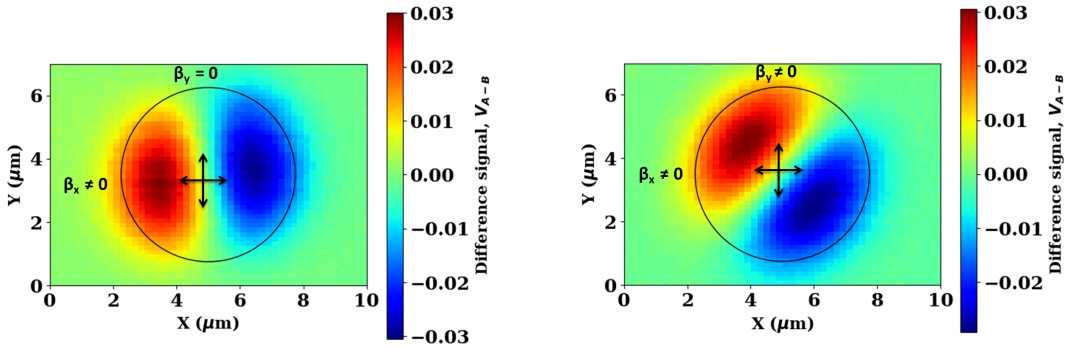

(a) **(b)**

Figure 4.11: Experimental 2D map of difference signal (A-B) for the photonic wire with top diameter of 5.5 μm. (a) Dove prism angle of 168°. (b) Dove prism angle 190.5°: rotating the prism by 22.5° results in the rotation of image by 45°.

4.3.1.5 Detectors

We have used three types of detectors in the experiments.

A) **Split photodiode (SPD):**

As mentioned before, SPD consists of two identical photodiodes placed close to each other namely, A and B. Its low-noise amplification electronics has been developed in collaboration with D. Lepoittevin from the Electronics department. Photodiode

used in this home made SPD is a Hamamatsu S4204 photodiode. It has an surface of $1\times$ 2 mm^2 with 20 µm of dead zone in between the two parts. Its spectral response range is in the interval from 320 nm to 1100 nm with peak responsitivity equal to 0.65 A/W at 960 nm; cut-off frequency equal to 30 MHz.

Each photodiode has two independent amplifiers for DC and high frequency (HF) signals. In DC path of the signal, a symmetric low-pass filter is used to cut off all signal components with frequencies higher than 10 kHz. This allows us to isolate only the DC component of the signal which is then amplified by the operational amplifier. In HF path of the signal, a capacitor is used to transmit only high frequency photocurrent fluctuations, which is then amplified using an operational amplifier. Frequency range for HF path is from 100 kHz to 20 MHz with HF gain being frequency dependent. Finally, there is a subtractor which is used to obtain a difference signal $V_{A-B} = V_A - V_B$. Two independent subtractors are used for DC and HF outputs. The photodiode has in total 4 output channels: two for DC signal for each photodiode (DC 'V_A' and DC 'V_B') and two for DC and HF difference signal (DC 'V_{A-B}' and HF 'V_{A-B}').

The HF and DC gain of SPD The DC and HF amplifier gain of the diode are different and are defined by the internal electrical circuit of amplifier. Since SPD consists of two identical photodiodes namely, A and B, the DC (HF) gains of the two photodiodes should be same. This has been verified experimentally.

DC gain To determine DC gain, we placed the laser beam on one photodiode (say A) of SPD and measured a ratio between the output voltage DC 'V_A' and incoming laser power. We also repeated the experiment for the other diode (B) to be sure that the two photodiodes have equal gains. The DC gain is measured to be equal to 620 µV/µW.

HF gain To determine HF gain, we used HF V_{A-B} output channel since there is no independent HF output for the diodes A and B. Laser is placed on one of the diode using the DC outputs such that the signal on the other photodiode is zero and we measured the HF gain of one photodiode. HF gain is frequency dependent. Therefore, we used VNA (presented in section 4.3.1.6). Using VNA we sweep a frequency from 10 kHz to 10 MHz and record the HF response from HF V_{A-B} channel. VNA measures the ratio of incoming signal to the outgoing signal. Therefore, to get the measured signal in voltage units, it has to be multiplied by the outgoing signal (see section 4.3.1.6 for details on this conversion). Finally dividing this measured signal by the incoming laser power, we get the HF response of the diode A (or B) in µV/µW. We know the DC gain presented above to be equal to 620 µV/µW. Therefore, the ratio of HF gain to DC gain can be calculated and is presented in figure 4.12(b). It shows a maximum value around 2 MHz.

B) **Quadrant photodiode (QPD):**

QPD consists of four identical photodiodes placed close to each other namely, A, B, C and D. Its amplification electronics is also developed in collaboration with D. Lepoittevin from the Electronics department. The advantage of QPD over SPD is

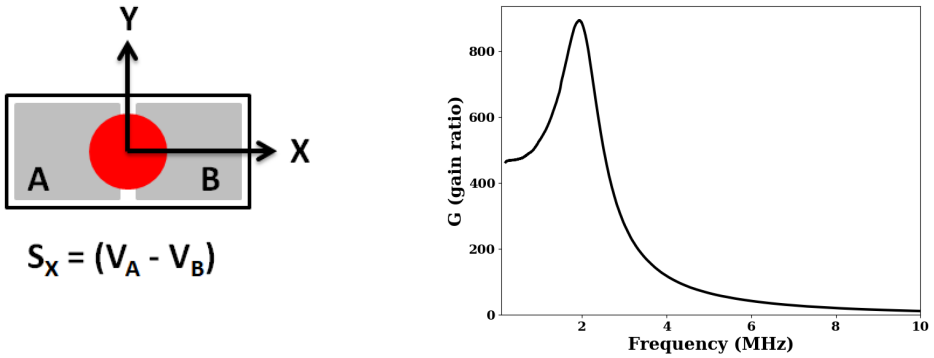

(a) (b)

Figure 4.12: (a) Sketch demonstrating SPD together with laser beam positioned at center. (b) Frequency dependence of ratio between HF and DC gain of SPD.

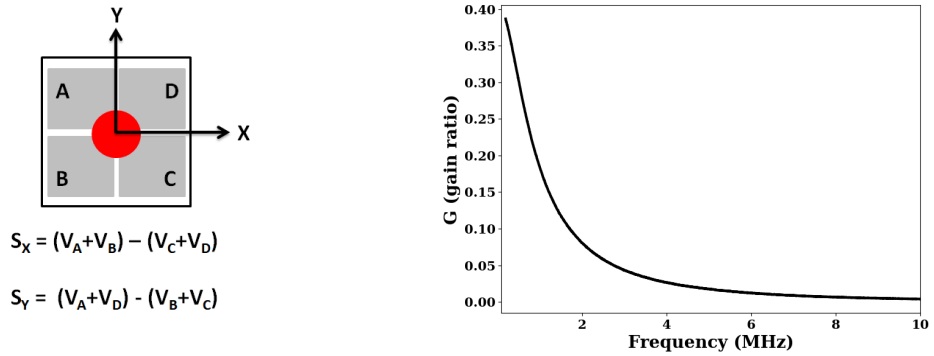

(a) (b)

Figure 4.13: (a) Sketch demonstrating QPD together with laser beam positioned at center. (b) Frequency dependence of ratio between HF and DC gain of QPD.

that with four photodiodes arranged as shown in figure 4.13(a) we have the possibility to measure the oscillations in both X and Y direction unlike SPD where we are only sensitive to changes in one direction.

Like SPD, each photodiode in QPD also has two independent amplifiers for (DC) and high frequency (HF) signals. It has 5 output channels in total: two for DC difference signal in x and y direction (DC '$V_A + V_B - (V_C + V_D)$' and DC '$V_A + V_D - (V_B + V_C)$') , two for HF difference signal (HF '$V_A + V_B - (V_C + V_D)$' and HF '$V_A + V_D - (V_B + V_C)$') and one for the sum of all the four photodiodes (DC '$V_A + V_B + V_C + V_D$').

The HF and DC gain of QPD The DC and HF amplifier gain of the diode are measured in the same way as explained above in the case of SPD. The DC gain of the diode is found to be 250 mV/μW which is higher than that in case of SPD. HF

gain on the other hand, is lesser than in case of SPD, resulting in smaller gain ratio as shown in figure 4.13(b). Therefore, QPD is not a best choice for measurements at high frequency especially at low optical powers.

C) **Avalanche photodiode (APD):**

An avalanche photodiode is a photodiode that operates under a high reverse bias condition. In this regime, carriers (electrons and holes) excited by absorbed photons are strongly accelerated in the strong internal electric field, so that they can generate more carriers and the process repeats. This avalanche action results in a very sensitive detector with low noise making it suitable for low optical power measurements.

APD used is a Thorlabs Si avalanche photodiode APD410A2. The main features of APD are low noise and high sensitivity and variable gain factor to tune the gain factor from 10 to 100, according to the requirement. The DC gain of the APD is measured to be 3.5 $\times 10^6$ V/W. The gain ratio plotted from 100 kHz to 10 MHz range is shown in figure 4.14(b). It is clear from the plot that in the frequency range of interest i.e. at few hundreds of kHz, the gain ratio is unity and drops slightly at higher frequencies.

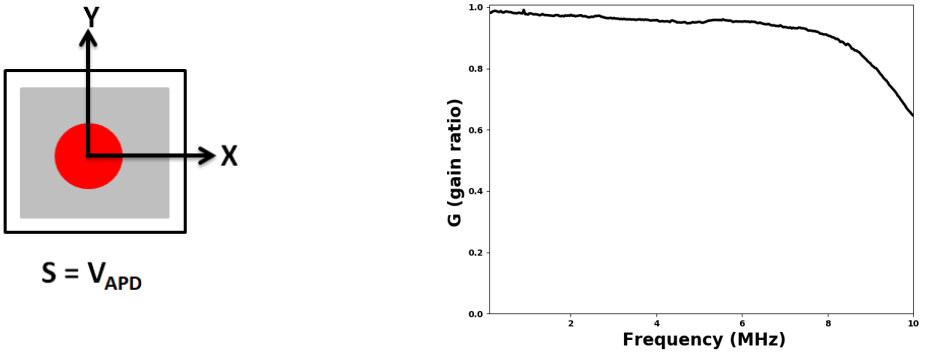

(a) (b)

Figure 4.14: (a) Sketch demonstrating APD together with laser beam positioned at center. (b) Frequency dependence of ratio between HF and DC gain of APD.

4.3.1.6 Measurement devices

The output voltage signal from the photodiode is fed to one of the following measurement devices, used during the course of this thesis.

A) **Spectrum Analyzer (SA):**

Spectrum analyzer is used to examine the frequency spectrum of radio frequency (RF) signals. It displays the power spectral density of input signal as a function of frequency within the chosen frequency range. The frequency range can be chosen by setting the start and stop frequency. Resolution bandwidth (RBW) is an important parameter which defines the RF noise floor and minimum separation of two frequency components that can be resolved by the analyzer. Decreasing RBW, decreases the measured noise floor. This is because with larger RBW more frequency components are passing through to the detector. The choice of RBW depends on several factors. Lower RBWs provide more detailed measurements with lower noise floor at the expanse of sweep time (time required for one measurement, which is inversely proportional to RBW). Higher RBW on the other hand, will give comparatively higher noise but faster measurements. The ultimate decision will depend upon the type of measurement.

The spectrum measured using spectrum analyzer is the power spectral density (PSD). PSD is a measure of the power present in each frequency component within the RBW, and has units of W/Hz or V^2/Hz (using $P = \frac{V^2}{R}$, with R = 50 ohms). It is often displayed as logarithmic quantity in units of dBm/Hz (with dBm = dB relative to 1 mW). PSD of a measured quantity (say, u) is denoted by S_{uu} and will be discussed in detail in section 4.4.2.

We have Tektronix RSA306B USB spectrum analyzer which can be easily connected to the computer and uses Tektronix SignalVu-PC RF signal analysis software to provide real time spectrum analysis for signal from 9 kHz to 6.2 GHz frequency range. In our experiments, SA is mainly used to characterize the mechanical properties of the trumpet by measuring the Brownian motion spectrum. It is discussed in detail in section 4.4.2.

B) **Vectorial Network Analyzer (VNA):**

While SA measures the applied input signal, Vector network analyzer (VNA), on the other hand, creates a signal and characterizes the reflection and transmission of the device that receive it. With VNA, Scattering parameters or S-parameters are the basic measured quantity. They describes how the device under test modifies a signal (created by the VNA) that is transmitted or reflected in forward or reverse direction. For a two port measurement the signal flow is shown in figure 4.15. We measure the signal in forward direction i.e. S_{21} parameter, which is forward transmission coefficient and is the ratio of the signal coming out of the device under test to the signal generated by the VNA.

With VNA, it is possible to detect other properties such as phase of the signal in addition to its amplitude. VNA we have is a Rhode & Schwarz ZNB4 two port network analyzer. It has the frequency span from 100 kHz to 4.5 GHz. The magnitude of the measured complex quantity $z = x + iy$ can be displayed either in linear ($|z| = \sqrt{(x^2 + y^2)}$) or logarithmic scale ($20\log|z|$). The phase values ($\phi = \arctan(\frac{y}{x})$) are wrapped in range $-180° < \phi < 180°$. One can also display real (x) and imaginary (y) part of z and calculate amplitude and phase from it. Nevertheless, in our mea-

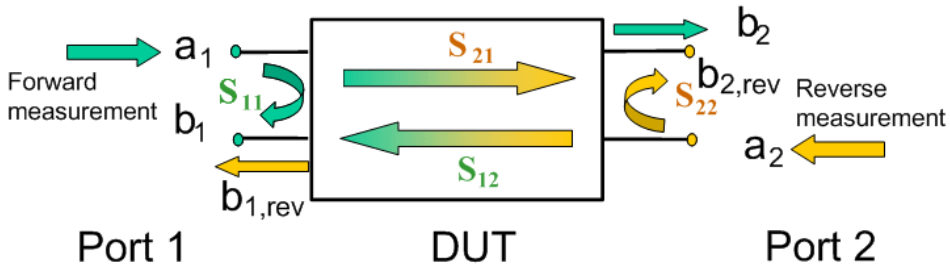

Figure 4.15: Sketch demonstrating the S-parameters for a two port network analyzer. Figure source: ZNB4 user manual from Rhode&Schwarz website.

surements we record the amplitude (in dB or lin scale) and phase spectrum. Since, VNA measures the ratio of incoming and outgoing signal, to calculate the amplitude of the incoming signal we should multiply the measured quantity by the amplitude of outgoing signal (in Volts). Therefore, it is important to get the measured signal also in volts units before performing this conversion.

The spectrum measured in dB scale represents the ratio of incoming to outgoing power, therefore, it is first converted to linear scale using $S_{lin} = 10^{(\frac{S_{dB}}{20})}$, where S_{dB} represents the ratio of powers in dB scale and S_{lin} represents the ratio of amplitudes (in terms of voltage). The amplitude of the driving signal send by the VNA is defined by the power P_{dBm}, which can be chosen directly on VNA. The peak to peak voltage of the driving signal can be calculated using

$$V_{out} = 2 \times 10^{(\frac{P_{dBm}-10}{20})} \tag{4.8}$$

Therefore, the measured signal in voltage units will be given by

$$V_{in} = V_{out} S_{lin} \tag{4.9}$$

The calibration from voltage units to meter units is discussed in section 4.4. It is important to note that if the measured signal is already in linear scale i.e. S_{lin}, then we can directly convert it into voltage V_{in} using eq. 4.9.

C) **Zürich instruments Lock-in amplifier:** In addition to SA and VNA, we have the third device which is a HF2LI (high frequency, 2 inputs) 50 MHz lock-in amplifier from Zürich instruments (Swiss company). It has been borrowed from O. Arcizet's group. It is a digital lock-in amplifier covering the frequency range from DC to 50 MHz. It features 2 input channels and 2 output channels with 210 MSa/s operation. In addition, it also has 4 auxiliary outputs and 2 auxiliary inputs with comparatively

slower operation rate 1 MSa/s and 400 kSa/s respectively. It incorporates two lock-in amplifiers and allows analysis of signals at upto 6 different frequencies with 6 local oscillators and 2 external oscillators. It is connected to computer by a high-speed USB interface (480 Mbit/s). Each instrument is equipped with LabOne user interface. With LabOne, it provides a browser based user interface which is an all in one platform for instrument control, data capture, data analysis, and data storage. This all-in-one methodology provides the possibility to use various tools from it's integrated toolset. It performs the role of both Spectrum analyzer and vector network analyzer with Spectrum and Sweeper tab respectively.

Spectrum tab allows us to measure the frequency spectrum around a specific frequency. This is done by doing the Fourier transform of the demodulated X and Y (or in-phase and quadrature)components of the signal. We can choose what we want to measure, i.e. the power spectrum (V^2) or spectral density (V^2/Hz) in the settings tab. The important parameter is the low pass filter bandwidth and it needs to be set at least as wide as the signal of interest.

The sweeper tab turns HF2LI into a frequency response analyzer where we record the frequency response of the device under test. It allows us to perform wide range of measurements by scanning parameters other than frequency such as amplitude, phase and auxiliary output voltages. It allows precise measurements with the possibility to choose resolution bandwidth even below 1 Hz which is the limit in case of VNA. In addition to SA and VNA, it also performs the role of an oscilloscope with a Scope tab. The functioning of other tools such as MOD (allows to perform modulation-demodulation at multiple frequencies for the direct analysis of side bands) and phase locked loop (PLL) to track the mechanical resonance frequency will be discussed in detail in chapter 5.

4.4 Motion calibration

The calibration of the output signal from the detector (in Volts) to the amplitude of photonic wire's top facet displacement (in units of length i.e. meters) can be done using detection sensitivity β. The experimental calculation of detection sensitivity can be achieved by taking the derivative of the recorded difference signal in case of SPD and total intensity in case of PD when the photonic wire is moved with respect to the laser or vice-versa as discussed in section 4.2. However, since the sample is inside a heavy cryostat that makes the realization of its small displacement difficult. Nevertheless, there are still two ways to achieve this. First, displacement of the sample is analogous to the displacement of the microscopic objective before it. The microscopic objective in our setup is placed on a three dimensional translation stage (see section 4.3.1.2) which allows us to move it with the help of piezo controllers with 20 nm accuracy. Second, there is possibility to move the beam with the help of mirror with piezo adjustments (see section 4.3.1.3). In either case, the signal from the detector is recorded for each position as the microscopic objective or

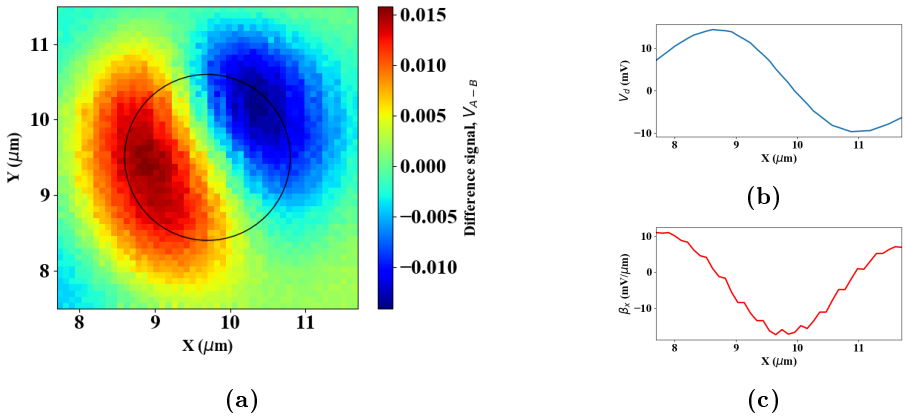

Figure 4.16: (a) Experimental 2D map of voltage at DC difference output V^{DC}_{A-B} of SPD for the photonic wire with top diameter of 2.2 μm. (b) Central horizontal cross-section of the difference signal shown in (a), and (c) DC detection sensitivity component β_x calculated by taking the derivative of difference signal (in (b)) along the central horizontal axis

the laser beam is moved keeping the other fixed.

Let's take as an example, the measurement done using SPD as detector. Using the software developed in [106], we make a point by point 2D scan of difference signal from SPD, recorded by moving the microscopic objective while the laser is positioned at the center of the top facet of photonic wire with top diameter of 2.2 μm. For each point we measure the DC 'V_{A-B}' signal. The final 2D map is shown in figure 4.16(a) and matches well with the difference signal I_d, calculated in simulations shown in figure 4.5(b). It is however, rotated because of the presence of Dove prism in the setup. Since the two orthogonal modes of the photonic wire are oscillating along the X and Y axis of the detector, therefore, we are only interested in the horizontal β_x and vertical β_y component of the detection sensitivity vector. β_x computed from the derivative of difference signal along the central horizontal cross-section is shown in figure 4.16(c) and is equal to 17 mV/μm. We can also determine the value of vertical component β_y along the central vertical cross-section which is equal to 11 mV/μm. Let's focus on the horizontal mode (oscillating along X axis) for the rest of the discussion.

The detection sensitivity obtained in this way is a DC detection sensitivity β_{DC} and must be scaled by ratio between HF and DC gains of the detector to determine the detection sensitivity at the frequency of oscillations i.e. β_{HF}. Since, HF gain is frequency dependent, therefore, detection sensitivity will also be frequency dependent. The relation between β_{DC} and β_{HF} via DC and HF gain of the detector will be discussed in detail in next section.

SA measurements:

The power or voltage spectral density S_{vv} (V^2/Hz) for the horizontal mode, measured from the spectrum analyzer can be converted to amplitude spectral density S_{xx} (m^2/Hz) using the following relation:

$$S_{xx} = \frac{S_{vv}}{\beta^2_{x,HF}(\Omega)} \tag{4.10}$$

where Ω represents the frequency and $\beta_{x,HF}$ is the frequency dependent high frequency horizontal component of detection sensitivity.

VNA measurements:

The measurement done with VNA can be converted in to voltage units using eq. 4.9. The amplitude of motion (in meters) of the top facet of the photonic wire can therefore written as

$$dx = 2 \times 10^{(\frac{P_{dBm} - 10}{20})} S_{max}(a.u) \frac{1}{\beta_{x,HF}(\Omega)} \tag{4.11}$$

where S_{max} is the value of the measured signal at mechanical resonance.

4.4.1 Relation between β_{DC} and β_{HF}

The voltage signal measured from the photodiode is proportional to the photocurrent produced as a result of the exposure to the incident light. Therefore, the signal is proportional to the intensity (I) of the incident light and can be written as

$$V = GI \tag{4.12}$$

where G is the gain of the photodiode.

In case of **SPD** the measured signal is the difference signal V_{A-B} which can be written as

$$\begin{aligned} V_{A-B} &= V_A - V_B \\ &= G_A I_A - G_B I_B \end{aligned} \tag{4.13}$$

where G_A, G_B and I_A, I_B are the gains and intensities on the diode A and B. In terms of the DC and HF components the above equation 4.13 can be written as

$$\begin{aligned} V^{DC}_{A-B} &= (G^{DC}_A I^{DC}_A - G^{DC}_B I^{DC}_B) \\ V^{HF}_{A-B}(\Omega) &= (G^{HF}_A(\Omega) I^{HF}_A - G^{HF}_B(\Omega) I^{HF}_B) \end{aligned} \tag{4.14}$$

From the definition of detection sensitivity, β_{DC} can be written as

$$\beta_{DC} = \frac{\delta V^{DC}_{A-B}}{\delta x^{DC}} \quad = \quad G^{DC}_A \frac{\delta I^{DC}_A}{\delta x^{DC}} - G^{DC}_B \frac{\delta I^{DC}_B}{\delta x^{DC}} \tag{4.15}$$

For a given static displacement δx^{DC}, if diode A will see an increase in intensity by δI^{DC}, than diode B will see the decrease by same amount. Therefore, we can say that $\delta I^{DC}_A = -\delta I^{DC}_B = \delta I^{DC}$. Eq. 4.15 can therefore be written as

$$\beta_{DC} = (G^{DC}_A + G^{DC}_B) \frac{\delta I^{DC}}{\delta x^{DC}} \tag{4.16}$$

Similarly for HF component, displacement δx^{HF} at high frequency will give change in intensity δI^{HF} such that $\delta I^{HF}_A = -\delta I^{HF}_B = \delta I^{HF}$. Therefore, high frequency detection sensitivity can be written as

$$\beta_{HF} = (G^{HF}_A(\Omega) + G^{HF}_B(\Omega)) \frac{\delta I^{HF}}{\delta x^{HF}} \tag{4.17}$$

For same displacement at low and high frequency i.e. $\delta x^{DC} = \delta x^{HF}$, if we assume that all the frequency dependency is put in the gain, we have: $\delta I^{DC} = \delta I^{HF}$. Therefore, from eq. 4.16 and 4.17 we have

$$\beta_{HF}(\Omega) = \frac{(G_A^{HF}(\Omega) + G_B^{HF}(\Omega))}{\delta x^{HF}} \frac{\beta_{DC}\delta x^{DC}}{(G_A^{DC} + G_B^{DC})}$$
$$\beta_{HF}(\Omega) = \frac{(G_A^{HF}(\Omega) + G_B^{HF}(\Omega))}{(G_A^{DC} + G_B^{DC})}\beta_{DC} \tag{4.18}$$

Following the same argument we can show that for a single **PD**

$$\beta_{HF}(\Omega) = \frac{G^{HF}(\Omega)}{G^{DC}}\beta_{DC} \tag{4.19}$$

Therefore, the ratio of the HF and DC sensitivities of the diodes is proportional to the ratio of the sum of the HF and DC gains of the photodiodes. The ratio (say G) of HF and DC gain for all the detectors is presented in section 4.3.1.5. Thus, for each measurement, β_{HF} is calculated at the frequency of oscillations using the gain ratio G (Ω) and the value of β_{DC} determined experimentally.

4.4.2 Brownian motion: thermal noise

Brownian motion is a random motion of a photonic wire in the absence of any external driving force, purely due to the thermal fluctuations, thereby called thermal noise. The dissipation in a system describes coupling of its mechanical motion to a heat reservoir. On one side this loss converts mechanical energy towards an external bath, whereas on the other side random thermal fluctuations are spontaneously converted back to mechanical fluctuations, as described by the fluctuation dissipation theorem (FDT) [107].

Temporal evolution of one dimensional mechanical resonator can be described by the simple equation of motion of a harmonic oscillator:

$$m_{eff}\frac{\partial^2 x(t)}{\partial t^2} + m_{eff}\Gamma_m\frac{\partial x(t)}{\partial t} + kx(t) = F_{ex}(t) \tag{4.20}$$

where m_{eff} is the effective mass, k is a spring constant, Γ_m is intrinsic damping rate and $F_{ex}(t)$ denotes the sum of all forces that are acting on the mechanical oscillator. Solution x(t) to eq. 4.20 can be Fourier transformed via

$$x(\Omega) = \int_{-\infty}^{\infty} x(t)e^{i\Omega t}dt \tag{4.21}$$

such that $x(\Omega) = \chi_m(\Omega)F_{ex}(\Omega)$, connects the external force to the response via mechanical susceptibility $\chi_m(\Omega)$ at a given frequency Ω, which is defined as:

$$\chi_m(\Omega) = \frac{1}{m_{eff}(\Omega_m^2 - \Omega^2 - i\Omega\Gamma_m)} \tag{4.22}$$

where Ω_m is a mechanical resonance frequency.

In the absence of any other external force, F_{ex} (t) is given by the thermal Langevin force [108], which is responsible for the Brownian motion. The mean position $\langle x \rangle$ of the oscillator remains zero, but it presents a non-zero variance $\langle (x(\Omega) - \langle x \rangle)^2 \rangle$. Since, $\langle x \rangle = 0$, therefore variance will be equal to $\langle x^2(\Omega) \rangle$, whose noise power spectral density S_{xx} is defined as

$$S_{xx}(\Omega) = \lim_{\tau \to \infty} \langle |x(\Omega)|^2 \rangle \tag{4.23}$$

According to Wiener-Khinchin theorem, the noise power spectral density and the autocorrelation function $\langle x(t)x(0) \rangle$ of x(t) are seen to be Fourier transform pair, and can be written as

$$S_{xx}(\Omega) \equiv \int_{-\infty}^{+\infty} \langle x(t)x(0) \rangle e^{i\Omega t} dt \tag{4.24}$$

From equations (4.23) and (4.24), we immediately obtain the important result that the area under the experimentally measured thermal noise spectrum yields the variance of the mechanical displacement $\langle x^2 \rangle$:

$$\int_{-\infty}^{+\infty} S_{xx}(\Omega) \frac{d\Omega}{2\pi} \quad = \quad \langle x^2 \rangle \tag{4.25}$$

Furthermore, in thermal equilibrium, the fluctuation dissipation theorem (FDT) relates the noise to the dissipative part of the linear response,

$$S_{xx}(\Omega) = 2\frac{k_B T}{\Omega} \mathrm{Im}\left[\chi_m(\Omega)\right] \tag{4.26}$$

From equations (4.22) and (4.26), we can write the thermal noise spectral density of a mechanical oscillator as:

$$S_{xx}(\Omega) = \frac{2\Gamma_m}{m_{eff}((\Omega_m^2 - \Omega^2)^2 + \Gamma_m^2\Omega^2)} k_B T \tag{4.27}$$

which is Lorentzian shaped and centered at the mechanical resonance frequency Ω_m. It has units of m^2/Hz. As discussed in section 4.3.1.6, a typical noise spectrum of a mechanical oscillator measured on spectrum analyzer (SA) gives the noise power spectral density S_{xx} given by eq. 4.27. For weak damping ($\Gamma_m \lll \Omega_m$), eq. (4.27) yields the variance:

$$\langle x^2 \rangle = \frac{k_B T}{m_{eff}\Omega_m^2} \tag{4.28}$$

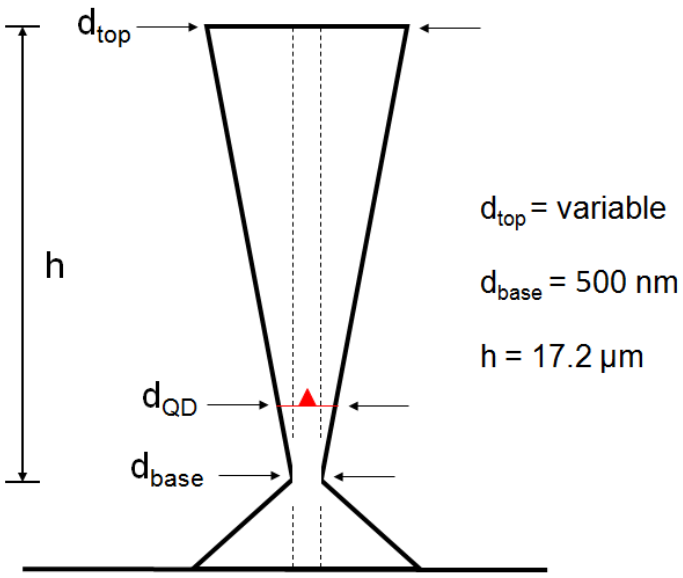

Figure 4.17: Sketch depicting the structure and dimensions of photonic wire investigated in this study. Red triangle represents the QD embedded within the wire. Sketch and dimensions provided by J. Claudon.

Thus, knowing the dimensions of photonic wire we can estimate the Brownian motion amplitude. The photonic wires used in this study have the shape of an inverted truncated cone as shown in figure 4.17. The volume V, of such a structure is given by

$$V = \frac{\pi}{3} \frac{h}{(r_{top} - r_{base})} (r_{top}^3 - r_{base}^3) \tag{4.29}$$

where h is the height of the photonic wire which is equal to 17.2 µm, r_{top} (variable) and r_{base} ($\sim$ 250 nm) are the radius of the top and bottom facet as shown in figure 4.17.

The geometric mass of the wire is given by, $m_{geo} = V\rho$, where $\rho = 5320$ kg/m^3 is the density of GaAs. The effective mass m_{eff} of the structure is smaller than its geometric mass m_{geo}. In case of a uniform structure (cylinder shaped), $m_{eff} \approx \frac{33}{140} m_{geo}$ (see Supplementary Information of Yeo et al. [35]). The exact relation between m_{eff} and m_{geo} in case of conical shape is not known. However, we can deduce m_{eff} from the Comsol simulation or from the Brownian motion measured experimentally as shown in the next section. The following section will first give the experimental estimation of Brownian motion amplitude by measuring the spectrum on spectrum analyzer and calibrating the motion amplitude using detection sensitivity as explained in section 4.4. Then, it will describe a way to estimate the effective mass m_{eff} and zero point fluctuations x_{ZPF} from the measured Brownian motion.

4.4.3 Measured Brownian motion

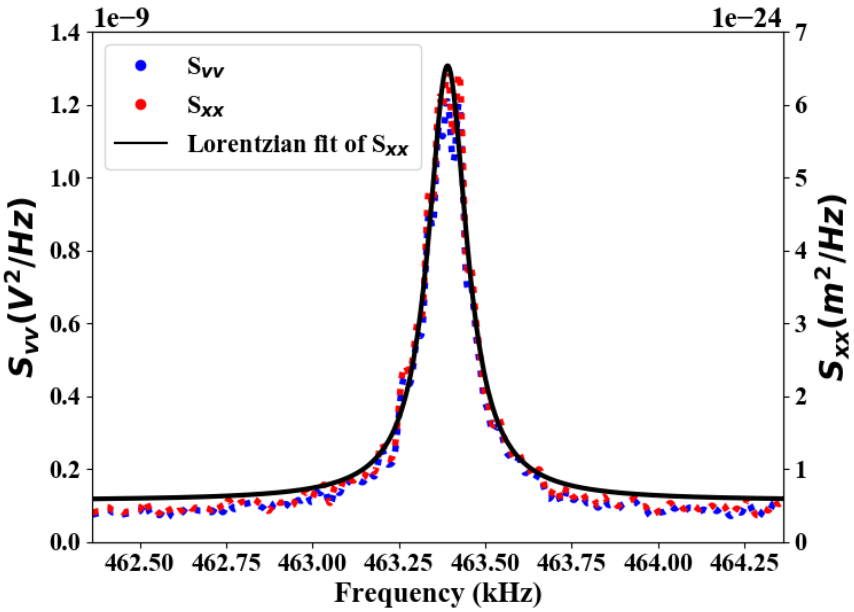

Figure 4.18: Noise spectrum of the photonic wire free end, S_{vv} (blue trace) and S_{xx} (red trace) measured at T = 5 K for a wire with top diameter of 1.88 μm. Black trace is the Lorentzian fit.

Figure 4.18 shows the measured response for the photonic wire with top diameter equal to 1.88 µm at 5 K. The blue trace in the plot represents the power spectral density i.e. S_{vv} and has units of V^2/Hz, whereas red trace represents S_{xx} with units of m^2/Hz. The conversion from S_{vv} to S_{xx} is done using eq. 4.10 and 4.18, with $\beta_{x,DC}$ around 30 (mV/µm) and gain ratio at the mechanical resonance frequency (463.4 kHz) approximately 455. The power spectrum S_{vv} or S_{xx} is fitted using a mechanical Lorentzian function and is shown

by black trace in the figure (refer to eq. 4.27),

$$S_{xx}(\Omega) = \frac{A\Gamma_m}{((\Omega_m^2 - \Omega^2)^2 + \Gamma_m^2\Omega^2)} \tag{4.30}$$

where $A = \frac{2k_BT}{m_{eff}}$ (m^2/sec^2). From the fit we obtain A, Γ_m and Ω_m. From these parameters we can compute:

1) the effective mass, given A;

$$m_{eff} = \frac{2k_BT}{A} \tag{4.31}$$

2) δx_{ZPF}, given the effective mass calculated above and Ω_m;

$$\delta x_{ZPF} = \sqrt{\frac{\hbar}{2m_{eff}\Omega_m}} \tag{4.32}$$

3) Finally the variance of the Brownian motion (refer eq. 4.28)

$$\langle \delta x_{th}^2 \rangle = \frac{k_BT}{m_{eff}\Omega_m^2} \tag{4.33}$$

Using the above equations we get: m_{eff} = 3 pg, δx_{ZPF} = 75 fm, and δx_{th} = 50 pm at 5 K for the spectrum shown in figure 4.18 for photonic wire with top diameter = 1.88 μm and mechanical resonance frequency $\Omega_m/2\pi$ = 463.4 kHz. However, if we compare the value of m_{eff} obtained from the Brownian motion (BM) spectrum ($\approx$ 3 pg) with the one obtained from the Comsol simulation ($\approx$ 30 pg) as presented in [35] for the photonic wire in the same sample with similar dimensions, there is a discrepancy of about a factor 10. This results in δx_{ZPF} and δx_{th} roughly 3 times higher than expected from the Comsol simulation.One plausible explanation would be the error in the sample temperature. The temperature used in the calculations above is the cryostat temperature T_{cryo} given by ITC 601. The cryostat temperature is actually the temperature of the cold finger below the sample holder. The actual temperature of the sample might be different. As we will see later in Appendix B, there is a difference of almost factor of 5 in the actual temperature and the cryostat temperature when T_{cryo} = 5K, which explains a large part of this discrepancy.

4.4.4 Power dependence

It has been mentioned in section 4.2, that the generated signal is proportional to the intensity of the light falling on the photodiode. Thus, both the signal level and the DC detection sensitivity β_{DC} will increase linearly with the probe laser power. Whereas, on the other hand, the optical noise (limited by shot noise) scales as the square root of power. Therefore, signal to noise ratio increases with probe laser power and it is favorable to work at higher probe laser powers. However, there might be some heating effects with too large probe laser power on the photonic wire. To see the effect of probe laser power on the Brownian motion amplitude of a photonic wire at 5 K, I did a power series with SPD as detector. This power series is performed on a photonic wire with top diameter of 2.2 µm. Figure 4.19(a) shows the plot of S_v (green) at mechanical resonance and the noise floor (red) as a function of probe laser power. It is clear that as the power increases, signal to noise ratio increases. Moreover to see the effect of laser power on motion amplitude, we plot amplitude spectral density S_x at resonance, which is converted from S_v using eq. 4.10 and 4.18. Figure 4.19(b) shows the dependence of β_{DC} and S_x on probe laser power. As the laser power increases, β_{DC} increases linearly like S_v. The amplitude spectral density at mechanical resonance is more or less constant with average value around 1.32 ± 0.05 pm/$\sqrt{\text{Hz}}$, which corresponds to $\delta x_{th} \approx 10 \pm 0.35$ pm (measured with 50 Hz bandwidth). Thus, we can conclude that there is no heating effect in the presence of high probe laser power.

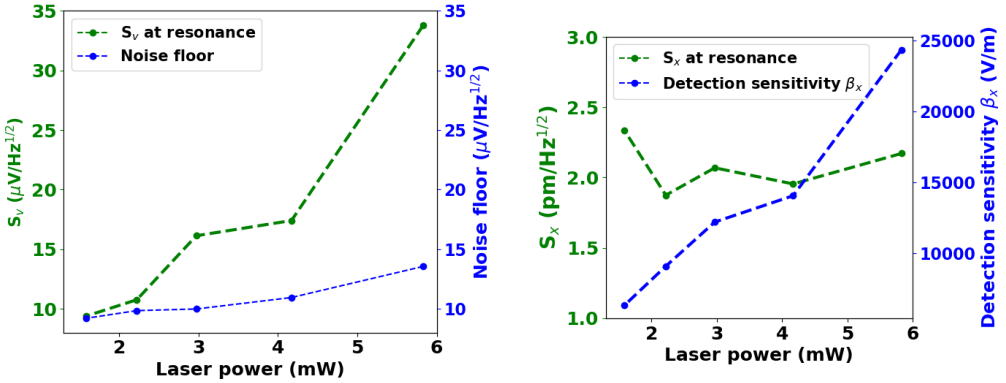

(a) (b)

Figure 4.19: Power dependence of Brownian motion amplitude on photonic wire with top diameter of 2.2 µm at 5 K with SPD as detector (a)Variation in S_v at resonance (green trace) and noise floor (red trace) with laser power. (b) Variation in S_x at resonance (green trace) and detection sensitivity (blue trace) with laser power.

Other important point is that as the probe laser power reduces below 1.5 mW, the signal level is getting lower than the noise floor resulting in signal to noise ratio of less than 1, making the detection difficult. Therefore, to be able to detect the motion the probe laser power should be at least few mW. However, as pointed in chapter 3, that probe laser has

an influence on the resonant emission of the QDs and the optimum power of probe laser is about 100 -200 µW. In order to realize the quantum hammer experiment, we need to have the two setups (namely, resonant excitation and optical motion detection) working simultaneously. Thus, it is important to have both motion detection and fluorescence detection possible at a certain probe laser power. This is why, we have changed the detector from SPD to APD for the quantum hammer experiment, owing to the higher sensitivity of APD at lower powers as shown in the following section.

4.4.5 Change of detector: from SPD to APD

As mentioned above, with SPD we can not detect the Brownian motion, if the probe laser power is below 1.5 mW as we are limited by the electronic noise of SPD. This brings us to the conclusion of replacing SPD as detector with the one which has lower noise floor and higher sensitivity. As discussed in section 4.3.1.5, the electronic and optical noise floor of APD is 30 dB lower than that of SPD making it a suitable choice for our experiments. The minimum power required to measure the 3 dB Brownian motion signal on SPD is equal to 1.5 mW whereas it is only 25 µW with APD. The possibility to vary the gain of APD allows us to go even lower than 25 µW. The lowest power at which we saw the BM signal (1.2 dB) was about 10 µW. Therefore, using APD as detector will allow us to have the simultaneous motion detection and fluorescence detection which is necessary to perform the quantum hammer experiment.

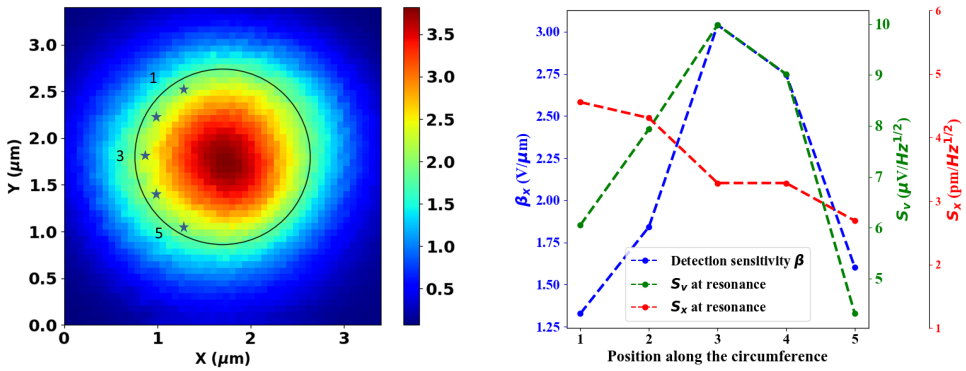

(a) (b)

Figure 4.20: (a) Experimental 2D map of voltage signal from APD for the photonic wire with top diameter 1.88 µm. Black circle represents the edge of the photonic wire's top facet. Stars presents different position of probe laser during the measurement. (b) Plot of detection sensitivity β_x (blue), measured voltage spectral density S_v (green) and amplitude spectral density S_x (red) of the photonic wire free end at each point.

As seen from the simulations, in case of single photodiode such as APD, the best position of probe laser is close to the edge of the photonic wire and depending on the mode

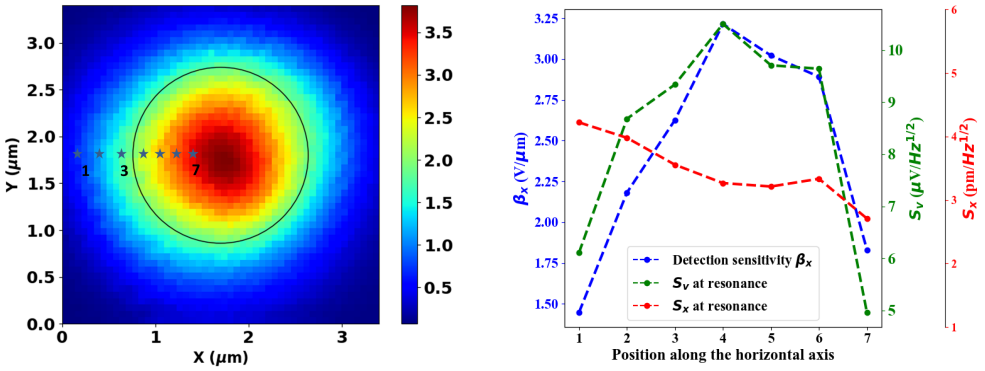

(a) (b)

Figure 4.21: (a) Experimental 2D map of voltage signal from APD for the photonic wire with top diameter 1.88 μm. Black circle represents the edge of the photonic wire's top facet. Stars presents different position of probe laser during the measurement. (b) Plot of detection sensitivity β_x (blue) , measured voltage spectral density S_v (green) and amplitude spectral density S_x (red) of the photonic wire free end at each point. Detection sensitivity is maximum at point 4 i.e. close to the edge of the photonic wire as expected.

direction we can move the beam along the circumference to find the optimum position. Figure 4.20(a) shows the point by point 2D reflection map of the total intensity signal from APD recorded by sweeping the probe laser over the photonic wire. To determine the best position to detect the mode oscillating in horizontal direction, I move the probe beam along the wire circumference (from star 1 to star 5) and recorded the magnitude of detection sensitivity horizontal component β_x and response spectrum for each point. The signal level at each point is compatible with a constant value (about 2 V), within the experimental error. As we go from point 1 to point 3, even though the signal level is same but β_x is changing, being maximum at point 3 (with β_y equal to zero) and decreasing as we go away from this point. This is plotted in figure 4.20(b) together with S_v and S_x values. S_v follows the same trend as β_x as higher detection sensitivity means more sensitive detection. However, S_x is not constant as expected. The variation in S_x values can be attributed to the error in detection sensitivity values resulting from the position drifts and laser power drifts. Chapter 5 presents the feedback loops employed to reduce the fluctuations in laser power, and position, thereby reducing the β fluctuations. Nevertheless, if we continue further along the circumference and take the spectrum at point 6, which is along the vertical axis, we did not detect this mode at all as β_x is equal to zero in this case. This confirms the orientation of this mode along the horizontal direction.

Once we know the orientation of mode, we can move the beam along this axis to know the position with maximum detection sensitivity. From simulation results presented in section 4.2.1, in figure 4.6 the best position for detection sensitivity is along the edge of the photonic wire which is also proved experimentally as shown in figure 4.21. Figure 4.21(a) shows the points along the horizontal cut at which the detection sensitivity and amplitude

spectral density are measured. Figure 4.21(b) shows that detection sensitivity (blue) is maximum at point 4, close to the edge of the wire and drops on both sides. The amplitude spectral density S_x is however varying because of the laser power fluctuations and position drifts during the measurements.

4.5 Motion actuation of photonic wire.

There are numerous ways to actuate the motion in micro-electromechanical systems (MEMS) and nano-electromechanical systems (NEMS). Two of these methods namely, actuation by a piezo electrical transducer glued at the back of the sample holder and optical actuation using the modulated laser beam have been demonstrated in our group before [35,39,41,42]. The goal of this thesis is to induce the motion in the photonic wire by the resonant excitation of the QD. However, to realize this effect it is important to know the mechanical properties of the photonic wire such as its mechanical resonance frequency, Quality factor and damping together with the optomechanical coupling strength of the system, g_m (discussed in chapter 2). The mechanical properties of the photonic wire can be determined from the Brownian motion measurements. However, with the actuated motion we can also estimate these properties together with the calculation of g_m for different QDs in the wire. The g_m values for different QDs are presented in chapter 5. In this section, I will briefly talk about the actuated motion technique together with the results.

For implementing the actuated motion, we chose optical actuation over piezo actuation because the response of piezo actuation is not flat in frequency owing to piezoelectric transducer internal resonances as shown in figure 4.22, where the response of the photonic wire is compared in case of piezo or optical actuation. The response from piezo actuation has some bumps (figure 4.22(a)) whereas the response from optical actuation is smoother (figure 4.22(b)). Moreover, the bandwidth of the piezo actuation is limited to few hundreds of kHz. Therefore, with piezo actuation, excitation of higher order modes is not possible unlike with optical actuation.

4.5.1 Optical actuation of photonic wire

There are two main effects when the laser beam falls on the photonic wire. First is due to the optical forces and second is the photothermal effect. Optical forces are the forces that arise when linear momentum is transferred from photons to matter, in light matter interaction. Optical forces are commonly classified as either gradient or scattering forces. The gradient force (or dipole force F_{dipole}) is an optical force which is perpendicular to the propagation direction of the excitation laser. This gradient force is well known for its applications in optical tweezers, where strong laser beam generates a piconewton force which manipulates the small dielectric particles such as DNA, enzymes, cells and bacteria.

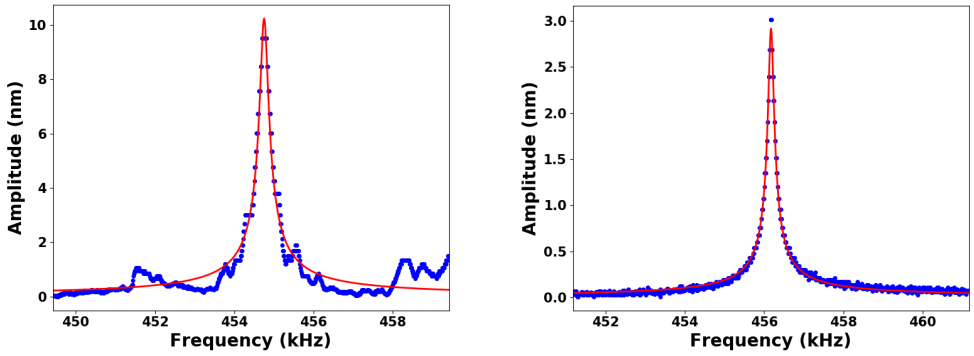

(a) (b)

Figure 4.22: Oscillation amplitude δx of the photonic wire free end versus drive frequency $\Omega/2\pi$ (a)Piezo actuation, and (b) Optical actuation of a photonic wire with top diameter 1.88 μm. Blue trace is the recorded data and red is the fit using mechanical Lorentzian function.

The physics behind can be understood by recognizing that a dielectric particle can lower its energy by moving towards a region with higher field intensity [109, 110]. It has been demonstrated that the gradient field around the nanophotonic waveguides could produce significant optical forces [111–113]. As opposed to the gradient force, the scattering force (or radiation pressure force F_{rad}) is an axial force, as a consequence of the momentum transfer parallel to the propagation direction of the excitation field. It has been investigated in the field of cavity optomechanics [114–116]. The possibility to amplify or damp (cool down) the mechanical oscillations through photon-phonon coupling [117–119], has attracted significant attention over the last fifteen years. Figure 4.23, shows the sketch demonstrating these forces, it is clear that the net force is such that trying to bend the wire towards the laser. So, in simple words, laser attracts the wire.

When the light falls on the structure it is partially reflected, imparting the momentum to the structure and partially absorbed, leading to the heating of the structure. This heating effect caused by the absorption of light is called photothermal effect. Although GaAs is transparent for wavelengths of both pump (used for optical actuation, see section 4.5.2) and probe lasers, heating effect has been observed as presented in [42]. It has been observed [42] that at room temperature, the experimental values for the torque exerted on the photonic wire ($\sim 10^{-16}$ N.m) is about 2 order of magnitude larger than the theoretical calculations of the optical forces only ($\sim 10^{-18}$ N.m). This discrepancy in the theoretical and experimental results can be explained by the contribution of photothermal effect. Photothermal effects are due to the asymmetric thermal expansion of the trumpet caused by geometrical or material imperfections. Moreover, going from room temperature to low temperature (5 K), the motion amplitude increases further by a factor of 10 with respect to that at room temperature and the behavior also changes. This increase in amplitude and change in response behavior is also explained on the basis of photothermal

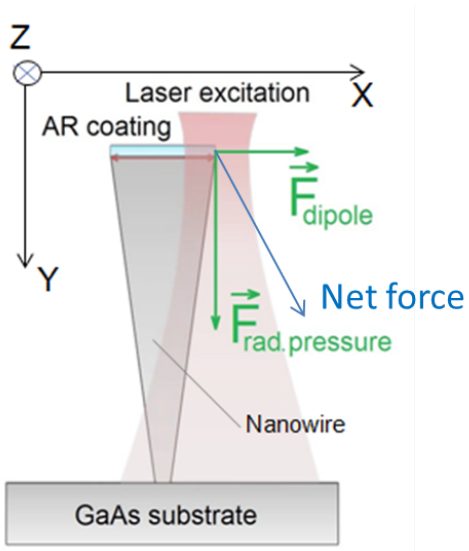

Figure 4.23: Sketch demonstrating the optical forces appearing in light matter interaction as a result of photons momentum transfer. [42]

effect. The heat diffusion coefficient for GaAs, D varies from 3.1 * 10^{-5} (m^2/s) at room temperature to 1 (m^2/s) at 5 K. This implies that at 5 K, heat will be redistributed over the wire much faster than at room temperature, resulting in larger motion. Therefore, to conclude, photothermal effect dominates the radiation pressure and dipole force effect at low temperature.

4.5.2 Experimental setup for optical actuation of photonic wires

The idea behind the implementation of optical actuation of photonic wires in our setup, was the possibility to characterize the mechanical properties of wires. Moreover, it would be required to determine the hybrid coupling g_m of different QDs to find the best candidate for the quantum hammer experiment. Measurement of g_m for different QDs is presented in Chapter 5. To realize optical actuation technique we need a laser modulated at the mechanical resonance frequency. Therefore, an additional laser is used for motion actuation at desired power level which could be separated from the spectrometer easily. This laser will be referred as pump laser. Pump laser is a CW diode laser BL976-PAG700 delivering the laser light through an optical fiber and controlled via CLD1015 driver. The wavelength of the laser is about 975 nm that corresponds to an energy below the band gap of GaAs. The controller for pump laser has modulation input with input voltage of ±10 V and modulation coefficient of 150 mA/V ± 5% with modulation bandwidth of 250 kHz. The laser intensity is modulated at the mechanical frequency Ω_m by modulating the current. The modulation is applied either by Vector Network analyzer (VNA) or Zürich instruments box HF2LI (see section 4.3.1.6). The amplitude of actuated motion is also detected by the

same device.

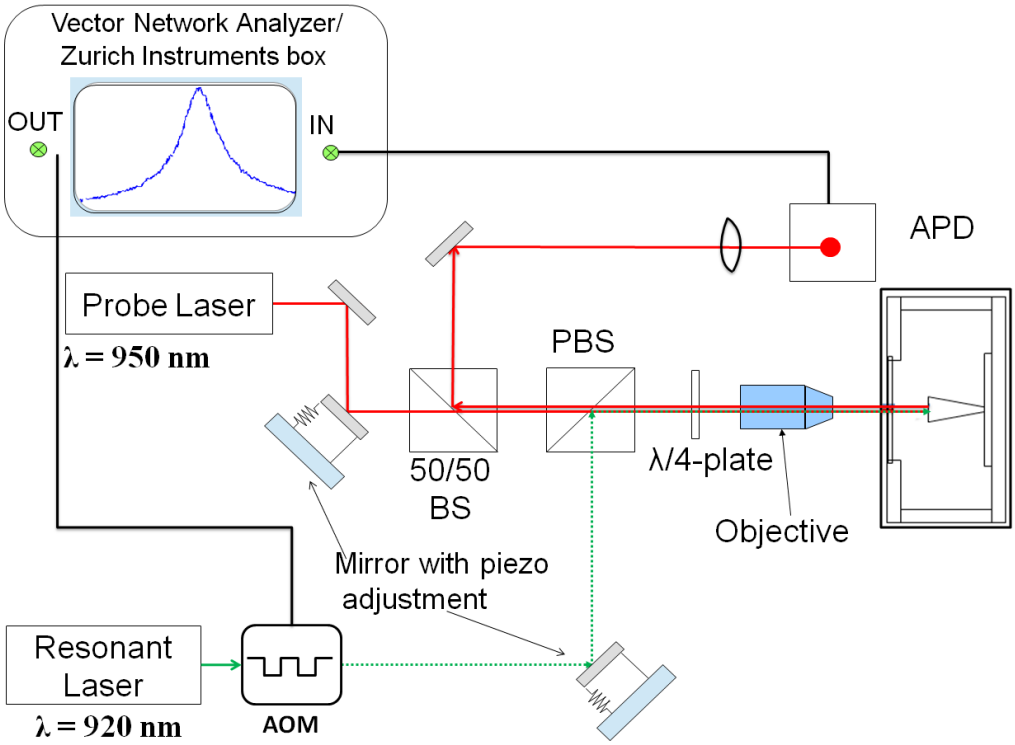

Figure 4.24: Experimental setup for detection of optically induced oscillations of photonic wires.

The experimental setup for the optical actuation of photonic wire is shown in figure 4.24. The pump laser, modulated at resonance frequency is directed towards the sample after passing through optical isolator, and pinhole (not shown in figure) to avoid back reflections and to adjust its shape and size respectively. It is merged with the probe laser at the polarizing beam splitter (PBS) and focused on top of the wire with the microscopic objective. If the light from the pump laser reaches the detector (APD 410A2) it brings strong parasitic signal, because the amplitude of modulation of intensity is much higher than the modulation of probe laser intensity caused by the oscillation of the photonic wire. To block the pump laser from reaching the APD, its linear polarization is chosen perpendicular to the linear polarization of the probe laser. Therefore, pump laser enters the PBS from other side and gets reflected through it back and forth and does not go towards the detection path. The extinction ratio of PBS is only about 20, which is not enough to filter out all the light from the pump laser. Therefore, in addition to it we place a short pass wavelength filter (FESH1000) with cut-off wavelength at 1000 nm before APD. The cut-off wavelength of these filters shifts to a shorter wavelength as the angle of incidence increases. When the angle of incidence goes from 0° to 45°, the cut-off wavelength shifts down by about 10%. Thus, by rotating the filter, we can tune the cut-off wavelength such that it will block the pump laser (λ = 975 nm), while still transmitting the probe laser

(λ = 950 nm). This optimization is done by monitoring the signal on spectrum analyzer (to block pump laser) and APD (to maximize the probe laser). The optimum position to completely block the pump laser is obtained at the cost of 10 % low probe laser signal on APD, which is a good trade off.

4.5.3 Measured response

The response spectrum of the actuated motion for the photonic wire with top diameter 1.86 μm is shown in figure 4.25. The mechanical resonance frequency, Ω_m = 404.5 kHz. Pump laser is positioned at the center of the photonic wire, whereas probe laser is positioned close to the edge of the wire along the horizontal axis, because we are detecting the mode which oscillates along the horizontal axis of the detector. The probe laser power is 100 μW and the measured value of the horizontal component of detection sensitivity, β_x = 1.5 V/μm.

The average pump laser power is 100 μW. The modulating signal sent from the Zürich Instruments HF2LI box is such that the peak to peak intensity modulation of pump laser at resonance frequency is 40 μW. The amplitude spectra recorded using HF2LI sweeper tab (in Volts) is converted into meters using detection sensitivity β_x and is plotted in figure 4.25. The peak to peak motion amplitude is equal to 5 nm.

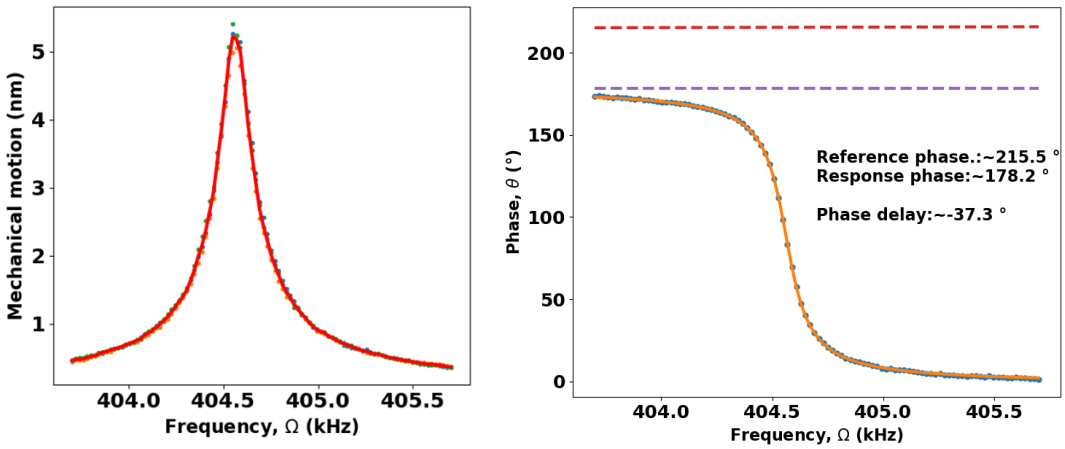

(a) (b)

Figure 4.25: Experimental spectra for the actuated motion in the photonic wire with top diameter 1.86 μm. (a) amplitude, and (b) phase. The peak to peak intensity modulation of pump laser at resonance frequency is 40 μW.

The phase of a driven oscillator should evolve from 0° to -180° across the resonance with the value at resonance equal to -90°, if the effect is instantaneous. However, it is found that at low temperature the effect is dominated by the photothermal effect and is

not instantaneous [42]. Moreover, to get the exact value of phase on resonance, we should take into account the phase delays related to the delay of electronics circuit, if any. To determine this value, the modulated laser is focused on the APD after reflecting from the substrate. The optical filters FESH1050 and FEL950, which are originally placed to select only probe laser and block other lasers to reach the motion detection APD, are removed from the setup. This reference phase depends on the frequency. Figure 4.26, shows the phase spectrum in the frequency range 100 kHz to 2 MHz for the modulated resonant laser. It is evident that we have a constant delay in time that leads to different phase delay depending on the frequency. The value of this reference phase is given by the red dashed line in figure 4.25(b) and is equal to 215.5° for the case of pump laser modulated at Ω_m. The phase of the mechanical response below the mechanical response is also marked on the figure and is equal to 178.2°. The difference between the reference phase and the mechanical response phase below resonance gives the phase delay of the photothermal response and is equal to 37.3°.

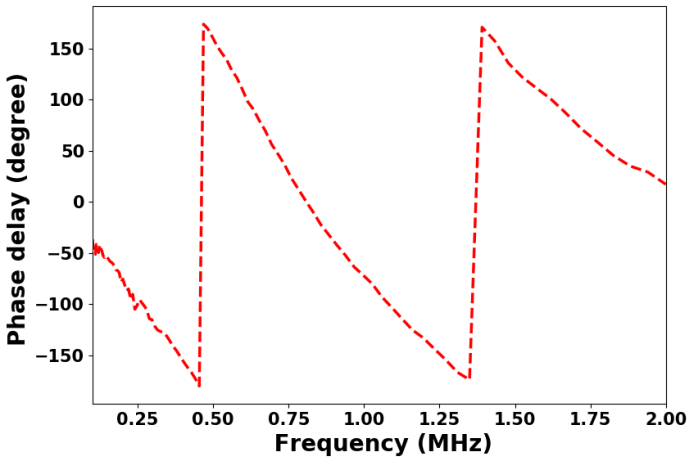

Figure 4.26: Phase delay due to signal propagation through the electric circuits of the experimental setup. This response is recorded when modulated resonant laser is reflected from substrate and focused on APD.

In order to understand the origin of this phase delay, we used other lasers at different wavelengths to actuate the photothermal response. The other lasers are the resonant laser and non-resonant laser at λ = 920 and 825 nm respectively. The idea is to see if the photothermal response have the same delay with these lasers or not. Since these lasers have comparatively higher energy and will be absorbed mainly at the QD level, one could expect a change in the phase delay if it is related to the heat absorption effect. However, as we can see in figure 4.27, the phase delay corresponding to the resonant laser and non-resonant laser is 35.7° and 28.8° respectively.

Thus, the delay in the photothermal response appears to be of the same order around 30°, with a spread of ± 5°, depending on the laser used. Therefore, it must be related to

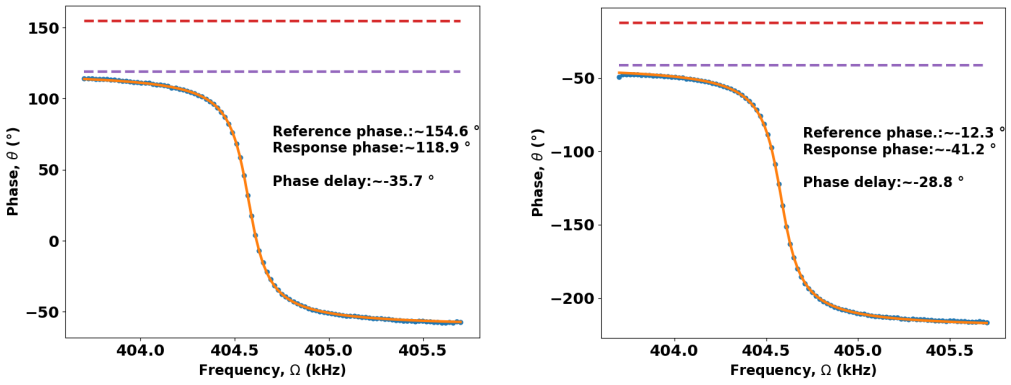

(a) (b)

Figure 4.27: Phase response for photonic wire with top diameter 1.86 µm,when the motion is actuated by (a) Resonant laser, and (b) Non-resonant laser.

the thermal properties of the photonic wire itself. This has been further verified by the calculations done by O. Bourgeois taking into account the properties of GaAs at T = 5 K. The characteristic time for heat propagation in the photonic wire is found out to be 0.35 µs which corresponds to about 1/10 of the mechanical period, i.e. to a delay of ≈ 35°.

4.5.4 Influence of resonant laser

During the final quantum hammer experiment, we will be performing the motion detection and resonant emission detection experiment simultaneously. This implies that the three lasers (probe laser for motion detection, and other two (resonant and non-resonant) for QD emission detection (as discussed in chapter 3), will be switched on and focused on the top facet of the photonic wire. The resonant laser will be modulated at the mechanical frequency and would induce photothermal motion. Although the resonant laser power will be in the range of few hundreds of nW, it is still important to know the influence of this laser on the photonic wire motion. Therefore, a power series at different resonant laser powers is made. The laser power is varied from 100 nW to few µW and the response is shown in figure 4.28.

As mentioned before, optical actuation of a mechanical oscillator is due to optical forces and photothermal effect [120]. As reported in [42], the effect due to optical forces is weak (2 orders of magnitude smaller) as compared to the photothermal effect and therefore can be neglected. With photothermal effect, the absorbed optical power heats the photonic wire leading to a deformation and bending of the structure by thermal expansion. For a particular photonic wire, the amplitude of motion will be directly proportional to the power of the laser as shown in figure 4.28(b). Here the power of resonant laser is changed using different density filters and allows us to go from 100 nW to 22 µW. The response

spectrum is shown in figure 4.28(a) for each power. The amplitude of motion is extracted and plotted in figure 4.28(b) and is directly proportional to the laser power which goes well with the theory explained above.

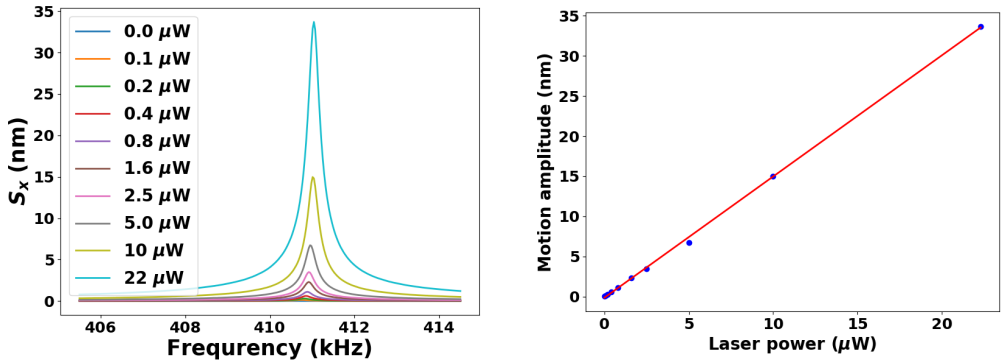

(a) (b)

Figure 4.28: (a) Response spectra for the actuated motion in the photonic wire with top diameter 1.86 μm at different laser powers. (b) Motion amplitude versus laser power. Blue points are the measured data and red is the linear fit.

4.6 Conclusion

This chapter focused on the optical motion detection technique, which is sensitive enough to detect the Brownian motion of the photonic wires around 10 pm at 5 K, while not perturbing too much the resonant emission of the quantum dot. In addition to optical detection, chapter also presented the optical actuation technique to induce the motion in the photonic wire based mainly on the photothermal force at low temperature [42]. This photothermal effect is also present during the quantum hammer measurement because of the modulated resonant laser. Therefore, its characterization is important. We have concluded that the photothermal response varies linearly with the laser power and has a phase delay of about $35 \pm 5^\circ$ due to the thermal properties of the photonic wires.

Chapter 5

Towards Quantum Hammer experiment

It has been demonstrated in the previous chapters that it is possible to perform both resonant excitation of the QDs and optical detection of photonic wire oscillations independently. To observe the Quantum Hammer effect experimentally, we have to perform both these techniques simultaneously. This chapter focuses on the final experiment setup which combines both resonant excitation and optical motion detection. It will present the various experimental challenges we faced in combining the setups and how we overcame them. Then, we will talk about the technical challenges that we had to face in order to reach the required sensitivity. The final section will present the results obtained on Quantum Hammer experiment.

Contents

5.1 Experimental setup

The goal of combining the setup of resonant excitation (discussed in Chapter 3) and optical detection (discussed in Chapter 4) is not as facile as it seems. The challenge is to combine four lasers, each with different wavelength and different power range and most importantly they have to be separated in the detection path for efficient detection. In order to understand the challenges easily, let us breakdown all the important points we had to keep in mind to design the new combined setup.

1) We have four lasers each with a different purpose and different wavelength: a) Resonant laser (RL) around 920 nm for the resonant excitation of QD; b) Non resonant laser (NRL) around 825 nm for non-resonant PL and stabilizing the QD as discussed in chapter 3; c) Probe laser around 950 nm for motion detection and d) Position stabilization (or locking) laser around 975 nm as discussed in section 5.3.2.2. This is the same laser which is presented in Chapter 4 section 4.5.2 as pump laser used for optical actuation of the photonic wire. For the present experiment, we are using it only for position locking, therefore, hereafter, it will be referred to as locking laser. As a consequence of different wavelengths of the lasers, we can use short/long pass filters that transmits the laser depending on the cut-off/cut-on wavelength, to block the residual light before detector.

2) In addition to the wavelength, we can also use the polarization of the laser beam as a tool to separate or combine the beams in the setup, by using polarizing beam splitters (PBS). To set the polarization of each laser, we place polarizers/half wave plates independently in each laser path.

3) As mentioned already, the required laser powers for RL and NRL are in the range of few nW to few μW; whereas that of probe laser will be few hundreds of μW, before the objective. Therefore, while combining the lasers using beam splitters, we have to choose them cautiously, so that on one hand, we have required power before objective for each laser and on the other hand, we do not loose much power of the reflected beam from the sample before reaching the detector (especially for probe laser). Maximum power at the laser output is around few tens of mW for all lasers. Thus, we can place the beam splitter (BS 1) to combine the beams such that we get 90% light from the probe laser but only 10% from RL and NRL on the way to the sample.

4) In addition to the incoming beams, it is also important to collect the reflected light efficiently. For example, probe laser has to be collected and directed towards the detection path for optical detection i.e. towards the SPD or APD for efficient motion detection. All the lasers have to be blocked form going towards the spectrometer for efficient detection of QD emission. This is achieved by using cross polarization scheme and short/long pass wavelength filters as discussed in previous chapters.

5) Lastly, because of the open-loop piezo controller of the nanomax stage (stage holding the microscopic objective), mechanical stability of the cryostat and pointing stability of the lasers, there is always a drift in the relative position of the lasers and the sample/photonic wire. This drift affects the QD excitation level. However, its main effect is on the detection sensitivity β measurement, which as a result affects the measured amplitude. To overcome this issue, we decided to lock the position of the photonic wire using a laser reflected from the top face of the photonic wire and focused on the quadrant photodiode (QPD) (allows us to compensate for both x and y drifts). We used the locking laser for this purpose, which is locked on the center of the photonic wire (see section 5.3.2.2). To simplify the experimental setup, we decided to decouple the path of this laser from other lasers such that any change in the position of probe laser or RL/NRL using piezo mirrors will not affect the locking laser position.

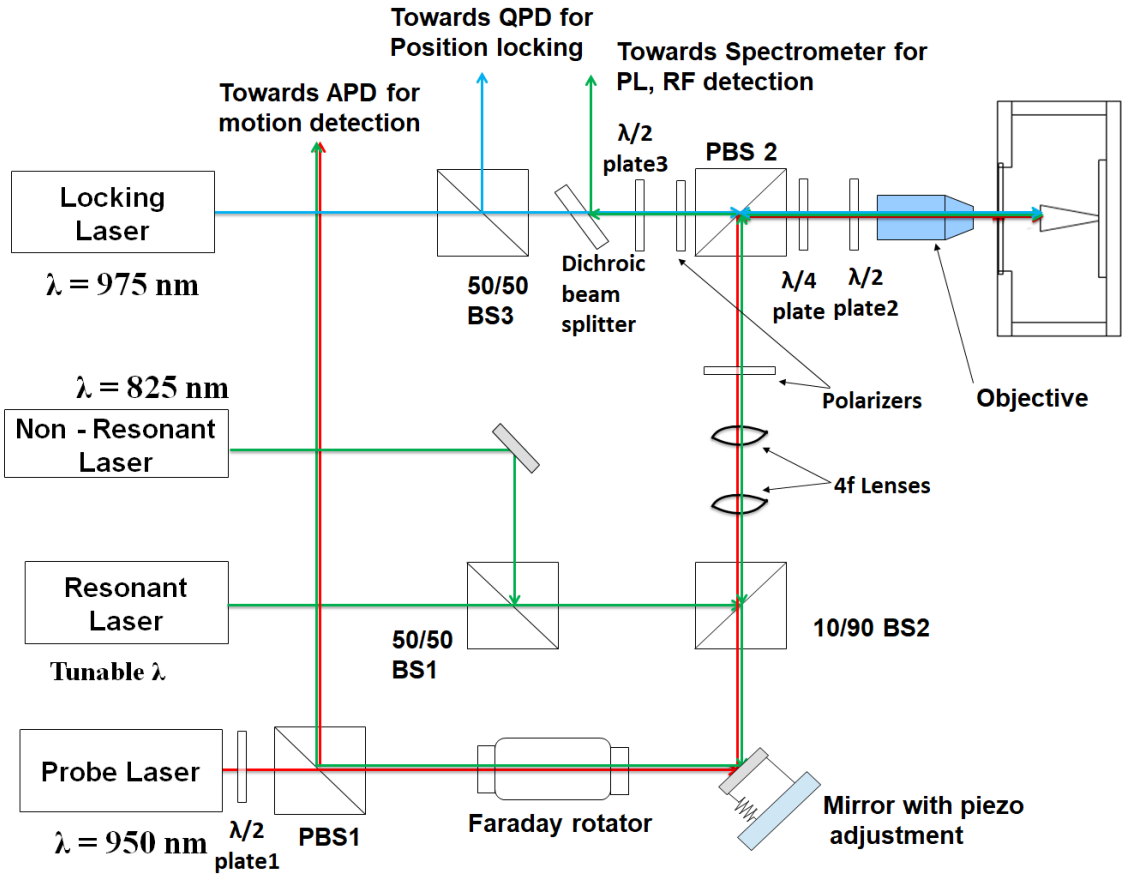

Figure 5.1: Sketch demonstrating the final working experimental setup for the realization of Quantum Hammer effect.

The sketch of the final working design for the experimental setup is shown in figure 5.1,

designed by keeping in mind all the points mentioned above. The position and power of the probe laser on top of the photonic wire is most important for efficient detection. As concluded in the section 4.2, that for maximum detection sensitivity in case of single photodiode (such as APD) as detector, probe laser should be placed close to the edge of the photonic wire. Therefore, we need a fine position tuning (mirror on a piezo controlled holder) mirror (see section 4.3.1.3) in the probe laser path, which allows us to modify the probe laser position with respect to the photonic wire. We place the piezo mirror before the beam splitter (BS2) which combines the probe laser with RL and NRL, to avoid the modification in other beams. The BS2 is chosen in a way that it transmits 90% light (probe laser) and reflects only 10% (RL and NRL). This is because the required powers of RL and NRL are in nW range, so getting only 10% reflected light through BS2 is acceptable. Once the lasers are combined, they go through a 4f system as explained in section 4.3.1.3, so that a tilt of the piezo-mounted mirror leads to a change of the laser angle at the entrance of the objective without changing the laser position. Following the 4f system, the lasers are directed towards the microscope objective passing via the polarizing beam splitter (PBS2), $\lambda/4$ waveplate and $\lambda/2$ waveplate. The purpose of using PBS and $\lambda/4$ waveplate is to have cross polarization scheme. As discussed in Chapter 3, this is useful in resonant emission detection to suppress the laser from reaching the spectrometer to have better QD emitted signal to laser background ratio. In the present setup, the purpose is same i.e. to suppress the lasers (probe laser, RL and NRL) in the QD emission detection path towards the spectrometer. Moreover, as mentioned before, the extinction ratio of the PBS is only about 20, which is not enough to filter out all the light from the lasers. Therefore, we used the wavelength filter (FES950) to suppress further the probe laser (NRL will not make a difference since its wavelength is far away, whereas probe laser, even though at 950 nm, does affect the PL spectrum as discussed in Chapter 3). All the lasers have a separate optical isolator and spatial filter (not shown in the figure) in the beam paths before combining them together.

Thus, the reflected laser light from the photonic wire top facet is collected by the objective and will be reflected back by the PBS2 towards the incoming beam path. In order to recover the probe laser signal for motion detection, we need to extract the reflected light and direct it towards APD without loosing much power. Since, the BS2 we used is 10/90 (R/T), the maximum amount of reflected signal (reflected from the sample) will be transmitted through it and then can be extracted using a Faraday rotator and PBS1 placed in the probe laser path. The role of Faraday rotator is to rotate the laser beam polarization passing through it, such that the light from the sample will be reflected by the PBS1 (instead of transmission into the incoming path) and can be directed towards APD for motion detection. The polarization of the laser at each point is very critical and therefore, we have different polarizers and $\lambda/2$ waveplates in the setup to tune the laser polarization accordingly.

For example, for the probe laser, on the way towards the sample, there is a $\frac{\lambda}{2}$ plate1 in the beam path which is set such that to have the light polarized parallel to the plane

of incidence (p polarized) to have it completely transmitted through PBS1. It then passes through the Faraday rotator. The Faraday rotator, rotates the beam polarization (by $\approx$ 45° in ideal case). The polarization of the beam at the output of the Faraday rotator is defined by the polarization axis of the output polarizer which is fixed such that we have the light polarized perpendicular to the plane of incidence (s polarized). This is because, finally we want the beam to get reflected towards the sample at PBS2. There is another polarizer before PBS2, to define the vertical polarization for all the laser beams, so that all the lasers are reflected towards the sample. On the way back from the sample, probe laser (and also RL and NRL even though weak) reflected from the sample are collected back by the same microscopic objective and again reflected by the PBS2 towards the incoming beam path. On passing the Faraday rotator in backward mode, polarization will be further rotated by the same amount such that when hitting the PBS1, a part of it will get reflected towards the detector (APD) and other part will go through towards the input beam. This arrangement is not perfect because the faraday rotator is not rotating by 45° but at some arbitrary angle. Therefore, the beam hitting PBS1 on the way back is not perfectly p polarized and we loose a part of it. The polarization of the output polarizer is chosen to have maximum possible back-reflected light at PBS1 measured with a power meter. The total loss on the detection path to APD is less than 50%, which includes the loss due to imperfect faraday rotator and losses at other optical elements. Nevertheless, this is still the best arrangement keeping in mind all the constraints. Moreover, the amount of reflected light reaching APD is enough to be able to perform the measurements (not limited by the electronic noise or shot noise).

In addition to these three lasers, the fourth laser, is the locking laser (see section 5.3.2.2), which is decoupled from the other lasers for simplicity. Therefore as seen in figure 5.1, its polarization is chosen perpendicular to the other lasers such that it enters PBS2 from the other side and transmitted towards the objective. The reflected locking light from the sample will also be transmitted through it together with the photons emitted by the QD. We placed a dichroic beam splitter to separate the locking laser from the QD emission light emitted by the QDs. Dichroic beamsplitters spectrally separate light by transmitting and reflecting light as a function of wavelength. We placed a longpass dichroic beam splitter DMLP950L with a cut-on wavelength at 950 nm. It is highly reflective below the cut-on wavelength (thereby reflecting the light emitted by QD which is around 920 nm) and highly transmissive above it (therefore the locking laser will be mainly transmitted). In addition to the wavelength, the amount of reflection and transmission depends also on the polarization of the laser beam, especially for the reflected beam at 920 nm. The values for reflection and transmission as a function of wavelength (975 nm for locking laser and 920 nm for QD emitted light) and polarization are given in the table 5.1. It is clear that for the transmitted light around 975 nm there is no major effect of polarization on the transmission percentage. However, for the reflected light around 920 nm, it is better to have the beam s-polarized to have about 96% reflection and only 2% transmission. The polarization of the QD emitted light is defined by the half plate2 placed between the objective and the cryostat and can be further adjusted by the half plate3 placed between PBS2 and the Dichroic beamsplitter to have maximum reflection for the emitted light.

	p - polarized	s - polarized
Reflection		
at 975 nm	2%	7%
at 920 nm	55%	96%
Transmission		
at 975 nm	98.5%	96%
at 920 nm	33.5%	2%

Table 5.1: Reflection and Transmission values through Dichroic beamsplitter (DML950L) for p-polarized and s-polarized light at 975 nm and 920 nm respectively.

5.2 Optomechanical coupling measurement

Another important aspect of realizing the quantum hammer effect is to find the QD suitable for the measurements. The most important parameter is the hybrid coupling g_m, which is higher for the QDs located close to the edge of the photonic wire [43]. On the other hand, optical coupling b_o decreases (see Chapter 2 section 2.2) for such dots. Since, Quantum Hammer effect involves the resonant excitation of the QD i.e. good coupling to the incoming laser light, implies good b_o is also important. Therefore, to be able to realize the experiment, we need to have the dot with reasonable hybrid and optical coupling i.e. there will be a trade off between the two couplings. In order to find the best candidate, we started with the measurement of hybrid coupling of the QDs. Once we have the hybrid coupling for different dots, we then proceed to check the resonant excitation of these dots in the order of decreasing hybrid coupling i.e. starting with the dot with large hybrid coupling.

Recalling from Chapter 2 equation 2.9, the hybrid coupling can be estimated experimentally by measuring the change in QD transition energy as the wire oscillates i.e. the ratio $\frac{\partial\omega}{\partial x}$. A simple way to measure this is to set the wire in motion along one of the mode via either the piezo electrical transducer or optical actuation as discussed in the previous chapter. Using the combined setup it is possible to detect the optically excited motion and the PL spectrum on the spectrometer simultaneously. In the experimental setup shown in figure 5.1, optical actuation can be performed using either RL ($\sim$ 920 nm) or locking laser (975 nm) modulated at the mechanical resonance frequency Ω_m. Without mechanical excitation, the PL spectrum of each QD is a Lorentzian peak as shown in figure 5.2(a) (blue plot) with a linewidth of about 20 μeV. When the photonic wire is excited, by modulating the locking laser exactly at the mechanical resonance frequency $\Omega = \Omega_m$, the PL spectrum of the QD gets broadened as a result of the oscillatory motion of the QD transition energy. At a certain oscillation amplitude (dx) of the photonic wire top facet, different QDs will undergo different amount of broadening depending on their position within the photonic wire. The PL spectrum when the wire is optically excited (using locking laser) is shown in figure 5.2(a) (orange and green plots corresponding to different oscillation amplitudes

dx), where the shape is like a 'camel-back' and is fitted using the oscillating Lorentzian function, which calculates the time average of a Lorentzian with oscillating center, given by

$$n_c(\omega) = \langle L(\omega - \omega_o - \delta\omega(\Omega_m)) \rangle \tag{5.1}$$

where $L(\omega)$ is the Lorentzian function, n_c is the photon counts, $\hbar\omega_o$ is the QD transition energy at rest, and $\hbar\delta\omega = A\sin(\Omega_m t)$ is the oscillation amplitude of the QD energy caused by the oscillations of the photonic wire, where A is the spectral broadening amplitude. Figure 5.2(c) shows the PL spectrum for QD1 (used for quantum hammer experiment) when the photonic wire is oscillating along the horizontal mode with dx = 12 nm. The characteristic lineshape obtained using equation 5.1 (black plot) matches well with the measured spectrum (red plot) and allows accurate determination of the shift in QD transition energy $\hbar\delta\omega$. Therefore, the hybrid coupling g_m can be estimated easily. It is important to note that the calibration of measured mechanical motion spectrum to the oscillation amplitude in nm is achieved with careful calibration of detection sensitivity β as explained in the previous chapter 4. The measured splitting for QD1 at different oscillation amplitudes is plotted in figure 5.2(d). The dashed red line is the linear fit to the measured data which gives a slope of 11.9 μeV/nm. It can be seen from the plot that the fit deviates for the first few points. This is because at very small oscillation amplitude, the spectral broadening is negligible and the estimated splitting value is limited by the linewidth of the line. The resulting coupling is equal to 11.9 μeV/nm and $g_m/2\pi \sim 75.4$ kHz (calculated using equation 2.9), when the photonic wire is excited along the horizontal mode. These values are calculated by taking $x_{ZPF} \approx 26$ fm and 29 fm, for mode H and V respectively, obtained from the Comsol simulations done by Pierre Louis de Assis.

Since the photonic wire has two orthogonal mode, and it has been mentioned before that depending on the QD location within the wire, it can have better coupling for one mode than the other. Therefore, it is important to check the coupling with both the modes. Figure 5.2(a) and 5.2(b) shows the PL spectrum for photonic wire with top facet diameter equal to 1.86 μm with and without the mechanical excitation along horizontal and vertical mode respectively. The coupling values for different lines are given in the table 5.2.

	Horizontal coupling		Vertical coupling	
	$\frac{\partial\omega}{\partial x}$ (μeV/nm)	$g_{m_x}/2\pi$ (kHz)	$\frac{\partial\omega}{\partial y}$ (μeV/nm)	$g_{m_y}/2\pi$ (kHz)
QD 1	11.9	75.4	6.0	42.4
QD 2	15.9	101.3	8.0	56.5
QD 3	18.8	119.1	5.1	36.0

Table 5.2: Hybrid coupling for different QD lines in the photonic wire with top diameter 1.86 μm along the horizontal and vertical mode.

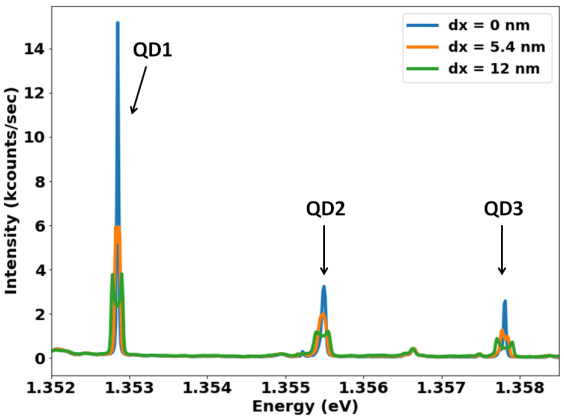

(a) Photonic wire is excited along horizontal mode.

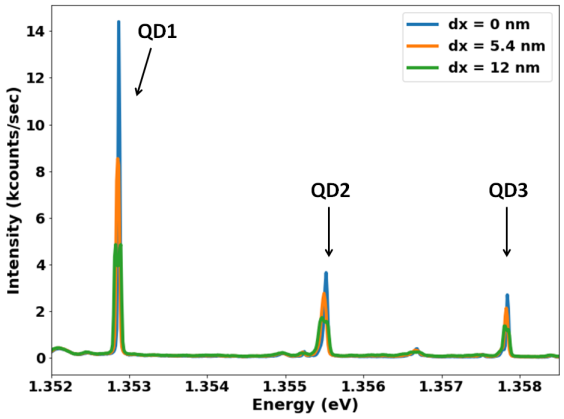

(b) Photonic wire is excited along vertical mode.

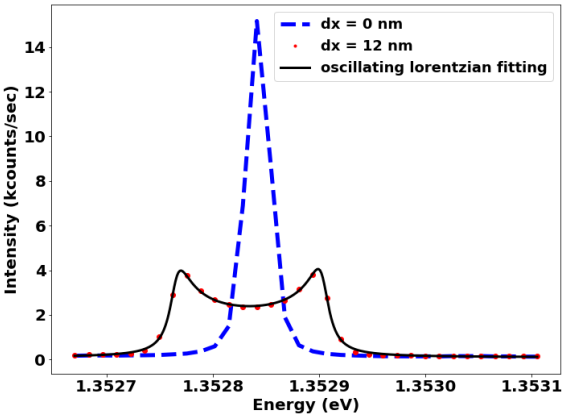

(c) Zoom in on the PL spectrum of QD1, without excitation (blue trace) and when excited along the horizontal mode (red trace).

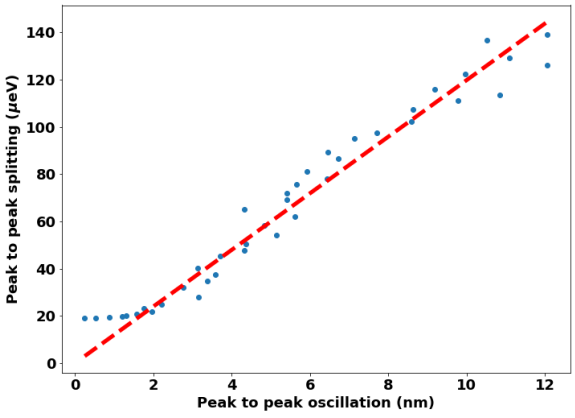

(d) Spectral broadening plotted versus the oscillation amplitude for QD1 when the wire is excited along the horizontal mode.

Figure 5.2: Photoluminescence (PL) spectrum of different QDs embedded in the photonic wire with top diameter of 1.86 μm, (blue trace) without mechanical excitation and (orange and green trace) when excited along (a) Horizontal mode and (b) Vertical mode. (c) Zoom-in on the PL spectrum of QD1 when excited along the horizontal mode. Black trace is the fit using eq. 5.1. (d) Measured spectral broadening versus oscillation amplitude of the photonic wire top facet when the wire is excited along the horizontal mode.

Thus, for this photonic wire, the best line in terms of the coupling is QD3. However, it is not possible to excite it resonantly. Similar was the case with the second best line i.e. QD2. Therefore, we proceeded with QD1 line which can be excited resonantly as shown in figure 3.19 (Chapter 3) and has reasonable coupling with both the modes. Thus, QD1 could be used to proceed with the Quantum Hammer experiments. Results presented later in this chapter are from the experiments performed on this line. We found other lines in different photonic wires as well but the coupling is either same or small, so we did not

proceed with them.

5.3 Expected signal to noise ratio

As mentioned in Chapter 2, the amplitude of quantum hammer effect induced motion in the photonic wire can be estimated from the mechanical properties of the photonic wire namely, mechanical resonance frequency Ω_m, Quality factor Q and zero point fluctuations x_{ZPF} together with the hybrid coupling g_m. Moreover, when comparing the quantum hammer induced motion amplitude to the Brownian motion amplitude for the parameters reported in [35], we found that the hammer induced motion is about five times larger than the Brownian motion amplitude. Different QDs in different photonic wires have been investigated for the estimation of g_m and results for the dots in one of the photonic wire are presented in the previous section. Measured g_m values are on the order of 10 less than what is reported in [35]. The reduction in coupling could be related to the changes in the structure happened when the sample was processed for the removal of the anti reflection layer during the beginning of this project. Moreover, it is important to note that for the quantum hammer experiment, we need the QD with good optical coupling as well (to excite the dot resonantly). Thus, the good candidate, in our case, will be the line located not very far from the center axis of the wire, in order to have both optical and coupling. Recalling eq. 2.24,

$$x_{QH} = \frac{2}{\pi} Q x_{zpf} \frac{g_m}{\Omega_m} \tag{5.2}$$

These reduced values of g_m will directly result in the reduced induced motion amplitude x_{QH}. For the photonic wire studied in this work, the resonance frequency of the vertical mode is $\Omega_m/2\pi = 330$ kHz with a Quality factor $Q = 2000$, degrading from 2750 to 1500 during the experimental run over the week, and $x_{ZPF} = 29$ fm at $T = 5$ K. Therefore, the expected amplitude is equal to ~ 5 pm for QD1 with coupling $g_m/2\pi = 42$ kHz with the vertical mode (see table 5.2). In order to compare with the variance of the Brownian motion, lets say x_{QH}^{rms} is the root mean value of the amplitude and is equal to ~ 3.5 pm . Variance of the Brownian motion amplitude $\delta\, x_{th}$ is given by (recall eq. 4.28)

$$\delta x_{th} = \sqrt{\frac{k_B T}{m_{eff} \Omega_m^2}} \tag{5.3}$$

Therefore,

$$\begin{aligned} \frac{x_{QH}^{rms}}{\delta x_{th}} &\approx \frac{1}{\sqrt{2}}\frac{2}{\pi} Q \frac{g_m}{\Omega_m}\sqrt{\frac{\hbar\Omega_m}{2k_B T}} \\ \frac{x_{QH}^{rms}}{\delta x_{th}} &\approx 0.15 \end{aligned} \tag{5.4}$$

i.e. the expected hammer induced motion amplitude is approximately seven times smaller than the Brownian motion amplitude and will be buried under it. The factor $1/\sqrt{2}$ in front is to convert the x_{QH} amplitude to the root mean value in order to compare it with the Brownian motion variance.

In addition to this theoretical prediction, we have to also take into account the experimental parameters which will impact x_{QH}. One such parameter is the broadening of the QD emission. The broadening in a QD includes homogeneous and inhomogeneous broadening (see section 3.3.2 for details). In addition to the broadening, other effect is blinking of the QD line, i.e. switching between the bright and dark states. Blinking can be attributed to the charging or activation of trapping process in nearby impurities. Due to this blinking effect, the overall resonant emission signal reduces. The typical time scale for the QD to be in bright or 'On' state is 10 % and dark or 'Off' state is 90 % [40]. Thus, the efficiency to excite the QD will be only 10 %. As a result, the expected quantum hammer signal will be reduced by a factor 10, resulting in even lower signal to noise ratio (SNR). One strategy for detecting the signal with below unity SNR is averaging and will be discussed in next section.

5.3.1 Brownian motion noise averaging in coherent signal detection

As explained in the previous section, the expected hammer signal is approximately 70 times below the Brownian motion by taking the blinking effect into account, leading to signal to noise ratio (SNR) much below unity. In order to extract the signal of interest, which is the quantum hammer induced motion, out of the noise one possible way is to average out the incoherent noises. This is valid in our case because the signal of interest is a coherent signal, expected to occur at the optical QD resonance i.e. when the QD is excited. All the other signals present, namely, Brownian motion, and photothermal response are not coherent to the optical resonance and thus could be averaged out. In this section, we will evaluate the minimum integration time required to average out the signal of interest, if it is limited by the Brownian motion (BM) noise. This section results from discussion and calculations by P. Verlot.

Let us note $X_{QH(t)} = x_{QH}\cos\Omega_m t$ a coherent motion of frequency $\Omega_m/2\pi$ to be detected. We assume the measurement to be primarily limited by the Brownian motion amplitude, $X_{th}(t) = x_{th,1}(t)\cos\Omega_m t + x_{th,2}(t)\sin\Omega_m t$, with $x_{th,1}$ and $x_{th,2}$ the quadratures of the thermal noise. The total signal, proportional to $X(t) = X_{QH}(t) + X_{th}(t)$, is assumed to be

demodulated at $\Omega_m/2\pi$, the slowly varying component X(t) of the resulting signal being retained:

$$X(t) = X_{th,1}(t) + X_{QH}(t) \tag{5.5}$$

We assume that reducing the impact of the thermal noise $X_{th,1}$ is performed by means of averaging. We subsequently define s(T) as a linear, unbiased estimator for the measurement of X_{QH}:

$$s(T) = \frac{1}{T}\int_0^T dtX(t), \tag{5.6}$$

with T the measurement averaging time. s(T) can be written as the sum of two contributions $s_{th}(T)$ and s_{QH} arising from the noise and signal, respectively:

$$\begin{aligned} s_{th}(T) &= \frac{1}{T}\int_0^T dTX_{th,1}(t), \\ s_{QH} &= X_{QH} \end{aligned} \tag{5.7}$$

The determination of minimal requirements for T requires defining a detection criterion. Let us assume that the detection is successful as soon as the dispersion of the estimator $\Delta s(T) = \sqrt{\Delta s^2(T)}$ is less than one fifth of the signal's expected value (also known as the 5-sigma criterion):

$$\begin{aligned} \Delta s(T) &\leq \frac{s_{QH}}{5} \\ &\leq \frac{X_{QH}}{5} \end{aligned} \tag{5.8}$$

The variance of s arises from that of s_{th}, whose mean value $\langle x_{th}\rangle$ is zero. One therefore has:

$$\Delta s^2(T) = \langle s^2(T)\rangle = \frac{1}{T^2}\int_0^T\int_0^T dt_1 dt_2 \langle X_{th,1}(t_1)X_{th,1}(t_2)\rangle$$

with $\langle ...\rangle$ denoting statistical averaging. The integrand in the above equation corresponds to the auto-correlation function of $X_{th,1}$. For Brownian motion, this auto-

correlation function is stationary and only depends on the time difference $t_2 - t_1$. Changing the variables t_1 and t_2 to $t_1' = t_1$ and $\tau = t_2 - t_1$, one straightly obtain:

$$\begin{aligned} \Delta s^2(T) &= \int_0^T \int_0^T dt_1' d\tau \langle X_{th,1}(0) X_{th,1}(\tau) \rangle \\ &= \frac{1}{T} \int_0^T d\tau \langle X_{th,1}(0) X_{th,1}(\tau) \rangle \end{aligned} \tag{5.9}$$

The auto-correlation function of any given quadrature of the Brownian motion can be shown to have the following expression:

$$\langle X_{th,1}(0) X_{th,1}(\tau) \rangle = \Delta x_{th}^2 \times e^{-\Gamma_m |\tau|/2}, \tag{5.10}$$

with Γ_m the mechanical damping rate and Δx_{th}^2 the Brownian motion variance. Using this result, Eq. 5.9 yields to:

$$\Delta s^2(T) = \frac{1}{T} \left[\frac{2\Delta x_{th}^2}{\Gamma_m} e^{-\Gamma_m t/2} \right]_0^T = \frac{2\Delta x_{th}^2 \left(1 - e^{-\Gamma_m T/2}\right)}{\Gamma_m T}$$

Assuming that averaging is required over a time much larger than the mechanical coherence time ($T \gg 1/\Gamma_m$), the 5-sigma criterion (Eq.5.8) yields to:

$$T \geq \frac{50}{\Gamma_m} \times \frac{1}{SNR}, \tag{5.11}$$

with $SNR = \dfrac{x_{QH}^2}{x_{th}^2}$ the signal-to-noise ratio. Eq. 5.11 shows that the minimum required averaging time is inversely proportional to the signal to noise ratio. In particular, it shows that for a SNR of 1, successful detection is achieved after averaging for a minimal duration representing 50 mechanical coherence times.

As shown in the previous section, (Eq. 5.4), $\dfrac{x_{QH}}{x_{th}} \approx 0.15$, giving $SNR \approx 0.04$. Moreover, taking the blinking effect into account (i.e. 10 % ON and 90 % OFF), SNR will become 0.000225. Therefore, for successful detection, we have to average for at least 30 minutes. However, as we will see later that in the experiment we are not limited by the Brownian motion. Detailed description of other technical noises and drifts limiting the hammer measurements is given in section 5.4.3.

5.3.2 Stability of the setup

There are various challenges which could hinder the successful and efficient realization of quantum hammer effect experiment. The source of these challenges are drifts in mechanical and optical resonance frequency, positional drifts and power fluctuations which will induce fluctuations in the measured signal. This section will present the steps taken to overcome these challenges in order to reduce the inaccuracy in the measurements.

5.3.2.1 Power drifts and fluctuations

Laser power fluctuations can reduce the performance of power sensitive experiments. Power fluctuations originates from two sources as mentioned earlier in Chapter 4. First, caused by the Poisson distribution of photons in the beam, known as the shot noise and varies as square root of the power. Second is known as technical noise, which varies linearly with power. Here, we are trying to address the challenge of reducing the fluctuations due to latter source.

There are 4 different lasers in the experiment. Fluctuations in probe laser will impact the detection sensitivity vector values which in turn will impact the measured amplitude value. On the other hand, fluctuations in resonant laser power will impact the photothermal motion induced due to the presence of the modulated resonant laser. Moreover, the fluctuations in locking laser power, which is mainly used for position locking (refer section 5.3.2.2), will affect the feedback loop employed for position stabilization. Therefore, it is important to stabilize the power of these lasers. One approach, which can be employed to tackle this issue, is to add a feedback control loop on the diode current (for probe laser and locking laser) [121], or on the acousto-optic modulator driving voltage (for resonant laser) [122]. This can be achieved easily by using a PID from HF2LI Zürich Instrument box or Red-pitaya box.

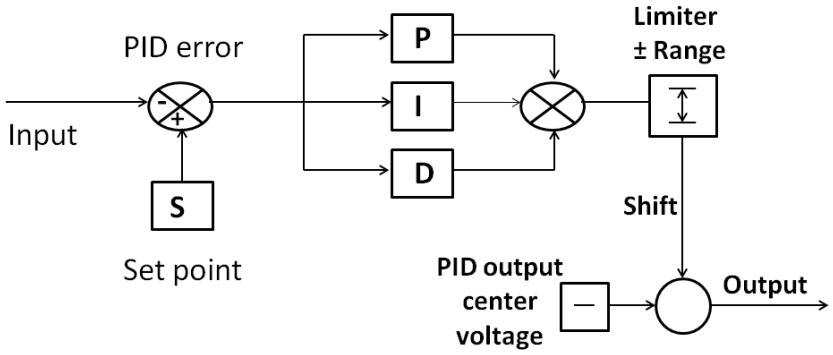

Figure 5.3: Block diagram of PID controller of HF2LI Zürich Instruments box. Figure adapted from [123].

As already mentioned that the expected hammer force induced motion amplitude is weak and buried inside the noise. Power fluctuations in different lasers will add up to the noise making the detection of the expected signal more difficult. Therefore, with the feedback loop we are aiming at locking the laser power and reducing the fluctuations on a "seconds" time scale. Figure 5.3, shows the block diagram of the PID controller employed in HF2LI box. As the name suggests it has three basic coefficients: Proportional, Integral and Derivative which are varied to get the optimal response to minimize the error value e(t). Error value is the difference between the set point value and the applied input signal.

Next step is to choose the values for PID controller. Proportional or P-controller gives output which is proportional to error signal e(t). In other words, the resulting error e(t) is multiplied with proportional constant to get the output. This controller never reaches the steady state condition, therefore, it requires biasing or manual reset when used alone. Due to this limitation of P-controller, I-controller is needed when there exists an offset between the input variable and set point. I-controller integrates the error over a period of time until error value reaches to zero. Thus, the output value to the final control device will be the one at which error becomes zero. The derivative or D-controller causes the output to decrease if the input variable is increasing rapidly. Its response is proportional to the rate of change of error with respect to time, multiplied by derivative constant. Increasing the derivative time (T_d) parameter will cause the control system to react more strongly to changes in the error term and will increase the speed of the overall control system response.

In our setup, we use PI controller as we want to correct only for drifts on "seconds" time scale. The values of proportional coefficient is P = 1.0 (Hz/deg) and integration coefficient is I = 10^3 (Hz/deg/sec). The main advantage of this feedback loop is in the case of resonant laser. As mentioned in Chapter 3, resonant laser power changes over the sweep across the QD. This power change could be something from 20 to 40 % depending on the alignment and absolute energy of the laser. On setting the power stabilization loop we could reduce this power change to 1-5 %. This implies that there will be 1-5 % fluctuations on photothermally induced motion, if any, due to the presence of modulated resonant laser and it has to be taken into account while analyzing the final results. Similarly on probe laser and locking laser we have fluctuations on the order of 1-2 % after the stabilization, which means fluctuations on detection sensitivity value and position stabilization input signal respectively.

5.3.2.2 Position drift

Position of laser with respect to the top facet of the photonic wire changes slowly with time because of various reasons. As mentioned in chapter 4 the nanomax stage holding the microscope objective has open loop piezo actuators which results in the positional drifts in the sample position. Moreover the translation stage holding the sample could also induce

some drifts due to the strain exerted by the helium transfer tube. In addition to this the creeps in the optical elements would result in the laser pointing drifts. Probe laser position with respect to the photonic wire top facet is very important as discussed in the previous chapter. These positional drifts will change the detection sensitivity vector values and impact the measurement accuracy. It will also reduce the excitation efficiency if the resonant laser is not positioned at the center of the top facet. Therefore, the alignment of the lasers with respect to the top facet is critical for efficient measurement.

The simplest way to overcome this issue is to position a laser on the center of the photonic wire top facet and reflect it onto a quadrant photodiode (QPD) (see section 4.3.1.5 for details on QPD). The signal from the QPD is used as an input to the feedback loop which will lock the signal at the set point by adjusting the PID controller values as discussed in the previous section. Although, to be able to monitor the drift in both horizontal (H) and vertical (V) direction, it is necessary to have the photodiode with which we are sensitive to the drifts in both directions. Therefore, we used quadrant photodiode (QPD) for this purpose. As shown in the experimental setup discussed in section 5.1, we used the locking laser for this purpose. This laser is at $\lambda = 975$ nm, therefore, it can be easily separated from the spectrometer path using wavelength sensitive optics. We used Dichroic beam splitter for this purpose which separates light on the basis of wavelength and polarization. Moreover, the average locking laser power used during the experiment is about 100 μW (measured before the objective), which is reasonable to track the position without affecting the QD emission. The laser is focused on the center of the photonic wire top facet and the reflected signal is directed towards the QPD after getting transmitted through Dichroic beam splitter (see figure 5.1). The two difference signals from QPD is then used to monitor the drifts along H and V directions by setting two PID control loops respectively. The output from the PID loop is applied to the X and Z channel of piezo controller controlling the X and Z axis of Nanomax stage (Y axis is the focal axis) to compensate for any drifts.

To set the PID controller for position locking, we used a Red Pitaya box as with HF2LI box we have limited number of inputs and outputs which are already employed for other purposes. Red Pitaya box has 2 RF inputs and outputs and 50 MHz bandwidth making it suitable for various applications. The output range for the Red Pitaya box is $\pm$ 1 V. However, the piezo controller can not take negative voltage, therefore, the used output range is 0 to 1 V. Initially, the output voltage on both the axis is set to 0.5 V. With the help of this feedback loop we are able to correct for the drifts on the order of seconds time scale. Figure 5.4 shows the output of the PID controllers corresponding to the position drifts for both horizontal and vertical axis respectively. The final value of parameters used is P = 0 (Hz/deg) and I = 10 (Hz/deg/sec). The output of the PID controllers is applied to the piezo controller which controls the nanomax stage holding the microscopic objective. 1 mV fluctuation in the output voltage corresponds to 2 nm of fluctuation in the position. This calibration is obtained by moving the laser on the sample for the full piezo controller range (0-75 V) and measuring the change in the position of the laser on sample. For these measurements, the laser is moved in between the photonic wires so that

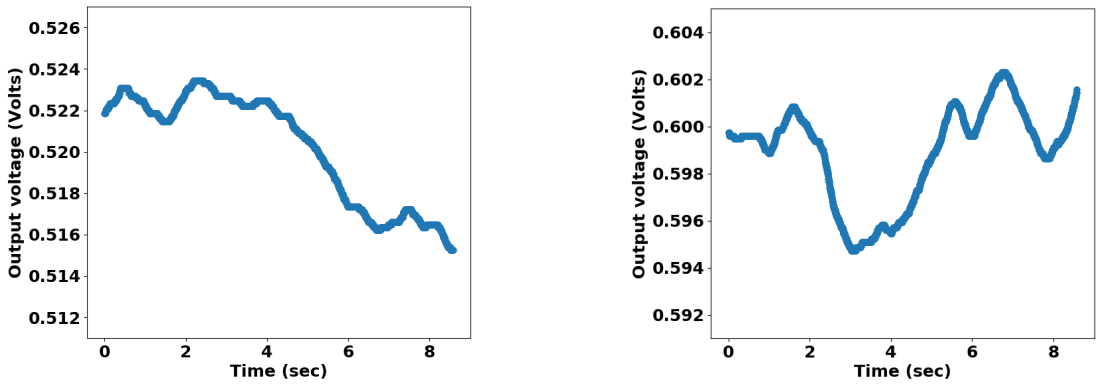

(a) (b)

Figure 5.4: Output voltage of the PID controller corresponding to the position drifts for (a) Horizontal axis (b) Vertical axis. These 10 mV fluctuations in the output voltage corresponds to $\approx$ 20 nm of position drifts. See text for this calibration.

the distance between the wires can be used a reference and we get the value of 0.25 µm/V (Note: here 1 V is on the piezo controller). The output range of 1 V from Red Pitaya box corresponds to roughly 9 V on the piezo axis. Thus, we are limited to a range of 2.3 µm , corresponding to the range of the Red Pitaya output. Position drifts of more than 2.3 µm will require manual realignment.

5.3.2.3 Mechanical resonance drift

As mentioned earlier the mechanical and optical resonance frequency drifts slowly with time. Tracking the mechanical resonance frequency is really important for the accuracy of the measurements. This is achieved using Phase-Locked loop (PLL) technique.

As the name suggests, in PLL, the key operation is the ability to detect the phase difference between the applied input signal and the reference phase value. This difference in the phase is then used to control the frequency of the loop. Figure 5.5 shows the frequency response of the phase of the mechanical oscillator. The phase value corresponding to the resonance frequency is given as the set point of the PLL loop. The PLL loop then compares the input phase (which is also the phase value at the mechanical resonance frequency) with the given set point. For any deviation from the set point, PLL acts on the frequency using the slope of phase to frequency i.e. $\frac{\mathrm{d}\theta}{\mathrm{d}\Omega}$. Thus, the knowledge of this slope is really important to convert back later any change in frequency to the phase change. This slope is linear within the linewidth of the oscillator Γ_m. This defines the range relative to the center frequency (or resonance frequency) for the proper functioning of the PLL loop. The next step is to find the suitable feedback parameters (P,I). This is done while monitoring the

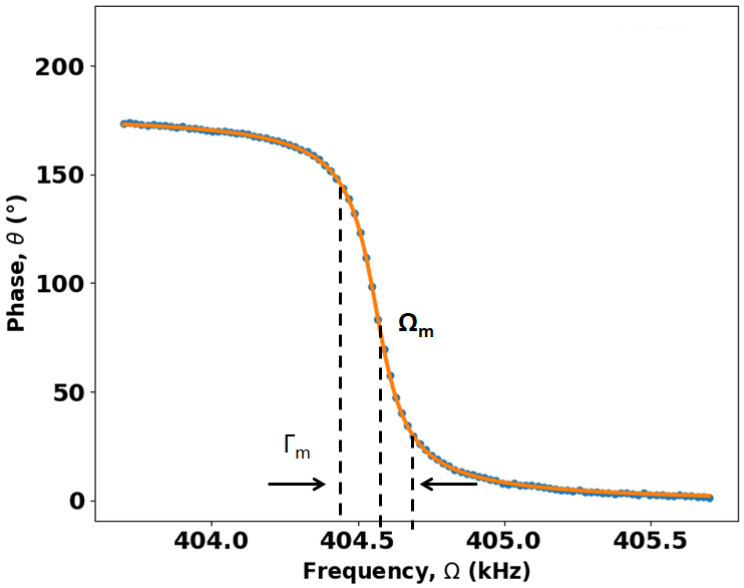

Figure 5.5: Frequency response of the mechanical resonance phase.

error on the phase and frequency signals with time with an aim to reduce this error. The final parameters are P = 50 (Hz/deg) and I = 100 (Hz/deg/sec), which allows us to track the mechanical resonance frequency upto 6 kHz range. The average drift in Ω_m is about 4 Hz/min. Thus, once set, PLL will track the frequency for up to one day, if everything stays stable. This allows us to run the experiment overnight.

5.4 Quantum Hammer effect: Experimental procedure and results

5.4.1 Measurement scheme

All the necessary tools required to realize the hammer effect, namely the combined resonance emission detection and motion detection experimental setups, and a candidate with reasonable coupling are now available. As shown in figure 5.6, the basic idea is to excite the QD using a laser, which is modulated at the mechanical resonance frequency, and measure the effect on the photonic wire motion when the dot is excited. Therefore, for successful measurement, knowledge of both optical and mechanical resonance is important. However, as mentioned earlier in Chapter 3 and 4, both optical and mechanical resonance frequencies are drifting with time. Keeping this in mind, the following experimental scheme is proposed and pursued in this work.

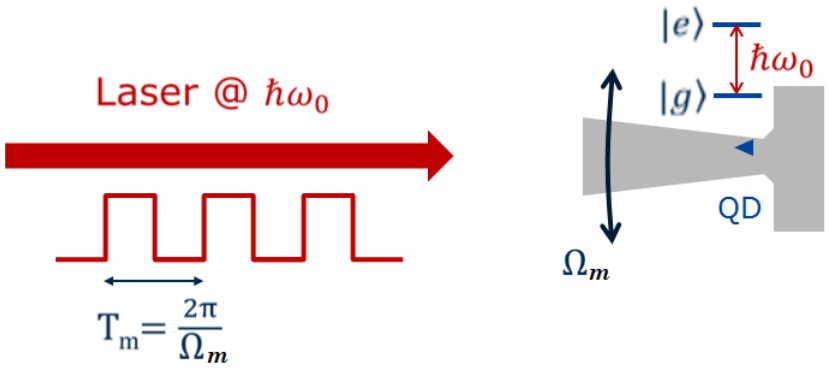

Figure 5.6: Sketch demonstrating the excitation scheme employed in the realization of quantum hammer experiment.

Mechanical resonance frequency is tracked using a phase locked loop (PLL) as shown in the previous section 5.3.2.3. The problem of optical resonance drift can be resolved using the strategy, where we sweep over the QD resonance with the resonant laser modulated at the mechanical resonance frequency and simultaneously measuring the mechanical response at the mechanical frequency (locked by PLL), thereby allows us to perform the experiment at both mechanical and optical resonance. The expected signal is shown in figure 5.7. When the resonant laser (RL) is out of QD resonance, the measured mechanical amplitude corresponds to the expected photothermal motion amplitude at the working RL power, and the thermal motion. At optical resonance, we expect an ascent or descent (if out of phase) in the mechanical motion amplitude with respect to the photothermal (out of optical resonance) motion amplitude.

However, as mentioned before in section 5.3.1, in order to see the resulting hammer signal we need to average for at least 30 minutes. As mentioned in chapter 3, QD line suffers drift and fluctuations due to charges in the environment. As a result, the QD resonance position fluctuates continuously. Since, the hammer induced effect in the mechanical amplitude is a resonant effect and will be corresponding to the QD resonance. Therefore, in order to follow the optical resonance drifts, we make multiple 1 minute sweeps over QD resonance and record the mechanical amplitude at the resonance frequency for each sweep. This strategy is illustrated in figure 5.8, and it is evident that QD resonance is fluctuating from one sweep to another. Therefore before averaging the acquired sweeps, it is necessary to correct for the QD resonance drifts to avoid averaging out the hammer effect in the mechanical response. It is also important to note that once the QD line drifts out of the window, sweeping range of the RL has to be manually set again to cover the resonance for each sweep and acquire meaningful data. The following section will give the description of how the simultaneous measurement of the resonant emission and mechanical response of the photonic wire is performed using the Zürich instruments box HF2LI.

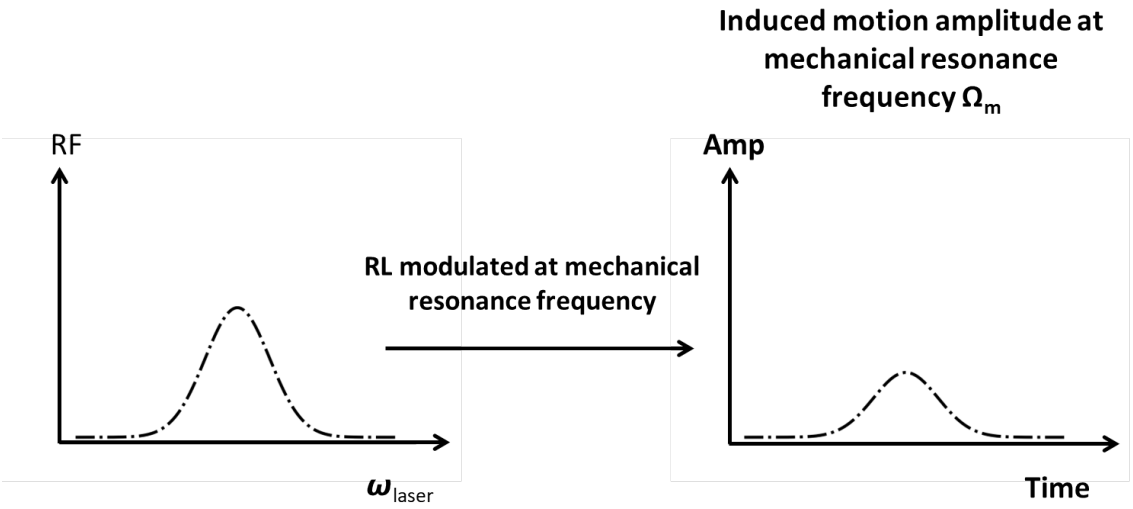

Figure 5.7: Sketch depicting experimental strategy to make sweep over the QD resonance and simultaneous measurement of induced mechanical motion at the mechanical resonance frequency.

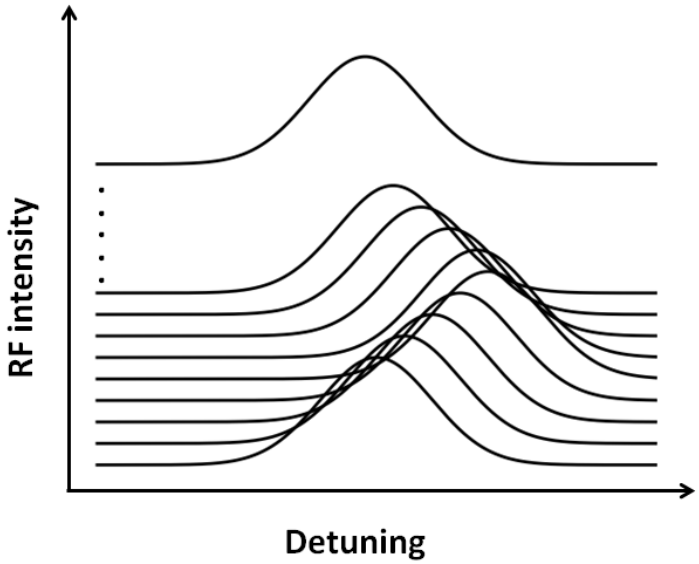

Figure 5.8: Revised experimental scheme: Multiple one minute sweeps over the QD resonance and simultaneous measurement of induced mechanical motion at the mechanical resonance frequency.

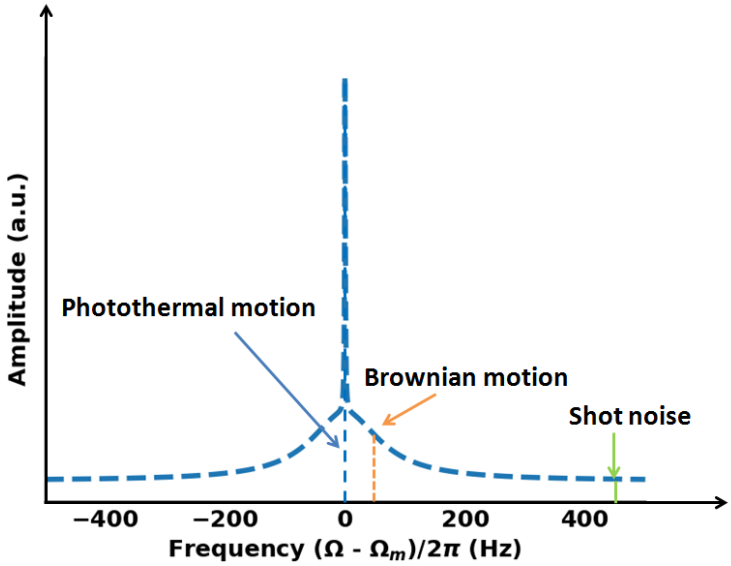

Figure 5.9: Measurement using HF2LI box using MOD function: Simultaneous measurement at mechanical resonance frequency for photothermal motion, at 45 Hz on the side for Brownian motion (BM) measurement and about 500 Hz on the side for shot noise measurement.

5.4.2 Measurement using HF2LI box

The browser based LabOne user interface in each device from the Zürich instruments allows us to perform multiple operations simultaneously. As already mentioned in the previous chapter, it performs the role of both Spectrum analyzer and vector network analyzer with Spectrum and Sweeper tab respectively. For the Quantum Hammer experiment we use the sweeper tab to sweep the RL over the QD resonance. Resonant emission (RE) signal is detected on the phonon side band using APD as described in Chapter 3. The signal from APD is connected to one of the inputs of the HF2LI box and on the other input we have the signal from the motion detection APD containing the mechanical response. Thus, it is possible to measure the QD emission and motion of the wire simultaneously.

HF2LI box has the possibility to perform the measurement at multiple modulation frequencies simultaneously using the "MOD" interface. It has two MOD modules, each engaging three demodulators. It allows us to set the frequency corresponding to the demodulator 2 and 3 with respect to the first one (which is fixed by the PLL at the mechanical resonance frequency $\Omega_m/2\pi$). We used this MOD tab to set the frequency of demodulator 2 (and 3) at 45 Hz (and 500 Hz) away from the resonance frequency to have the information about the Brownian motion (BM) amplitude (and shot noise level) during the measurement as shown in figure 5.9. Frequency for Brownian motion is chosen such that a) it is not too close to the resonance frequency to be influenced by the photothermal motion, b) it should be smaller than the width of the BM peak, and c) it is not chosen equal to 50 Hz

as this is the typical frequency of the power cables and hence it could pick up 50 Hz noises. Therefore, the frequency is chosen to be around 45 Hz. For the shot noise level, one can choose any frequency sufficiently away from the resonance frequency. In our experiment, we chose 500 Hz.

Once we set the frequency at which we want to measure in MOD tab, we can simply choose the different parameters (such as amplitude r, phase θ, quadratures X and Y, frequency etc.) to be recorded corresponding to each demodulator in the sweeper tab. Thus, when the sweeper will sweep the RL over the QD resonance, it will record the RF signal from the APD, photothermal motion at the mechanical resonance frequency $\Omega_m/2\pi$, BM at $\Omega_m/2\pi$ + 45 Hz and shot noise level at $\Omega_m/2\pi$ + 500 Hz simultaneously.

This possibility of simultaneous measurement of the photothermal motion, BM and shot noise allows us to evaluate the noise associated with each of them in the experiment as a function of the number of acquired sweeps.

5.4.3 Noise evolution

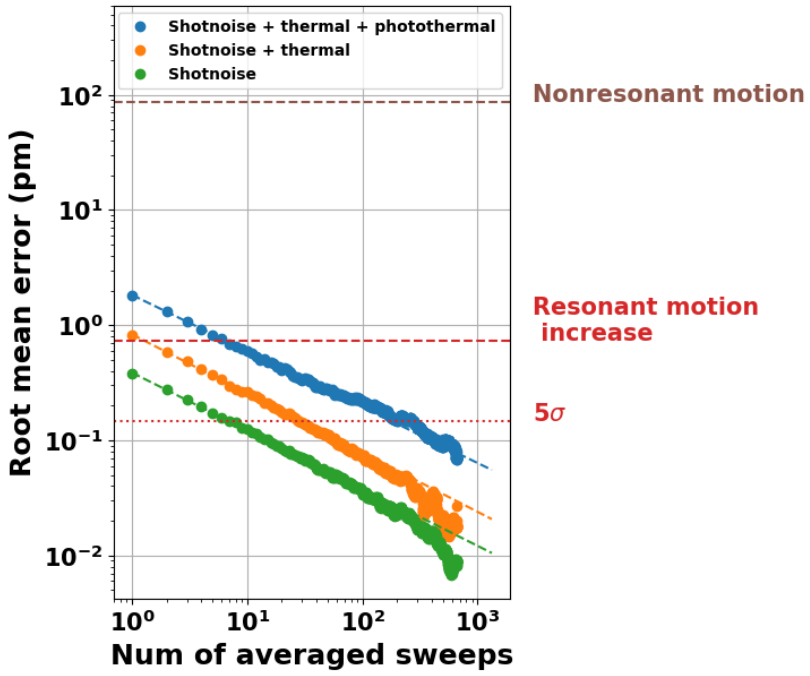

Figure 5.10: Noise evaluation of different experimental noises as a function of number of averaged sweeps. To have signal to noise ratio equal to 5 σ, the required number of sweeps to be averaged is about 240. This means that we need to do the measurements for at least 4 hours.

It is clear from section 5.3, that the signal of interest, i.e. the motion induced as a result of the quantum hammer effect, is a weak signal (1/70 of the BM amplitude; with blinking effect). Calculations shown in section 5.3.1 shows that we need to integrate for at least 30 minutes in order to reduce the noise associated with the BM, which is obscuring the signal of interest. However, from the experimental results performed using the strategy presented in the last two sections, we found that the measurement time is much longer than 30 minutes to extract the signal out of noise. Therefore, it is important to evaluate different experimental noises and their evolution as a function of number of sweeps.

As presented in the previous section, with the MOD tab of HF2LI box, it is possible to measure the photothermal motion, Brownian motion, and shot noise level simultaneously for each sweep point as the RL is sweeped over the QD resonance. In order to predict the uncertainty of a single sweep point, the root mean error is calculated. The evolution of uncertainty is derived, by averaging an increasing number of sweeps, and calculating the standard deviation of all the averaged points at same detuning. The mean uncertainty from all detunings is plotted against the number of averaged sweeps as shown in figure 5.10. The non-resonant motion, which corresponds to the photothermal motion induced by the modulated RL, is about 85 pm (when RL is out of QD resonance). Quantum hammer force induced motion, marked as resonant motion increase, is found to be around 0.7 pm. The evolution of uncertainty from the experimental data validates the theoretical calculation shown in the section 5.3.1 that we need approximately 30 minutes of averaged data to reach 5σ level, if the limiting noise is associated with the BM. However, we are limited by the photothermal noise caused by the resonant laser intensity noise and to reach 5σ level we need to average approximately 240 sweeps i.e. $\approx$ 4 hours of acquired data.

In addition to the photothermal noise, there are technical noises associated with the fluctuations in the laser powers, position of the wire with respect to the lasers, drifts in the mechanical resonance frequency and some other unknown sources. Despite of the stabilization of known fluctuations and drifts as presented in section 5.3.2, there is still some influence on the measurement and it increases the measurement time from 4 hours to more than 15 hours for the detection of hammer induced signal.

5.5 Experimental results

This section will present the experimental results for the quantum hammer effect achieved with the hybrid system investigated in this work. Different laser powers are as follows: Probe laser = 100 µW, resonant laser = 150 nW , non-resonant laser = 150 nW and locking laser = 100 µW as measured before the objective. As pointed out so far, the expected signal is very weak and buried under the measurement and other technical noises. Therefore, we had to acquire hours of data to average out the signal of interest from all the noises. However, this is not an easy task considering the unstability of the setup due to

various controllable and uncontrollable drifts. Nevertheless, we managed to acquire data from approximately 20 hours (not continuous of course) in multiple blocks of few hours each. Before, presenting the final result it is however important to present the steps taken to correct for different kinds of drifts present in the measurement before taking the average of the acquired data.

5.5.1 Data analysis

5.5.1.1 Long term drifts

Since the measurement time scale is on the order of few hours, the setup is susceptible to some drifts in the acquired data. Some of the sources of this drifts are as follows: a) change in the focus on the wire (focusing distance is not controlled by the feedback loop set on the position stabilization 5.3.2.2) will result in the change of laser powers in the trumpet. As mentioned earlier change in the probe laser position will affect the detection sensitivity, and resonant laser will impact the QD emission signal, b) drift in the relative position of locking laser with other lasers because of the creep in the optical components in the setup will also affect the relative position of other lasers with respect to the wire, c) fluctuations in the temperature and presence of ice on the sample can also induce some drifts.

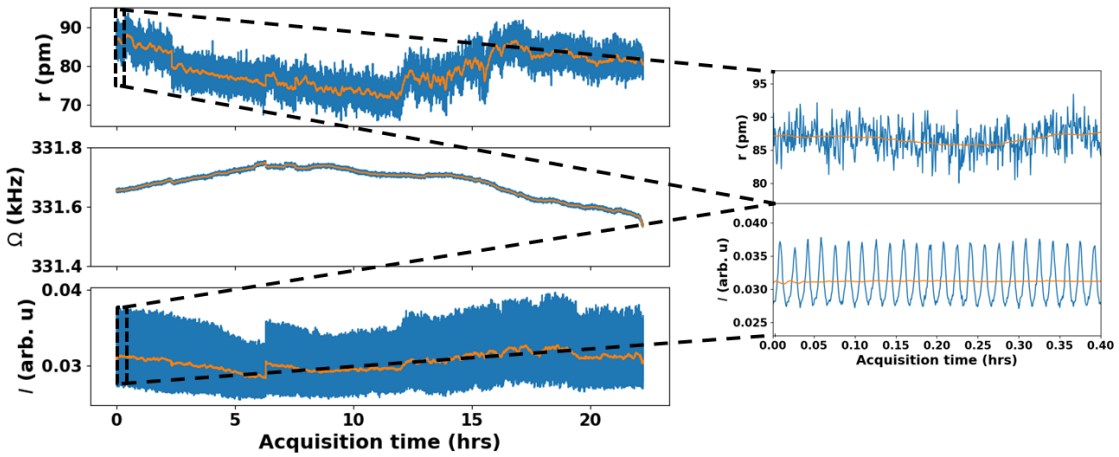

Figure 5.11: Creep in optical components, mechanical screws, temperature changes etc leads to long term drift in the acquired data. Figure on the left shows the variation of the mechanical motion, mechanical resonance frequency, and RE intensity measured at phonon side band as a function of time (blue trace). All the acquired sweeps are plotted in continuation to monitor the long term drifts. Figure on the right is the zoom-in on the dashed box to show the first 24 sweeps. Orange line is the running average of the continuously acquired data. Different laser powers are as follows: Probe laser = 100 µW, resonant laser = 150 nW , non-resonant laser = 150 nW and locking laser = 100 µW.

Figure 5.11, shows the variation of the data over time. In this figure, I have plotted (in blue) all the acquired resonance sweeps and corresponding mechanical motion, and mechanical resonance frequency. It is more evident from the zoom-in image on the right, which shows the first 24 sweeps. Each peak in the bottom trace of the zoom-in image corresponds to the RE spectra in one sweep. Each sweep takes approximately 1 minute. The abrupt jump in data on the left, corresponds to the start of the new block after realignment. One block is defined by the one sweep range of RL. Orange line is the running average of continuously acquired data. This deviation is compensated by **time-dependent correction:** each data point is divided by the ratio of drift average (running average over consecutive points, window centered on data point) and data set average (average over all data points). To avoid in-continuities after realignment steps, block-wise analysis is done.

5.5.1.2 Short term changes

A) **Resonant laser power change:**

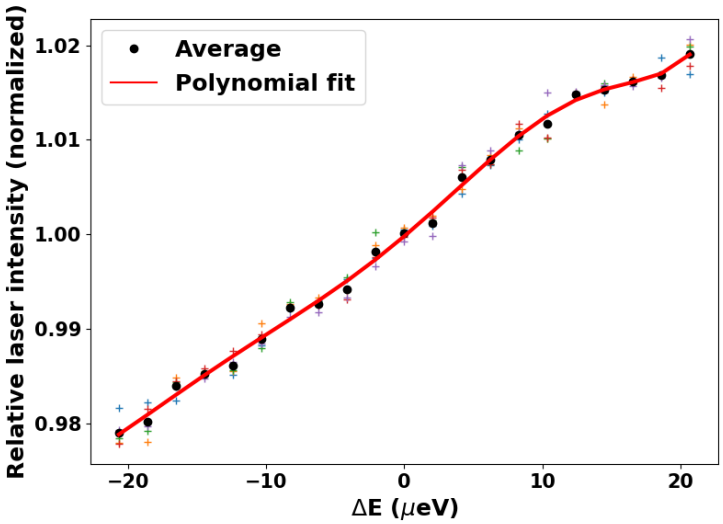

Figure 5.12: Resonant laser (RL) power calibration: Five calibration traces of RL power as a function of detuning taken before the first measurement block. Black circles shows the average power change and red line is the polynomial fit. Resonant laser power = 150 nW (measured before the objective).

In addition to the long term drifts presented in the previous section, there are also some short term changes to be taken into consideration. First is the change in the resonant laser (RL) power depending on the detuning in spite of the power stabilization. This change will directly impact the photothermal motion amplitude. As shown in chapter 4, photothermal motion varies linearly with the RL power. Therefore if we know the change in the power we can compensate it from the acquired

data. The observed change in the power in the sweep range varies from 1 to 5 % depending on the absolute energy (or wavelength) of the RL. Moreover, this change is not necessarily linear over the sweep range. Therefore, before the start of each measurement block we record the RL power as a function of the detuning. We take 5 such traces, which are then averaged and fitted with a polynomial function to find the relative change in the RL power for that block. One measurement block corresponds to the set of consecutive sweeps with same RL sweep range.

Figure 5.12 shows the normalized relative change in the RL power as a function of detuning for the first measurement block of the data shown in figure 5.11. The change in the power is about 2 %. However, this 2 % change is of the order of the noise in the measured photothermal amplitude. Therefore, its effect is not evident in the zoom-in figure 5.11. But, if it is not compensated we would then see a background slope (symmetric or asymmetric) on the final averaged data depending on the variation of the RL power. Therefore, it is important to correct for the RL power change for each sweep data.

B) **Spectral Wandering:**

Second and most important is the jitter and drift in the quantum dot optical resonance caused by charges in the environment. Since, the quantum hammer effect is a resonant effect, it is expected to occur at the QD resonance. Thus, for different sweeps, hammer effect induced motion will be at different detunings. Left plot of the figure 5.13 depicts spectral wandering. Each horizontal line is one sweep over the QD resonance and it is evident that QD resonance shifts from one sweep to another. Therefore, it is crucial to correct for this shifts in the QD resonance before averaging the motion data.

For time scales slower than the sweep time this shifts can be monitored and corrected. To precisely determine the position along the sweep axis, a Gaussian peak is fitted to all RE sweeps. Sweeps where fitting is not possible or where the peak position is outside a certain range are discarded. From the Gaussian fit parameters, we get the value of detuning corresponding to the optical resonance for each sweep. The sweeps are then shifted, such that the points corresponding to the maximum are at zero detuning as shown in the right plot of the figure 5.13. It is important to note that, the shift derived from the optical resonance is equally applied to the other measured quantities as well such as motion amplitude. Thus, we can extract out the effect resonant with the optical resonance from the other non-resonant effect by finally taking the average of the data. The final results are presented in the following section.

5.5.2 Observation of Quantum Hammer effect

After correcting for all the drifts as explained in the previous section, the data can now finally be averaged to bring out the hammer induced signal, which is resonant with the

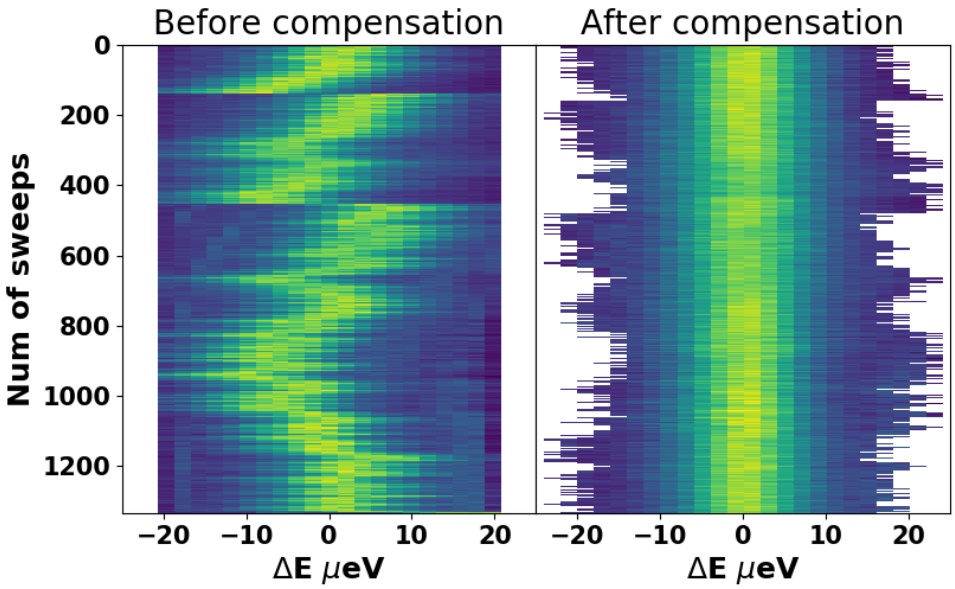

Figure 5.13: Plot showing the resonant emission intensity for all the acquired sweeps (along Y axis) as a function of detuning (along x axis). Left plot clearly depicts the shift in QD optical resonance from one sweep to other. Plot on the right is after the QD resonance shift has been corrected and all the sweeps are shifted to align the QD resonance to zero detuning. Different laser powers are as follows: Probe laser = 100 μW, resonant laser = 150 nW , non-resonant laser = 150 nW and locking laser = 100 μW.

optical resonance, from the non-resonant photothermal motion. Figure 5.14 shows the averaged data corresponding to the QD resonance, mechanical motion amplitude, and mechanical resonance frequency respectively. A Gaussian fit (red line) to the RE data is equally applied to the mechanical amplitude and frequency, keeping the center and full width half maximum (FWHM) from the RE fit. It is evident that when the QD is excited (i.e. on resonance) we observe increase in the amplitude of the mechanical motion. This is a clear indication of the quantum hammer induced force. Moreover, this observation is supported by the mechanical frequency plot. Since, frequency is locked by the PLL, it should have remained constant if there is no phase change occurring when the RL is sweeped over the QD resonance. But, the observed change in the frequency, also corresponding to the optical resonance, clearly indicates the presence of some resonant phase shifts of the mechanical motion.

In order to estimate the phase shift induced by this resonant effect, which is hidden in the frequency response, the original phase is recovered and plotted in the complex plane as shown in figure 5.15. As depicted on the right side figure, blue dashed line is the photothermal response which is delayed by 35° with respect to phase of the resonant laser modulation at mechanical resonance frequency. The hammer effect is expected to be in phase with the laser (small orange line), therefore at optical resonance, the resulting

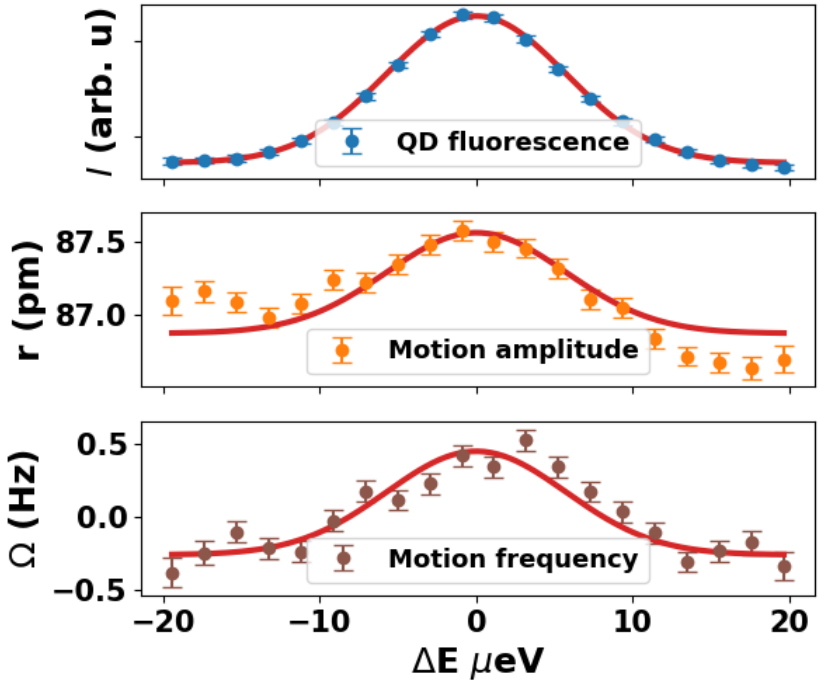

Figure 5.14: Final averaged plot depicting the presence of the quantum hammer force corresponding to the QD resonance. The three plots shows phonon sideband QD resonance, mechanical motion root mean amplitude (r^{rms}), and mechanical resonance frequency (locked by PLL) as a function of resonant laser detuning. Different laser powers are as follows: Probe laser = 100 μW, resonant laser = 150 nW , non-resonant laser = 150 nW and locking laser = 100 μW.

response is given by green line. This is consistent with what we obtained experimentally as shown on the main plot. When the motion vector is plotted in the Fresnel plane, the points corresponding to the data of motion amplitude in figure 5.14 are shown in blue in figure 5.15, locked to a phase of 35 °. For each data point, the frequency shift (from figure 5.14 bottom plot) can be converted to the phase shift knowing the phase slope, $\frac{d\theta}{d\Omega}$, at the mechanical resonance. This is plotted in orange color, which corresponds to the motion vector if the PLL would have been switched off. The vertical orientation of the orange points indicates that the motion induced by the quantum hammer effect is in phase with the phase of the modulated laser as expected. This observation of phase change when the dot is excited rules out the possibility of other physical effects such as resonant photothermal effect which should also have the phase delay of 35° like the non-resonant photothermal effect. Resonant photothermal effect means the photothermal effect occuring when the laser is in resonance with the QD, due to absorption of an additional photon not absorbed by the dot. We expect a phase delay of 35 ° for resonant photothermal effect because the observed phase delay is due to the thermal properties of the wire and is independent of the energy of the laser used as shown in section 4.5.3.

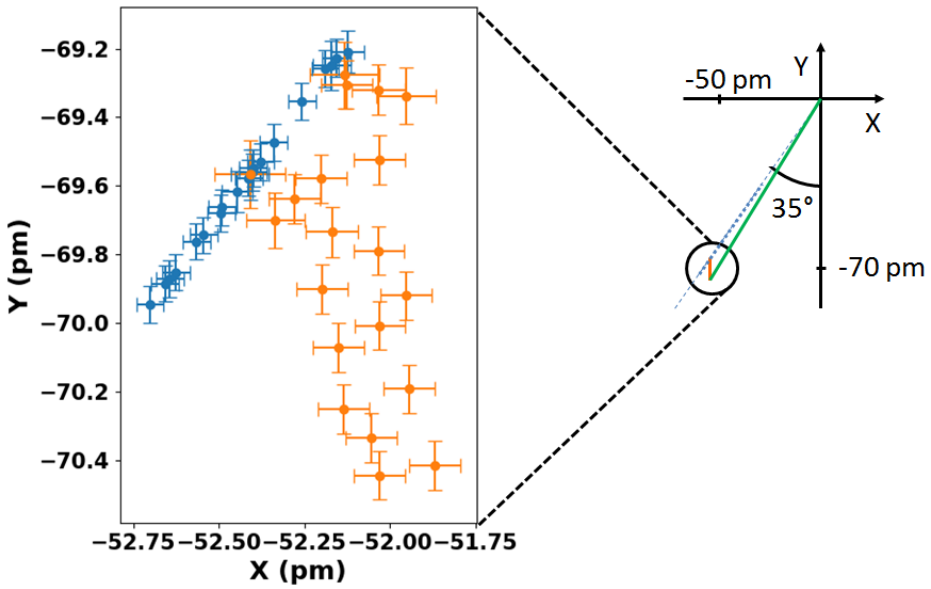

Figure 5.15: Phase information in the complex plane: Phase at resonance when fixed by PLL at $\approx 35°$ (blue points). The original phase is recovered (orange points) with the knowledge of phase slope at the mechanical resonance and is found to be same as the phase of the resonant modulation. The X and Y axis shows the rms values of the two quadratures.

Thus, at QD resonance, we observe a quantum hammer force which is in phase with the laser. The measured rms amplitude is approximately 0.85 pm on top of the 87 pm of photothermal motion. This rms amplitude is actually the amplitude of the Gaussian peak in the middle plot in figure 5.14 divided by $\cos(35°)$ corresponding to the fact that increase of the motion vector modulus results from the projection of the quantum hammer motion vector on the photothermal motion vector. This result gives the evidence of the first experimental realization of the quantum hammer effect and hence the primary goal defined at the beginning of this thesis is achieved. The following section will make a quick comparison of the measured and expected quantum hammer amplitude.

5.5.3 Comparison of the experimental and theoretical quantum hammer amplitude

The voltage measured on the Zürich box is the root mean square voltage V_{rms} by default. Therefore, the values presented in the previous section are the root mean square values both for the photothermal motion amplitude and quantum hammer amplitude. All the values for the amplitude presented in this section are the rms values. Therefore, we have

$$x_{QH_{exp.}} = 0.85 \quad \text{pm}, \tag{5.12}$$

From the theoretical calculations presented in section 5.3, we have the root mean value for the expected quantum hammer,

$$x_{QH_{theo.}} = 3.5 \quad \text{pm}, \tag{5.13}$$

This discrepancy in the measured and expected value could be attributed to the effective blinking with $\approx 25\%$ of "ON" periods as observed with similar QDs [40].

The calculation of the expected quantum hammer amplitude is done by taking the Comsol simulated values of m_{eff} and x_{ZPF} provided by Pierre Louis de Assis. However, recalling the discrepancy of factor 10 observed in the effective mass estimated from the experiment (Brownian motion) and Comsol simulation (see section 4.4.3 for details). One possible explanation for this discrepancy could be the error in the calibration of the measured signal i.e. error in detection sensitivity β_{HF} measured at the mechanical resonance frequency $\Omega_m = 330$ kHz. β_{HF} is related to β_{DC} via the gain ratio (eq. 4.19). In case of APD as a detector (4.3.1.5), this gain ratio is unity. Therefore, $\beta_{HF} = \beta_{DC}$, and the error could be attributed to the detection sensitivity measured experimentally. We can estimate the detection sensitivity from the measured Brownian Motion spectra given the effective mass of the photonic wire (which is known from the Comsol simulation and is equal to $\sim$ 30 pg). Lets call this estimated value as $\beta_{DC_{theo.}}$. Recalling eq.4.28 and using the relation $\beta = \frac{\delta V}{\delta x}$ we get,

$$\beta_{DC_{theo.}} = \beta_{HF_{theo.}} = \sqrt{\frac{m_{eff}\Omega_m^2(\delta V_{th})^2}{k_B T}}, \tag{5.14}$$

where δV_{th}^2 is the rms voltage measured on the Zürich box for the thermal motion.

On comparing $\beta_{DC_{theo.}}$ with the value measured experimentally (see section 4.4 for details on experimental measurement), we get

$$\frac{\beta_{DC_{theo.}}}{\beta_{DC_{exp.}}} = 2.5 \tag{5.15}$$

Let us see how this change in beta value will affect the theoretical and experimental values of the quantum hammer amplitude. Lets call them $x_{QH_{theo.2}}$ and $x_{QH_{exp.2}}$, where

2 denotes that it is calculated with $\beta_{DC_{theo.}}$, to avoid confusion with the previous values corresponding to beta value measured experimentally $\beta_{DC_{exp.}}$.

We know that $\delta x = \delta V/\beta$. Therefore, the measured amplitude is inversely proportional to β value i.e. $\delta x_{QH_{exp.}} \propto \frac{1}{\beta}$. Therefore, the ratio of experimentally measured rms amplitudes corresponding to $\beta_{DC_{exp.}}$ and $\beta_{DC_{theo.}}$ will be,

$$\frac{x_{QH_{exp.2}}}{x_{QH_{exp.}}} = \frac{\beta_{DC_{exp.}}}{\beta_{DC_{theo.}}} = \frac{1}{2.5}, \tag{5.16}$$

On the other hand, the expected value is estimated using the following equation (recall 2.24):

$$\begin{aligned} x_{QH_{theo.}} &= \frac{2}{\pi} Q x_{zpf} \frac{g_m}{\Omega_m}, \\ x_{QH_{theo.}} &\propto \frac{2}{\pi} Q x_{zpf}^2 \frac{1}{\Omega_m} \frac{\delta\omega}{\delta x} \end{aligned} \tag{5.17}$$

The theoretical value $x_{QH_{theo.}} + = 3.5$ pm was was obtained using $x_{zpf} = 29$ fm, taken from the Comsol simulations (section 5.2), therefore, β value will affect only the coupling term g_m which is inversely proportional to δx and hence directly proportional to β i.e. $\delta x_{QH_{theo.}} \propto \beta$. As a result, the ratio of expected rms amplitudes corresponding to $\beta_{DC_{exp.}}$ and $\beta_{DC_{theo.}}$ will be,

$$\frac{x_{QH_{theo.2}}}{x_{QH_{theo.}}} = \frac{\beta_{DC_{theo.2}}}{\beta_{DC_{exp.}}} = 2.5, \tag{5.18}$$

Therefore, for $\beta_{DC} = \beta_{DC_{theo.}}$, where $\beta_{DC_{theo.}}$ is estimated from the measured Brownian motion spectrum, we get the following values for the experimental and expected signal,

$$\begin{aligned} x_{QH_{exp.2}} &\approx 0.34 \quad \text{pm}, \\ x_{QH_{theo.2}} &\approx 2.12 \quad \text{pm}. \end{aligned} \tag{5.19}$$

Thus, for $\beta = \beta_{DC_{theo.}}$, the experimentally measured root mean square value is roughly 8 times smaller than the expected root mean square value (after taking the 25% blinking effect into account). Whereas, for $\beta = \beta_{DC_{exp.}}$, the two values are roughly the same (eq. 5.12 and 5.13 (after taking the 25% blinking effect into account)). However, at present, we do not know which β value is to be trusted. Therefore we do not know which of the

two sets, of the experimental and theoretical values of quantum hammer effect, is correct. Hence, there is an urgent need to have the precise estimation of β values and this requires experimental investigations.

One such investigation with the temperature of the wire is presented in Appendix B. From the temperature analysis it is clear that the discrepancy in effective mass is coming from the temperature difference between the wire temperature T_{wire} and cryostat temperature T_{cryo} and we can say that calibration of the measured signal is done right in the first place. Therefore, we can say that the first set of the experimental and theoretical values of quantum hammer effect is correct.

Thus, we have verified the effect of excited QD on the motion of the photonic wire. We observed a change in the amplitude of the photonic wire when the dot is excited. The measured amplitude is either similar to the expected value by taking the blinking effect with $\approx 25\%$ "ON" period into account. The measurements are still running, now with the horizontal mode. It would be interesting to compare the measured amplitude for two modes as it should be related to the coupling g_m for the two modes.

5.6 Conclusion

This chapter focused on the details of the experimental realization of quantum hammer effect. After coping with the various challenges faced during the course we managed to observe the effect of the QD, driven resonantly by a modulated laser, on the mechanical motion. The effect is lower than what is predicted in [44] because of the fact that in order to get the dot optically coupled for the resonant excitation, the hybrid coupling g_m gets reduced. In addition to this, the amplitude also gets reduced because of the blinking effect.

The observed change in the amplitude of the wire when the dot is excited is also supported by the change in the phase. When the dot is not excited, the overall phase of the wire motion is 35° with respect to the phase of the resonant modulation at the mechanical resonance frequency. When the dot is excited we see a phase change which is in phase with the modulated laser phase, thereby confirming that the effect is instantaneous and is due to the quantum hammer effect.

Chapter 6

Summary and Perspectives

This thesis work is focused on the study of reverse optomechanical interactions in a hybrid system, consisting of self assembled InAs quantum dots (QDs) embedded within a GaAs photonic wire. This reverse coupling appears as the manipulation of the photonic wire motion when the QD is under modulated resonant optical excitation. This realizes a nano engine run by a single QD on one hand and allows single shot detection of QD state via nanomechanical motion on the other hand. We have successfully completed the primary goal of realizing the quantum hammer effect experimentally.

Thesis begins, in chapter 2, with an overview about the two components of the hybrid system investigated in this work i.e. QDs and photonic wire. General properties of the semiconductor QDs and their energy levels were presented. The description of the "trumpet-like" design of the photonic wires, which was the result of enhancing the extraction efficiency was given. Extraction efficiencies up to 75 % have been obtained [36] therefore allowing the realization of efficient single photon sources [37,38]. The fabrication process and the final sample was also presented. Second part of this chapter focused on the strain mediated optomechanical coupling which couples the two components of the hybrid system. The influence of this strain coupling on the QD optical properties were evidenced both via dynamic [35, 41] and static modulation [39, 42]. As a result of this effect, it is possible to map the position of the QDs within the wire [43]. Moreover, with static strain tuning we could bring two or more QDs in resonance [39] which opened the way for collective effects such as superradiance. Finally, the chapter presented the theoretical aspects of the quantum hammer effect, whose experimental realization was the main goal of this work and is described in detail in Chapter 5.

Chapter 3 presented the photoluminescence spectroscopy and resonant excitation spectroscopy used to characterize the QDs investigated during the course of this work. Resonant excitation spectroscopy was performed in the cross-polarized setup to suppress the

back-reflected laser from the emission detection. One of the main QD which was used in the quantum hammer experiment was characterized using the non-resonant and resonant power and polarization measurements. This QD line showed linear dependence with the non-resonant laser power. To know the exact nature of the line, polarization measurement was performed. Fine structure splitting was not observed indicating that the line is most probably a charged exciton (or trion) with a circular polarization. However, we did observe the change in intensity as the angle of half wave plate is changed. One possible explanation for this observation is the coupling of the emitted light with one of the polarized mode of the trumpet. Moreover, the intensity of the resonant signal also follow the same trend as the PL signal but with a shift of $\approx 25°$. The same trend of the resonant signal indicates that it does not depends on the polarization of the excitation laser, which again confirms that the line is circularly polarized. The observed shift is, however, not understood completely so far. This chapter also presented the power series of the resonant emission (RE) signal of the QD1, used for quantum hammer experiment, with both the non-resonant laser and resonant laser to find the optimum powers for the quantum hammer experiment.

The next chapter focused on the optical detection technique to detect the photonic wire's motion. This method was already implemented successfully in the team by the previous student. Using this technique, it is possible to detect the Brownian motion of the photonic wire of the order of few tens of pm at 5 K. In addition to optical detection, chapter also presented the optical actuation technique to induce the motion in the photonic wire based mainly on the photothermal force at low temperature [42]. We used optical actuation of the photonic wire to determine the coupling $g_m/2\pi$ of QD. Knowledge of the coupling of different QDs is necessary to perform the quantum hammer experiment using the QD with high coupling.

Finally in the last chapter, experimental realization of quantum hammer effect was presented. Chapter started with the description of the experimental setup designed for simultaneous measurement of the QD emission and motion of the photonic wire. At the end of chapter 2, it was predicted that for the system with very strong coupling $g_m/2\pi$, the expected hammer effect induced motion amplitude is about 5 times above the Brownian motion. However, after taking into account the coupling value for the QD studied in this work, the expected signal is instead found to be weak with signal to noise ratio below unity. Thus, it requires longer integration time to average out the incoherent noises and observe the hammer effect. In addition to this, there are various other parameters hindering the observation of hammer effect such as position drifts, power drifts and resonance frequency drifts. To overcome these challenges, the drifts in different parameters is controlled using the stabilization setups. After integrating for about 15-20 hours in stable conditions, we managed to successfully realize the quantum hammer effect. We observed an increase in the amplitude corresponding to the QD resonance. Moreover, the observed effect is in phase with the phase of the resonant laser modulated at mechanical frequency, thereby, proving it to be induced by the quantum hammer effect unlike the photothermal effect which is delayed by approximately 30 ± 5 °.

This result gives the evidence of the first experimental realization of the quantum hammer effect. This opens the possibility to realize a quantum state of motion via the transfer of the "quantumness" of a two-level system towards the motion of a macroscopic oscillator. However, the measured amplitude is very low as compared to that predicted theoretically [44]. One way to improve the signal is to develop the system with high coupling $g_m/2\pi$, and reduced dimensions which will lead us towards the ultimate goal of achieving a quantum limited integrated sensor with ultimate sensing sensibility. With the improved coupling, it would be interesting to perform the "Optical spring effect" measurement. The observation of spring effect will be another way of observing the back action of two-level system on the photonic wire, which appears as a change in its stiffness. This allows non-destructive mechanical readout of the QD population as in the case of quantum hammer effect.

Appendices

Appendix A

Fourier series expansion of square periodic function

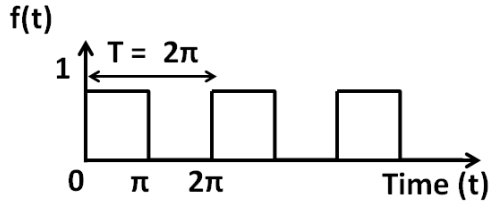

Figure A.1: Sketch of a square function with period 2π.

Using a Fourier series expansion, any periodic function can be represented as an infinite sum of weighted cosines and sines functions of different periods. Figure A.1 shows a square wave function, f(t) with a period 2π, which can be written as follows

$$f(t) = a_0 + a_1\cos(t) + a_2\cos(2t) + a_3\cos(3t) + ... + b_1\sin(t) + b_2\sin(2t) + b_3\sin(3t) + ... \quad \text{(A.1)}$$

where

$$\begin{aligned} a_0 &= \frac{1}{2\pi}\int_0^{2\pi} f(t)dt, \\ a_n &= \frac{1}{\pi}\int_0^{2\pi} f(t)\cos(nt)dt, \quad \texttt{and} \\ b_n &= \frac{1}{\pi}\int_0^{2\pi} f(t)\sin(nt)dt \end{aligned} \quad \text{(A.2)}$$

are the coefficients to be determined by solving eq. A.2. A definite integral from 0 to 2π can be written as the sum of two integrals from [0 to π] and [π to 2π] respectively i.e.

$$\frac{1}{2\pi}\int_0^{2\pi} f(t)dt = \frac{1}{2\pi}\int_0^{\pi} f(t)dt + \frac{1}{2\pi}\int_{\pi}^{2\pi} f(t)dt \tag{A.3}$$

One important thing to note here is that the square wave function is one from 0 to π and zero from π to 2π (fig A.1). This is similar to the hammer induced force as described in chapter 2. Therefore, the second term in eq. A.3 will be zero. This will be true for the determination of all the three coefficients. Therefore,

$$\begin{aligned} a_0 &= \frac{1}{\pi}\int_0^{\pi} f(t)dt \\ &= \frac{1}{\pi}\int_0^{\pi} 1dt \\ &= \frac{1}{\pi}\left[t\right]_0^{\pi} = \frac{1}{2\pi}\pi \\ a_0 &= \frac{1}{2} \end{aligned} \tag{A.4}$$

Similarly,

$$\begin{aligned} a_n &= \frac{1}{2\pi}\int_0^{\pi} f(t)dt \\ &= \frac{1}{2\pi}\int_0^{\pi} 1\cos(nt)dt \\ &= \frac{1}{2\pi}\left[\frac{1}{n}\sin(nt)\right]_0^{\pi} \\ &= \frac{1}{2\pi}\left[\frac{1}{n}\sin(n\pi) - \sin(0)\right] \end{aligned} \tag{A.5}$$

Since, $\sin(n\pi) = 0$ for all n. This will give

$$a_n = 0, \quad \texttt{for all n} \tag{A.6}$$

$$\begin{aligned} b_n &= \frac{1}{\pi}\int_0^{\pi} f(t)dt \\ &= \frac{1}{\pi}\int_0^{\pi} 1\sin(nt)dt \\ &= \frac{1}{\pi}\left[\frac{1}{-n}\cos(nt)\right]_0^{\pi} \\ &= \frac{1}{\pi}\left[\frac{1}{-n}\cos(n\pi) - \cos(0)\right] \end{aligned} \tag{A.7}$$

Since $\cos(n\pi)$ = -1 for odd n, and = 1 for even n, giving

$$b_n = \begin{cases} \frac{2}{n\pi}, & \texttt{for odd n} \\ 0, & \texttt{for even n} \end{cases} \tag{A.8}$$

Hence, the final expansion function from eq. A.1, A.4, A.6, and A.8 is

$$f(t) = \frac{1}{2} + \frac{2}{\pi}\sin(t) + \frac{2}{3\pi}\sin(3t) + ... \tag{A.9}$$

Appendix B

Temperature investigation

As mentioned in Chapter 4 section 4.4.3, that there is a discrepancy of factor 10 in the value of effective mass m_{eff} of the photonic wire obtained from the Comsol simulations ($\approx$ 30 pg) and from the Brownian motion measurement ($\approx$ 3 pg). We tried to link this discrepancy to the error in the calibration of the measured signal i.e. error in the detection sensitivity β_{HF} measurement (see Chapter 5 section 5.5.3 for more details). However, on further investigation we found that this discrepancy is mainly coming from the temperature difference between the sample and the cryostat.

The temperature of the sample used in all the calculations is the one displayed on ITC 601 temperature controller. This is in fact the temperature of the cold finger located below the sample holder. So far we have assumed that the temperature of the sample or the photonic wires is same as that of the cold finger. The temperature extracted from the Brownian motion corresponds to the actual temperature of the photonic wire. Therefore, to cross check the relation between the temperature extracted from the Brownian motion spectrum and the temperatures displayed on ITC 601, we measured the Brownian motion at different temperatures and when we back-calculated the temperature from the Brownian motion spectrum we found out that the actual temperature of the wire T_{wire} is not same as that indicated on the ITC 601 controller T_{cryo}.

In order to extract the temperature from the Brownian motion we do the back calculation using the following equation (recalling 5.14)

$$\beta_{DC_{theo.}} = \sqrt{\frac{m_{eff}\Omega_m^2(\delta V_{th})^2}{k_B T}}, \tag{B.1}$$

Assuming the value for effective mass $m_{eff} = 0.3\ m_{geo}$, where m_{geo} is the geometrical

mass = 90 pg, we calculate $\beta_{DC_{theo.}}$ by taking T as the temperature displayed on the cryostat and $(\delta V_{th})^2$ is the uncalibrated rms voltage as measured on the measurement device. This estimated value of $\beta_{DC_{theo.}}$ is then compared with the one measured experimentally $\beta_{DC_{exp.}}$. The difference between $\beta_{DC_{theo.}}$ and $\beta_{DC_{exp.}}$ is compensated by changing m_{eff} by the same amount. Therefore, for each value of T_{cryo} we will get $m_{eff_{meas}}$ for which $\beta_{DC_{theo.}} = \beta_{DC_{exp.}}$.

Finally we extract the temperature of the wire using the following equation

$$T_{wire} = T_{cryo} \frac{m_{eff_{real}}}{m_{eff_{meas}}}, \tag{B.2}$$

where $m_{eff_{real}} = 0.4\ m_{geo} = 37$ pg is the value of effective mass for which $T_{wire} = T_{cryo}$ iff $T_{cryo} > 40$ K. As shown in figure B.1, T_{wire} is higher than T_{cryo} for lower temperatures, and for both the linear polarizations (H and V) of the fundamental flexural modes. As a result, at the operating cryostat temperature of $T_{cryo} = 5$ K, the actual temperature of the wire is $T_{wire} = 25$ K.

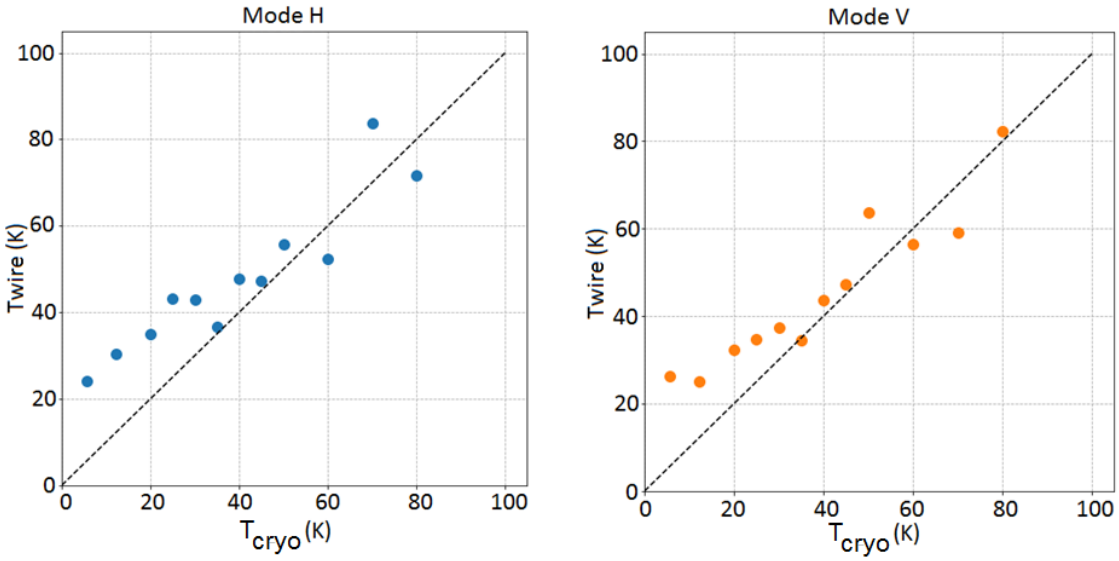

Figure B.1: Bownian temppeature versus cryostat temperature: The wire temperature extracted from a Brownian motion measurement is plotted as a function of the temperature of the cryostat, for both the linearly polarized modes of the photonic wire with top diameter 1.86 µm.

Bibliography

[1] P. Treutlein, C. Genes, K. Hammerer, M. Poggio, and P. Rabl, *"Hybrid mechanical systems"*, In *"Cavity Optomechanics"*, Springer (2014)

[2] I. A. Martínez, É. Roldán, L. Dinis, D. Petrov, J. M. Parrondo, and R. A. Rica, *"Brownian carnot engine"*, Nat. Phys. **12**, 67–70 (2016)

[3] Y. Wen, N. Ares, F. Schupp, T. Pei, G. Briggs, and E. Laird, *"A coherent nanomechanical oscillator driven by single-electron tunnelling"*, Nat. Phys. **16**, 75–82 (2020)

[4] A. D. O'Connell, M. Hofheinz, M. Ansmann, R. C. Bialczak, M. Lenander, E. Lucero, M. Neeley, D. Sank, H. Wang, M. Weides, et al., *"Quantum ground state and single-phonon control of a mechanical resonator"*, Nature **464**, 697–703 (2010)

[5] J. D. Teufel, T. Donner, D. Li, J. W. Harlow, M. Allman, K. Cicak, A. J. Sirois, J. D. Whittaker, K. W. Lehnert, and R. W. Simmonds, *"Sideband cooling of micromechanical motion to the quantum ground state"*, Nature **475**, 359–363 (2011)

[6] G. Anetsberger, E. Gavartin, O. Arcizet, Q. P. Unterreithmeier, E. M. Weig, M. L. Gorodetsky, J. P. Kotthaus, and T. J. Kippenberg, *"Measuring nanomechanical motion with an imprecision below the standard quantum limit"*, Phys. Rev. A **82**, 061804 (2010)

[7] E. Gavartin, P. Verlot, and T. J. Kippenberg. *"A hybrid on-chip optonanomechanical transducer for ultra-sensitive force measurements"*. In *"Conference on Lasers and Electro-Optics (CLEO)"*, page CW1M.3. Ieee, 2012

[8] G. Binnig, C. F. Quate, and C. Gerber, *"Atomic force microscope"*, Phys. Rev. Lett. **56**, 930 (1986)

[9] R. G. Knobel and A. N. Cleland, *"Nanometre-scale displacement sensing using a single electron transistor"*, Nature **424**, 291–293 (2003)

[10] M. LaHaye, O. Buu, B. Camarota, and K. Schwab, *"Approaching the quantum limit of a nanomechanical resonator"*, Science **304**, 74–77 (2004)

[11] H. Mamin and D. Rugar, *"Sub-attonewton force detection at millikelvin temperatures"*, Appl. Phys. Lett. **79**, 3358 (2001)

[12] K. Jensen, K. Kim, and A. Zettl, *"An atomic-resolution nanomechanical mass sensor"*, Nat. Nano. **3**, 533–537 (2008)

[13] A. N. Cleland and M. L. Roukes, *"A nanometre-scale mechanical electrometer"*, Nature **392**, 160–162 (1998)

[14] D. Rugar, R. Budakian, H. Mamin, and B. Chui, *"Single spin detection by magnetic resonance force microscopy"*, Nature **430**, 329–332 (2004)

[15] H. G. Craighead, *"Nanoelectromechanical systems"*, Science **290**, 1532–1535 (2000)

[16] S. Pairis, F. Donatini, M. Hocevar, D. Tumanov, N. Vaish, J. Claudon, J.-P. Poizat, and P. Verlot, *"Shot-noise-limited nanomechanical detection and radiation pressure backaction from an electron beam"*, Phys. Rev. Lett. **122**, 083603 (2019)

[17] C. M. Caves, *"Quantum-mechanical noise in an interferometer"*, Phys. Rev. D **23**, 1693–1708 (1981)

[18] J. D. Teufel, T. Donner, M. Castellanos-Beltran, J. W. Harlow, and K. W. Lehnert, *"Nanomechanical motion measured with an imprecision below that at the standard quantum limit"*, Nat. Nano. **4**, 820–823 (2009)

[19] T. P. Purdy, R. W. Peterson, and C. Regal, *"Observation of radiation pressure shot noise on a macroscopic object"*, Science **339**, 801–804 (2013)

[20] J. Chan, T. M. Alegre, A. H. Safavi-Naeini, J. T. Hill, A. Krause, S. Gröblacher, M. Aspelmeyer, and O. Painter, *"Laser cooling of a nanomechanical oscillator into its quantum ground state"*, Nature **478**, 89–92 (2011)

[21] P. Rabl, P. Cappellaro, M. G. Dutt, L. Jiang, J. Maze, and M. D. Lukin, *"Strong magnetic coupling between an electronic spin qubit and a mechanical resonator"*, Phys. Rev. B **79**, 041302 (2009)

[22] O. Arcizet, V. Jacques, A. Siria, P. Poncharal, P. Vincent, and S. Seidelin, *"A single nitrogen-vacancy defect coupled to a nanomechanical oscillator"*, Nat. Phys. **7**, 879–883 (2011)

[23] S. Bennett, S. Kolkowitz, Q. Unterreithmeier, P. Rabl, A. B. Jayich, J. Harris, and M. D. Lukin, *"Measuring mechanical motion with a single spin"*, New J. Phys. **14**, 125004 (2012)

[24] S. Kolkowitz, A. C. B. Jayich, Q. P. Unterreithmeier, S. D. Bennett, P. Rabl, J. Harris, and M. D. Lukin, *"Coherent sensing of a mechanical resonator with a single-spin qubit"*, Science **335**, 1603–1606 (2012)

[25] S. Hong, M. S. Grinolds, P. Maletinsky, R. L. Walsworth, M. D. Lukin, and A. Yacoby, *"Coherent, mechanical control of a single electronic spin"*, Nano Lett. **12**, 3920–3924 (2012)

[26] J. Teissier, A. Barfuss, P. Appel, E. Neu, and P. Maletinsky, *"Strain coupling of a nitrogen-vacancy center spin to a diamond mechanical oscillator"*, Phys. Rev. Lett. **113**, 020503 (2014)

[27] P. Ovartchaiyapong, K. W. Lee, B. A. Myers, and A. C. B. Jayich, *"Dynamic strain-mediated coupling of a single diamond spin to a mechanical resonator"*, Nat. Commun. **5**, 4429 (2014)

[28] B. Pigeau, S. Rohr, L. M. De Le[8]pinay, A. Gloppe, V. Jacques, and O. Arcizet, *"Observation of a phononic mollow triplet in a multimode hybrid spin-nanomechanical system"*, Nat. Commun. **6**, 8603 (2015)

[29] M. LaHaye, J. Suh, P. Echternach, K. C. Schwab, and M. L. Roukes, *"Nanomechanical measurements of a superconducting qubit"*, Nature **459**, 1603–1606 (2009)

[30] J.-M. Pirkkalainen, S. Cho, J. Li, G. Paraoanu, P. Hakonen, and M. Sillanpää, *"Hybrid circuit cavity quantum electrodynamics with a micromechanical resonator"*, Nature **494**, 211–215 (2013)

[31] G. A. Steele, A. K. Hüttel, B. Witkamp, M. Poot, H. B. Meerwaldt, L. P. Kouwenhoven, and H. S. van der Zant, *"Strong coupling between single-electron tunneling and nanomechanical motion"*, Science **325**, 1103–1107 (2009)

[32] G. Sallen, A. Tribu, T. Aichele, R. André, L. Besombes, C. Bougerol, S. Tatarenko, K. Kheng, and J. P. Poizat, *"Exciton dynamics of a single quantum dot embedded in a nanowire"*, Phys. Rev. B **80**, 085310 (2009)

[33] S. D. Bennett, L. Cockins, Y. Miyahara, P. Grütter, and A. A. Clerk, *"Strong electromechanical coupling of an atomic force microscope cantilever to a quantum dot"*, Phys. Rev. Lett. **104**, 017203 (2010)

[34] M. Montinaro, G. Wüst, M. Munsch, Y. Fontana, E. Russo-Averchi, M. Heiss, A. Fontcuberta i Morral, R. J. Warburton, and M. Poggio, *"Quantum dot opto-mechanics in a fully self-assembled nanowire"*, Nano Lett. **14**, 4454–4460 (2014)

[35] I. Yeo, P.-L. De Assis, A. Gloppe, E. Dupont-Ferrier, P. Verlot, N. S. Malik, E. Dupuy, J. Claudon, J.-M. Gérard, A. Auffèves, et al., *"Strain-mediated coupling in a quantum dot–mechanical oscillator hybrid system"*, Nat. Nanotech. **9**, 106–110 (2014)

[36] M. Munsch, N. S. Malik, E. Dupuy, A. Delga, J. Bleuse, J.-M. Gérard, J. Claudon, N. Gregersen, and J. Mørk, *"Dielectric gaas antenna ensuring an efficient broadband coupling between an inas quantum dot and a gaussian optical beam"*, Phys. Rev. Lett. **110**, 177402 (2013)

[37] J. Claudon, J. Bleuse, N. S. Malik, M. Bazin, P. Jaffrennou, N. Gregersen, C. Sauvan, P. Lalanne, and J.-M. Gérard, *"A highly efficient single-photon source based on a quantum dot in a photonic nanowire"*, Nat. Photonics **4**, 174–177 (2010)

[38] H. A. Nguyen, *"Non-linéarité optique géante à deux modes à partir d'une boîte quantique semi-conductrice dans un fil photonique"*, PhD thesis, Grenoble Alpes (2016)

[39] D. Tumanov, N. Vaish, H. Nguyen, Y. Curé, J.-M. Gérard, J. Claudon, F. Donatini, and J.-P. Poizat, *"Static strain tuning of quantum dots embedded in a photonic wire"*, Appl. Phys. Lett. **112**, 123102 (2018)

[40] M. Munsch, A. V. Kuhlmann, D. Cadeddu, J.-M. Gérard, J. Claudon, M. Poggio, and R. J. Warburton, *"Resonant driving of a single photon emitter embedded in a mechanical oscillator"*, Nat. Commun. **8**, 76 (2017)

[41] I. Yeo, *"Une boite quantique dans un fil photonique: spectroscopie et optomécanique"*, PhD thesis, Université de Grenoble (2012)

[42] D. Tumanov, *"Actuation and motion detection of different micro-and nano-structures"*, PhD thesis, Université Grenoble Alpes (2017)

[43] P.-L. De Assis, I. Yeo, A. Gloppe, H. Nguyen, D. Tumanov, E. Dupont-Ferrier, N. Malik, E. Dupuy, J. Claudon, J.-M. Gérard, et al., *"Strain-gradient position mapping of semiconductor quantum dots"*, Phys. Rev. Lett. **118**, 117401 (2017)

[44] A. Auffèves and M. Richard, *"Optical driving of macroscopic mechanical motion by a single two-level system"*, Phys. Rev. A **90**, 023818 (2014)

[45] L. E. Brus, *"Electron–electron and electron-hole interactions in small semiconductor crystallites: The size dependence of the lowest excited electronic state"*, J. Chem. Phys **80**, 4403–4409 (1984)

[46] T. Jamieson, R. Bakhshi, D. Petrova, R. Pocock, M. Imani, and A. M. Seifalian, *"Biological applications of quantum dots"*, Biomaterials **28**, 4717–4732 (2007)

[47] J. Wu, S. Chen, A. Seeds, and H. Liu, *"Quantum dot optoelectronic devices: lasers, photodetectors and solar cells"*, J. Phys. D: Appl. Phys. **48**, 363001 (2015)

[48] P. Martyniuk and A. Rogalski, *"Quantum-dot infrared photodetectors: Status and outlook"*, Prog. Quantum Elec. **32**, 89–120 (2008)

[49] O. E. Semonin, J. M. Luther, and M. C. Beard, *"Quantum dots for next-generation photovoltaics"*, Materials today **15**, 508–515 (2012)

[50] X. Gong, Z. Yang, G. Walters, R. Comin, Z. Ning, E. Beauregard, V. Adinolfi, O. Voznyy, and E. H. Sargent, *"Highly efficient quantum dot near-infrared light-emitting diodes"*, Nat. Photonics **10**, 253–257 (2016)

[51] N. Somaschi, V. Giesz, L. De Santis, J. Loredo, M. P. Almeida, G. Hornecker, S. L. Portalupi, T. Grange, C. Antón, J. Demory, et al., *"Near-optimal single-photon sources in the solid state"*, Nat. Photonics **10**, 340–345 (2016)

[52] X. Ding, Y. He, Z.-C. Duan, N. Gregersen, M.-C. Chen, S. Unsleber, S. Maier, C. Schneider, M. Kamp, S. Höfling, et al., *"On-demand single photons with high extraction efficiency and near-unity indistinguishability from a resonantly driven quantum dot in a micropillar"*, Phys. Rev. Lett. **116**, 020401 (2016)

[53] P. Senellart, G. Solomon, and A. White, *"High-performance semiconductor quantum-dot single-photon sources"*, Nat. Nano. **12**, 020401 (2017)

[54] D. Bera, L. Qian, T.-K. Tseng, and P. H. Holloway, *"Quantum dots and their multimodal applications: a review"*, Materials **3**, 2260–2345 (2010)

[55] N. S. Malik, *"Photonic nanowires : a new geometry to realize bright sources of quantum light"*, PhD thesis, Université Grenoble Alpes (2011)

[56] C. Cohen-Tannoudji, *"B. diu, and f. laloe"*, Quantum Mechanics **1** (1977)

[57] R. Heitz, A. Kalburge, Q. Xie, M. Grundmann, P. Chen, A. Hoffmann, A. Madhukar, and D. Bimberg, *"Excited states and energy relaxation in stacked inas/gaas quantum dots"*, Phys. Rev. B **57**, 9050–9060 (1998)

[58] J. Finley, A. Ashmore, A. Lemaître, D. Mowbray, M. Skolnick, I. Itskevich, P. Maksym, M. Hopkinson, and T. Krauss, *"Charged and neutral exciton complexes in individual self-assembled in (ga) as quantum dots"*, Phys. Rev. B **63**, 073307 (2001)

[59] I. Friedler, C. Sauvan, J.-P. Hugonin, P. Lalanne, J. Claudon, and J.-M. Gérard, *"Solid-state single photon sources: the nanowire antenna"*, Opt. Express **17**, 2095–2110 (2009)

[60] J. Bleuse, J. Claudon, M. Creasey, N. S. Malik, J.-M. Gérard, I. Maksymov, J.-P. Hugonin, and P. Lalanne, *"Inhibition, enhancement, and control of spontaneous emission in photonic nanowires"*, Phys. Rev. Lett. **106**, 103601 (2011)

[61] K. J. Vahala, *"Optical microcavities"*, Nature **424**, 839–846 (2003)

[62] L. Lanco and P. Senellart, *"A highly efficient single photon-single quantum dot interface"*, In *"Engineering the Atom-Photon Interaction"*, Springer (2015)

[63] J. Gérard, B. Sermage, B. Gayral, B. Legrand, E. Costard, and V. Thierry-Mieg, *"Enhanced spontaneous emission by quantum boxes in a monolithic optical microcavity"*, Phys. Rev. Lett. **81**, 1110–1113 (1998)

[64] J. P. Reithmaier, G. Sęk, A. Löffler, C. Hofmann, S. Kuhn, S. Reitzenstein, L. Keldysh, V. Kulakovskii, T. Reinecke, and A. Forchel, *"Strong coupling in a single quantum dot–semiconductor microcavity system"*, Nature **432**, 197–200 (2004)

[65] A. Dousse, L. Lanco, J. Suffczyński, E. Semenova, A. Miard, A. Lemaître, I. Sagnes, C. Roblin, J. Bloch, and P. Senellart, *"Controlled light-matter coupling for a single quantum dot embedded in a pillar microcavity using far-field optical lithography"*, Phys. Rev. Lett. **101**, 267404 (2008)

[66] Y. Akahane, T. Asano, B.-S. Song, and S. Noda, *"High-q photonic nanocavity in a two-dimensional photonic crystal"*, Nature **425**, 944–947 (2003)

[67] S. Cortez, O. Krebs, P. Voisin, and J. Gérard, *"Polarization of the interband optical dipole in inas/gaas self-organized quantum dots"*, Phys. Rev. B **63**, 233306 (2001)

[68] N. Gregersen, T. R. Nielsen, J. Claudon, J.-M. Gérard, and J. Mørk, *"Controlling the emission profile of a nanowire with a conical taper"*, Opt. Lett. **33**, 1693–1695 (2008)

[69] I. Yeo, N. S. Malik, M. Munsch, E. Dupuy, J. Bleuse, Y.-M. Niquet, J.-M. Gérard, J. Claudon, É. Wagner, S. Seidelin, et al., *"Surface effects in a semiconductor photonic nanowire and spectral stability of an embedded single quantum dot"*, Appl. Phy. Lett. **99**, 233106 (2011)

[70] G. W. Bryant, M. Zieliński, N. Malkova, J. Sims, W. Jaskólski, and J. Aizpurua, *"Controlling the optics of quantum dots with nanomechanical strain"*, Phys. Rev. B **84**, 235412 (2011)

[71] K. Jöns, R. Hafenbrak, R. Singh, F. Ding, J. Plumhof, A. Rastelli, O. Schmidt, G. Bester, and P. Michler, *"Dependence of the redshifted and blueshifted photoluminescence spectra of single in x ga 1- x as/gaas quantum dots on the applied uniaxial stress"*, Phys. Rev. Lett. **107**, 217402 (2011)

[72] P. Stepanov, M. Elzo-Aizarna, J. Bleuse, N. S. Malik, Y. Curé, E. Gautier, V. Favre-Nicolin, J.-M. Gérard, and J. Claudon, *"Large and uniform optical emission shifts in quantum dots strained along their growth axis"*, Nano Lett. **16**, 3215–3220 (2016)

[73] A. Auffèves, D. Gerace, S. Portolan, A. Drezet, and M. F. Santos, *"Few emitters in a cavity: From cooperative emission to individualization"*, New J. Phys. **13**, 093020 (2011)

[74] F. Wu, R. Grove, and S. Ezekiel, *"Investigation of the spectrum of resonance fluorescence induced by a monochromatic field"*, Phys. Rev. Lett. **35**, 1426–1429 (1975)

[75] G. Wrigge, I. Gerhardt, J. Hwang, G. Zumofen, and V. Sandoghdar, *"Efficient coupling of photons to a single molecule and the observation of its resonance fluorescence"*, Nat. Phys. **4**, 60–66 (2008)

[76] O. Astafiev, A. M. Zagoskin, A. Abdumalikov, Y. A. Pashkin, T. Yamamoto, K. Inomata, Y. Nakamura, and J. Tsai, *"Resonance fluorescence of a single artificial atom"*, Science **327**, 840–843 (2010)

[77] A. Muller, E. B. Flagg, P. Bianucci, X. Wang, D. G. Deppe, W. Ma, J. Zhang, G. Salamo, M. Xiao, and C.-K. Shih, *"Resonance fluorescence from a coherently driven semiconductor quantum dot in a cavity"*, Phys. Rev. Lett. **99**, 187402 (2007)

[78] S. Ates, S. Ulrich, S. Reitzenstein, A. Löffler, A. Forchel, and P. Michler, *"Post-selected indistinguishable photons from the resonance fluorescence of a single quantum dot in a microcavity"*, Phys. Rev. Lett. **103**, 167402 (2009)

[79] C. Santori, D. Fattal, J. Vučković, G. S. Solomon, E. Waks, and Y. Yamamoto, *"Submicrosecond correlations in photoluminescence from inas quantum dots"*, Phys. Rev. B **69**, 205324 (2004)

[80] C. Matthiesen, A. N. Vamivakas, and M. Atatüre, *"Subnatural linewidth single photons from a quantum dot"*, Phys. Rev. Lett. **108**, 093602 (2012)

[81] H.-S. Nguyen, G. Sallen, C. Voisin, P. Roussignol, C. Diederichs, and G. Cassabois, *"Ultra-coherent single photon source"*, Appl. Phys. Lett. **99**, 261904 (2011)

[82] H. S. Nguyen, G. Sallen, M. Abbarchi, R. Ferreira, C. Voisin, P. Roussignol, G. Cassabois, and C. Diederichs, *"Photoneutralization and slow capture of carriers in quantum dots probed by resonant excitation spectroscopy"*, Phys. Rev. B **87**, 115305 (2013)

[83] H.-S. Nguyen, G. Sallen, C. Voisin, P. Roussignol, C. Diederichs, and G. Cassabois, *"Optically gated resonant emission of single quantum dots"*, Phys. Rev. Lett. **108**, 057401 (2012)

[84] H. Nguyen, T. Grange, B. Reznychenko, I. Yeo, P.-L. De Assis, D. Tumanov, F. Fratini, N. Malik, E. Dupuy, N. Gregersen, et al., *"Giant nonlinear interaction between two optical beams via a quantum dot embedded in a photonic wire"*, Phys. Rev. B **97**, 201106 (2018)

[85] A. V. Kuhlmann, J. Houel, D. Brunner, A. Ludwig, D. Reuter, A. D. Wieck, and R. J. Warburton, *"A dark-field microscope for background-free detection of resonance fluorescence from single semiconductor quantum dots operating in a set-and-forget mode"*, Rev. Sci. Instrum. **84**, 073905 (2013)

[86] S. Jung, H. Yeo, I. Yun, J. Leem, I. Han, J. Kim, and J. Lee, *"Size distribution effects on self-assembled inas quantum dots"*, Journal of Materials Science: Materials in Electronics **18**, 191–194 (2007)

[87] G. Sęk, P. Podemski, J. Misiewicz, L. Li, A. Fiore, and G. Patriarche, *"Photoluminescence from a single ingaas epitaxial quantum rod"*, Appl. Phys. Lett. **92**, 021901 (2008)

[88] J. Kettler, M. Paul, F. Olbrich, K. Zeuner, M. Jetter, P. Michler, M. Florian, C. Carmesin, and F. Jahnke, *"Neutral and charged biexciton-exciton cascade in near-telecom-wavelength quantum dots"*, Phys. Rev. B **94**, 045303 (2016)

[89] J. Finley, D. Mowbray, M. Skolnick, A. Ashmore, C. Baker, A. Monte, and M. Hopkinson, *"Fine structure of charged and neutral excitons in inas-al 0.6 ga 0.4 as quantum dots"*, Phys. Rev. B **66**, 153316 (2002)

[90] N. Cade, H. Gotoh, H. Kamada, H. Nakano, and H. Okamoto, *"Fine structure and magneto-optics of exciton, trion, and charged biexciton states in single inas quantum dots emitting at 1.3 μ m"*, Phys. Rev. B **73**, 115322 (2006)

[91] S. Amloy, K. Karlsson, T. Andersson, and P.-O. Holtz, *"On the polarized emission from exciton complexes in gan quantum dots"*, Appl. Phys. Lett. **100**, 021901 (2012)

[92] J. Claudon, N. Gregersen, P. Lalanne, and J.-M. Gérard, *"Harnessing light with photonic nanowires: fundamentals and applications to quantum optics"*, ChemPhysChem **14**, 2393–2402 (2013)

[93] M. Munsch, J. Claudon, J. Bleuse, N. S. Malik, E. Dupuy, J.-M. Gérard, Y. Chen, N. Gregersen, and J. Mørk, *"Linearly polarized, single-mode spontaneous emission in a photonic nanowire"*, Phys. Rev. Lett. **108**, 077405 (2012)

[94] C. Cohen-Tannoudji, J. Dupont-Roc, and G. Grynberg, *"Atom-photon interactions: basic processes and applications"*, Atom-Photon Interactions: Basic Processes and Applications, by Claude Cohen-Tannoudji, Jacques Dupont-Roc, Gilbert Grynberg, pp. 678. ISBN 0-471-29336-9. Wiley-VCH, March 1998. (1998)

[95] G. Sallen, A. Tribu, T. Aichele, R. André, L. Besombes, C. Bougerol, M. Richard, S. Tatarenko, K. Kheng, and J.-P. Poizat, *"Subnanosecond spectral diffusion measurement using photon correlation"*, Nat. Photonics **4**, 696–699 (2010)

[96] J. Seufert, R. Weigand, G. Bacher, T. Kümmell, A. Forchel, K. Leonardi, and D. Hommel, *"Spectral diffusion of the exciton transition in a single self-organized quantum dot"*, Appl. Phys. Lett. **76**, 1872–1874 (2000)

[97] H. Kamada and T. Kutsuwa, *"Broadening of single quantum dot exciton luminescence spectra due to interaction with randomly fluctuating environmental charges"*, Phys. Rev. B **78**, 155324 (2008)

[98] A. Berthelot, I. Favero, G. Cassabois, C. Voisin, C. Delalande, P. Roussignol, R. Ferreira, and J.-M. Gérard, *"Unconventional motional narrowing in the optical spectrum of a semiconductor quantum dot"*, Nat. Phys. **2**, 759–764 (2006)

[99] A. Majumdar, E. D. Kim, and J. Vučković, *"Effect of photogenerated carriers on the spectral diffusion of a quantum dot coupled to a photonic crystal cavity"*, Phys. Rev. B **84**, 195304 (2011)

[100] A. Högele, S. Seidl, M. Kroner, K. Karrai, R. J. Warburton, B. D. Gerardot, and P. M. Petroff, *"Voltage-controlled optics of a quantum dot"*, Phys. Rev. Lett. **93**, 217401 (2004)

[101] K. Konthasinghe, J. Walker, M. Peiris, C.-K. Shih, Y. Yu, M. Li, J. He, L. Wang, H. Ni, Z. Niu, et al., *"Coherent versus incoherent light scattering from a quantum dot"*, Phys. Rev. B **85**, 235315 (2012)

[102] A. Reinhard, T. Volz, M. Winger, A. Badolato, K. J. Hennessy, E. L. Hu, and A. Imamoğlu, *"Strongly correlated photons on a chip"*, Nat. Photonics **6**, 93–96 (2012)

[103] O. Gazzano, S. M. De Vasconcellos, C. Arnold, A. Nowak, E. Galopin, I. Sagnes, L. Lanco, A. Lemaître, and P. Senellart, *"Bright solid-state sources of indistinguishable single photons"*, Nat. Commun. **4**, 1–6 (2013)

[104] X. Lu, J. Vaillancourt, and H. Wen, *"Temperature-dependent energy gap variation in inas/gaas quantum dots"*, Appl. Phys. Lett. **96**, 173105 (2010)

[105] K. Konthasinghe, C. Chakraborty, N. Mathur, L. Qiu, A. Mukherjee, G. D. Fuchs, and A. N. Vamivakas, *"Rabi oscillations and resonance fluorescence from a single hexagonal boron nitride quantum emitter"*, Optica **6**, 542–548 (2019)

[106] A. Gloppe, *"Nano-optomechanics at the waist of a focused laser beam : cartography of the optical force field and bidimensional backaction"*, PhD thesis, Université de Grenoble (2014)

[107] R. Kubo, *"The fluctuation-dissipation theorem"*, Rep. Prog. Phys. **29**, 255–284 (1966)

[108] M. Aspelmeyer, T. J. Kippenberg, and F. Marquardt, *"Cavity optomechanics"*, Rev. Mod. Phys. **86**, 1391–1452 (2014)

[109] A. Ashkin, J. M. Dziedzic, and T. Yamane, *"Optical trapping and manipulation of single cells using infrared laser beams"*, Nature **330**, 769–771 (1987)

[110] A. Ashkin, *"Acceleration and trapping of particles by radiation pressure"*, Phys. Rev. Lett. **24**, 156–159 (1970)

[111] M. L. Povinelli, S. G. Johnson, M. Lončar, M. Ibanescu, E. J. Smythe, F. Capasso, and J. Joannopoulos, *"High-q enhancement of attractive and repulsive optical forces between coupled whispering-gallery-mode resonators"*, Opt. Express **13**, 8286–8295 (2005)

[112] M. L. Povinelli, M. Lončar, M. Ibanescu, E. J. Smythe, S. G. Johnson, F. Capasso, and J. D. Joannopoulos, *"Evanescent-wave bonding between optical waveguides"*, Opt. Lett. **30**, 3042–3044 (2005)

[113] G. S. Wiederhecker, L. Chen, A. Gondarenko, and M. Lipson, *"Controlling photonic structures using optical forces"*, Nature **462**, 633–636 (2009)

[114] H. Rokhsari, T. J. Kippenberg, T. Carmon, and K. J. Vahala, *"Radiation-pressure-driven micro-mechanical oscillator"*, Opt. Express **13**, 5293–5301 (2005)

[115] M. Eichenfield, R. Camacho, J. Chan, K. J. Vahala, and O. Painter, *"A picogram- and nanometre-scale photonic-crystal optomechanical cavity"*, Nature **459**, 550–555 (2009)

[116] M. Li, W. Pernice, C. Xiong, T. Baehr-Jones, M. Hochberg, and H. Tang, *"Harnessing optical forces in integrated photonic circuits"*, Nature **456**, 480–484 (2008)

[117] O. Arcizet, P.-F. Cohadon, T. Briant, M. Pinard, and A. Heidmann, *"Radiation-pressure cooling and optomechanical instability of a micromirror"*, Nature **444**, 71–74 (2006)

[118] S. Gigan, H. Böhm, M. Paternostro, F. Blaser, G. Langer, J. Hertzberg, K. C. Schwab, D. Bäuerle, M. Aspelmeyer, and A. Zeilinger, *"Self-cooling of a micromirror by radiation pressure"*, Nature **444**, 67–70 (2006)

[119] P. Verlot, A. Tavernarakis, T. Briant, P. F. Cohadon, and A. Heidmann, *"Back-action amplification and quantum limits in optomechanical measurements"*, Phys. Rev. Lett. **104**, 133602 (2010)

[120] O. Hahtela and I. Tittonen, *"Optical actuation of a macroscopic mechanical oscillator"*, Appl. Phys. B **81**, 589–596 (2005)

[121] H. S. Lee and S. H. Yang, *"Long-term stabilization of the frequency and power of a laser diode"*, Rev. Sci. Instrum. **67**, 2671–2674 (1996)

[122] F. Tricot, D. Phung, M. Lours, S. Guérandel, and E. De Clercq, *"Power stabilization of a diode laser with an acousto-optic modulator"*, Rev. Sci. Instrum. **89**, 113112 (2018)

[123] Z. Instruments. *"Hf2 user manual."*, 2018